DNA Origami Catalysts

By

Klaudia Englert

UNIVERSITY OF BIRMINGHAM

A thesis submitted to the

University of Birmingham

for the degree of

DOCTOR OF PHILOSOPHY

School of Chemistry

College of Engineering and Physical Science

University of Birmingham

November 2019

DEFCON 705 – Full Rights Version

Full Rights Version
UK OFFICIAL
CONDITIONS OF SUPPLY – FULL RIGHTS This document is supplied in confidence to MOD in accordance with Contract No DSTLX-1000098487. The document comprises information proprietary to University of Birmingham and whose unauthorised disclosure would cause damage to the interests of University of Birmingham. The document is supplied to MOD as a FULL RIGHTS VERSION under the terms of DEFCON 705 (Edn 11/02) and, except with the prior written permission of University of Birmingham, MOD's rights of use and dissemination in the document are limited to those set out in Clause 12 of DEFCON 705 (Edn 11/02) for the use of Full Rights Versions of Technical Deliverables. Requests for permission for wider use or dissemination should be made to University of Birmingham.

Abstract

DNA has a vast amount of applications beyond being a principle molecular component of life. DNA nanotechnology plays an important role within the field of synthetic biology, which has been referred to as one of the flagships of the Fourth Industrial Revolution, as it explores a broad range of interdisciplinary fields in order to tackle some of the greatest challenges of the modern world. One of these challenges is increasing power demand and storage, for which generating cheaper fuel cells with improved efficiencies is an active area of research. The work described in this thesis has largely focused on exploiting DNA nanotechnology to provide new assemblies that could act as material precursors for next-generation fuel cells. It is divided into four sections:

1. DNA extracted from salmon milt was used as a scaffold for fuel cell catalyst precursor development. Through the addition of cisplatin, a range of platinum loadings within the DNA scaffold were determined and analysed using spectroscopic techniques.
2. A range of DNA duplexes, nanostructures and origami assemblies were employed as a scaffold for the precise placement of platinum metals along the DNA backbone through the addition of cisplatin.
3. Iron was explored as an alternative metal to platinum that is cheaper and more readily available. It was incorporated into various DNA duplexes and nanostructures in the form of ferrocene using automated solid phase synthesis.
4. An approach to develop more robust DNA nanostructures was explored through the application of anthracene photocyclisation to covalently link assemblies together.

Acknowledgements

I would like to start by thanking my supervisors; Professor James Tucker, Professor Alexander Robinson and Doctor Neil Rees for giving me the opportunity of completing this PhD. You had such an amazing connection and created a truly exceptional trio – a real pleasure to work with! Jim, thank you for always having trust in me and my scientific capabilities. You have never doubted me which filled me with confidence from day one, you greatly contributed to my professional growth throughout the past four years and exercised a lot of patience in me. Alex, your amazing idea is what started this project and your patience is what saw it through to the end. Neil, I can't thank you enough for the support and understanding you gave me over the years! Your sense of humour was pivotal in the success of my PhD.

I would like to thank the past and present members of the Tucker group. Your knowledge and experience is invaluable. Thank you for being so approachable and being there for me whenever I needed it. Special thanks to Media Ismail, Ed Wilkinson, Georgina Leck, Charlotte Farrow, Marium Rana and Lily Baily for your friendship, advice, many many coffee breaks and support in my unstable personal life. I feel very lucky to have you all! Thank you to the Grainger and Cox Groups for creating a 'one of a kind' atmosphere in our office; your laughs, jokes and even dramas will all be missed! Nick Cundy, I can't thank you enough for the last minute organic chemistry advice which helped me secure the best job ever! Thank you to all the staff part of the Chemistry Analytical Facility. Most of all, I would like to thank Chi Tsang. You made my PhD happen! Through your always accurate technical advice, and much needed personal support – You are the reason why I didn't need any extra mental help! You made me believe everything was possible and showed me how to achieve it. Thank you for becoming the very best friend I could ask for!

To the DSTL cohort. Thank you, Petra Oyston for organising this exceptional PhD scheme. Thank you to all DSTL PhD students – we have formed such an amazing network! I'm especially grateful to Ruba Hendi, my twin PhD, who has worked so hard to give meaning to my work. Thank you to Oliver Daubney, Paul Teare and Paolo

Passaretti for the serious and also not-so-serious conversations. Special thanks to Ioannis Zampetakis for making me re-evaluate my life's choices.

To the D'Sa and Pereira families. You have created a second home for me and have accepted me with open arms into your life. You have been there for me when my own family couldn't. I will be forever grateful for all the help and support you have given me, and I only wish I can do the same for you. Quinn, you were, and are and always will be the most special person in my life. I love you.

To my family who has been there for me since I can remember. Thank you for being so open minded and allowing me to pursue my goals even though it was difficult for you. Mom and Dad, thank you for being so understanding and putting up with me throughout all these years. You are the most loving and caring parents a child can be blessed with. I love you all so much.

I am thankful to so many of you I came across in the past four years. You have all contributed to my success and who I am today.

Table of Contents

Abbreviations

2D	Two-dimensional
3D	Three-dimensional
3LL	Three-Layer Logpile
3PS	Three Point Star
ABPP	Activity-based protein profiling
ACN	Acetonitrile
AFC	Alkaline Fuel Cells
AFM	Atomic Force Microscopy
APS	Ammonium persulphate
CAR	Collision-activated-reaction
CD	Circular Dichroism
Cis-DDP	*Cis*-diamminedichloroplatinum (II)
cisPt	Cisplatin
Cp	Cyclopentadiene
CPG	Controlled pore glass
CT-DNA	Calf Thymus - Deoxyribose Nucleic Acid
CTAB	Cetyltrimethylammonium bromide
CTMA-Cl	Cetyltrimethylammonium chloride
Cy3	Cyanine 3
DCM	Dichloromethane

DIPEA	N,N-Diisopropylethylamine
DMAP	4-Dimethylaminopyridine
DMF	Dimethylformamide
DMFC	Direct Methanol Fuel Cells
DMT	N,N-Dimethyltryptamine
DNA	Deoxyribose Nucleic Acid
dpp	2,9-diphenyl-1,10-N,N-phenanthroline
ds	Double stranded
DX	Double-crossover
E. coli	Escherichia coli
EBL	Electron blocking layer
EBL / e-beam	Electron Beam Lithography
ECL	Enhanced Chemiluminescence
ED	Electroless deposition
EDTA	Ethylenediaminetetraacetic acid
ESI-CID	Electrospray Ionisation Collision Induced Dissociation
ESI-MS	Electrospray Ionisation Mass Spectrometry
EtBr	Ethidium bromide
ETT	Ethylthiotetrazole
Fc	Ferrocene
FFAs	Free fatty acids
HA	Hexylamine

HBTU	N,N,N',N'-Tetramethyl-O-(1H-benzotriazol-1-yl)uranium hexafluorophosphate
HFIP	Hexafluoro-2-propanol
iPSCs	Induced pluripotent stem cells
kb	Kilobase
LC	Liquid chromatography
MALDI	Matrix-assisted laser desorption/ionization
MCFC	Molten Carbonate Fuel Cell
mRNA	Messenger RNA
MS/MS	Tandem Mass Spectrometry
MUC-1	Mucin 1
N7	Nitrogen 7
NIR	Near-infrared
NMI	N-methylimidazole
NMR	Nuclear Magnetic Resonance
OFETs	Organic Field Effect Transistors
OLED	Organic light emitting diodes
OPV	Organic photovoltaic
PAFC	Phosphoric Acid Fuel Cell
PAGE	Polyacrylamide Gel Electrophoresis
PCR	Polymerase chain reaction
PEG	Polyethylene glycol

PEMFC	Polymeric Electrolyte Membrane Fuel Cells
PHAs	Polyhydroxyalkanoates
PMMA	Polymethyl methacrylate
Pt	Platinum
RNA	Ribose Nucleic Acid
RP-HPLC	Reversed-Phase High Performance Liquid Chromatography
Ru	Ruthenium
SAM	Self-assembled Monolayer
SDS	Sodium dodecyl sulphate
SEA	Strong electrostatic adsorption
SEC	Size Exclusion Chromatography
Si	Silicon
SNP	Single Nucleotide Polymorphism
SOFC	Solid Oxide Fuel Cell
ss	Single stranded
ST-DNA	Salmon Testes - Deoxyribose Nucleic Acid
STEM	Scanning transmission electron microscopy
STM	Scanning tunnelling microscopy
TAMg	Tris Acetate Magnesium
TBE	Tris Borate EDTA
TCA	Trichloroacetic acid

TEA	Triethylamine
TEAA	Triethylamine acetate
TEMED	Tetramethylethylenediamine
THF	Tetrahydrofurane
TOF	Time-of-flight
UPLC	Ultra-Performance Liquid Chromatography
UTP	Uridine-5'-triphosphate
UV/Vis	Ultraviolet-visible

DNA bases

A	Adenine
C	Cytosine
G	Guanine
T	Thymine

Chapter 1 - Introduction

1.1 Introduction

This chapter provides an introduction to DNA Nanotechnology and synthetic biology as well as their applications. It begins with a background to DNA chemistry and recent progress in the development of DNA nanostructure assemblies. Furthermore, cisplatin and its modes of binding to DNA will be covered. An emerging field of synthetic biology is discussed with its abundant range of applications. Finally, fuel cell technology is described along with its limitations, particularly involving catalysis.

1.2 DNA

DNA is a bio-polymer which stores genetic information in all living organisms. The structure of this biomolecule was a matter of debate for some time until the work of Rosalind Franklin, James D. Watson and Francis Crick[1, 2], who along with Maurice Wilkins, were awarded a Nobel Prize in Physiology or Medicine in 1962 for the discovery of secondary structure of DNA.[3]

1.2.1 DNA structure

Deoxyribonucleic acid (DNA) is composed of repeating monomers called nucleotides. These monomers are composed of a deoxyribose sugar, a phosphate group and a heterocyclic base. Adjacent nucleotides are linked by a phosphate group in a specific direction from 3' carbon of one sugar unit to the 5' carbon of the next unit (Figure 1.1). There are four types of nucleobases; two purines: adenine (A) & guanine (G),

and two pyrimidines: thymine (T) & cytosine (C), as shown in Figure 1.2.[4] The order of the nucleobases in a DNA sequence encodes genetic information in living organisms, translated to assemble amino acids, the building blocks of proteins.

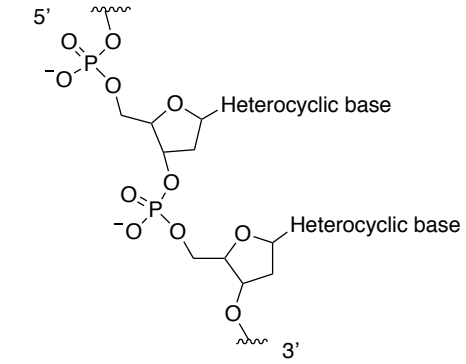

Phosphate Deoxyribose Sugar Backbone

Figure 1.1 – Structure of Phosphate Deoxyribose sugar DNA backbone.

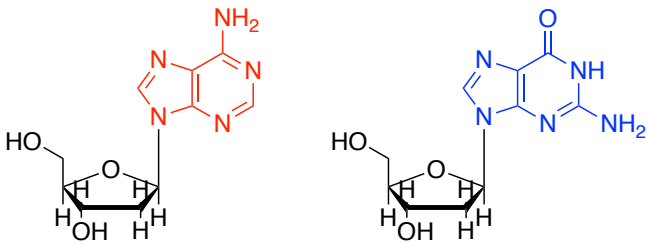

Adenosine

Guanosine

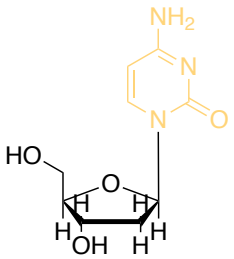

Cytidine

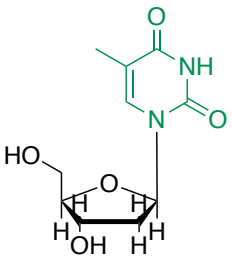

Thymidine

Figure 1.2 – DNA bases: Adenosine, Guanosine, Cytidine and Thymidine.

Two single strands of DNA are linked by base pairing forming a double-helical structure. This process of duplex formation is known as hybridisation and proceeds by two DNA strands, oriented in an anti-parallel direction, spontaneously assembling into a duplex structure. The A base is paired with the T base via two hydrogen bonds and G base is paired with C base via three hydrogen bonds (Figure 1.3). This type of interaction contributes to the stability of the structure. This Watson-Crick base pairing process is highly selective and occurs only if the bases are complementary to each other.[5] Another type of interaction in a DNA duplex is π- π stacking which is induced by adjacent bases of the bio-polymer. The double helical structure is stabilised by these π- π stacking interactions while the negatively charged phosphodiester linkages are pushed to the outside of the helix. Solvent cations balance the negative charge of the phosphate backbone stabilising the structure further.[6]

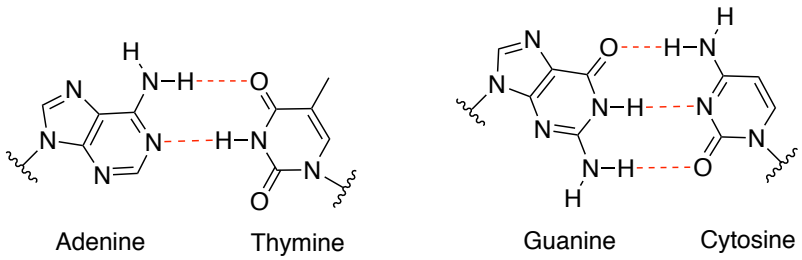

Figure 1.3 – Hydrogen bonding and its selectivity.

There are three main secondary structures of DNA, namely A, B and Z forms, that can be adopted by a duplex (Figure 1.4). There are a number of factors that determine the conformation, which include base composition, water content, salt concentration and the countercation. The B-form is the most common in prokaryotic

and eukaryotic cells, generally characterised by mixed sequences.[7] It is a right handed helix with approximately 10 base pairs per helical turn and a distance of 0.34 nm between the adjacent base pairs. A significant feature of the B-form is the presence of a major and a minor groove which accommodates protein interactions. Moreover, in this conformation, DNA bases are oriented perpendicular to the helix axis.[8] A-DNA is a more compact right-handed helix with a base distance of 0.28 nm. Z-DNA form is a left-handed helix and is formed by sequences rich in alternating guanine and cytosine bases.[4, 7, 9]

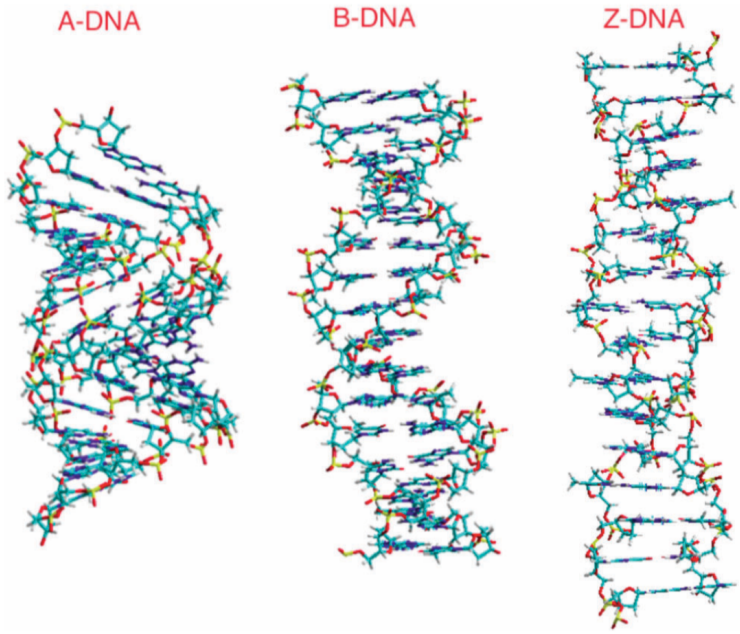

Figure 1.4 – Structures of three different DNA conformations; A-DNA, B-DNA and Z-DNA,

Reproduced with permission from Bayden Wood.[7] Copyright 2016, Royal Society of Chemistry.

1.2.2 DNA nanotechnology

The field of DNA nanotechnology exploits a bottom-up approach to the design of structures at the nanoscale by using internal information within molecules. DNA-based assemblies have made a major contributions to the field of nanoscience due to its stability, programmability, binding specificity, well-defined structure and ease of synthesis and modification.[10]

1.2.2.1 2D DNA structures

The very first DNA nanostructure[11] was produced by Nadrian Seeman, who introduced a four-arm Holliday junction. This research inspired many studies into two-dimensional DNA array designs. For example, the study conducted by the Turberfield group[12] introduced the design for a Three-Layer Logpile (3LL) made from four double stranded DNA arms with sticky ends consisting of 6 unpaired bases to form the extended array (Figure 1.5). This assembly is especially interesting due to its superiority over similar designs as a result of its relatively small unit cell (~15.6 nm) and simple motif, allowing resulting helices to be straight with few distortions.

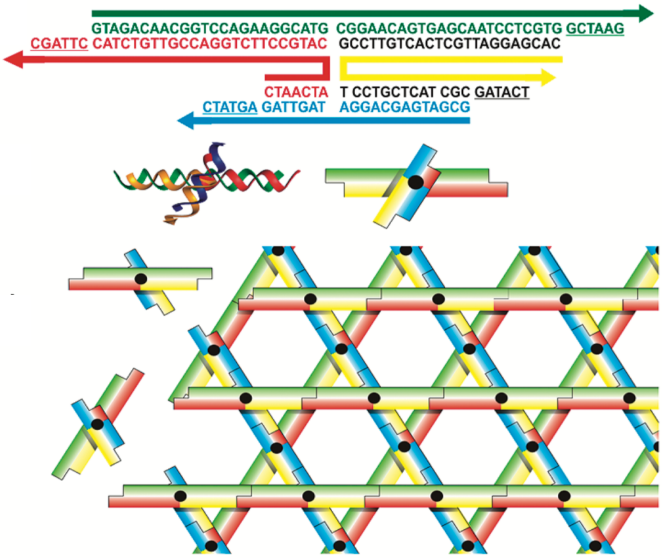

Figure 1.5 – Three-layer logpile design showing the structural unit, arrangement of sticky ends and a schematic representation of the lattice. *Reprinted with permission from Malo et al.*[12] *Copyright 2009 American Chemical Society.*

The single strand exchange method present in Holliday junctions was later improved by introducing two strand exchange called a double-crossover (DX) motif.[13] This type of structural motif was not the only one explored over the years. 2D DNA arrays were studied extensively by applying various monomers, such as the three-point[14] and six-point star[15] motifs designed by He and co-workers. A more recent example of a three-point star motif to form extended arrays is the work of Avakyan *et al.*[16] discussed in more detail in Chapter 6. Tensegrity triangles were designed by Liu *et al.*[17] to allow for a more rigid geometrical structure and later its application in the design of an organic semiconductor was explored by X. Wang[18]. T-shaped DNA junctions were designed by the Murata[19] to provide a right angle geometry and enrich the variety of DNA self-assembled structures available. Finally, 'Wang tiles'[20]

were fabricated based on a computed binary function of a fractal pattern called Sierpinski triangle. In this study, the tiles were translated to form double crossover DNA motifs and originated the growth of these tiles into algorithmic crystals.

1.2.2.2 DNA origami and brick assembly

DNA origami is a method for DNA construction introduced by Paul Rothemund in 2006,[21] wherein a viral single stranded DNA 'scaffold' folds into a desired pattern by addition of short staple strands (Figure 1.6a). Another approach similar to the DNA origami but without using the long scaffold strand is brick assembly (Figure 1.6b).[22] This method is aided by computer software which designs a structure and generates hundreds of DNA single strands to translate it into a desired structure. Both approaches have a common limitation, namely the use of a great number of DNA oligonucleotides, which makes it an expensive process. However, with the advancement of technology the costs are decreasing, thus making it more feasible for the wider scientific community.[10]

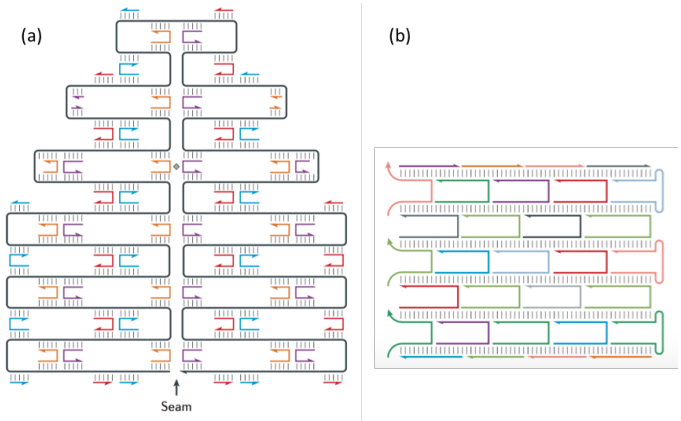

Figure 1.6 – DNA origami (a) and DNA brick assembly (b). *Reprinted with permission from Seeman et al.*[10] *Copyright © 2017, Springer Nature.*

1.2.2.3 3D DNA structures

Early solid-supported techniques of producing 3D DNA structures resulted in low yields. Not until an octahedron was constructed by Shih *et al.*[23] via annealing of a long 1.7 kb DNA with five short staple strands, was the yield improved. In another study by the Turberfield group, a DNA tetrahedron[24] was assembled with four distinct DNA single strands (Figure 1.7). Since then, various DNA polyhedra were constructed. The work by the Sleiman group[25] is exemplar as they demonstrate triangular, cubic, pentameric and hexameric prisms. The Seeman group constructed a DNA cube[25] and a DNA truncated octahedron[26]. DNA origami can also be folded into a 3D structure.[27-29]

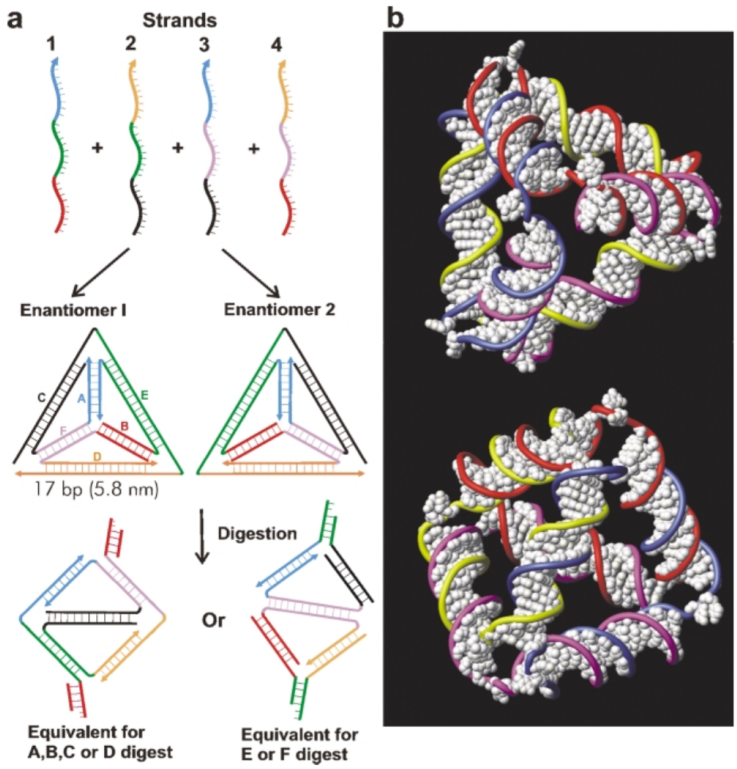

Figure 1.7 – DNA tetrahedron; synthetic scheme (a) and 3D model (b). *Reproduced with permission from Goodman et al.*[24] *Copyright 2004, Royal Society of Chemistry.*

1.2.2.4 Dynamic DNA structures

The idea of dynamic DNA structures originated in 2000 with the term "DNA machines". It is based on a concept of isothermal DNA strand displacement wherein a DNA 'fuel' strand closes the DNA 'tweezer' and addition of another strand re-opens it.[30] An example of this system is a reversible *cis*/*trans* trapezoid[31] which alternates between the two isomers via a strand rotation of a single strand relative to the other by 180°. DNA 'walkers' have become popular amongst DNA experts. A few examples of this system include a two-legged DNA unit[32, 33] which is capable of walking autonomously in a specific direction on a track, DNA 'gears'[34] that can 'roll' against one another, and a DNA 'spider'[35] that can walk on a DNA origami track.

1.2.2.5 Organising transition metals, polymers, lipids, proteins and enzymes

Programmed organisation of metals is interesting for various applications in nanoelectronics, nano-optics, molecular magnetic behaviour, data storage, catalysis and light harvesting.[10] One of the first metal-DNA self-assembly structures was produced with ruthenium bipyridine complexes.[36, 37] This assembly was shown to form into a cyclic moiety when the two ruthenium containing metal complexes came into close proximity. Another example of a metal-DNA framework is a 3D DNA cage with transition metals at specific locations in the vertices of the structure.[38] Selectivity for a specific transition metal ion was demonstrated by the Sleiman group,[39] wherein three different environments were created with the use of

terpyridine and phenantroline ligands (Figure 1.8). An error correction mechanism was demonstrated in this system upon addition of the incompatible metal ion.

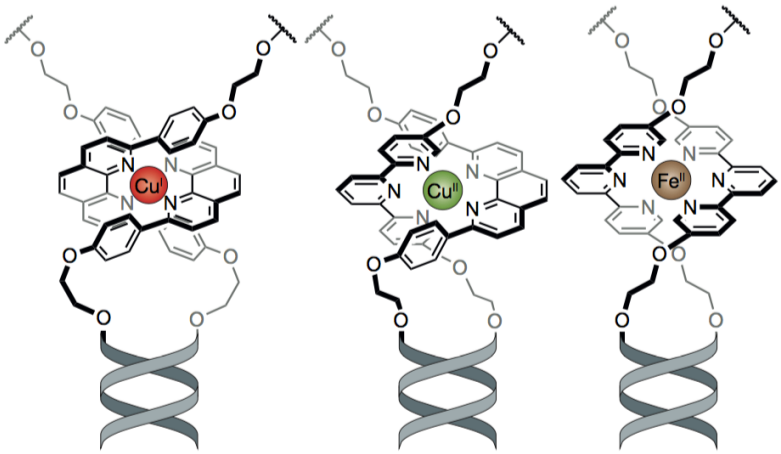

Figure 1.8 – DNA templated metal coordination. *Reprinted with permission from Seeman et al.*[10]

Polymers can also be organised using DNA nanotechnology. One example of this is the work by Edwardson *et al.,*[40] where a monodispersed and sequence specific DNA-polymeric block was produced. In another study, polymers were arranged on the inside and outside of the DNA cage and shown to form a micelle structure on the inside.[41] Lipids are another type of molecule that has been attached to DNA. A study by Yang *et al.*[42] demonstrated encapsulation of lipids within a DNA origami structure and provided a good indication of lipid environments. The use of supported lipid bilayers has been efficient in assisting the 2D lattice formation from DNA origami.[43]

DNA nanotechnology was used to organise proteins into well-defined patterns. In a study by the Turberfield group,[44] an ordered protein array was formed by attaching

the proteins to a 2D DNA lattice. The structure of the proteins could then be resolved by cryo-electron microscopy. The same group was also able to encapsulate a protein in a DNA cage.[45] Organisation of metabolic proteins on DNA scaffolds allowed for formation of enzyme cascades as demonstrated by Niemeyer *et al*.,[46] wherein two enzymes were organised in this manner. The product of the first enzyme was a substrate for the second enzyme and the close proximity of the two enzymes made the process more efficient.[47] In another study, a DNA swinging arm was engineered to carry a reaction substrate from one enzyme to the next.[48]

1.2.2.6 DNA mediated gold nanoparticle assembly

Organising gold nanoparticles into desired structures yields materials for electronic, catalytic and sensing applications. The first assembly of gold nanoparticles with DNA was achieved by mono-functionalising them with a single DNA strand.[49] Poly-functionalising gold nanoparticles resulted in spectral changes which became the foundation for a sensitive detection technique.[50] Nowadays, complex DNA scaffolds are used for nanoparticle assembly. A good example is the work by the Sleiman group,[51] wherein a re-usable DNA scaffold was generated (Figure 1.9). In this work, the parent DNA template is molecularly imprinted onto the gold nanoparticle material, allowing it to assemble without the use of DNA scaffold, with the DNA template able to be re-used. In another study, 3D DNA origami nanostructures were used as a container to grow a gold nanoparticle within it.[52] Finally, a crystalline diamond-like array was formed by encapsulating gold nanoparticles within a 2D

triangular DNA origami and assembling them on a surface made of isotropic spherical particles.[53]

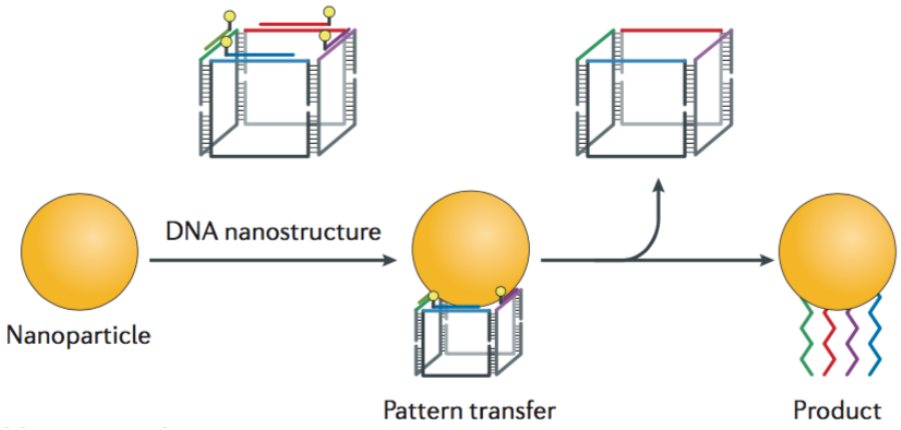

Figure 1.9 – Schematic representation of a molecular printing process of DNA strand pattern on gold nanoparticle. *Reprinted with permission from Seeman et al.*[10] *Copyright © 2017, Springer Nature.*

1.2.2.7 Biomedical applications

DNA nanotechnology offers unique sets of properties to enrich the area of biomedical applications with their programmability and compatibility with many chemistries.[10] In a study conducted by the Turberfield group,[54] DNA cages were observed to enter cells without the use of any agents, exhibiting higher translocation efficiency than ss and ds DNA. In another study, DNA structures were used to carry the anticancer drug doxorubicin into drug resistant cells, resulting in apoptotic cell death.[55] A different study focused on DNA cages labelled with MUC-1 aptamers which allowed for selectivity in targeting cancer cells.[56] DNA nanostructure allows for selective release of cargo in response to the environment.[10] A good example of this is a study by Douglas *et al.,*[57] wherein antibodies were encapsulated in a DNA

cage equipped with two aptamer switches. The cage structure opened upon exposure to antigen protein, allowing for therapeutic cargo release. In another study, a DNA cage was developed that bound to human serum albumin, resulting in gene silencing.[58] Finally, a DNA structure was used to engineer an extracellular matrix scaffold.[59] The authors were able to successfully grow cervical cancer cells and measure changes in cell behaviour.

1.3 Metal modified DNA

Covalent incorporation of various metals into DNA is desirable from a materials science and biotechnology point of view. This is even more so in the case if the metals can be precisely arranged at the nanoscale, which would present significant implications in nanoelectronics and development of devices for catalysis or artificial photosynthesis.[60] Such promising applications call for development of methods to incorporate a variety of metals into DNA in a site-specific manner, cost-effectively and with the ability to undergo a scale-up in the industry. There are three general methods of specifically incorporating metals into DNA: metal binding to unmodified DNA (Figure 1.10a), attachment of metal to ligand-modified DNA (Figure 1.10b), and pre-synthesis of a metal complex, followed by its attachment to DNA either during or after DNA synthesis (Figure 1.10c).

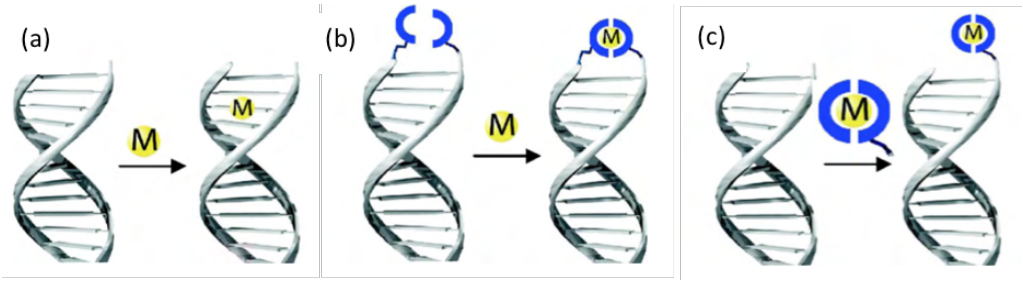

Figure 1.10 – Schematic representation of methods via which site specific functionalisation of DNA can be achieved: (a) metal binding to unmodified DNA, (b) metal binding to the ligand following its prior incorporation to the DNA, (c) metal complex attachment to DNA. *Reproduced with permission from Yang et al.*[60] *Copyright 2010, Elsevier B.V.*

The first approach avoids having to modify DNA however, it often lacks high specificity. The other two approaches enable a more controlled incorporation of a wide range of metals into DNA. The second method illustrated in Figure 1.10b requires the incorporation of a metal binding ligand either by modifying a DNA base or the phosphate backbone, before subsequently binding the metal to the ligand-modified DNA sequence (Figure 1.10b). The last approach takes advantage of the automated solid phase DNA synthesis process to incorporate a metal complex into DNA (Figure 1.10c). It requires prior functionalisation of the metal complex with a phosphoramidite group, through which the complex will attach to the previous base of the growing DNA oligonucleotide. [60]

1.3.1 Metal binding to unmodified DNA

Methods allowing for high specificity in metal placement often require a precise design and lengthy synthesis of the ligands and metal complexes. For industrial

applications, cost effective approaches are as important and therefore using cheap and easy accessible unmodified DNA would be advantageous for metal binding.[60]

Due to the negative phosphate backbone of DNA, metal ions can interact with it or they can disrupt Watson-Crick base pairing by replacing hydrogen atoms. This is a well-known phenomenon exploited in the use of buffer system (K^+, Na^+, Mg^{2+}) to stabilise the structure of DNA and for its duplex formation.[61] In a study by the Lee group, divalent metal ions such as Zn^{2+} formed complexes with unmodified DNA.[62] Further studies on this type metal-DNA complex revealed no evidence for expected metallic or semiconductor behaviour. Although AFM results confirmed the retention of the B-DNA form.[63] This approach was not base selective so specific control of metal placement was difficult to achieve.

More site-specific metal DNA structures have been reported by Tanaka group, where they bound Hg^{2+} to two thymines in a DNA duplex (Figure 1.11).[64] This interaction was studied by ^{15}N NMR and ESI-MS spectroscopy which confirmed the formation of up to five Hg atoms stacked in a row. The presence of mercury was found to stabilise the T-T mismatch.[64]

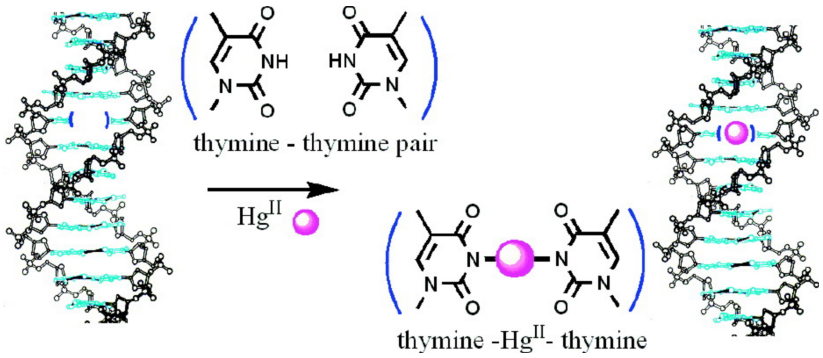

Figure 1.11 – Schematic representation of the formation of Thymine-Hg^{II}-Thymine base pair in DNA.

Reprinted with permission from Ono et al.[64] Copyright 2006 American Chemical Society.

Similarly, interaction between Ag^{+} and C-C mismatch in a DNA duplex have been studied by the same group, selectively binding and stabilising the C-C mismatch.[65] The results showed that silver can accumulate in commercially available oligonucleotides and can be applied to various scientific fields, such as the development of DNA nano-architectures. In the study by Day *et al.*[66] an i-Motif DNA was studied, wherein Cu^{2+} are used to alter its conformation into an alternative hairpin structure. This change in conformation was found to be reversible upon chelation with EDTA.

One of the best examples of metal complex binding to unmodified DNA is cisplatin which is discussed in detail later in this chapter (Section 1.4).

1.3.2 Metal coordination to ligand modified DNA

It can be advantageous to first attach a ligand to DNA and then coordinate the metal post-synthetically (Figure 1.10b). The main advantage of such an approach is that a

wider range of kinetically labile metals can be incorporated into the DNA without the need to survive harsh conditions of the standard DNA solid phase synthesis. In addition, the ligands can be incorporated anywhere in the DNA sequence and being different from DNA bases, they can bind the metals selectively.[60]

The replacement of the H-bonded DNA base pairs with a metal complex in the interior of the DNA duplex enables the formation of a so-called "metal base pair", which is a good approach to incorporate metals into DNA.[67] The Shionoya group were the first to report such a system incorporating a Pd^{2+} into amine modified bases.[68] Since then, they have reported many examples of ligands for metal-mediated base pairing in DNA, incorporating copper[69], silver[70] and boron[71]. The Shultz group has also reported silver[72] and copper[73] mediated base pairs in DNA. A first Ni^{2+} mediated base pair was accomplished by Switzer *et al*.[74]

Naturally, it is interesting to gauge the stability of metal-mediated base pairs within DNA. Thermal melting studies have been employed by Meggers *et al*.[75] to study copper mediated DNA base pairs. It was found that while the absence of the metal strongly destabilised the DNA duplex, the addition of one equivalent of Cu^{2+} per base pair promoted base pairing, with a thermal melting temperature comparable to an A-T base pair. Further addition of excess amounts of the metal ion did not have a significant effect on duplex stability.

A true highlight of metal-mediated base pairs was the incorporation of multiple units into a DNA duplex as a stack, as demonstrated by the Shionoya group. This resulted in not only a highly stable structure, but also electronic and magnetic interactions due to the close contact of metal centres.[60] Tanaka *et al*. reported the formation of such a structure with a row of five copper complexes incorporated into the DNA strand, with a C-G pair at each end of the sequence (Figure 1.12).[76]

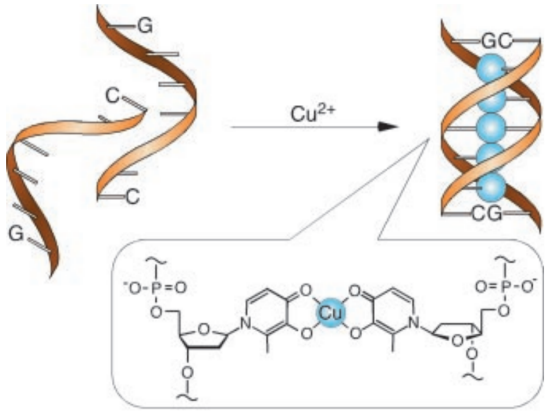

Figure 1.12 – Copper mediated duplex formation where five natural DNA bases were replaced by hydroxypyridone nucleobases. *Reproduced with permission from Tanaka et al.[76] Copyright 2003 by the American Association for the Advancement of Science.*

Choi *et al*.[77] found that upon modification of DNA strands with terpyridine, followed by addition of Fe^{2+} and separation by gel electrophoresis, the formation of discrete triangle structures occurred. Another study by the Kramer group used terpyridine-modified DNA to form a switchable structure. In this study, addition of Zn^{2+} ions caused cyclisation of a single DNA strand, whilst an excess of these ions reopened the structure.[78]

Bipyridine and phenanthroline are two other ligands used for coordinating metals to DNA. For instance, Sugimoto's group used bypiridine-modified G-quadruplexes to assemble higher order structures by incorporating Ni^{2+}.[79] Sleiman's group constructed dpp (2,9-diphenyl-1,10-N,N-phenanthroline) modified complementary strands of DNA which upon duplex formation, brought the ligands into close proximity for metal incorporation, while retaining the right-handed helicity.[80] This strategy can be used to generate 2D and 3D DNA based structures. A good example of this is a 3D DNA prismatic structure which contains six $(dpp)_2$ ligand pockets linked together to form a framework that incorporates exactly six metal ions within the pockets (Figure 1.13).[81]

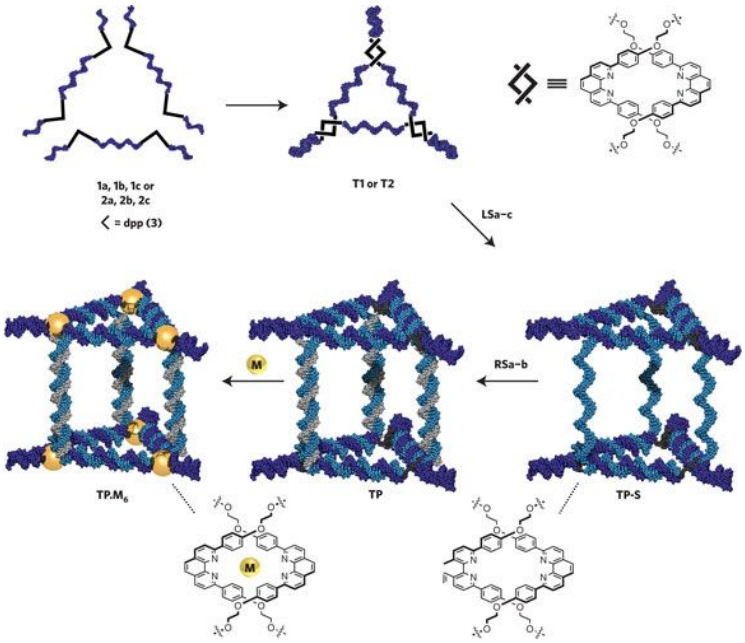

Figure 1.13 – Schematic representation of the assembly of metal-DNA cage structure. *Reprinted with permission from Yang et al.*[81] *Copyright 2009 Springer Nature.*

1.3.3 Metal complex-modified DNA

Automated solid phase DNA synthesis offers a convenient way to incorporate tags (molecules/metal complexes) into a DNA strand. However, one potential drawback of this strategy is the relatively harsh conditions of this method, which limits the number of metal complexes that can be used, which explains why stable organometallic species such as ferrocene are commonly used for DNA modification.[82] Ferrocene nucleic acids chemistry is detailed in Chapter 5. One of the best examples of metal-modified DNA which withstands the aforementioned harsh conditions was reported by Duprey *et al.*[83] wherein a macrocyclic cyclidene complex containing a Cu^{2+} or Ni^{2+} cation was incorporated into a DNA strand during solid phase synthesis. In this study, two structural designs were explored, namely a tag system, where the metal complex acts as an intercalator, and a linker system, which sees the metal complex incorporated into the DNA backbone (Figure 1.14). It was found that the tag system could electrochemically detect the identity of the nucleobase opposite the metal complex and as such could be used as a SNP (Single Nucleotide Polymorphism) sensor, which detects DNA polymorphisms in the human genome.[83]

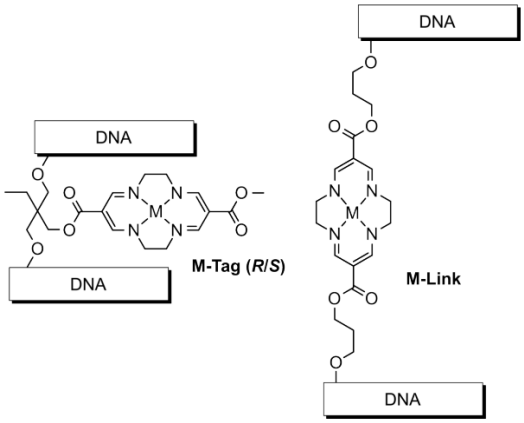

Figure 1.14 – Metal (M=Cu or Ni) complexes incorporated into DNA either as tag (M-Tag) or link (M-Link) systems. *Reproduced with permission from Duprey et al.[83] Copyright 2016 American Chemiscal Society.*

Mitra *et al.*[84] created a metal-DNA nanostructure containing two DNA helical arms and two $[Ru(bpy)_3]^{2+}$ vertices. This was accomplished by synthesising the oligonucleotides on the solid support and then reacting them with the ruthenium complex, before oxidation and cleavage from the solid support. In another study, the McLaughlin group used a combination of the solid phase DNA synthesis and reverse synthesis (from 5' to 3') to produce a ruthenium complex centre with six DNA arms[85] and a nickel complex centre with four DNA arms.[86] These findings may contribute to the construction of 3D DNA assemblies. Solid phase synthesis was once again exploited by Hurley *et al.*[87] to couple ruthenium and osmium complexes to oligonucleotides who found that ruthenium emission was quenched by osmium as the distance between the two complexes got smaller.

1.4 Cisplatin and its interaction with DNA

Cis-diamminedichloroplatinum(II) (*cis*-DDP), commonly referred to as cisplatin, is a neutral complex of square-planar geometry (Figure 1.15).[88] Out of the four ligands, two of them are labile chloride atoms, and two are inert groups. This transition metal complex can undergo hydrolysis, wherein the chloride ligands are substituted by water. One of the driving forces in this reaction is the formation of hydroxy species (Figure 1.16).

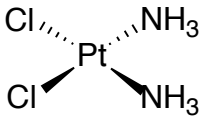

Figure 1.15 – Chemical structure of cisplatin.

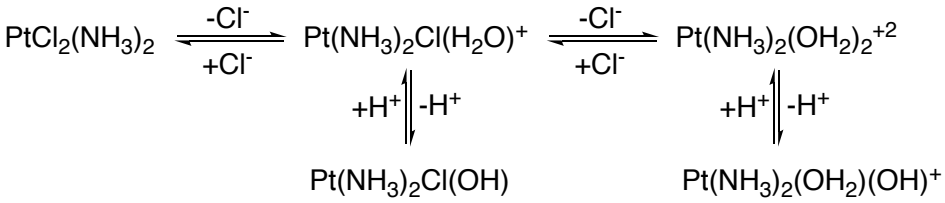

Figure 1.16 – Hydrolysis of cisplatin.

Cisplatin has been used to treat different types of cancer since 1979, when it received FDA approval.[88] Once it had been established that the drug targets DNA, multiple studies emerged in order to investigate the binding modes and characterise the adducts formed.[89] Hydrolysis has been found to be vital in the mechanism of action, which is kinetically controlled and dependent on the chloride ion concentration.[90] The drug is administered to patients in its dichloro form and it is maintained in such form in plasma, which has a high chloride concentration, reportedly 103 mM.[90] Upon cell entry, the low intracellular chloride concentration

of 4 mM promotes hydrolysis. This hydrolysis is the rate-limiting step in the DNA binding with a half-life estimated to about 2 h.[91, 92] Aquated cisplatin binds to the N7 position on guanine by displacing one water molecule, forming a mono-adduct. Hydrolysis of the second chloride ligand allows formation of the bis-adduct.[93] Low levels of drug have been found to decrease the rate of bis-adduct formation.

Despite there being two geometric isomers of diamminedichloroplatinum(II), only the *cis* isomer exhibits antitumour activity. This is explained by the different adduct formation with DNA.[89] Three main binding modes were identified as: (a) intrastrand or (b) interstrand DNA crosslinks and (c) protein-DNA crosslinks (Figure 1.17).[88] The drug targets the N7 atom of guanine and adenine due to ease of access (sterics), however only the *cis* isomer can form the 1,2-intrastrand crosslinks due to its stereochemistry.[94]

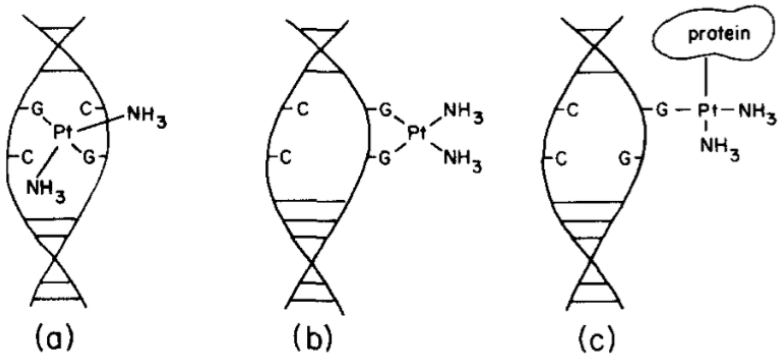

Figure 1.17 – Schematic representation of the three cisplatin-DNA adducts, (a) DNA interstrand crosslink, (b) DNA intrastrand crosslink, (c) DNA-protein crosslink. *Reproduced with permission from Pinto et al.[88] Copyright 1985 Elsevier.*

In vitro experiments conducted by Reedijk *et al.*[95] and Eastman *et al*.[96] provided evidence for the formation of these cisplatin-DNA adducts, which also showed that 1,2-intrastrand crosslinks form a majority of adducts, with *cis*-GG comprising 47-50%[95] and 65%.[96] In vitro studies of white blood cells taken from cancer patients further confirmed these results.[97] It can be concluded that around 50% cisplatin-DNA adducts are bound to two guanines, providing a considerable amount of specificity of this reaction.

DNA structure is distorted upon binding to cisplatin. Studies have shown that this drug causes DNA unwinding and shortening of the duplex by up to 50%. Destabilisation of the helix was also found upon conducting calorimetric studies (of 6.3 kcal/mol)[98] as well as denaturing gel electrophoresis studies.[99] X-ray crystallography was also most informative as it revealed a change in dihedral angle between the guanine rings ranging from 76^{o} to 87^{o}, suggesting destacking of the bases.[100] NMR experiments also confirmed the duplex distortions with larger values than in the *x*-ray studies, which may have been influenced by crystal packing.[101]

UV/Vis spectroscopy is another method used to study structural changes in DNA. In a study by N'soukpoe-Kossi *et al.*, binding of cisplatin to calf thymus DNA (CT-DNA) was explored,[102] wherein the concentration of CT-DNA was kept constant (20 μM) and cisplatin concentration was varied (Figure 1.18). The purpose of this study was to find the binding constant of the drug to the DNA, which was estimated to be *K* =

5.73 x 10^4 M^{-1}. The UV absorbance spectrum of free cisplatin at 40 µM concentration (Figure 1.18, spectrum b), indicates its low UV absorbance in relation to DNA.

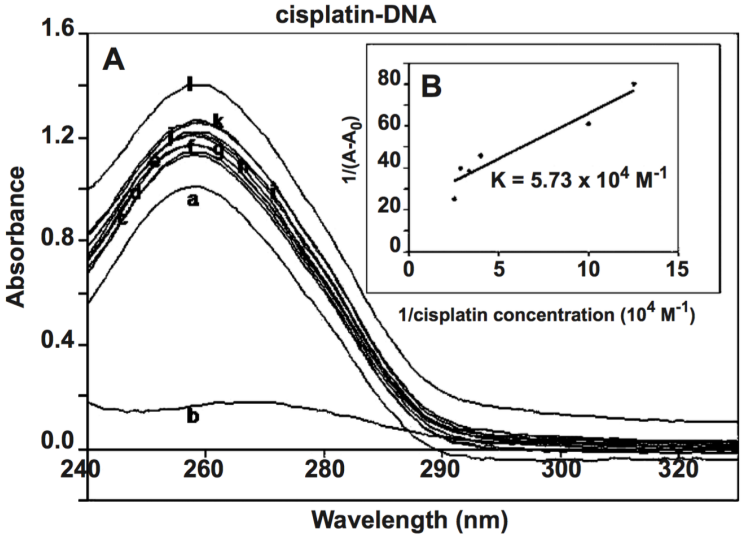

Figure 1.18 – UV/Vis spectrum of CT-DNA and cisplatin: a – free DNA, b – free cisplatin, (c-l) DNA cisplatin complexes with varying concentration of cisplatin of 2 µM (c), 5 µM (d), 8 µM (e), 10 µM (f), 15 µM (g), 20 µM (h), 25 µM (i), 30 µM (j), 35 µM (k) and 40 µM (l). *Reproduced with permission from N'soukpoe-Kossi et al.*[102] *Copyright 2008, Mary Ann Liebert, Inc.*

Another technique which provides insight into the DNA structure is circular dichroism (CD) spectroscopy. The study undertaken by Macquet and Butour on various platinum complexes with E. *coli* DNA is a good example (Figure 1.19).[103] They reported an initial increase of the positive band at 280 nm up until the addition of 0.125 equivalents of the metal complex, coupled with a decrease of the negative band at 230 nm. The increase of positive band at 280 nm is ascribed to the exposure of bases upon cisplatin binding event. Further increases in the metal complex to DNA ratio caused both bands to decrease.

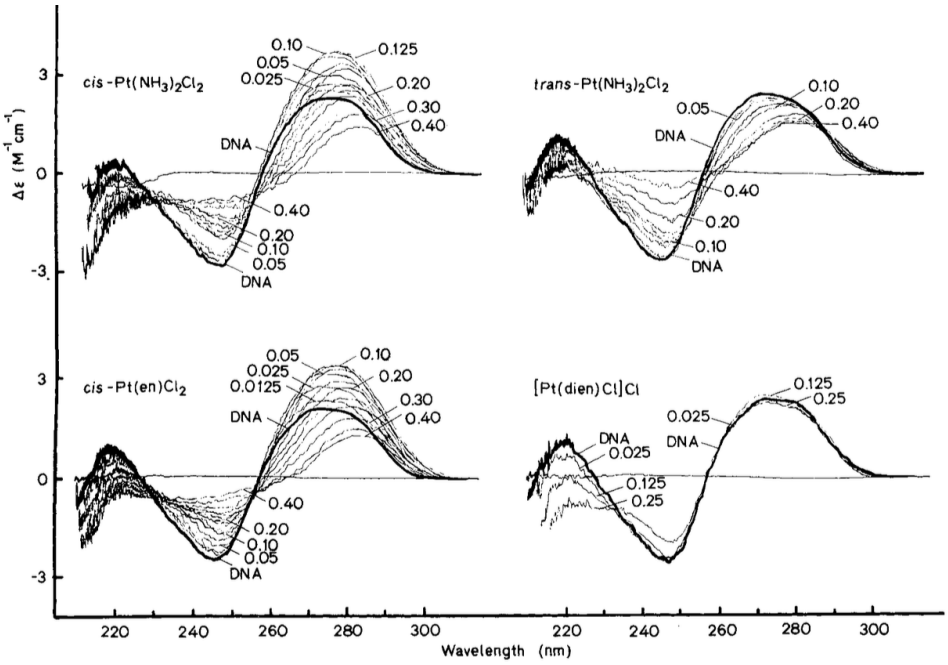

Figure 1.19 – CD spectra of E. *coli* DNA with increasing equivalents of platinum complexes.

Reproduced with permission from Macquet and Butour.[103] Copyright 2008 John Wiley and Sons.

1.5 Synthetic Biology

Synthetic Biology is an emerging field which encompasses a broad range of scientific disciplines including biochemistry, biophysics, molecular cell biology, chemical engineering, biomedical engineering, electrical engineering and computer science.[104] These fields come together in a common goal to find constructive approaches to understand and manipulate biological systems. The origins of this field can be traced back to the work by Jacob and Monod[105] who studied cellular responses to the environment. It provided a valuable insight into the existence of regulatory circuits. This visionary idea, in combination with the discovery of

transcriptional regulation in bacteria and technological advancements in molecular cloning, PCR, as well as automated DNA synthesis and computational tools, has paved the way to the field as we know it today.[106]

It has been suggested that synthetic biology, being at the interface of the disciplines mentioned above, should become one of the flagships of the Fourth Industrial Revolution.[107] Therefore, it is not surprising that researchers have been looking in this field for answers to environmental crises that include overpopulation, loss of biodiversity and pollution. Most specifically, climate change and limiting the use of fossil fuels are the driving force for researching alternative energy sources.[108] One of the proposed solutions is the rational design of microbial hosts that produce a variety of materials and chemicals. Polyhydroxyalkanoates (PHAs) are a family of biopolyesters that have been proposed for applications in environmentally friendly packaging, medicine and smart materials (Figure 1.20).[108] It was shown possible to produce copolymers, block copolymers and homopolymers by engineering bacterial genomes in such a way as to maintain an original chain length of a fatty acid fed to the bacteria.[109] This allows for functional groups to be incorporated into the PHA, resulting in a large variety of materials that can be obtained.

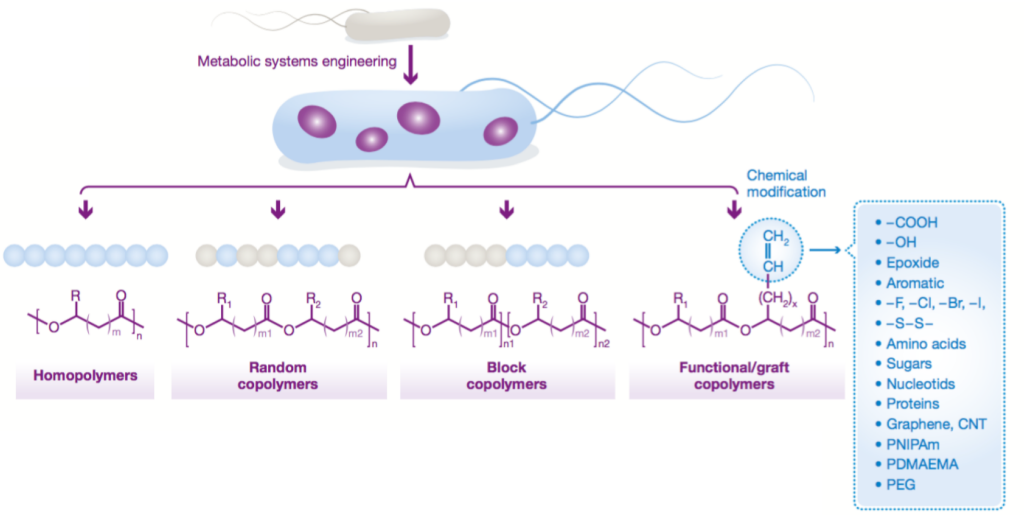

Figure 1.20 – Schematic representation of pathway to production of biomaterials by engineered microorganisms, *reproduced from Lorenzo et al.*[108] *Copyright 2018 Creative Commons Attribution License.*

For example, Saccharomyces cerevisiae, a species of yeast, was engineered to produce free fatty acids (FFAs) for use as biofuel precursors.[110] The authors reported the highest titre of FFAs achieved so far of up to 10.4 g L^{-1} and studied pathways for efficient conversion of the fatty acids into alkanes and fatty alcohols. In fact, biofuels production is one of the proposed solutions to target the challenges created by global petroleum supply and climate change. Synthetic biology approaches involving engineering the metabolism of microorganisms is believed to maximise such biofuel production.[111] The general procedure for biofuels production involves the supply of feedstock into the host, conversion of that feedstock into fuel and its harvest (Figure 1.21).

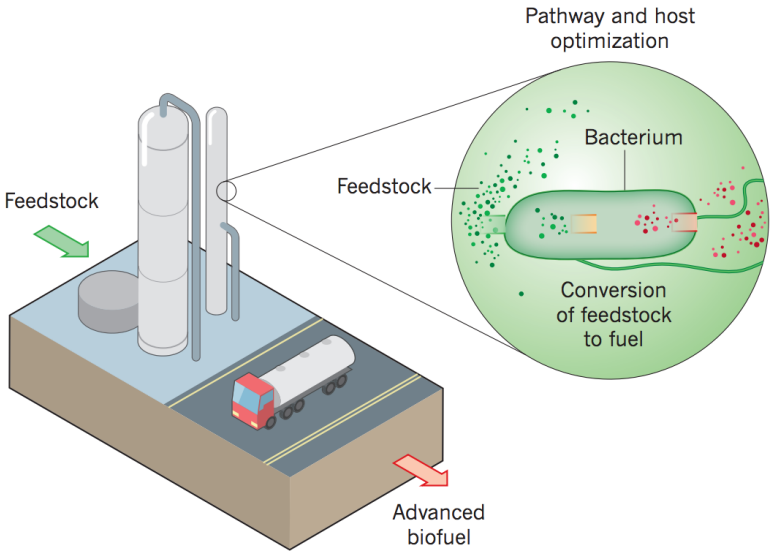

Figure 1.21 – Schematic representation of advanced biofuel production. *Reproduced with permission from Peralta-Yahya et al.*[111] *Copyright 2012 Springer Nature.*

An example of a successful development of a biofuel production pathway was accomplished by Bond-Watts et al.[112] In this study, the authors constructed a chimeric pathway for production of n-butanol which uses an enzyme (*trans*-enoyl-CoA reductase) mechanism to amplify the yield of the product. More recently, a high-pressure fermentation strategy was developed by the Thompson group,[113] wherein a $scCO_2$-tolerant strain of bacteria, *Bacillus megaterium,* was engineered, allowing for the use of supercritical carbon dioxide as a solvent. This resulting CO_2 has been proposed to be superior for green biofuel production compared to other methods.

Synthetic biology can help in developing new materials. In particular, materials exhibiting rare and useful properties such as adaptation to environment, self-healing

and growth are amongst the most sought after. Bacteria have been suggested to help produce such materials. This is due to the nature of bacterial proliferation, which consists of secretion of an extracellular matrix for survival in harsh and nutrient-poor environments.[114] This extracellular matrix consists of amyloid fibres which have been extensively studied for a number of applications such as antibiotics resistance[115], toxins detoxification[116], electron transport[117], morphological differentiation[118] and adhesive properties[119]. One of the recent examples of this was a study by Huang *et al.*[120] who developed a flexible and tuneable living material from *Bacillus subtilis* biofilm. This was accomplished by engineering the TasA amyloid machinery to offer various functionalities, for example self-assembly around living cells to form nanoarchitectures while maintaining its self-regenerative and viscoelastic properties (Figure 1.22).

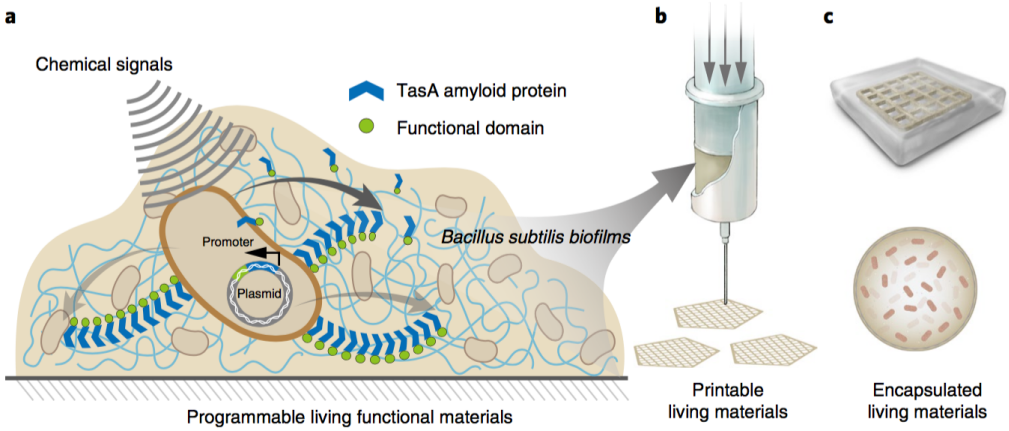

Figure 1.22 – Design of the Bacillus subtilis biofilm production; a - chemical inducers program secretion of engineered TasA amyloid proteins by the bacteria, b – 3D printing of the material, c – encapsulation of the biofilm in hydrogels or microcapsules. *Reproduced with permission from Huang et al.*[120] *Copyright 2018 Springer Nature.*

In another study, the same bacterial strain was used to engineer an adhesive material. This was accomplished by functionalising the amyloid protein biofilm with mussel foot protein and an engineered hydrophobin-like protein.[121] This smart-living glue type-material exhibited dynamic and self-healing properties.

One of the materials attracting a vast amount of interest from researchers is spider silk. The main reason for this is its astonishing properties, namely high tensile strength and extensibility, making it a stronger material than the strongest man-made to date (Kevlar).[122] Unfortunately, spider farming is not feasible due to their territorial and aggressive nature. Therefore, much research has been done into finding a foreign host for production of this fibre. One of the approach was to explore the use of E. *coli* to express a spider silk protein Nephila clavipes, which was then successfully spun into a fiber.[123] A yeast species *Pichia pastoris*[124] as well as mammalian cells[125] were explored hosts for spider silk production. More recently, an improved synthetic biology approach was developed that exploited *E. coli* to express elevated levels of MaSp2 protein by down-shifting the induction temperature, resulting in the highest (3.6 g l^{-1}) reported titre of spider silk protein.[126]

Another promising example involving engineered E. *coli* as proposed by Antonovsky *et al.*[127], who produced sugars by applying Calvin-Benson-Basham cycle in this bacterial species. The bacteria were shown to generate hexose, pentose and triose sugars autocatalitically from CO_2, without any organic carbon input into the cycle.

Synthetic Biology has great therapeutic potential. One of the best examples of this is the production of a precursor to the antimalarial drug artemisinin.[128] This was accomplished by engineering of yeast species *Saccharomyces cerevisiae* to produce high amounts of artemisinic acid and transport it outside to enable an easy purification process. Engineered bacteriophages offer a solution to antibiotic resistant bacterial strains.[129] Phage therapy to kill bacteria is not a new concept however, with phage-resistance an ongoing problem Lu and Collins[130] managed to overcome this by targeting the SOS DNA repair system in bacteria. This was accomplished by engineering the lexA3 gene in M13 phage which is a repressor of the SOS network (Figure 1.23). As a result, antibiotics treatment was successful and caused a 5000-fold increase in killing of the bacteria than with antibiotics alone.

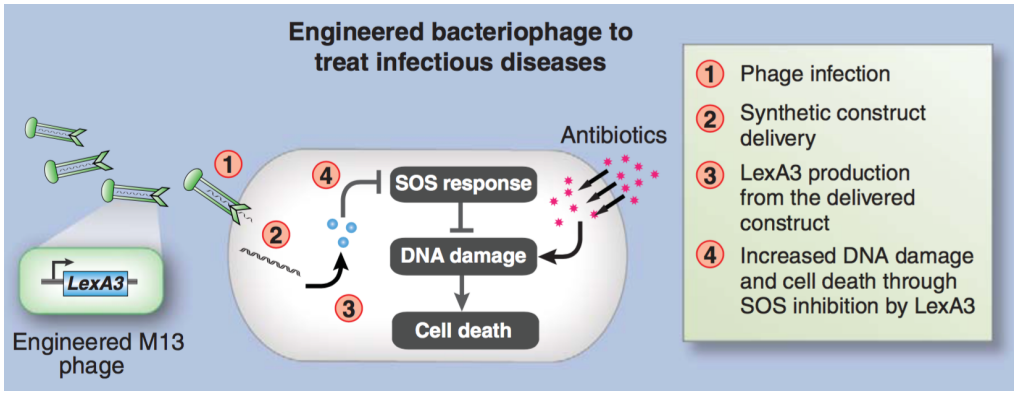

Figure 1.23 – Mechanism of improving antibiotic activity by engineering of bacteriophage gene. *Reproduced with permission from Ruder et al.[129] Copyright 2011 American Association for the Advancement of Science.*

In another study, Li and coworkers[131] engineered cancer invading bacteria to reduce CTNNBI gene overexpression, which is responsible for many colon cancers. The engineered bacteria produced short hairpin RNAs which bound to mRNA transcripts of the CTNNBI gene as well as lysteriolysin O, which enabled its efficient transfer. Significant CTNNBI gene silencing was found upon administration of this treatment in mice. In a more recent study, a photo-controlled bacterial metabolite therapy was designed by combining carbon nitride (C3N4) with *E*. *coli* carrying nitric oxide.[132] Light irradiation transfers photoelectrons from the carbon nitride to *E*. *coli,* generating cytotoxic NO. This treatment resulted in 80% inhibition of tumour growth in mice.

Regenerative medicine's main goal will ultimately rely on using tissues created from a patient's own stem cells.[129] Synthetic biology may be able to offer solutions to the encountered challenges in this field. One of the problems is a limited derivation of induced pluripotent stem cells (iPSCs), which results in a low number of clinically useful cell types. A new approach to cell reprogramming was developed by Warren and coworkers.[133] In this study, modified RNA molecules were inserted into cells to target transcripts of the genes responsible for cell reprogramming. The transcripts were translated into proteins and induced pluripotency in cells. This method was proven to be successful in creating iPSCs with a higher efficiency than using an alternative viral delivery system.

1.6 Fuel Cell Technology

The concept of a fuel cell was first discovered by C.F. Schönbein in 1838 and a year later Sir W.R. Grove demonstrated the first working fuel cell.[134] Commercial application of a fuel cell was unexplored until 1960s when the first patents were filed by the US space program. Over the next half a century, there was much technical and commercial development in fuel cell technology, allowing for their use in a variety of applications.

A Fuel Cell is an electrochemical device which works by converting chemical energy (fuel) into electrical energy.[134] The basic operation of such device is accomplished by delivering a fuel to the negative electrode (anode) and an oxidant to the positive electrode (cathode). Electric current is produced by the electrochemical reactions (Equation 1-3) occuring at the electrodes.

$$\text{Anodic reaction : } H_2 \rightarrow 2H^+ + 2e^-$$

Equation 1.1 – Electrochemical reaction at the anode.

$$\text{Cathodic reaction : } \frac{1}{2}O_2 + 2H^+ + 2e^- \rightarrow H_2O$$

Equation 1.2 – Electrochemical reaction at the cathode.

$$\text{Overall reaction : } H_2 + \frac{1}{2}O_2 \rightarrow H_2O + heat\ (exothermic\ , \Delta\text{H} = -286\ \text{kJ}\ mol^{-1})$$

Equation 1.3 – Overall electrochemical reaction.

There are many fuel cell technologies available which differ depending on the temperature range of their operation, type of fuel, type of catalyst or their electrolyte system and consequently on their operational efficiency. Some of them are: Polymeric Electrolyte Membrane Fuel Cells (PEMFC), Direct Methanol Fuel Cells (DMFC), Alkaline Fuel Cells (AFC), Phosphoric Acid Fuel Cell (PAFC), Molten Carbonate Fuel Cell (MCFC) and Solid Oxide Fuel Cell (SOFC). This thesis is concerned with the eventual use of DNA-based material in Polymeric Electrolyte Membrane Fuel Cells; this technology is therefore described in more detail below.

1.6.1 Polymeric Electrolyte Membrane Fuel Cells (PEMFCs)

The efficient energy conversion and environmental friendly nature of polymer electrolyte fuel cells makes them a potential solution to tackling future energy demands. Electrical energy is generated by the hydrogen oxidation and oxygen reduction reactions with the use of a catalyst.[134] The environmental compatibility of this technology is due to the side products of its reactions being water and heat.

The PEM fuel cells operate at temperatures between 70 ^{o}C and 100 ^{o}C. It consists of three basic parts, namely the anode, the cathode and the membrane (Figure 24). The membrane is made of a polymer electrolyte type material, which separates the fuel from the oxidant. The membrane allows for hydrogen ions to migrate to the cathode, after their prior release at the anode. The release of electrons from hydrogen generates an electrical current. One of the drawbacks of this technology is

the requirement of a noble-metal catalyst such as platinum to start the electrochemical process at low temperatures. Nonetheless, low operating temperature conditions mean that lower energy costs are required to starting up the fuel cell, which is desirable and results in a more durable system.

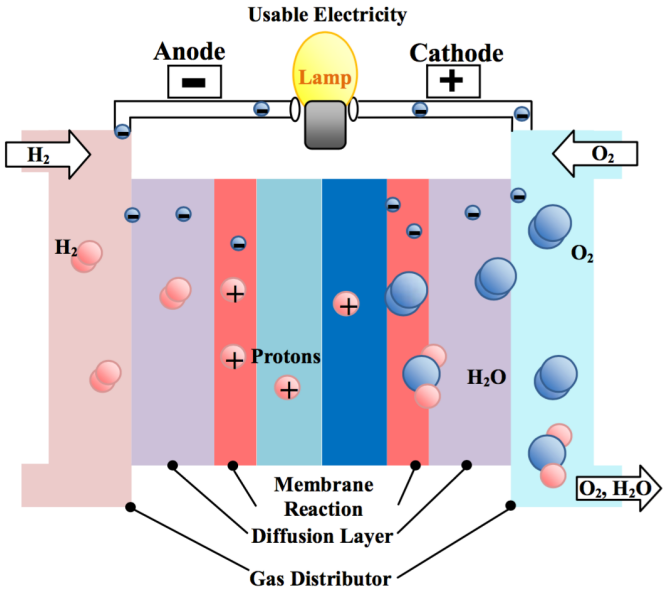

Figure 1.24 – Schematic representation of the Polymeric Electrolyte Membrane Fuel Cell, *reproduced from Giorgi et al.*[134] *Copyright 2013 Creative Commons Attribution License.*

The main advantages of this type of fuel cell technology, in addition to its environmental friendly nature, is high power density, the low cost of materials due to the low operating temperature and a large operating pressure difference between the anode and the cathode, making it easy to operate with a pressurised system. On the contrary, the disadvantages of this technology include low temperature of recovered waste heat and difficulty in water management of the membrane electrolyte, which still require improvement.[135]

Some of these challenges are being addressed by researchers. For example, a new water management strategy was developed, wherein capillary arrays were drilled with lasers into the land of flow-fields and connected to water channels.[136] The water is then removed or supplied according to the demand of the system. In another study, a new MgH_2/ 5 wt. % $TiMn_2$ nanocomposite powder was developed for solid-hydrogen storage which is the primary fuel for PEM fuel cells.[137] This new material possesses good hydrogenation/ dehydrogenation capacity at low temperatures (250 ^{o}C) and long life-cycle of 1400 h.

The platinum content in the catalyst is a matter of interest as most of the costs associated with fuel cell technology lie in its expense. Interestingly, it has been found that a decrease of platinum loading to a level as low as 0.025 mg cm^{-2} does not exhibit noticeable transport-related losses.[138] Moreover, it has been found that downsizing Pt nanoparticle sizes to single atoms and nanoclusters improves the efficiency of the catalyst by utilisation of all platinum atoms within the matrix, ensuring greater utilisation of the platinum atoms. In a study by Cheng *et al.*[139] single platinum atom catalysts were found to possess enhanced catalytic activity by up to 37 times and higher stability compared to the commercial platinum catalysts. In another study, ss DNA was employed to produce a Pt containing catalytic composite.[140] The presence of DNA not only enhanced resistance to the CO poisoning, but also was found to induce the formation of favourable (flower-like)

platinum nanoparticles. The catalytic activity of the Pt-containing DNA/ graphene composite surpassed the commercial platinum nanoparticle catalysts.

It has been suggested that doping the platinum catalyst with ruthenium can reduce poisoning of the fuel cell catalyst in direct methanol fuel cells.[141] Moreover, other 3D metal alloys have been studied by Stamenkovic *et al.*[142] for their catalytic activity. The metals tested in the study were nickel, cobalt, iron and titanium. The results revealed that all tested alloys exhibited better performance expressed as current density in comparison to the platinum electrode (Figure 1.25).

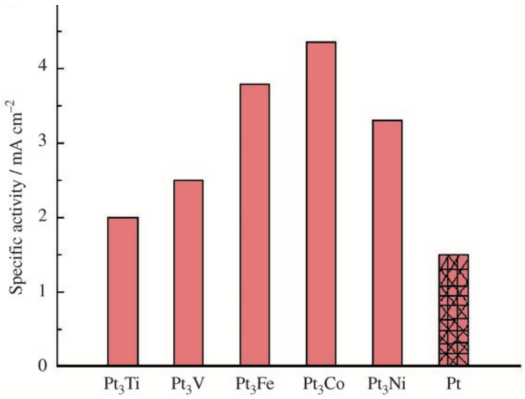

Figure 1.25 – Activity of the metal alloys compared to the neat platinum electrode expressed as kinetic current density for the ORR at 0.9 V (0.1 M $HClO_4$, 333 K). *Reproduced with permission from Stamenkovic et al.*[142] *Copyright 2006 John Wiley and Sons.*

More recently, as researchers have focused on developing catalysts from nanoparticles, the catalytic material composites doped with ruthenium nanoparticles have emerged. In a study by the Monnier group[143], a Ru-Pt bimetallic catalyst was developed from the corresponding nanoparticles on a carbon support. The platinum nanoparticles were deposited first via the strong electrostatic

adsorption (SEA), followed by the ruthenium nanoparticles using the electroless deposition (ED) method. The results of methanol oxidation showed four times higher activity with this catalyst compared to pure Pt and two times higher compared to the bulk commercial Pt/ Ru catalyst.

In order to substitute the expensive platinum catalyst, a study conducted by Chandran *et al.*[144] developed a palladium-cobalt alloy supported on a nitrogen-doped reduced graphene oxide nanocomposite. This system achieved a power density of 68 mW cm^{-2}, which is much lower compared to power densities achieved by the platinum based systems. Nevertheless, this study pioneered the use of a non-platinum based PEM fuel cell.

1.7 Thesis outline

Chapter 2 describes the key techniques used in order to conduct research with the results presented in the following chapters.

Chapter 3 investigates the design of a lightweight DNA based material precursor for a fuel cell catalyst. This is aimed to be accomplished by derivatising salmon DNA with cisplatin, with successful binding studied using spectroscopic techniques.

Chapter 4 addresses the need to precisely control the metal placement in a DNA material for potential use as a precursor to a fuel cell catalyst. Cisplatin is once again used as a source of platinum atoms and DNA oligonucleotides are used as a scaffold for metal placement. Furthermore, the design of DNA nanostructures and arrays is presented containing the cisplatin molecule in desired locations.

Chapter 5 concerns the use of an alternative metal, namely iron for placement in a precursor to a fuel cell catalyst. This metal is incorporated into DNA oligonucleotides via automated solid-phase DNA synthesis and subsequently assembled into various DNA nanostructures.

Chapter 6 presents a method for synthesising more robust DNA nanostructures that are able to withstand denaturing conditions. This is accomplished by employing photochemistry wherein anthracene molecules are incorporated in DNA

oligonucleotides via automated solid-phase DNA synthesis, assembled into nanostructures and irradiated with UV light in order to photocrosslink the anthracene molecules and render the resulting nanostructures more robust.

Chapter 7 covers the experimental methods and procedures used within this thesis.

1.8 References

1. R. E. Franklin and R. G. Gosling, *Acta Crystallogr.*, 1953, **6**, 673-677.
2. J. D. Watson and F. H. C. Crick, *Nature*, 1953, **171**, 737-738.
3. F. H. C. Crick, J. D. Watson and M. H. F. Wilkins, The Nobel Prize in Physiology or Medicine http://www.nobelprize.org/nobel_prizes/medicine/laureates/1962., (accessed 20.08.2019).
4. S. Neidle, in *Principles of Nucleic Acid Structure*, Academic Press, 2008, pp. 20-37.
5. E. T. Kool, J. C. Morales and K. M. Guckian, *Angew. Chem. Int. Ed.*, 2000, **39**, 990-1009.
6. E. T. Kool, *Chem. Rev.*, 1997, **97**, 1473-1487.
7. B. R. Wood, *Chem. Soc. Rev.*, 2016, **45**, 1980-1998.
8. R. E. Dickerson, *Sci. Am.*, 1983, **249**, 94-110.
9. R. R. Sinden, *DNA structure and function*, Academic Press, Inc, California, 2012.
10. N. C. Seeman and H. F. Sleiman, *Nat. Rev.*, 2018, **3**, 1-23.
11. N. R. Kallenbach, R. I. Ma and N. C. Seeman, *Nature*, 1983, **305**, 829-831.
12. J. Malo, J. C. Mitchell and A. J. Turberfield, *J. Am. Chem. Soc.*, 2009, **131**, 13574-13575.
13. T. J. Fu and N. C. Seeman, *Biochemistry*, 1993, **32**, 3211-3220.
14. Y. He, Y. Chen, H. Liu, A. E. Ribbe and C. Mao, *J. Am. Chem. Soc.*, 2005, **127**, 12202-12203.
15. Y. He, Y. Tian, A. E. Ribbe and C. Mao, *J. Am. Chem. Soc.*, 2006, **128**, 15978-15979.
16. N. Avakyan, J. W. Conway and H. F. Sleiman, *ACS*, 2017, **139**, 12027-12034.
17. D. Liu, M. Wang, Z. Deng, R. Walulu and C. Mao, *J. Am. Chem. Soc.*, 2004, **126**, 2324-2325.
18. W. Wang, *Angew. Chem. Int. Ed.*, 2017, **56**, 6445-6448.
19. S. Hamada and S. Murata, *Angew. Chem. Int. Ed.*, 2009, **48**, 6820-6823.
20. P. W. Rothemund, N. Papadakis and E. Winfree, *PLOS Biology*, 2004, **2**.
21. P. W. K. Rothemund, *Nature*, 2006, **440**, 297-302.
22. B. Wei, M. J. Dai and P. Yin, *Nature*, 2012, **485**, 623-626.
23. W. M. Shih, J. D. Quispe and G. F. Joyce, *Nature*, 2004, **427**, 618-621.
24. R. P. Goodman, R. M. Berry and A. J. Turberfield, *Chem. Comm.*, 2004, 1372-1373.
25. J. H. Chen and N. C. Seeman, *Nature*, 1991, **350**, 631-633.
26. Y. W. Zhang and N. C. Seeman, *J. Am. Chem. Soc.*, 1994, **116**, 1661-1669.
27. W. M. Shih and C. Lin, *Curr. Opin. Struc. Biol.*, 2010, **20**, 276-282.
28. S. M. Douglas, H. Dietz, T. Liedl, B. Högberg, F. Graf and W. M. Shih, *Nature*, 2009, **459**, 414-418.
29. Y. Ke, S. M. Douglas, M. Liu, J. Sharma, A. Cheng, A. Leung, Y. Liu, W. M. Shih and H. Yan, *J. Am. Chem. Soc.*, 2009, **131**, 15903-15908.

30. B. Yurke, A. J. Turberfield, A. P. Mills, F. C. Simmel and J. L. Neumann, *Nature*, 2000, **406**, 605-608.
31. H. Yan, X. Zhang, Z. Shen and N. C. Seeman, *Nature*, 2002, **415**, 62-65.
32. W. B. Sherman and N. C. Seeman, *Nano Lett.*, 2004, **4**, 1203-1207.
33. T. Omabegho, R. Sha and N. C. Seeman, *Science* 2009, **324**, 67-71.
34. Y. Tian and C. D. Mao, *J. Am. Chem. Soc.*, 2004, **126**, 11410-11411.
35. K. Lund, A. J. Manzo, N. Dabby, N. Michelotti, A. Johnson-Buck, J. Nangreave, S. Taylor, R. Pei, M. N. Stojanovic, N. G. Walter, E. Winfree and H. Yan, *Nature*, 2010, **465**, 206-210.
36. I. Vargas-Baca, D. Mitra, H. J. Zulyniak, J. Banerjee and H. F. Sleiman, *Angew. Chem. Int. Ed.*, 2001, **40**, 4629-4632.
37. D. Mitra, N. D. Cesare and H. F. Sleiman, *Angew. Chem. Int. Ed.*, 2004, **43**, 5804-5808.
38. H. Yang, C. K. McLaughlin, F. A. Aldaye, G. D. Hamblin, A. Z. Rys, I. Rouiller and H. F. Sleiman, *Nat. Chem.*, 2009, **1**, 390-396.
39. H. Yang, A. Z. Rys, C. K. McLaughlin and H. F. Sleiman, *Angew. Chem. Int. Ed.*, 2009, **48**, 9919-9923.
40. T. G. Edwardson, K. M. Carneiro, C. J. Serpell and H. F. Sleiman, *Angew. Chem. Int. Ed.*, 2014, **53**, 4567-4571.
41. T. G. Edwardson, K. M. Carneiro, C. K. McLaughlin, C. J. Serpell and H. F. Sleiman, *Nat. Chem.*, 2013, **5**, 868-875.
42. Y. Yang, J. Wang, H. Shigematsu, W. Xu, W. M. Shih, J. Rothman and C. Lin, *Nat. Chem.*, 2016, **8**, 476-483.
43. Y. Suzuki, M. Endo and H. Sugiyama, *Nat. Commun.*, 2015, **6**, 8052.
44. D. N. Selmi, R. J. Adamson, H. Attrill, A. D. Goddard, R. J. Gilbert, A. Watts and A. J. Turberfield, *Nano Lett.*, 2011, **11**, 657-660.
45. C. M. Erben, R. P. Goodman and A. J. Turberfield, *Angew. Chem. Int. Ed.*, 2006, **45**, 7414-7417.
46. C. M. Niemeyer, T. Sano, C. L. Smith and C. R. Cantor, *Nucleic Acids Res.*, 1994, **22**, 5530-5539.
47. O. I. Wilner, Y. Weizmann, R. Gill, O. Lioubashevski, R. Freeman and I. Willner, *Nat. Nanotechnol.*, 2009, **4**, 249-254.
48. J. Fu, Y. R. Yang, A. Johnson-Buck, M. Liu, Y. Liu, N. G. Walter, N. Woodbury and H. Yan, *Nat. Nanotechnol.*, 2014, **9**, 531-536.
49. A. P. Alivisatos, K. P. Johnsson, X. Peng, T. E. Wilson, C. J. Loweth, M. P. Bruchez and P. G. Schultz, *Nature*, 1996, **382**, 609-611.
50. C. A. Mirkin, R. L. Letsinger, R. C. Mucic and J. J. Storhoff, *Nature*, 1996, **382**, 607-609.
51. T. G. Edwardson, K. L. Lau, D. Bousmail, C. J. Serpell and H. F. Sleiman, *Nat. Chem.*, 2016, **8**, 162-170.
52. S. Helmi, C. Ziegler, D. J. Kauert and R. Seidel, *Nano Lett.*, 2014, **14**, 6693-6698.
53. W. Liu, M. Tagawa, H. L. Xin, T. Wang, H. Emamy, H. Li, K. G. Yager, F. W. Starr, A. V. Tkachenko and O. Gang, *Science*, 2016, **351**, 582-586.

54. A. S. Walsh, H. F. Yin, C. M. Erben, M. J. Wood and A. J. Turberfield, *ACS Nano*, 2011, **5**, 5427-5432.
55. Q. Jiang, C. Song, J. Nangreave, X. Liu, L. Lin, D. Qiu, Z. G. Wang, G. Zou, X. Liang, H. Yan and B. Ding, *J. Am. Chem. Soc.*, 2012, **134**, 13396-13403.
56. E. W. Orava, N. Cicmil and J. Gariepy, *Biochim. Biophys. Acta*, 2010, **1798**, 2190-2200.
57. S. M. Douglas, I. Bachelet and G. M. Church, *Science*, 2012, **335**, 831-834.
58. A. Lacroix, T. G. W. Edwardson, M. A. Hancock, M. D. Dore and H. F. Sleiman, *J. Am. Chem. Soc.*, 2017, **139**, 7355-7362.
59. F. A. Aldaye, W. T. Senapedis, P. A. Silver and J. C. Way, *J. Am. Chem. Soc.*, 2010, **132**, 14727-14729.
60. H. Yang, K. L. Metera and H. F. Sleiman, *Coord. Chem. Rev.*, 2010, **254**, 2403-2415.
61. A. Buzdin and S. Lukyanov, *Nucleic Acids Hybridization: Modern Applications*, Springer, Netherlands, 2007.
62. J. S. Lee, L. J. Latimer and R. S. Reid, *Biochem. Cell Biol.*, 1993, **71**, 162.
63. F. Moreno-Herrero, P. Herrero, F. Moreno, J. Colchero, C. Gómez-Navarro, J. Gómez-Herrero and A. M. Baró, *Nanotechnology*, 2003, **14**, 128.
64. Y. Miyake, H. Togashi, M. Tashiro, H. Yamaguchi, S. Oda, M. Kudo, Y. Tanaka, Y. Kondo, R. Sawa, T. Fujimoto, T. Machinami and A. Ono, *J. Am. Chem. Soc.*, 2006, **128**, 2172-2173.
65. A. Ono, S. Cao, H. Togashi, M. Tashiro, T. Fujimoto, T. Machinami, S. Oda, Y. Miyake, I. Okamoto and Y. Tanaka, *Chem. Comm.*, 2008, **0**, 4825-4827.
66. H. A. Day, E. P. Wright, C. J. MacDonald, A. J. Gatesbc and Z. A. E. Waller, *Chem. Comm.*, 2015, **51**, 14099-14102.
67. K. Tanaka and M. Shionoya, *Coord. Chem. Rev.*, 2007, **251**, 2732-2742.
68. K. Tanaka and M. Shionoya, *J. Org. Chem.*, 1999, **64**, 5002.
69. K. Tanaka, A. Tengeiji, T. Kato, N. Toyama, M. Shiro and M. Shionoya, *J. Am. Chem. Soc.*, 2002, **124**, 12494-12498.
70. K.Tanaka, Y. Yamada and M. Shionoya, *J. Am. Chem. Soc.*, 2002, **124**, 8802-8803.
71. H. Cao, K. Tanaka and M. Shionoya, *Chem. Pharm. Bull.*, 2000, **11**, 1745-1748.
72. N. Zimmermann, E. Meggers and P. G. Schultz, *J. Am. Chem. Soc.*, 2002, **124**, 13684-13685.
73. S. Atwell, E. Meggers, G. Spraggon and P. G. Schultz, *J. Am. Chem. Soc.*, 2001, **123**, 12364-12367.
74. C. Switzer, S. Sinha, P. H. Kim and B. D. Heuberger, *Angew. Chem. Int. Ed.*, 2005, **44**, 1529-1532.
75. E. Meggers, P. L. Holland, W. B. Tolman, F. E. Romesberg and P. G. Schultz, *ACS Nano*, 2000, **122**, 10714-10715.
76. K. Tanaka, A. Tengeiji, T. Kato, N. Toyama and M. Shionoya, *Science*, 2003, **299**, 1212-1213.
77. J. S. Choi, C. W. Kang, K. Jung, J. W. Yang, Y. G. Kim and H. Han, *J. Am. Chem. Soc.*, 2004, **126**, 8606-8607.
78. M. Göritz and R. Krämer, *J. Am. Chem. Soc.*, 2005, **127**, 18016-18017.

79. D. Miyoshi, H. Karimata, Z. M. Wang, K. Koumoto and N. Sugimoto, *J. Am. Chem. Soc.*, 2007, **129**, 5919.
80. H. Yang and H. F. Sleiman, *Angew. Chem. Int. Ed.*, 2008, **47**, 2443.
81. H. Yang, C. K. McLaughlin, F. A. Aldaye, G. D. Hamblin, A. Z. Rys, I. Rouiller and H. F. Sleiman, *Nat. Chem.*, 2009, **1**, 390-396.
82. J.-L. H. A. Duprey and J. H. R. Tucker, *Chem. Lett*, 2014, **43**, 157-163.
83. J.-L. H. A. Duprey, J. Carr-Smith, S. L. Horswell, J. Kowalski and J. H. R. Tucker, *J. Am. Chem. Soc.*, 2016, **138**, 746-749.
84. D. Mitra, N. Cesare and H. F. Sleiman, *Angew. Chem. Int. Ed.*, 2004, **43**, 5808.
85. K. M. Stewart, J. Rojo and L. W. McLaughlin, *Angew. Chem. Int. Ed.*, 2004, **43**, 5808 - 5811.
86. K. M. Stewart and L. W. McLaughlin, *J. Am. Chem. Soc.*, 2004, **126**, 2050-2057.
87. D. J. Hurley and Y. Tor, *J. Am. Chem. Soc.*, 2002, **124**, 3749-3762.
88. A. L. Pinto and S. J. Lippard, *Biochim. Biophys. Acta*, 1985, **780**, 167-180.
89. E. R. Jamieson and S. J. Lippard, *Chem. Rev.*, 1999, **99**, 2467-2498.
90. M. C. Lim and R. B. Martin, *J. Inorg. Nucl. Chem.*, 1976, **38**, 1911-1914.
91. D. P. Bancroft, C. A. Lepre and S. J. Lippard, *J. Am. Chem. Soc.*, 1990, **112**, 6860-6871.
92. P. J. Sadler, K. J. Barnham, S. J. Berners-Price and U. Frey, *Chem.: Eur. J.*, 1996, **2**, 1283-1291.
93. E. Bernal-Méndez, M. Boudvillain, F. González-Vílchez and M. Leng, *Biochemistry*, 1997, **36**, 7281-7287.
94. C. A. Lepre, K. G. Strothkamp and S. J. Lippard, *ACS*, 1987, **26**, 5651-5657.
95. A. M. J. Fichtinger-Schepman, J. L. v. d. Veer, J. H. J. d. Hartog, P. H. M. Lohman and J. Reedijk, *J. Biochem.*, 1985, **24**, 707-713.
96. A. Eastman, *Biochemistry*, 1986, **25**, 3912-3915.
97. A. M. J. Fichtinger-Schepman, A. T. Oosterom, P. H. M. Lohman and F. Berends, *Cancer Res.*, 1987, **47**, 3000-3004.
98. N. Poklar, D. S. Pilch, S. J. Lippard, E. A. Redding, S. U. Dunham and K. J. Breslauer, *Proc. Natl. Acad. Sci.*, 1996, **93**, 7606-7611.
99. L. J. Naser, A. L. Pinto, S. J. Lippard and J. M. Essigmann, *Biochemistry*, 1988, **27**, 4357-4367.
100. S. E. Sherman, D. Gibson, A. H. J. Wang and S. J. Lippard, *J. Am. Chem. Soc.*, 1988, **110**, 7368-7381.
101. A. Gelasco and S. J. Lippard, *Biochemistry*, 1998, **37**, 9230-9239.
102. C. N. N. s.́-Kossi, C. Descoteaux, E. Asselin, H.-A. Tajmir-Riahi and G. Berube, *DNA Cell Biol.*, 2008, **27**, 101-107.
103. J.-P. Macque and J.-L. Butour, *Eur. J. Biochem.*, 1978, **83**, 375-387.
104. A. A. Cheng and T. K. Lu, *Annu. Rev. Biomed. Eng.*, 2012, **14**, 155-178.
105. J. Monod and F. Jacob, *Cold Spring. Harb. Symp. Quant. Biol.*, 1961, **26**, 389-401.
106. D. E. Cameron, C. J. Bashor and J. J. Collins, *Nat. Rev.*, 2014, **12**, 381-390.
107. K. Schwab, The Fourth Industrial Revolution, https://www.weforum.org/about/the-fourth-industrial-revolution-by-klaus-schwab, (accessed 20/09/2019).

108. V. Lorenzo, K. L. J. Prather, G.-Q. Chen, E. O'Day, C. Kameke, D. A. Oyarzún, L. Hosta-Rigau, H. Alsafar, C. Cao, W. Ji, H. Okano, R. J. Roberts, M. Ronaghi, K. Yeung, F. Zhang and S. Y. Lee, *Sci. Soc.*, 2018, **19**, 1-6.
109. D.-C. Meng and G.-Q. Chen, *Adv. Biochem. Engin./Biotechnol.*, 2017, **162**, 147-174.
110. Y. J. Zhou, N. A. Buijs, Z. Zhu, J. Qin, V. Siewers and J. Nielsen, *Nat. Commun.*, 2016, **7**, 1-9.
111. P. P. Peralta-Yahya, F. Zhang, S. B. Cardayre and J. D. Keasling, *Nature*, 2012, **488**, 320-329.
112. B. B. Bond-Watts, R. J. Bellerose and M. C. Y. Chang, *Nat. Chem. Biol.*, 2011, **7**, 222-228.
113. J. T. Boock, A. J. E. Freedman, G. A. Tompsett, S. K. Muse, A. J. Allen, L. A. Jackson, B. Castro-Dominguez, M. T. Timko, K. L. J. Prather and J. R. Thompson, *Nat. Commun.*, 2019, **10**, 1-12.
114. M. Tallawi, M. Opitz and O. Lieleg, *Biomater. Sci.*, 2017, **5**, 887-900.
115. V. Donato, A. F.R, S. Cogliati, C. Bauman, J. G. Costa, C. Leñini and R. Grau, *Nat. Commun.*, 2017, **8**, 14332.
116. S. J. Edwards and B. V. Kjellerup, *Appl. Microbiol. Biotechnol.*, 2013, **97**, 9909–9921.
117. M. D. Yates, S. M. Strycharz-Glaven, J. P. Golden, J. Roy, S. Tsoi, J. S. Erickson, M. Y. El-Naggar, S. C. Barton and L. M. Tender, *Nat. Nanotechnol.*, 2016, **11**, 910–913.
118. L. Hobley, C. Harkins, C. E. MacPhee and N. R. Stanley-Wall, *FEMS Microbiol. Rev.*, 2015, **39**, 649–669.
119. E. P. DeBenedictis, J. Liu and S. Keten, *Sci. Adv.*, 2016, **2**, e1600998.
120. J. Huang, S. Liu, C. Zhang, X. Wang, J. Pu, F. Ba, S. Xue, H. Ye, T. Zhao, K. Li, Y. Wang, J. Zhang, L. Wang, C. Fan, T. K. Lu and C. Zhong, *Nat. Chem. Biol.*, 2019, **15**, 34–41.
121. C. Zhang, J. Huang, J. Zhang, S. Liu, M. Cui, B. An, X. Wang, J. Pu, T. Zhao, C. Fan, T. K. Lu and C. Zhong, *Mater. Today*, 2019, **28**, 40-48.
122. A. Rising and J. Johansson, *Nat. Chem. Biol.*, 2015, **11**, 309-315.
123. X.-X. Xia, Z.-G. Qian, C. S. Ki, Y. H. Park, D. L. Kaplan and S. Y. Lee, *PNAS*, 2010, **32**, 14059-14063.
124. S. R. Fahnestock and L. A. Bedzyk, *Appl. Microbiol. Biotechnol.*, 1997, **47**, 33-39.
125. A. Lazaris, S. Arcidiacono, Y. Huang, J.-F. Zhou, F. Duguay, N. Chretien, E. A. Welsh, J. W. Soares and C. N. Karatzas, *Science*, 2002, **295**, 472-476.
126. Y.-X. Yang, Z.-G. Qian, J.-J. Zhong and X.-X. Xia, *Process Biochem.*, 2016, **51**, 484-490.
127. N. Antonovsky, S. Gleizer, E. Noor, Y. Zohar, E. Herz, U. Barenholz, L. Zelcbuch, S. Amram, A. Wides, N. Tepper, D. Davidi, Y. Bar-On, T. Bareia, D. G. Wernick, I. Shani, S. Malitsky, G. Jona, A. Bar-Even and R. Milo, *Cell*, 2016, **166**, 115-125.

128. D.-K. Ro, E. M. Paradise, M. Ouellet, K. J. Fisher, K. L. Newman, J. M. Ndungu, K. A. Ho, R. A. Eachus, T. S. Ham, J. Kirby, M. C. Y. Chang, S. T. Withers, Y. Shiba, R. Sarpong and J. D. Keasling, *Nature* 2006, **440**, 940-943.
129. W. C. Ruder, T. Lu and J. J. Collins, *Science*, 2011, **333**, 1248-1252.
130. T. K. Lu and J. J. Collins, *PNAS*, 2009, **12**, 4629-4634.
131. S. Xiang, J. Fruehauf and C. J. Li, *Nat. Biotech.*, 2006, **24**, 697-702.
132. D.-W. Zheng, Y. Chen, Z.-H. Li, L. Xu, C.-X. Li, B. Li, J.-X. Fan, S.-X. Cheng and X.-Z. Zhang, *Nat. Commun.*, 2018, **9**, 1-12.
133. L. Warren, P. D. Manos, T. Ahfeldt, Y.-H. Loh, H. Li, F. Lau, W. Ebina, P. K. Mandal, Z. D. Smith, A. Meissner, G. Q. Daley, A. S. Brack, J. J. Collins, C. Cowan, T. M. Schlaeger and D. J. Rossi, *Cell Stem Cell*, 2010, 618–630.
134. L. Giorgi and F. Leccese, *Open Fuel Cells J.*, 2013, **6**, 1-20.
135. O. Okada and K. Yokoyama, *Fuel Cells*, 2001, **1**, 72-77.
136. J. I. S. Cho, T. P. Neville, P. Trogadas, J. Bailey, P. Shearing, D. J. L. Brett and M.-O. Coppens, *Int. J. Hydrog. Energy*, 2018, **43**, 21949-21958.
137. M. S. El-Eskandarany, E. Shaban, F. Aldakheel, A. Alkandary, M. Behbehani and M. Al-Saidi, *Sci. Rep.*, 2017, **7**, 13296 13291-13216.
138. A. Kongkanand, N. P. Subramanian, Y. Yu, Z. Liu, H. Igarashi and D. A. Muller, *ACS Catal.*, 2016, **6**, 1578-1583.
139. N. Cheng, S. Stambula, D. Wang, M. N. Banis, J. Liu, A. Riese, B. Xiao, R. Li, T.-K. Sham, L.-M. Liu, G. A. Botton and X. Sun, *Nat. Commun.*, 2016, **7**, 13638 13631-13639.
140. M. Li, Y. Pan, X. Guo, Y. Liang, Y. Wu, Y. Wen and H. Yang, *J. Mater. Chem. A*, 2015, **3**, 10353-10359.
141. C. Suo, W. Zhang, X. Shi and C. Ma, *AIP Adv.*, 2014, **3**, 031340 031341 - 031310.
142. V. Stamenkovic, B. S. Mun, K. J. J. Mayrhofer, P. N. Ross, N. M. Markovic, J. Rossmeisl, J. Greeley and J. K. Nørskov, *Angew. Chem. Int. Ed.* , 2006, **45**, 2897-2901.
143. B. A. T. Mehrabadi, R. White, A. Shakouri, J. R. Regalbuto, J. W. Weidner and J. R. Monnier, *Catal. Today*, 2018, **334**, 156-161.
144. P. Chandran, A. Ghosh and S. Ramaprabhu, *Sci. Rep.*, 2018, **8**, 3591 3591-3511.

Chapter 2 - Techniques

2.1 Oligonucleotide synthesis

Solid phase synthesis was first developed in the 1960s by Bruce Merrifield[1], which became of such importance that he was later awarded the Nobel Prize for Chemistry. Many researchers aspired to develop a solution-based method for oligonucleotide synthesis. Michelson and Todd[2] designed H-phosphonate and phosphotriester approaches to achieve this goal while, Khorana[3] developed a phosphodiester-based method. Unfortunately, significant drawbacks of these methods did not allow for exploitation of the solid-phase technology to its fullest. This changed when Marvin Caruthers[4] pioneered his phosphoramidite approach (Figure 2.1) which has become the standard procedure for oligonucleotide synthesis today. Oligonucleotide synthesis via this route proceeds in the 3' to 5' direction. It is a stepwise procedure in which individual bases of an oligo are added in sequence to the first base pre-attached to the controlled pore glass (CPG) resin. The main steps are: detritylation, activation and coupling, capping, oxidation, cleavage and deprotection, which are discussed below.[5]

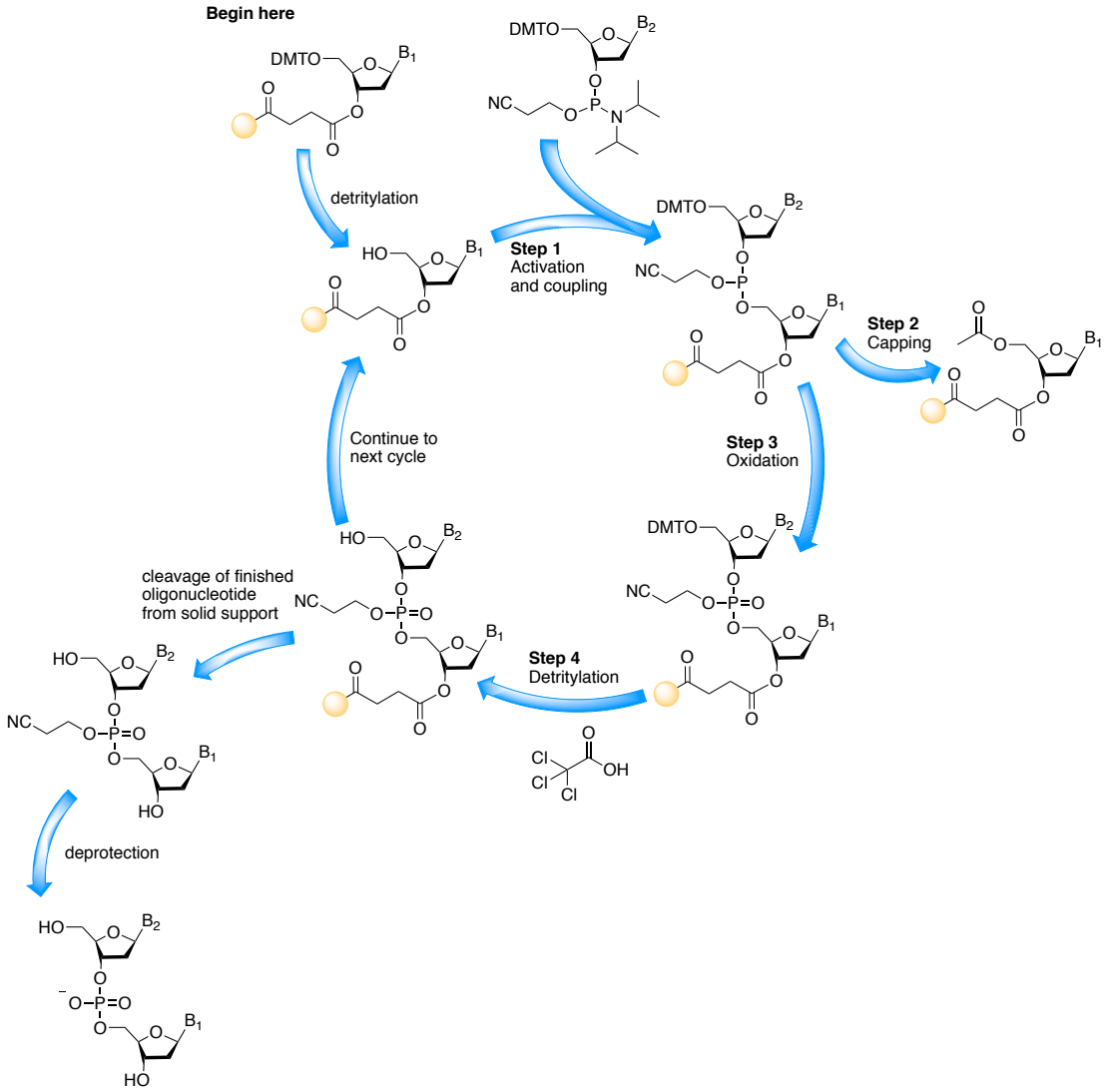

Figure 2.1 – Phosphoramidite solid-phase DNA synthesis.[5]

2.1.1 Detritylation

The first step in the oligonucleotide synthesis is to remove the 4,4'-dimethoxytrityl (DMT) protecting group from the support-bound oligonucleotide on the CPG resin (Figure 2.2). The purpose of the DMT is to ensure no polymerisation occurs while functionalising the resin. The removal of this group is necessary to proceed with the synthesis cycle.

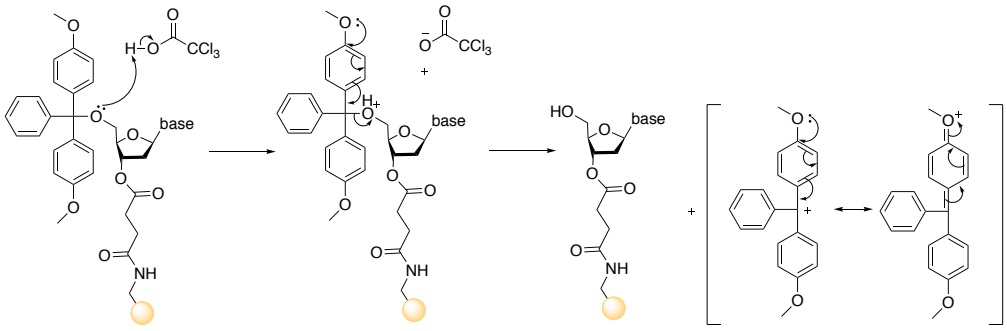

Figure 2.2 – Mechanism of the detritylation step of the phosphoramidite synthesis.[5]

2.1.2 Activation and Coupling

In this step, the deprotected nucleoside bound to the solid support can now be reacted with a nucleoside phosphoramidite monomer, which is introduced to the resin alongside an activator (e.g. tetrazole) in acetonitrile solvent. Protonation of the nucleoside is assisted by the activator, which results in the displacement of the diisopropylamine group and the formation of the phosphite triester.

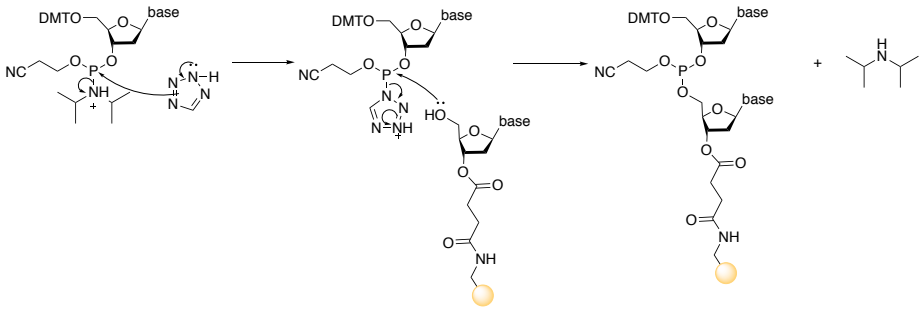

Figure 2.3 – Mechanism of the activation and coupling step of the phosphoramidite synthesis.[5]

2.1.3 Capping

A 100% yield cannot be expected from the couplings, leaving the unreacted 5' hydroxyl groups on the nucleotide available for further reaction. Addition of the next phosphoramidite at this point would result in a base deletion and ultimately, in a mixture of oligonucleotides of different sequences, difficult to separate. This can be avoided by introducing a capping step (Figure 2.4), wherein the 5' OH is acetylated with acetic anhydride and an N-methylimidazole (NMI) solution containing pyridine to maintain basic pH.

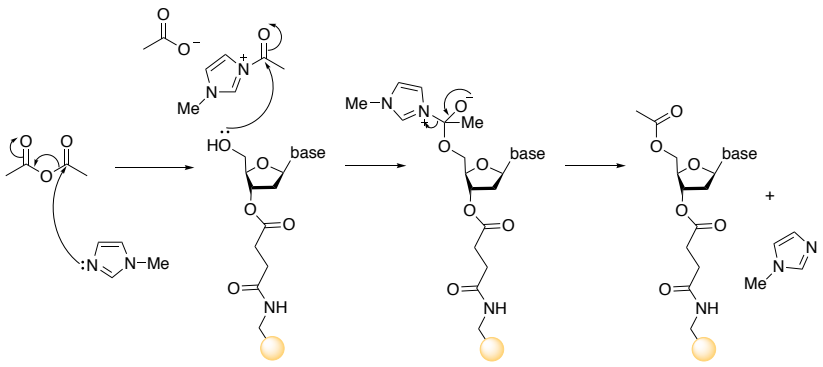

Figure 2.4 - Mechanism of the capping step of the phosphoramidite synthesis.[5]

2.1.4 Oxidation

In this step, iodine oxidation, in the presence of water and pyridine, is employed to convert the acid sensitive phosphite-triester (III) to a stable phospho-triester (V) (Figure 2.5). The presence of 2-cyanoethyl group bound to the phosphorus inhibits possible undesired reactions during the next synthesis steps.

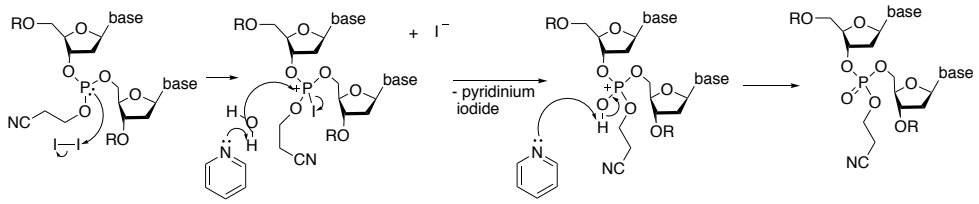

Figure 2.5 - Mechanism of the oxidation step of the phosphoramidite synthesis.[5]

This step completes the synthesis cycle for the addition of one base and is repeated for the next base addition until the desired sequence is synthesised.

2.1.6 Cleavage and deprotection

Once the desired oligonucleotide sequence has been made, it is necessary to cleave it off the solid support (Figure 2.6). This is done automatically on the synthesiser by delivering an ammonia solution to the CPG resin and collecting it into a glass vial. Following this, the aqueous ammonia solution containing the oligonucleotide is heated in order to remove the protecting groups from the bases and phosphates. Finally, the oligonucleotide samples are lyophilised before the purification can take place.

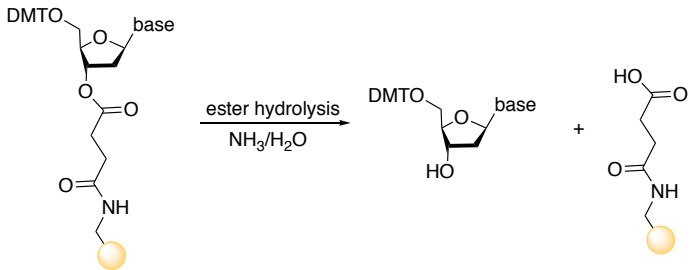

Figure 2.6 - Mechanism of the cleavage step of the oligonucleotide from the solid support.[5]

2.2 Liquid Chromatography

Liquid chromatography (LC) is an accurate separation technique which can be employed for efficient oligonucleotide purification and in combination with mass spectrometry offers a precise quantitative and qualitative analysis of even complex mixtures.[6] Amongst the most common modes used in separation of oligonucleotides are size exclusion and ion exchange chromatography as well as ion-pair reversed-phase high performance liquid chromatography.[7]

There are two main components of Liquid Chromatography (LC), namely a stationary phase and a mobile phase. Technological advances introduced smaller particle sizes to the stationary phase, which in turn led to the need to apply higher pressure in order to force the mobile phase through the column.[8] This was the beginning of High Performance Liquid Chromatography (HPLC), which is essentially an advanced form of liquid chromatography, separating molecules based on their polarity. Molecules of higher polarity will interact with the stationary phase more and will be eluted slower than the molecules of lower polarity which will interact with the solvent (mobile phase) and be eluted faster.[9, 10] A UV/Vis detection system allows for the retention time to be recorded and the purity of different components of the mixture to be monitored.

2.2.1 Ion-Pair Reversed-Phase High Performance Liquid Chromatography

Reversed phase HPLC is a variation of the aforementioned technique wherein the polarities of the mobile and stationary phases are reversed. The mobile phase is polar (e.g. water) and the stationary phase – silica - is coated with hydrophobic molecules, making it non-polar.[10] The interactions of the non-polar molecules with the aliphatic hydrocarbons allows for the separation to take place.[11] This method has been found to work well for peptides[11] and oligonucleotides.[12]

Reversed phase liquid chromatography is not suitable for oligonucleotides unless ion pairing is applied to balance the negative charge of the stationary phase as well as the oligonucleotides themselves (Figure 2.7).[6]

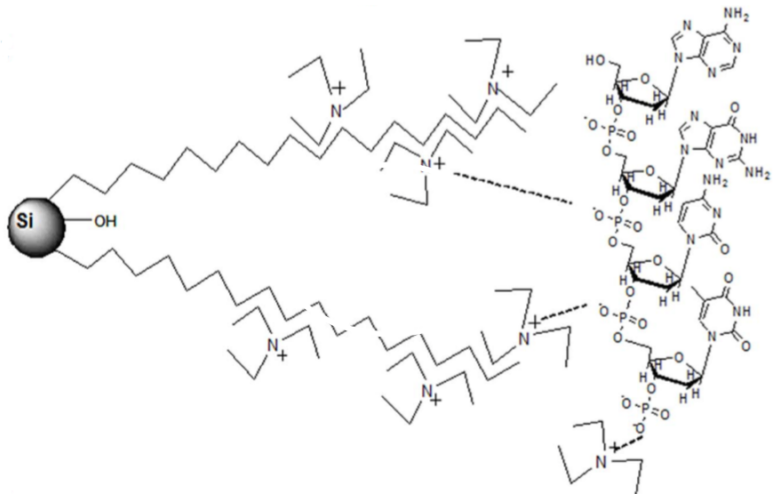

Figure 2.7 – Representation of interaction between oligonucleotide and stationary phase in ion pair reversed phase liquid chromatography. *Reproduced with permission from Studzinska et al.*[6]

The most common additives used in the mobile phase are triethylammonium or hexylammonium acetate and hexafluoroisopropanol.[13] The complex retention mechanism of chromatographic separation involves electrostatic and hydrophobic interactions, and depends greatly on the ion pair as well as its interactions with the stationary phase.[14] Charges in the oligonucleotide structure and any secondary structure it may exhibit also play an important role in the separation.[15] The commercially available stationary phase is most commonly produced and pre-packed on non-porous polymer-based alkylated microspheres.[6] Oligonucleotide separation was found to be enhanced with a decrease in the stationary phase particle size.[16]

2.3 Size Exclusion Chromatography

Size Exclusion Chromatography (SEC) is a separation technique for isolation of molecules based on their size and shape.[17] It is often used for desalting or buffer exchange. This technique consists of a porous stationary phase which traps smaller molecules within it, while the larger molecules are eluted faster as they cannot penetrate the stationary phase.[18] The stationary phase is normally silica based or a polymer such as Sephadex or a dextran polysaccharide. The main advantage of the SEC columns is a high recovery of biomolecules which means they are often used in biological applications.[17]

2.4 Mass Spectrometry

Mass spectrometry is an analytical technique which is used to determine the molecular weight of molecules. The first step is to produce gaseous ions of the molecule to be analysed, which in the case of oligonucleotides in this study, is achieved using an Electrospray Ionisation (ESI) technique. ESI uses an electrified needle which ionises and injects the analyte.[19]. ESI or Matrix Assisted Laser Desorption/Ionisation (MALDI) are preferred as they are soft ionisation techniques which often allow for non-covalent complexes to be ionised. These ions travel to the Time of Flight (TOF) detector, where they are separated according to their mass-to-charge ratio and detected according to their abundance.[20] The mass spectrum is then generated from the raw data of ion abundance versus mass-to-charge ratio.

The analysis of oligonucleotides is usually accomplished in negative ion mode as it provides better sensitivity and resolution.[20]

Mass spectrometry is a powerful tool for analysing DNA oligonucleotides due to its accurate identification and quantification.[21] It can provide useful information in regards to the purity of synthetic oligonucleotides, impurities, metabolites and post-synthetic modifications.[6] Mass spectrometry can assist in the analysis of oligonucleotides and in determining of their sequence as well as in genotyping.[22]

Oligonucleotides are compatible with (ESI-MS) since they undergo conversion to gas-phase negative ions due to the presence of the phosphate groups, producing multiply charged ions.[6] These molecular-related ions exhibit a characteristic series of signals in the MS, and come from multiply deprotonated ions $(M\text{-}nH)^{n-}$, giving rise

to the charge distribution in the negative mode ESI.[6] ESI-MS can be successfully applied to confirm the sequence of oligonucleotide metabolites,[23] failure products[24] or impurities from solid phase synthesis[25].

2.4.1 Tandem Mass Spectrometry (MS/MS)

Tandem mass spectrometry pioneered by McLucky *et al.*[26], allows for qualitative analysis of oligonucleotides which is done based on the specificity of MS/MS signals present after fragmentation. The fragments are generated by the cleavage of phosphodiester DNA backbone and result in formation of specific ions which can serve in determination of the nucleotide order in the sequence. The most abundant ions in a DNA spectra are *a-B* and *w* ions, and *c* and *y* in RNA (Figure 2.8).[27]

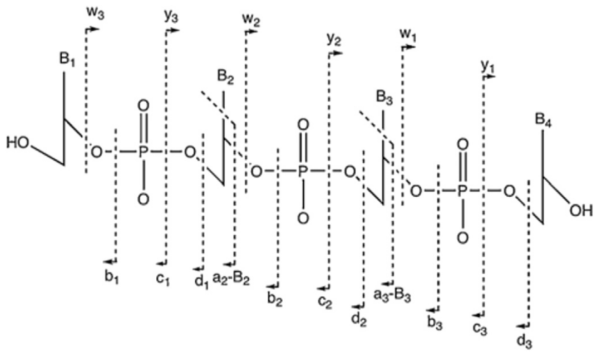

Figure 2.8 – Schematic representation of fragmentation pattern of DNA and RNA, *Reproduced with permission from McLucky et al.*[27] *Copyright 1993 American Chemical Society.*

The fragmentation is shown to begin by a loss of nucleobase from the 5' end, followed by cleavage of the 3' C-O in the sugar, and consequently a base loss from both ends may be observed.[26-28]

Tandem mass spectrometry (MS/MS) contains two stages of mass analysis.[20] The first stage is to isolate a precursor ion in an analyser. This ion then undergoes fragmentation upon activation with energy and gives rise to product ions and neutral fragments. These fragments are then analysed by a second spectrometer (Figure 2.9).

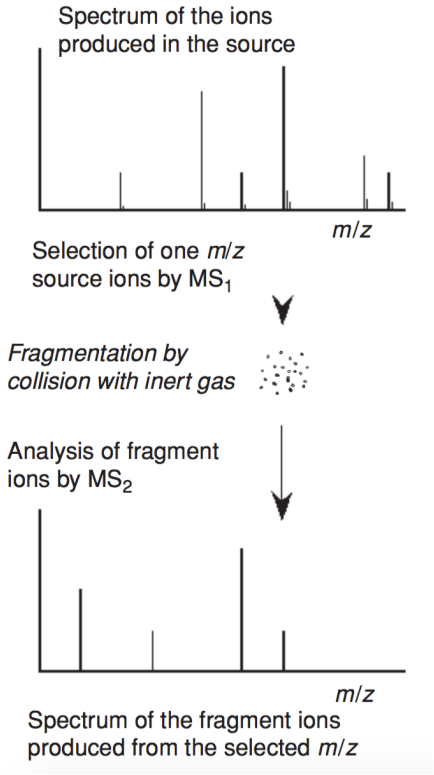

Figure 2.9 – Principle of Tandem Mass Spectrometry. *Reproduced with permission from Hoffmann et al.[20] Copyright 2007, John Wiley and Sons.*

This mass spectrometry technique can be performed in space (with the use of two instruments) or in time (by performing sequence of events). In this thesis, the former approach was used and experiments performed on the Waters Synapt G2 with a quadrupole analyser. There are four different scan modes that can be performed. In

the study described in Chapter 4, product ion scan was used, where a parent ion was chosen and the daughter ions were determined. Daughter ions are produced in the collision cell via a collision-activated-reaction (CAR) and application of a reactive gas.[20]

There are many applications of MS/MS. It can help in structure elucidation or elementary composition, determination of fragmentation mechanisms as well as in high selectivity and high sensitivity analysis.[20] In this thesis, this technique was used to determine the binding position of cisplatin in a DNA oligonucleotide sequence. This was possible because the ionisation method used in the fragmentation process yields few structurally distinct fragments. An array of mass-to-charge ratio fragments can be identified and matched to the pieces of oligonucleotide in the study.

One of the interesting applications of tandem mass spectrometry is in studying drug molecules bound to DNA in order to determine their exact position and provide insight into the DNA-drug interactions.[29] Naturally, cisplatin was amongst other drugs to be tested with this technique. Nyakas *et al.*[30] studied the cisplatin 1,2-intrastrand DNA crosslinks by ESI-CID-MS (Electrospray Ionisation Collision Induced Dissociation) and analysed their results using a time-of-flight (TOF) mass spectrometer with nanoelectrospray ionisation. The presence of cleavage of the 3'-OH phosphodiester bond next to the intrastrand crosslink was found and was in agreement with earlier studies. Moreover, the cisplatin DNA adduct exhibited less fragments and was deemed to reflect more stabilised form of DNA.[30]

Another study on cisplatin DNA adduct was done by Stucki *et al.*[31] who explored the DNA quadruplex structure. The dissociation pattern of platinated quadruplexes was found to vary depending on the type of structures. Tetramolecular quadruplexes release an unplatinated strand in the fragmentation and formation of platinated triplex, whereas in bimolecular quadruplexes, strand separation dominates.[31] Moreover, the study confirmed that platination occurs preferentially at the terminal regions.[31]

Kinetics of the platination reaction and the binding mode were studied by Egger *et al.*[32] in a study which employed the use of FT-ICR-MS. The study compared a more favourable platination site, namely GG, which was found to form an adduct after an hour of incubation, whereas the less favourable site, GTG, formed the adduct after 3 h of incubation.[32]

2.5 Spectroscopy

Spectroscopy is the study of interactions between atoms or molecules with the electromagnetic spectrum. It can be divided into three main subjects: absorption, emission and scattering (beyond the scope of this thesis).[33] Emission takes place when excess energy is emitted as a photon upon de-excitation from a high energy state to a lower energy state. Absorption spectroscopy is a technique that measures the net absorption of a sample subjected to monochromatic radiation.[34] A Jablonski diagram shows the processes which happen when a molecule absorbs light and is

shown here for reference (Figure 2.10). In this work, absorption spectroscopy will be discussed in more detail.

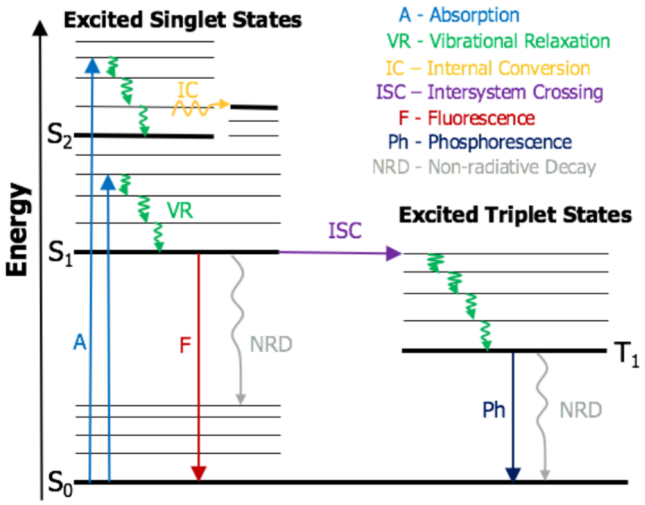

Figure 2.10 – Jablonski diagram illustrating processes such as absorption, relaxation, fluorescence and phosphorescence among others. *Reproduced with permission from J.R. Lakowicz.*[35] *Copyright 1990 PLENUM.*

2.5.1 Ultraviolet Visible Spectroscopy

Ultraviolet visible (UV/Vis) spectroscopy is a technique which studies light absorption of a molecule at any given wavelength between 170-800 nm. It is often used to quantify molecules present in a sample (e.g. DNA at ~260 nm). Spectrophotometers record the difference between the absorbed and transmitted light by the molecule and calculates the transmittance by:

$$T = \frac{I}{I_0}$$

Equation 2.1 – Equation for calculating transmittance.[34]

Where T is transmittance, I_0 is the intensity of the incident light and I is the light reaching to the detector. It is then straightforward to calculate the absorbance (A) by a logarithm of the transmittance:

$$A = \log\left(\frac{I^0}{I}\right)$$

Equation 2.2 – Equation for calculating absorbance.[34]

The concentration (c) of a sample in solution can then be easily calculated via the Beer-Lambert law (Equation 2.3) from the absorbance obtained by the spectrometer:

$$A = \varepsilon\, l\, c$$

Equation 2.3 – The Beer-Lambert law.[34]

A is the absorbance, ε is the extinction coefficient of the measured compound and l is the path length of the sample. This principle is used in this work to calculate concentration of all DNA samples.

2.5.2 Thermal Denaturation of DNA

Thermal denaturation of DNA is the reverse of hybridisation, wherein the duplex DNA is split into two single strands upon heating.[36] This event can be studied using

UV-Vis spectroscopy which monitors the absorbance change of a DNA duplex at 260 nm upon increasing temperature (Figure 2.11). The transition of double stranded DNA into a single stranded DNA results in an increase in absorption at that wavelength known as the hyperchromic effect.[37] During this transition, DNA bases become more exposed (for absorption of UV light) as the duplex unravels. The temperature at which 50% of duplex DNA is denatured into single strands is called the melting temperature (T_m).[38]

The study of DNA thermal denaturation can be a good source of valuable information on the stability of the DNA duplex as well as the secondary structure formed in case of DNA assemblies. The latter often tends to exhibit multiple transitions as shown in Chapter 4.[39]

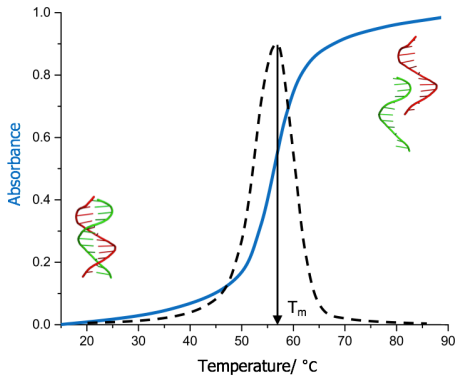

Figure 2.11 – Thermal melting curve of DNA duplex. The increase of absorbance with increased temperature is shown in blue and the calculated Tm by derivatisation (dashed) is shown in black. *Reprinted with Permission from H.A. Little.[40] Copyright 2017 University of Birmingham.*

2.5.3 Circular Dichroism Spectroscopy

Circular dichroism (CD) spectroscopy is a method which studies chiral molecules in solution.[41] This technique is ideal for studying biological molecules, such as DNA and proteins, as they contain chiral subunits and fold into secondary structures which exhibit a defined CD signal.[42]

CD measures the difference in absorbance (ΔA) of left and right circularly polarised light (Equation 2.4) at a given wavelength.

$$\Delta A = A_L - A_R$$

Equation 2.4 – Circular Dichroism equation.

A CD signal arises if a molecule absorbs either left or right circularly polarised light more than the other at a specific wavelength. This means that a CD spectrum can have positive and negative signals across a measured wavelength range. The positive signal results from a molecule absorbing A_L and negative is due to A_R absorption.[42]

As previously mentioned, DNA is a chiral molecule which has been found to exhibit three different forms A, B and Z as discussed in Chapter 1. All of these three morphological arrangements produce a different CD signal. B-DNA form is a right-handed double stranded DNA which, exhibits a positive band at 280 nm and a negative band at 245 nm. Whereas, the A-form gives a positive band at 260 nm and

a negative one at 230 nm. The Z-form is a left handed double helix giving a CD signal with a positive band at 280 nm and a broad negative band at 220 and 260 nm.[42]

The base sequence plays a significant role in the appearance of a CD spectrum. A random sequence with a mixture of all four bases gives a spectrum likeness to that of calf thymus DNA. However, a poly A sequence exhibits a less profound negative band or in case of a poly AT sequence, the positive band is split into two smaller bands (Figure 2.12).[43]

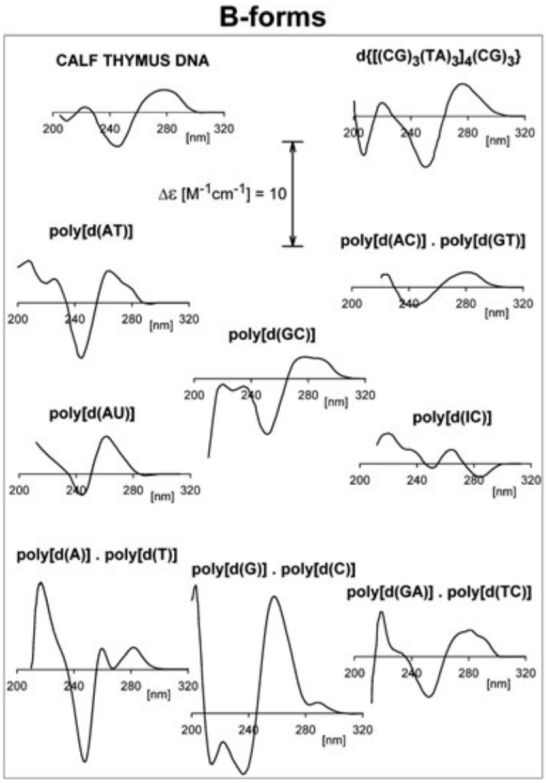

Figure 2.12 – Sequence dependent B-form DNA CD spectra. *Reproduced with permission from Vorlickova et al.*[43] *Copyright 2012 Wiley Periodicals Inc.*

2.6 Gel Electrophoresis

Gel electrophoresis is a separation technique used for biomolecules such as proteins, DNA and RNA due to them having an electrical charge.[44] This technique exploits this property of biomolecules which are placed in an electric field and travel to the electrode of opposite charge. For example, DNA having a negative charge due to the phosphate backbone travels towards the positive electrode. The separation happens according to size, shape and charge of the biomolecules.[45] Smaller molecules travel faster in the gel matrix. The gel matrix also plays a significant role in separation. Also its porosity and viscosity as well as the temperature at which the gel is run are all important.[44] In this thesis, gel electrophoresis was used to separate DNA oligonucleotides and DNA assemblies using agarose and polyacrylamide gel electrophoresis which are discussed in the following two sections:

2.6.1 Agarose Gel Electrophoresis

Agarose is a polymer based matrix which consists of a disaccharide agarobiose. This matrix is used commonly due to a uniform degree of porosity and simplicity in adjusting the pore size. A low agarose concentration gives a large pore size and high concentrations give a small pore size. This technique is used for separating DNA fragments between 100 bp to 25 kb.[46] The DNA migration rate depends on: the size of the molecules, concentration of the agarose, DNA conformation (linear/circular), the voltage and buffer.[47] In Chapter 4, agarose gel electrophoresis was used to

visualise DNA Origami Triangle made from M13 genomic DNA. In this study, the gel was post-stained and visualised under UV light.

2.6.2 Polyacrylamide Gel Electrophoresis (PAGE)

Acrylamide polymerises via methylene bridge (N,N' methylene bisacrylamide) forming a strong and chemically inert gel with highly controlled porosity.[44] The porosity can be easily controlled by varying the concentration of acrylamide or the amounts of the initiator reagents; Tetramethylethylenediamine (TEMED) and ammonium persulphate (APS). This gel matrix is ideal for high-resolution separation of small DNA fragments such as oligonucleotides.

This thesis describes the application of two types of polyacrylamide gels, namely denaturing and native. Native polyacrylamide gel is used to visualise double stranded DNA (ds) as opposed to the denaturing polyacrylamide gel which contains a denaturing agent such as urea or formamide. Denaturing agents destroy the hydrogen bonding in DNA which is of use during gel purification, wherein it is important to remove any unwanted secondary structures of DNA which would negatively affect the separation. Native polyacrylamide gel electrophoresis, maintains secondary structure, is used in this thesis as an important indication of DNA duplex and DNA assembly formation. It is important to note here, that the mobility of double stranded DNA has been found to be affected by the sequence composition which can result in an abnormal migrations.[48]

Buffering systems play an important role in gel electrophoresis. Tris-borate-EDTA (TBE) is a commonly used buffer, because it is of high conductance and reduces overheating of gels when run for a prolonged period of time.[49] Buffers containing divalent magnesium cations are used for DNA assemblies to ensure the structure is maintained during the running of the gel.[50] This type of gels is often run at 4 ^{o}C in order to minimise the possibility of denaturing DNA assemblies due to heat.

Visualisation of the gels in this thesis was done using Diamond^{TM} Nucleic Acid Dye[51, 52] which is a low toxicity stain compared to ethidium bromide (EtBr) used in the past. Additionally, it exhibits high DNA sensitivity and reduced staining time. The excitation wavelength of this dye is at 495 nm, which reduces DNA damage from UV light.

2.7 Atomic Force Microscopy (AFM)

The main principle of Atomic Force Microscopy (AFM) is to measure forces or interactions between a sharp tip and a sample surface.[53] The basic operation of this technique depends on the tip being attached to a cantilever-type-spring which is deflected upon contact with a sample (Figure 2.13).[54] Images are then produced by scanning the tip over the area of the sample (z-movement) which is digitised as a function of the lateral position x, y. There are two main modes of operation, namely contact and non-contact. The non-contact mode allows for studying magnetic, electrostatic, van der Waals and capillary forces which supply a vast amount of

information about the sample topography, magnetic domain, distributions of charge or liquid film distribution.[53] In contact mode, higher resolution of images can be achieved and frictional forces can be measured.[53]

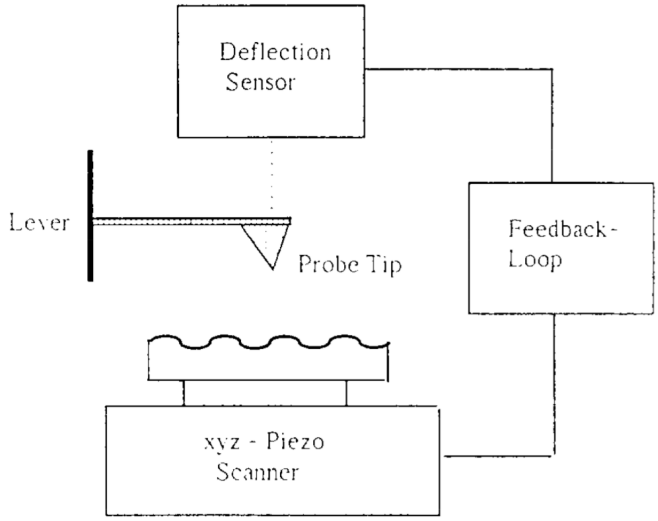

Figure 2.13 – Basic principle of AFM. *Reproduced with permission from E. Meyer.[53] Copyright 1992 Elsevier B.V.*

Due to its versatility, AFM is a method of choice in biological applications.[55] DNA self-assemblies have been extensively studied using this technique.[56, 57] In Chapter 6, AFM is employed to study an anthracene-modified DNA Three Point Star assembly on mica in a liquid mode. Ni^{2+} were used to neutralise the charge repulsion of the DNA backbone and the mica surface to enable imaging. This experiment was done by the collaborators in McGill University on the Nanoscope V controller (Bruker) in ScanAsyst mode and images were processed by Nanoscope Analysis 1.5 software (Bruker).

2.8 References

1. R. B. Merrifield, *J. Am. Chem. Soc.*, 1963, **85**, 2149-2154.
2. A. M. Michelson and A. R. Todd, *J. Chem. Soc.*, 1955, 2632-2638.
3. P. T. Gilham and H. G. Khorana, *J. Am. Chem. Soc.*, 1958, **80**, 6212-6222.
4. M. D. Matteucci and H. Caruthers, *J. Am. Chem. Soc.*, 1981, **103**, 3185-3191.
5. T. Brown and T. J. Brown, Nucleic Acids Book 2013, https://www.atdbio.com/content/17/Solid-phase-oligonucleotide-synthesis, (accessed 25/07/2019).
6. S. Studzińska, *Talanta*, 2018, **176**, 329-343.
7. A. C. McGinnis, B. Chen and M. G. Bartlett, *J. Chromatogr. B*, 2012, **883**, 76-94.
8. V. R. Meyer, *Practical High-Performance Liquid Chromatography*, John Wiley and Sons Ltd., United Kingdom, 2010.
9. L. R. Snyder, J. J. Kirkland and J. L. Glajch, *Practical HPLC Method Development*, Wiley, New York, 1988.
10. B. A. Bidlingmeyer, *Practical HPLC Methodology and Applications*, Wiley, New York, 1992.
11. M.-I. Aguilar, Springer, 2004, vol. 251, pp. 9-22.
12. K. Ashman, A. Bosserhoff and R. Frank, *J. Chromatogr.*, 1987, **397**, 137-140.
13. M. Gilar, *Anal. Biochem.*, 2001, **298**, 196-206.
14. M. Gilar, K. J. Fountain, Y. Budman, U. D. Neue, K. R. Yardley, P. D. Rainville, R. J. Russell and R. C. Gebler, *J. Chromatogr. A*, 2002, **958**, 167-182.
15. M. Dickman, *J. Chromatogr. A*, 2005, **1076**, 83-89.
16. M. Gilar and U. D. Neue, *J. Chromatogr. A*, 2007, **1169**, 139-150.
17. L. Hagel and J.-C. Janson, *J. Chromatogr. Libr.*, 1992, **51**, A267-A307.
18. J. M. Walker and R. Rapley, *Molecular Biomethods Handbook*, Humana Press, 2008.
19. C. S. Ho, C. W. K. Lam, M. H. M. Chan, R. C. K. Cheung, L. K. Law, L. C. W. Lit, K. F. Ng, M. W. M. Suen and H. L. Tai, *Clin. Biochem. Rev.*, 2003, **24**, 3-12.
20. E. Hoffmann and V. Stroobant, *Mass Spectrometry*, Wiley, England, 2007.
21. Z. J. Lin, W. Li and G. Dai, *J. Pharm. Biomed. Anal.*, 2007, **44**, 330–341.
22. P. F. Crain and J. A. McCloskey, *Curr. Opin. Biotech.*, 1998, **9**, 25-34.
23. P. Deng, X. Chen, G. Zhang and D. Zhong, *J. Pharm. Biomed. Anal.* , 2010, **52**, 571-579.
24. K. Fountain, M. Gilar and J. Gebler, *Rapid Commun. Mass Spectrom.*, 2003, **17**.
25. C. Kurata, K. Bradley, H. Gaus, N. Luu, I. Cedillo, V. T. Ravikumar, K. V. Sooy, J. V. McArdle and D. C. Capaldi, *Bioorg. Med. Chem. Lett.*, 2006, **16**, 607-614.
26. S. McLuckey, G. V. Berker and G. Glish, *J. Am. Soc. Mass Spectrom.*, 1992, **3**, 60.
27. S. McLuckey and S. Habibi-Goudarzi, *J. Am. Chem. Soc.*, 1993, **115**, 12085.
28. J. Ni, S. Pomerantz, J. Rozenski, Y. Zhang and J. McCloskey, *Anal. Chem.*, 1996, **68**, 1989.

29. C. Silvestri and J. S. Brodbelt, *Mass Spectrom. Rev.*, 2013, **32**, 247-266.
30. A. Nyakas, M. Eymann and S. Schurch, *J. Am. Soc. Mass Spectrom.*, 2009, **20**, 792-804.
31. S. R. Stucki, A. Nyakas and S. Schurch, *J. Mass Spectrom.*, 2011, **46**, 1288-1297.
32. A. E. Egger, C. G. Hartinger, H. B. Hamidane, Y. O. Tsybin, B. K. Keppler and P. J. Dyson, *Inorg. Chem.*, 2008, **47**, 10626-10633.
33. J. M. Hollas, *Modern Spectroscopy*, Wiley, Fourth edn., 2003.
34. P. Atkins and J. D. Paula, *Physical Chemistry*, W.H. Freeman, 8th edn., 2006.
35. J. R. Lakowicz, *Principles of Fluorescence Spectroscopy*, Springer.
36. D. W. Ussery, *Elsevier*, 2001, 550-553.
37. R. Thomas, *GENE*, 1993, **135**, 77-79.
38. M. Mandel and J. Marmur, *Methods Enzymol.*, 1968, **12**, 195-206.
39. J. Malo, J. C. Mitchell and A. J. Turberfield, *J. Am. Chem. Soc.*, 2009, **131**, 13574-13575.
40. H. A. Little, University of Birmingham, 2017.
41. D. M. Gray, R. L. Ratlif and M. R. Vaughan, *Methods Enzymol.*, **211**, 389-406.
42. B. Nordén, A. Rodger and T. R. Dafforn, *Linear Dichroism and Circular Dichroism: A textbook on Polarized-Light Spectroscopy*, Royal Society of Chemistry, 1 edn., 2010.
43. M. Vorlickova, I. Kejnovska, K. Bednarova, D. Renciuk and J. Kypr, *Chirality*, 2012, **24**, 691-698.
44. P. R. Reddy and N. Raju, ed. S. Magdeldin, InTech, Croatia, 2012, ch. 2.
45. T. Rabilloud, *Proteome research: two-dimensional gel electrophoresis and identification methods*, Springer Science & Business Media, Berlin, 1999.
46. J. Sambrook and D. W. Russell, *Molecular Cloning*, Cold Spring Harbor Laboratory Press, New York, 2001.
47. P. Y. Lee, J. Costumbrado, C.-Y. Hsu and Y. H. Kim, *J. Vis. Exp.*, 2012, **62**, 3923.
48. R. E. Harrington, *Electrophoresis*, 1993, **14**, 732-746.
49. P. S. Bisen, *Laboratory protocols in applied life sciences*, CRC Press, Boca Raton, 2014.
50. D. R. Duckett, A. I. H. Murchie and D. M. J. Lilley, *EMBO*, 1900, **9**, 583-590.
51. Promega, *Diamond™ Nucleic Acid Dye* Promega, USA, 2013.
52. A. M. Haines, S. S. Tobe, H. J. Kobus and A. Linacre, *Electrophoresis*, 2015, **36**, 941-944.
53. E. Meyer, *Prog. Surf. Sci.*, 1992, **41**, 3-49.
54. P. Parot, Y. F. Dufrene, P. Hinterdorfer, C. L. Grimellec, D. Navajas, J.-L. Pellequer and S. Scheuring, *J. Mol. Recognit.*, 2007, **20**, 418-431.
55. V. J. Morris, A. R. Kirby and A. P. Gunning, *Atomic Force Microscopy for Biologists*, Imperial College Press, London, 1999.
56. N. C. Seeman, *Nature*, 2003, **421**, 427-431.
57. C. Mao, W. Sun and N. C. Seeman, *J. Am. Chem. Soc.*, 1999, **121**, 5437-5443.

Chapter 3 – The binding of Pt and Ru metal complexes with salmon DNA

3.1 Introduction

This chapter introduces salmon testes DNA (ST-DNA) as well as its surfactant derivative CTMA-DNA. Several metal complexes are then introduced that can interact with DNA. ST-DNA binding studies involving some of these metal complexes are then described in order to synthesise a suitable material for catalytic applications in fuel cells.

3.1.1 Salmon DNA

Salmon DNA (ST-DNA) is derived from salmon testes sperm cells, which are themselves extracted from the waste of fishing industry. Extraction of DNA from yeast, mammalian tissues and salmon spermatozoa was first successfully accomplished by Chargaff and co-workers[1] in 1950-1951 who pioneered this field and established protocols for efficient extraction and purification of this DNA material. This is accomplished by homogenising biological tissue in water followed by enzyme treatment to remove proteins (Figure 3.1).[2] To complete the purification, the mixture is then filtered and precipitated. Today, ST-DNA is commercially available[3] and provides an inexpensive source of DNA for research applications.

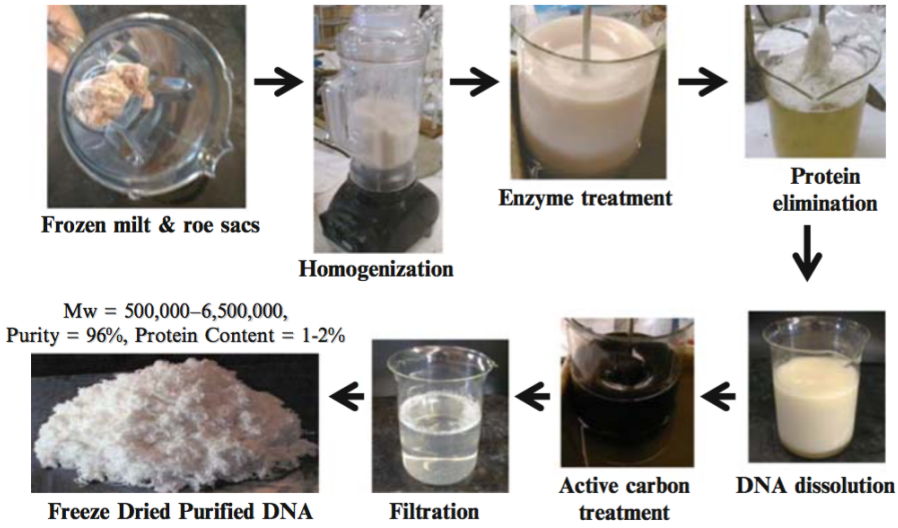

Figure 3.1 – Purification steps of ST-DNA from the raw salmon biological material. *Reproduced with permission from Singh et al.[2] Copyright 2009 Springer Nature.*

ST-DNA is a double stranded molecule with a %GC content given by the manufacturer as 41.2%[3] and an estimated molecular mass ranging from 1300 kDa[3] to 8000 kDa[4]. Such a high molecular weight material is difficult to process due to its highly viscous nature in solution. For this reason, an ultrasonic procedure is adapted in order to reduce the molecular weight of the material to as low as 200 kDa,[4] which is around 300 base pairs. The sonication procedure randomly breaks ST-DNA into a Gaussian-type distribution of molecular weights. Therefore, it is only possible to know the mean of this molecular weight distribution. The sonicated DNA material can be monitored by means of agarose gel electrophoresis.[4] However, this technique is not employed for purification purposes due to the increased costs associated and is therefore not viable for industrial applications.

Purified ST-DNA is soluble only in aqueous solvents. The resulting material is therefore water sensitive and does not exhibit sufficient mechanical strength required for fabrication processes.[2] Additionally, many particulates are observed in the salmon DNA material, again making it undesirable for such processes. Therefore, further refinement of ST-DNA is needed to render it more suitable for industrial processes and applications.

3.1.2 Surfactant DNA

The DNA backbone is negatively charged due to its phosphate groups. In order to balance this negative charge, inorganic cations such as sodium, potassium and magnesium, which occur naturally in the cells of organism, bind to the backbone of DNA, making it water soluble. However, many industrial processes require the use of organic solvents in order to produce materials that are not affected by moisture.[2] Consequently, it has become important to modify DNA to address those industrial challenges.

Osica *et al.*[5] found a cationic surfactant that interacts electrostatically with DNA. Shortly after this pioneering discovery, Morimoto's group[6] managed to selectively precipitate this surfactant-DNA material. Following these studies, Ghirlando *et al.*[7] thoroughly characterised its properties, enabling progression of this scientific field. The surfactant-DNA precipitation procedure used by Ghirlando employed an ion exchange reaction wherein a cationic surfactant complex, namely

cetyltrimethylammonium bromide (CTAB), was mixed in an aqueous solution of purified DNA.[7] The resulting DNA-lipid complex became water insoluble, rendering it suitable for industrial applications. The most common surfactant used in the literature is cetyltrimethylammonium chloride (CTMA-Cl).[2, 8, 9] It has a long (>16) alkyl chain which makes it insoluble in water (Figure 3.2). However, longer alkyl chains are undesirable since they damage the double helical structure of DNA.[2] Nevertheless, this surfactant is commercially available and relatively inexpensive, which makes it a desirable component to use in industrial processes.

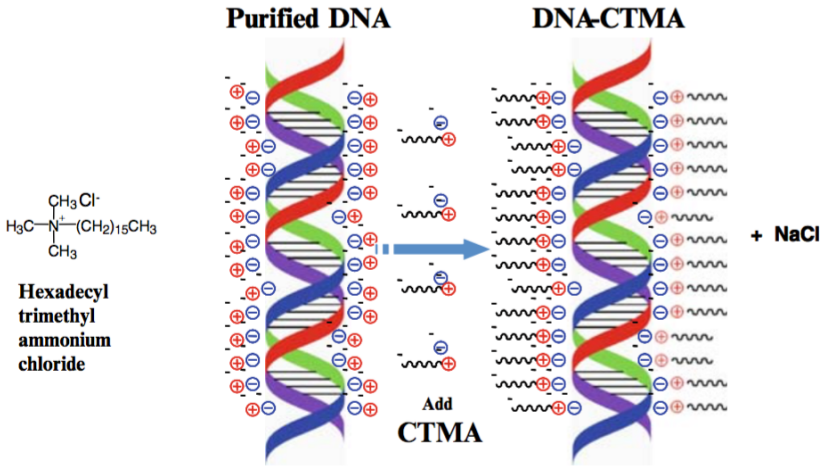

Figure 3.2 – Schematic representation of the formation of CTMA-DNA. *Reproduced with permission from Singh et al.[2] Copyright 2009 Springer Nature.*

CTMA-DNA is soluble in solvents such as chloroform, ethanol, methanol, butanol or their blends. Therefore, it can be used in standard deposition processes such as spin coating or drop casting.[2] CTMA-DNA has been found to possess an excellent (100%) transmission encompassing a wide wavelength range (400 – 1600 nm) for a 3 µm thick film.[4] Additionally, this material can also be used in optics with a refractive

index span between 1.526 and 1.540, electrical resistivity of 10^9 - 10^{14} Ω cm, dielectric constant of 7.8 - 6 and thermal stability of up to 230 °C.[10]

3.1.3 Transition metal complexes and their interactions with DNA

Transition metals are of particular interest in medicinal chemistry due to their unique properties that enable their specific interactions with biomolecules.[11] The different types of metal complex with their various oxidation states, different coordinated ligands and a selection of sizes and shapes, enable high levels of selectivity towards various biological targets.[12] Due to the structural complexity of DNA discussed in Chapter 1.2, transition metal complexes can interact with it in various ways. These include covalent binding, reversible groove association and intercalation.[13]

3.1.3.1 Covalent binding to DNA

Covalent binding of metals to DNA is irreversible and consists of strong covalent inter- or intrastrand crosslinks.[14] Such covalent adducts can cause DNA backbone distortion, which in turn affects transcription and replication in the cell.[15] Cisplatin, a common anticancer drug, is one of the best examples of a strong covalent binder which binds to DNA via hydrolysis of its chloride ligands, as detailed in Chapter 1.4. An example of a covalent metal – DNA adduct and associated disturbance of the DNA double helical structure is shown in Figure 3.3 for both cisplatin and oxoliplatin.

Other known covalent binders are: Busulfan, Chlorambucil, Clomesone and Cyclodisone, however they do not contain any metal atoms in their structure.[16]

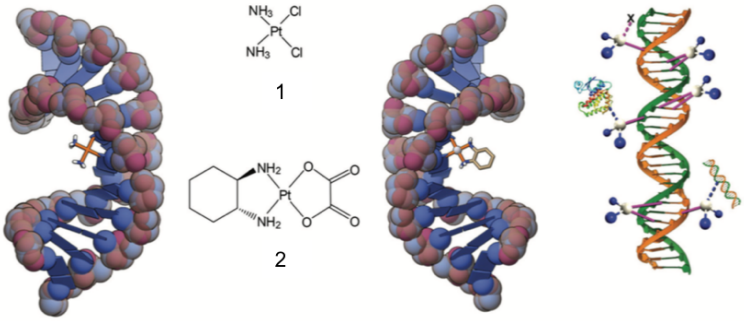

Figure 3.3 – Structural representations of intrastrand adducts formed between DNA and cisplatin (1), oxoliplatin (2) as well as schematic representation of possible adduct formations. *Reproduced with permission from Pages et al.*[12] *Copyright 2015 Royal Society of Chemistry.*

Covalent binders trigger characteristic spectral changes to the UV/Vis spectrum of DNA, whereby both a red shift and a hyperchromic shift are observed.[16] For example, Gosh *et al.* studied the interaction of various zinc complexes with calf thymus DNA (CT-DNA), which showed such spectral changes (Figure 3.4).[17]

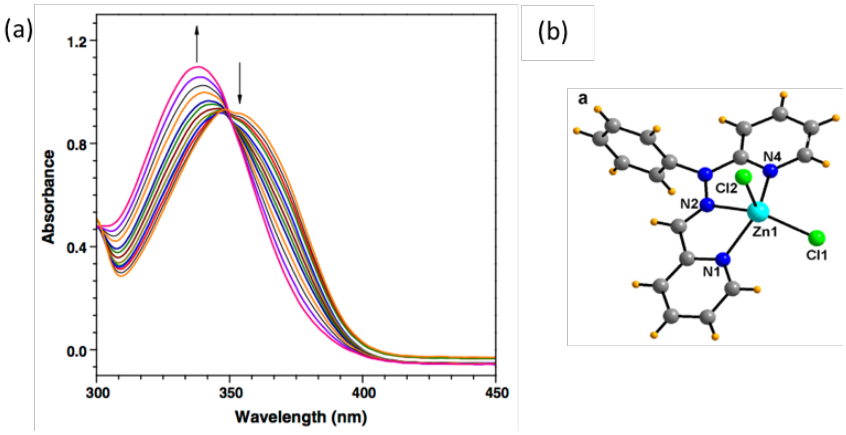

Figure 3.4 – (a) The effect on the absorption spectrum of $[Zn(Pyimpy)(Cl)_2]$ complex upon the addition of increasing amounts of DNA in 0.1 M phosphate buffer (pH 7.2); (b) crystal structure of the complex. *Reproduced with permission from Ghosh et al.*[17] *Copyright 2011 Elsevier B.V.*

Another example of a covalent binder is the complex $[RuCl_2(DMSO)_4]$, which exists in two isomeric forms, *cis* and *trans*, both of which exhibit antitumor activity.[18] Both complexes have been studied extensively in water and found to exchange three ligands (for the *trans* complex) and two ligands (for the *cis* complex) for water molecules (Figure 3.5).[19]

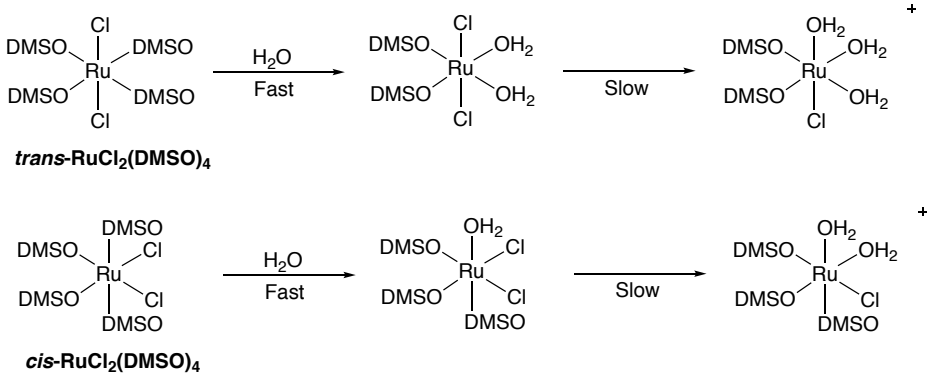

Figure 3.5 – Schematic representation of aqueous chemistry of *cis*- and *trans* - $[RuCl_2(DMSO)_4]$, adapted from J.M. Davey et al.[20]

This exchange behaviour in water facilitates covalent binding to the purine bases in DNA.[20] This was demonstrated by work of Cauci *et al.*,[21] Coluccia *et al.*[22] and later by Hazarika *et al.*[23]

3.1.3.2 Noncovalent modes of binding to DNA

Non-covalent binding between DNA and metal complexes is reversible and generally deemed to be less toxic than the covalent form of binding, which reduces undesired side effects of the drug.[16] Non-covalent binding is differentiated into three types: intercalation, grove binding and external binding.[24]

Intercalation happens when a planar polycyclic molecule carrying a positive charge is inserted between two adjacent base pairs of DNA.[25] This form of binding is stabilised by π-π stacking interactions between the two molecules and results in the DNA helix being stabilised, unwound, lengthened and stiffened.[26] The stability of the DNA-intercalator complex is strengthened by van der Waals interactions and electrostatic forces as well as hydrogen bonding.[27-29] Intercalation is preferred in the presence of extended fused aromatic ligands as seen in the ruthenium phenanthroline (Figure 3.6)[30, 31] or bipyridine[32-34] systems.

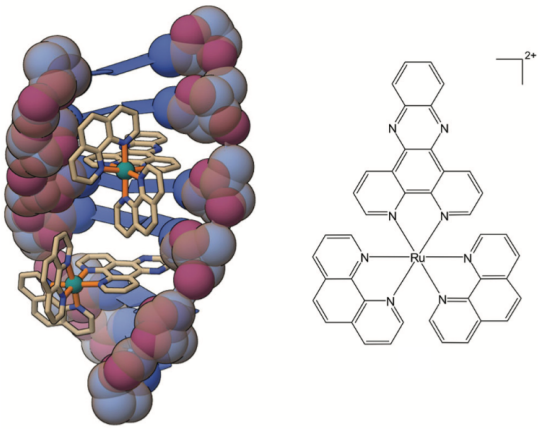

Figure 3.6 – Crystal structure of the complex rac-[Ru(phen)2(dppz)]$^{2+}$ intercalated with DNA, *Reproduced with permission from Pages et al.[12] Copyright 2015 Royal Society of Chemistry.*

More recently, a study by the Thomas group[35] identified a threading type intercalation binding mode of dinuclear ruthenium(II) polypyridyl complexes with DNA, by separation of three isomers of the ruthenium complexes and a study of their interactions with DNA by NMR. In another study by the Cardin group,[36] the binding

mode of a ruthenium complex K-$[Ru(TAP)_2(dppz)]^{2+}$ with a G-quadruplex DNA was investigated by *X*-ray crystallography and found to exhibit affinity to thymine and G-quadruplex loop binding.

Groove binding is another form of metal complex interaction with DNA, wherein the metal compound binds to the major or minor groove of DNA as well as its loop regions by hydrogen bonding and van der Waals interactions.[16] The isohelical or crescent shape of the groove binders is crucial for their effective binding to DNA, as it promotes van der Waals interactions.[37] Moreover, they have been found to have greater affinity to adenine-thymine rich sequences.[38] Good examples of groove binders are $[Ru(bpy)_3]^{2+}$ and $[Ru(Me_4phen)_3]^{2+}$ (Figure 3.7).

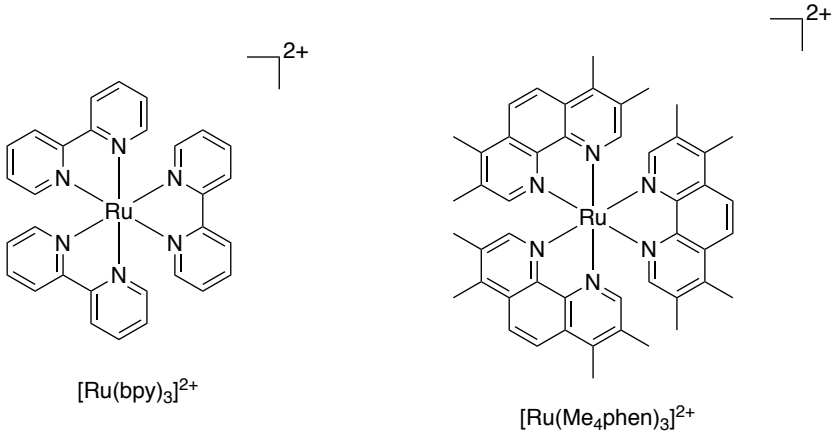

Figure 3.7 – Structure of $[Ru(bpy)_3]^{2+}$ (left) and $[Ru(Me_4phen)_3]^{2+}$ (right) which are common DNA groove binders, adapted from Pages *et al*.[12]

So-called external binding to DNA is an electrostatic interaction between metal complexes and DNA. This mode of binding occurs when the metal complex forms

complex cationic aggregates which stick to the anionic DNA to reduce charge-charge repulsions between the charged complexes.[16 38]

3.1.4 Uses of DNA in nanofabrication

CTMA-DNA exhibits interesting properties as described in Chapter 3.1.2. For this reason, it has been explored in various applications as summarised in this section.

One of many novel applications for CTMA-DNA is to act as a waveguide in nonlinear optics, as shown in Heckman *et al.,*[39] where it was found to improve poling efficiency (waiting time of a controlling device for the readiness of an external device) of polymers with large nonlinear optical coefficients to 96%. Moreover, CTMA-DNA films have been found to become resistant to its initial solvent system during processing by curing due to its ability to form cross links.[40]

CTMA-DNA has also found use in enhancing light emission in Organic Light Emitting Diodes (OLEDs) due to its large band gap of 4.7 eV.[2] CTMA-DNA was successfully investigated as an electron blocking layer (EBL), whereby incorporating it in a fluorescent type OLED system resulted in a 10 times improved efficiency and 30 times stronger luminescence compared to ordinary OLED systems.[41]

Singh et al.[42] demonstrated another use for CTMA-DNA, namely as a dielectric in low voltage operating Organic Field Effect Transistors (OFETs), wherein the smoothness

of the DNA layer forms a better interface for charge transport. Moreover, CTMA-DNA films have been found to form self-organised structures, which is proposed to arise from perpendicularly oriented alkyl chains to the film plane, while DNA helices were oriented parallel to that plane (Figure 3.8).[43]

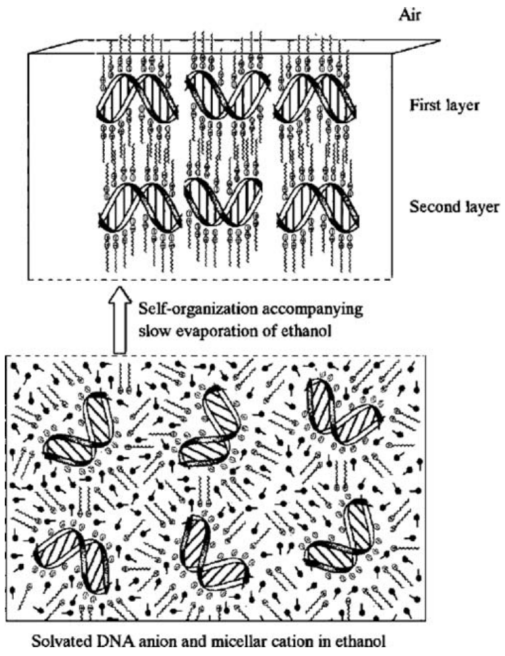

Figure 3.8 – Schematic model of the proposed assembly process of CTMA-DNA in ethanol.

Reproduced with permission from Wang et al.[43] Copyright 2001 American Chemical Society.

CTMA-DNA has also been studied for applications in energy storage devices. Norwood *et al.*[44] showed a sol-gel material doped with 5% w/t CTMA-DNA which exhibited an energy storage capacity of 20 J cm^{-3}, which is 50 times larger than the commercial polypropylene capacitors.

Not surprisingly DNA surfactant materials have been extensively explored in polymer solar cells. Lee and co-workers[45] demonstrated the use of a 2D CTMA-DNA lattice as

an electron blocking layer and found an improved power conversion efficiency from about 10 % to 160 %. Dagar *et al.*[46] used ST-DNA as an effective electron extracting layer, resulting in improvements in rectifying behaviour, photovoltaic parameters and power conversion efficiencies. The device architecture designed by the authors is presented in Figure 3.9.

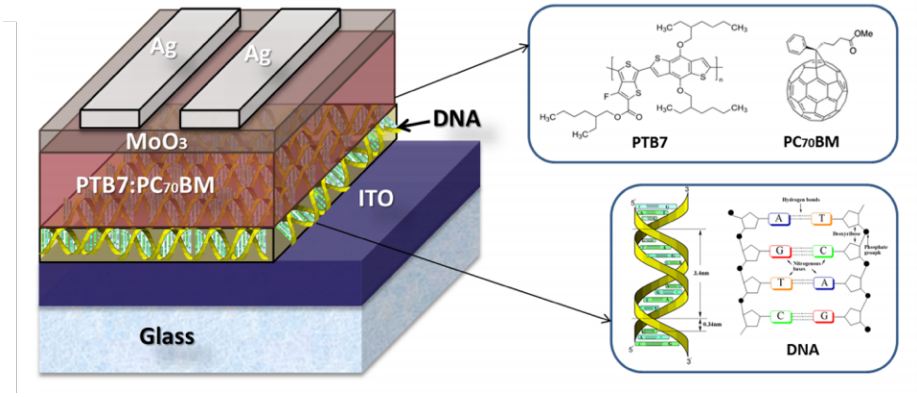

Figure 3.9 – Schematic representation of the DNA doped polymer solar cell device structure (left) with its components chemical structures (right). *Reproduced with permission from Dagar et al.*[46] *Copyright 2016 American Chemical Society.*

Yusoff *et al.*[47] investigated the use of CTMA-DNA as a hole-transport layer in Perovskite Solar Cells with improved lifetimes, while recently Elfwing and co-workers[48] explored CTMA-DNA as optical absorption dilutor in polymer solar cells, wherein it has been demonstrated to work effectively for bulk heterojunction organic photovoltaic devices (OPV).

3.2 Project aims

The project aim was to design and synthesise a novel lightweight DNA-based material for use as a precursor for a fuel cell catalyst. This was to be accomplished by functionalising salmon derived DNA with metal complexes that serve as catalytic centres (Figure 3.10). The metal complexes to be used in this study were cisplatin, a source of platinum atoms, and two ruthenium complexes, a source of ruthenium atoms. Two spectroscopic techniques, namely UV/Vis spectroscopy and circular dichroism spectroscopy were to be employed to establish the desired loading of the metal within the material. In order to render the material more suitable for fabrication processes, the use of a surfactant complex was applied.

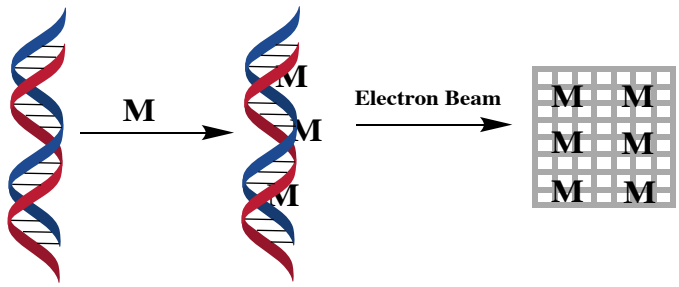

Figure 3.10 – Schematic representation of the fabrication process.

3.3 Metal loading of the material precursor

In order to synthesise considerable quantities of the material precursor for the development of the fuel cell catalyst, it was decided to use Salmon DNA (ST-DNA). As described earlier, ST-DNA is commercially available in the form of a sodium salt

and can be purchased in large quantities for a relatively low price (1 g - £ 98.20)[49], enabling the synthetic biology approach outlined in Chapter 1.

The approach for the synthesis of the material precursor was undertaken by exploring a well-known reaction between cisplatin and DNA bases, as detailed in Chapter 1.3, wherein covalent binding of cisplatin to the N7 atom of the purine bases is described. This was to ensure that a robust material precursor for the fuel cell catalyst could form. Additionally, ruthenium was also chosen to be explored, since its presence alongside platinum catalysts can reduce poisoning.[50] Therefore two ruthenium complexes, *trans*-[$RuCl_2DMSO_4$] and *cis*-[$RuCl_2DMSO_4$], were also to be studied as well as cisplatin.

The desired loading of metal in the material precursor was unknown. Hence a series of samples with varying metal content were produced in order to establish the optimal DNA : metal ratio for use in further experiments. The concentration of ST-DNA was determined using the Beer-Lambert Law using a base-pair molar extinction coefficient of 6600 L mol^{-1} cm^{-1} at 260 nm,[51] and kept at a constant base-pair concentration of 1000 µM. The range of metal complex concentrations used in this study is shown in Table 3.1.

Table 3.1 – Concentrations of metal complex used and their ratio in relation to an unchanging concentration of ST-DNA with a base-pair concentration of 1000 μM.

ST-DNA : metal ratio	Concentration of metal complex (μM)
1:0	0
1:0.25	250
1:0.5	500
1:1	1000
1:1.5	1500
1:2	2000

It was also postulated that lower loadings of metal could be more advantageous for the material precursor development, as this would limit the amount of unbound metal complex in the sample and further improve the efficiency of the catalyst. Thus, another set of samples was made with lower concentrations of cisplatin as shown in Table 3.2.

Table 3.2 – Concentrations of cisplatin (low loadings) used and their ratio in relation to an unchanging concentration of ST-DNA with a base-pair concentration of 1000 μM.

ST-DNA : cisplatin ratio	Concentration of cisplatin (μM)
1:0	0
1:0.0001	0.1
1:0.001	1
1:0.01	10
1:0.1	100
1:1	1000

The procedure for cisplatin DNA adduct formation was based upon the standard method used in the literature for cancer applications.[52] However, it is important to note that unlike the literature, the use of any buffer system was avoided here, as the

presence of additional chloride anions in the reaction mixture could potentially inhibit effective platination. Moreover, the presence of inorganic salts would not be beneficial to the catalytic material synthesis via the graphitisation process. Therefore, the synthesis of the material precursor was limited to an aqueous solution of ST-DNA and metal complex which was incubated in the dark at 37 ^{o}C overnight as detailed in Chapter 7.4.1. Thus prepared samples were characterised by means of UV/Vis and CD spectroscopy prior to handing them over to the collaborators in Chemical Engineering for further testing.

3.4 UV/Vis kinetic binding studies

The literature[52] suggested a ten-hour reaction time to allow the metal complex with DNA to fully form. However, a study was undertaken to determine how the UV absorbance changed over that period of ten hours. Equimolar amounts of ST-DNA and the metal complex were chosen for this purpose. The UV/Vis spectra were recorded between 220 – 400 nm, with the first measurement at time 0 taken immediately after inserting the cuvette into the cell changer, and consecutive measurements taken every hour. The result of the study is presented in Figure 3.11.

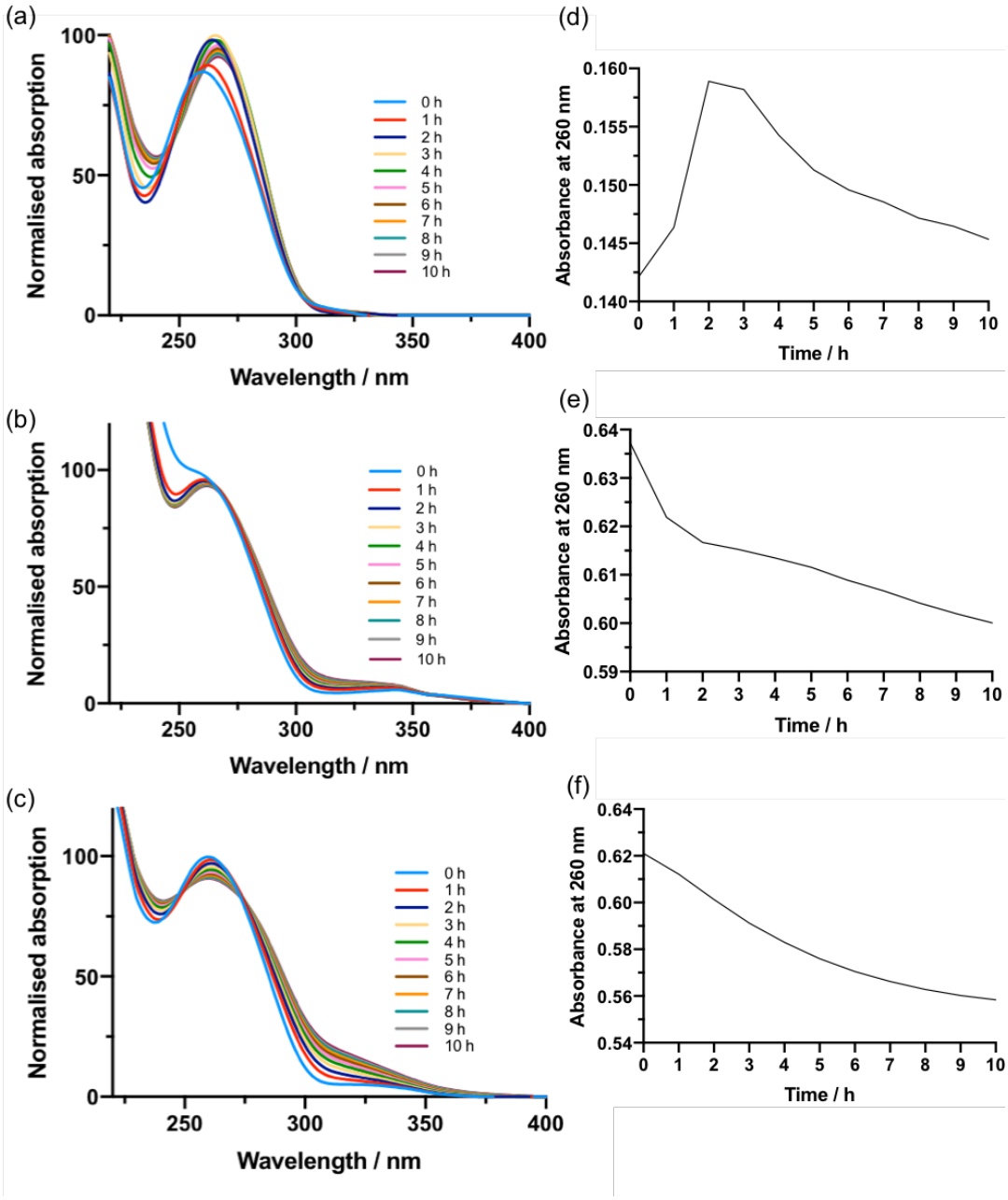

Figure 3.11 – UV/Vis measurements of the metalation reaction with 1000 µM ST-DNA (1:1 ratio) at 37 °C over a time period of 10 h in 1 h intervals in MilliQ water, a – with cisplatin (1000 µM), b – with *cis*-[$RuCl_2DMSO_4$] (1000 µM), c – with *trans*-[$RuCl_2DMSO_4$] (1000 µM). Binding curves of the metalation reaction showing change in absorbance as a function of time, d - with cisplatin, e – with *cis*-[$RuCl_2DMSO_4$], f – with *trans*-[$RuCl_2DMSO_4$].

The data recorded show an increase in absorbance at 260 nm from t = 0 h until a maximum is reached at t = 3 h (Figure 3.11a). This hyperchromic effect suggests reduction of base stacking in DNA as a result of binding to cisplatin.[16] Subsequently, the absorbance at 260 nm decreases for the rest of the experiment (until t = 10 h). This secondary hypochromic effect may be due to unspecific binding of additional cisplatin, which can interact electrostatically with the negatively charged phosphate backbone of the DNA, which makes it more compact, with less bases exposed.[16] In addition to the changes, a bathochromic effect can be observed over this period where the absorbance at 260 nm shifts towards higher wavelengths. Additionally, the change in absorbance is shown as a function of time in Figure 3.11d. The binding kinetics was found to be 0.49 $^{-}$h and 0.27 $^{-}$h, whereas half-life times were 1.4 h and 4.7 h respectively for the two transitions. This data suggests that the specific cisplatin DNA binding undergoes relatively fast under these conditions after which, the remaining cisplatin binds to other sites on the DNA.

The binding kinetics of *cis*-[$RuCl_2DMSO_4$] and *trans*-[$RuCl_2DMSO_4$] to ST-DNA is shown in Figure 3.11b and 3.11c respectively. The UV data for *cis*-[$RuCl_2DMSO_4$] DNA complex suggests little structural change has taken place during this reaction. However, the data for *trans*-[$RuCl_2DMSO_4$] suggests a change in the DNA structure where a decrease in absorbance at 260 nm throughout the 10 h period can be seen. This reaches a plateau between the time 8 – 10 h, where it can be assumed that the reaction is complete. The literature[21-23] states that these ruthenium complexes bind to DNA covalently, although UV/Vis studies were not undertaken. The hypochromic

effect shown here may be a result of either binding modes being present, such as electrostatic interactions that possibly overshadow the effect of covalent binding. Additionally, the change in absorbance is shown as a function of time in Figure 3.11e for the *cis*-[$RuCl_2DMSO_4$] complex and Figure 3.11f for the *trans*-[$RuCl_2DMSO_4$]. The binding kinetics were found to be 0.38 $^{-}$h and 0.21 $^{-}$h respectively, whereas half-life times were 1.8 h and 3.3 h.

3.5 UV/Vis stoichiometric binding studies

A series of UV/Vis experiments was performed on an array of samples with varying metal loadings as described in Chapter 3.3. This was carried out in order to determine the optimum metal loading needed for the graphitisation process and the subsequent electrochemical studies. Each ST-DNA - metal complex sample was subjected to an overnight incubation at 37 ^{o}C in the dark prior to the study in order to ensure that the reaction has gone to completion.[52] The UV/Vis spectra were recorded between 220 – 400 nm with the results presented in Figure 3.12.

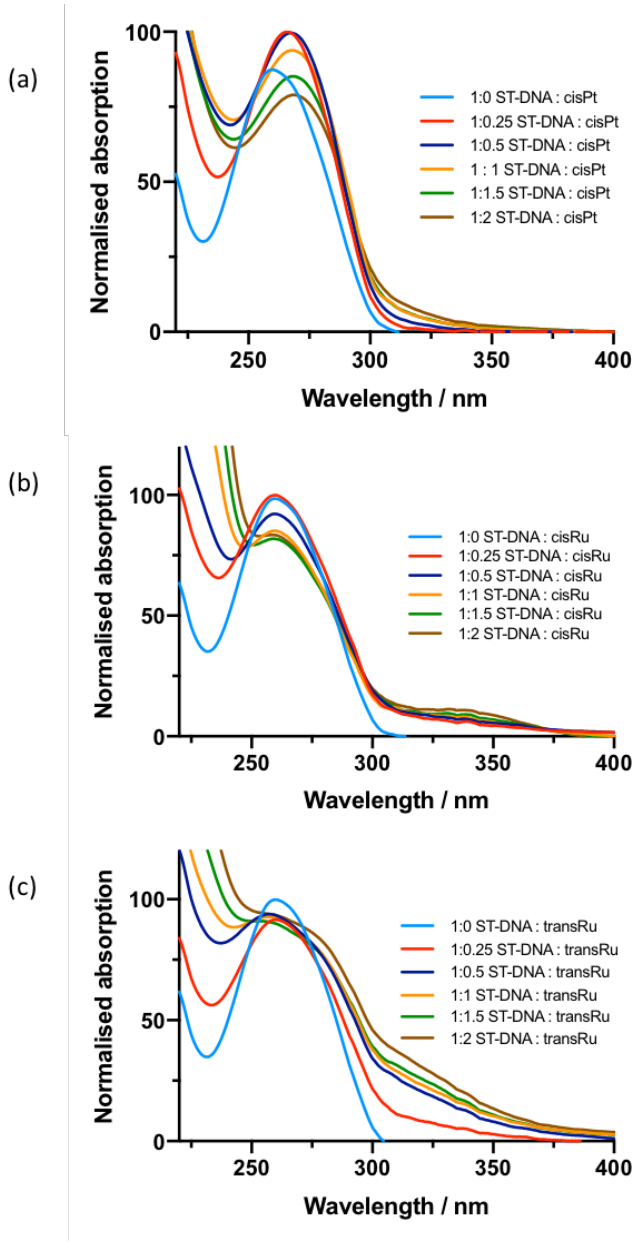

Figure 3.12 - UV/Vis measurements of an array of ST-DNA (1000 µM) samples with varying metal loadings (0 – 2000 µM) in MilliQ water after an overnight incubation at 37 ^{o}C in the dark, a – with cisplatin, b – with *cis*-[$RuCl_2DMSO_4$], c – with *trans*-[$RuCl_2DMSO_4$].

The data recorded for the platinated ST-DNA samples follow a similar trend to those seen for the kinetic studies at equimolar concentrations. An increase in absorbance at 260 nm is shown for the 1:0.25 and 1:0.5 metal loadings, implying a hyperchromic

effect due to covalent binding mode of cisplatin to DNA (Figure 3.12a). Further increases in platinum loading cause a decrease in absorbance at that wavelength, with this hypochromic shift in turn ascribed to a change in binding mode to unspecific electrostatic. A bathochromic shift is also apparent, further indicating the covalent interactions between cisplatin and ST-DNA.

The UV/Vis data for *cis*-[$RuCl_2DMSO_4$] and *trans*-[$RuCl_2DMSO_4$] – ST-DNA adducts are shown in Figure 3.12b and 3.12c respectively. Only one mode of binding seems to dominate the interactions in these cases, namely electrostatic as evidenced by the hypochromic shift as well as the lack of any hyperchromic shift in the absorption band. The data for *cis*-[$RuCl_2DMSO_4$] DNA complex is more profound here in comparison to the kinetic study shown in Figure 3.11b. This is likely associated with instrument difficulties which might have occurred during earlier kinetic studies.

As it was decided to explore low loadings of platinum for the development of the fuel cell catalytic material precursor (see Section 3.3.), a series of samples with low platinum loadings, were also studied with the results shown in Figure 3.13. It is important to note that the data for 1 : 0.001 ST-DNA : cisPt and for 1 : 0.01 ST-DNA : cisPt are not visible due to being overlaid by the neighbouring data points.

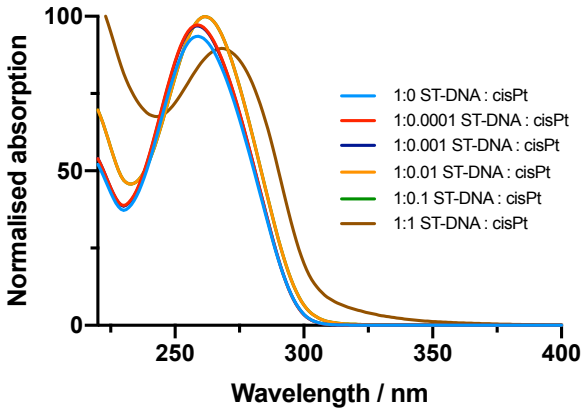

Figure 3.13 – UV/Vis measurements of an array of ST-DNA (1000 µM) samples in MilliQ water with low loadings (0 – 1000 µM) of cisplatin after an overnight incubation at 37 ^{o}C in the dark.

The small hyperchromic effect indicates that the covalent mode of binding dominates for low platinum loadings indicating that covalent adduct formation is favoured, with unspecific binding reduced to a minimum. The equimolar ST-DNA to cisplatin sample, wherein hypochromic effect dominates, is given here as a comparison to the low loadings samples.

A control UV/Vis spectroscopy experiment was conducted wherein an array of samples with varying concentrations of metal complex in the absence of DNA was studied to compare with the corresponding DNA - containing samples. The UV/Vis spectra were recorded between 220 and 400 nm, with the results presented in Figure 3.14.

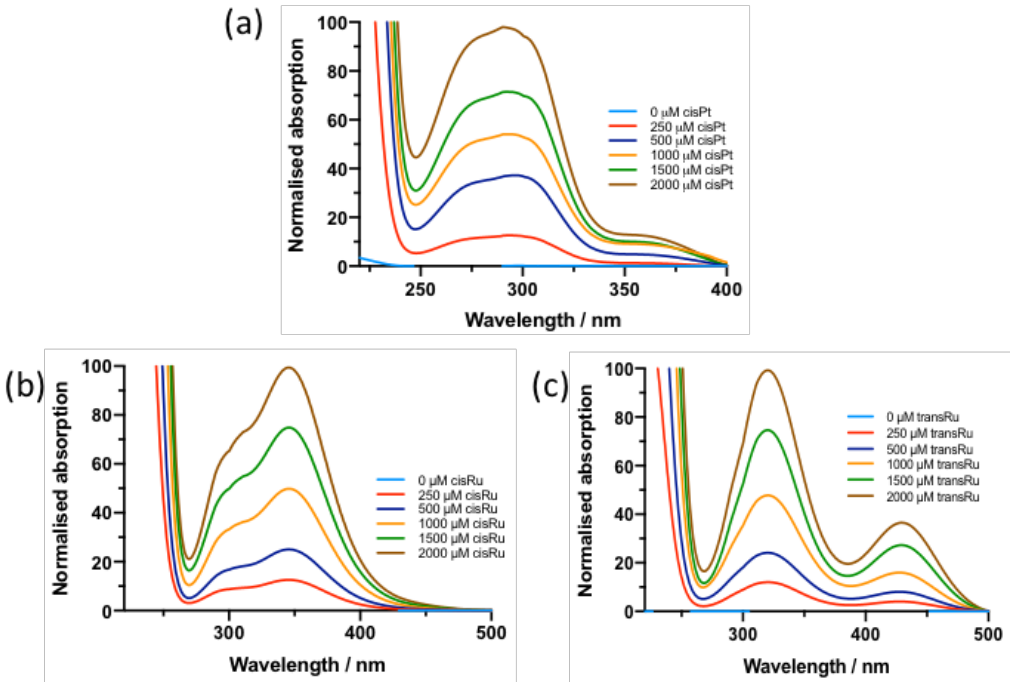

Figure 3.14 - UV/Vis measurements of an array of samples with varying concentrations of metal (0 – 2000 µM), a – cisplatin, b – with *cis*-[$RuCl_2DMSO_4$], c – with *trans*-[$RuCl_2DMSO_4$] in MilliQ water after an overnight incubation at 37 ^{o}C in the dark.

The spectroscopic data recorded for cisplatin shows a distinct broad peak at 280 nm, which increases from 250 µM to 2000 µM as expected (Figure 3.14a). Similar behaviour is observed in the case of the ruthenium complexes (Figure 3.14b and Figure 3.14c). The cis-$RuCl_2DMSO_4$ complex shows one peak at 350 nm, shouldering towards the shorter wavelength. The *trans*-$RuCl_2DMSO_4$ complex shows two peaks: one at 320 nm and one at 420 nm, corresponding with the literature data.[23] The data indicates that the absorption due to the complexes may affect the spectra of the ST-DNA samples but their concentration at the maximum absorbance for DNA (260 nm) is relatively small.[53]

3.6 Circular Dichroism stoichiometric binding studies

Another technique used to study the interaction of the metal complexes with ST-DNA, while at the same time determining the desirable metal loading for further experiments, was circular dichroism (CD) spectroscopy. A CD study was performed on an array of samples with varying metal loadings as described in Section 3.3, following the UV/Vis experiment. The CD spectra were recorded between 220 – 400 nm, with the results presented in Figure 3.15.

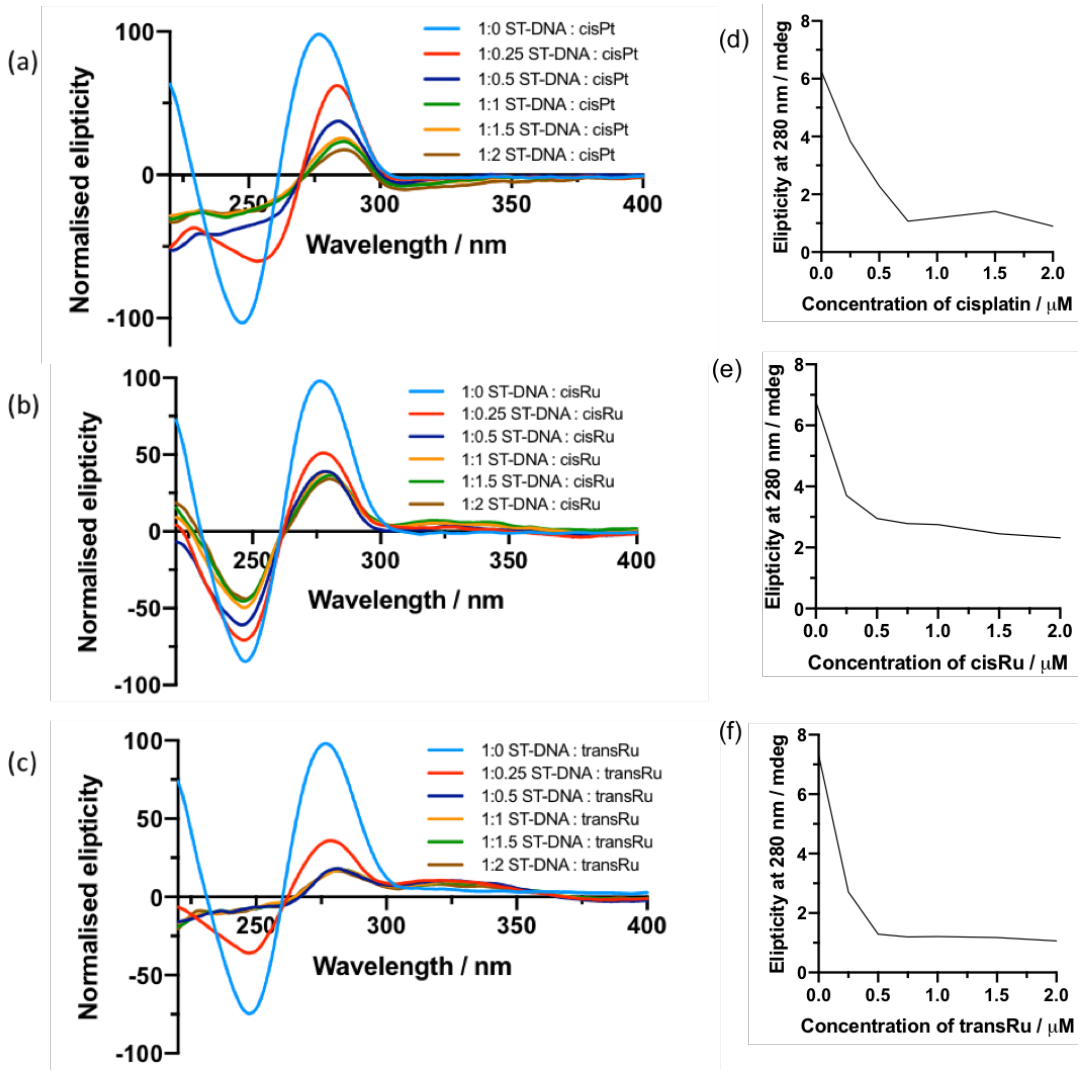

Figure 3.15 - CD measurements of an array of 1000 μM ST-DNA samples with varying metal loadings (0 – 2000 μM) after an overnight incubation at 37 ^{o}C in the dark, a – with cisplatin, b – with *cis*-[$RuCl_2DMSO_4$], c – with *trans*-[$RuCl_2DMSO_4$]. Binding curves of the metalation reaction showing change in elipticity at 280 nm as a function of metal complex concentration, d - with cisplatin, e – with *cis*-[$RuCl_2DMSO_4$], f – with *trans*-[$RuCl_2DMSO_4$].

The CD results for platinated ST-DNA show variations in the negative band amplitude at 245 nm and the positive band amplitude at 280 nm with increasing platinum loadings (Figure 3.15). The positive band reduces sharply in intensity from 1:0 to

1:0.5 cisplatin loading. Further increases in metal concentration appear to decrease the band intensity slightly, suggesting a loss in B-DNA structure, which then remains unchanged at the same level for ratios of 1 : 0.75 to 1 : 2. This behaviour is consistent with the UV/Vis data, which suggest that the covalent mode of binding peaks at the 1 : 0.5 cisplatin loading, is also consistent with the literature.[54] The disappearance of the negative band at 1 : 0.5 cisplatin loading is further evidence for the saturation point being reached. Moreover, a bathochromic shift is also present, again consistent with the UV/Vis spectra (Section 3.5). Additionally, elipticity is shown as a function of cisplatin concentration in Figure 3.15d. The binding constant was found to be - 0.51. Negative value of the binding constant confirms the disruptive character of cisplatin on the DNA structure.

The CD results for the ruthenium complexes ST-DNA, namely *cis*-[$RuCl_2DMSO_4$] and *trans*-[$RuCl_2DMSO_4$] – ST-DNA adducts, show a disappearance in the negative band at 245 nm and a decrease in the band at 280 nm with increased amounts of metal loadings for both ruthenium complexes. For both complexes, the saturation point was at the 1 : 0.5 ST-DNA to ruthenium complex ratio, at which point the change does not vary significantly with increasing metal loadings. The changes to the CD bands, namely the disappearance of the negative band and the decrease in the positive band with increasing metal loadings, suggest that electrostatic interactions of the ruthenium complexes cause disruption to the B form of DNA. The degree of this disruption seems to be more apparent for *trans*-[$RuCl_2DMSO_4$], which suggests that it binds more strongly than the *cis* isomer. Additionally, elipticity is shown as a

function of ruthenium complex concentration in Figure 3.15e for the *cis* isomer and Figure 3.15f for the *trans* isomer. The binding constant was found to be - 0.34 and - 0.52 respectively. Negative value of the binding constant confirms the disruptive character of the metal complexes on the DNA structure.

As it was decided to explore low loadings of platinum for the development of the fuel cell catalytic material precursor, a series of samples of low platinum loadings were next characterised by CD spectroscopy (Figure 3.16), as also done earlier using UV/Vis spectroscopy.

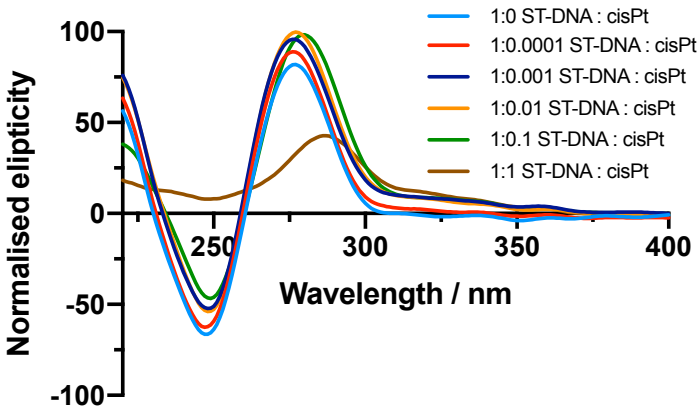

Figure 3.16 - CD measurements of an array of ST-DNA (1000 µM) samples in MilliQ water with low loadings (0 – 1000 µM) of cisplatin after an overnight incubation at 37 ^{o}C in the dark.

The data presented in Figure 16 clearly shows that binding sites on the ST-DNA are not saturated for low loadings of cisplatin. This is evidenced by the presence of a distinct negative band at 245 nm and a small increase in the positive band at 280 nm with increasing platinum loadings. The equimolar ST-DNA to cisplatin loading is given here as a comparison to the low loadings samples. The CD data are consistent with

the UV/Vis spectroscopy results in that the covalent mode of binding dominates for ST-DNA samples with low loadings of platinum.

A control experiment was undertaken wherein Circular Dichroism spectroscopy was undertaken on the metal complexes without DNA present. There was no signal present for any of the three complexes within the study and therefore the data for this experiment was not shown here.

3.7 CTMA – DNA

Following the study with DNA derived from salmon testes, it became important to study the behaviour of CTMA modified DNA which had been deemed to be more suitable for lithographic approaches[2] and ultimately for fuel cell catalytic applications. This required a successful conversion of salmon DNA in a form of sodium salt into a CTMA salt, soluble in organic solvents. Since it was observed that the *trans*-[$RuCl_2DMSO_4$] complex interacts stronger with DNA, it was decided that it should become the source of the ruthenium in the target catalytic material, the *cis* isomer was not shown.

A series of ST-DNA samples were produced with varied metal loadings (Table 1) as previously described in water (Chapter 7.4.1). Subsequently, the samples were cation exchanged into CTMA salts, as described in Chapter 7.4.2. This produced metal containing CTMA-DNA samples, dissolved in methanol which were

characterised using UV/Vis spectroscopy (Figure 3.17) and CD spectroscopy (Figure 3.18). Platination reaction on the CTMA-DNA was avoided since the reaction requires aqueous conditions to take place.[52, 55]

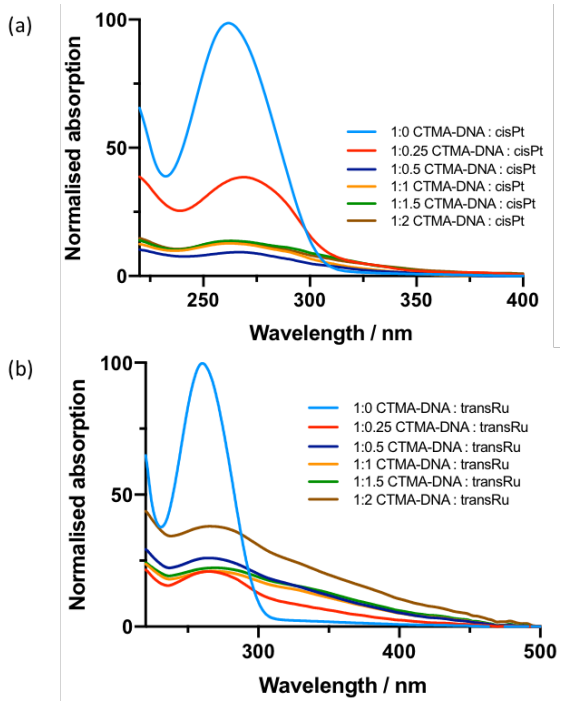

Figure 3.17 – UV/Vis measurements of an array of CTMA-DNA (1000 µM) samples in methanol with varying metal loadings (0 – 2000 µM): a – with cisplatin and b – with *trans*-[$RuCl_2DMSO_4$].

The data presented for both metal complexes show a decrease in absorbance at 260 nm with increasing metal loading (Figure 3.17). This shows that cisPt containing samples do not dissolve well in methanol, which can be explained by either the platinum reducing the solubility or by incomplete cation exchange. Moreover, the UV/Vis signals of metallised CTMA-DNA seemed to be inconsistent, which can also be explained by a possible loss of material during the purification of the CTMA-DNA. Nonetheless, it is important to note that the solubility of metallised CTMA-DNA seems to decrease with an increase in metal loading. This can be explained by non-

specific electrostatic interaction between the metal complexes and the DNA phosphate backbone, which then inhibits binding of the CTMA countercation.

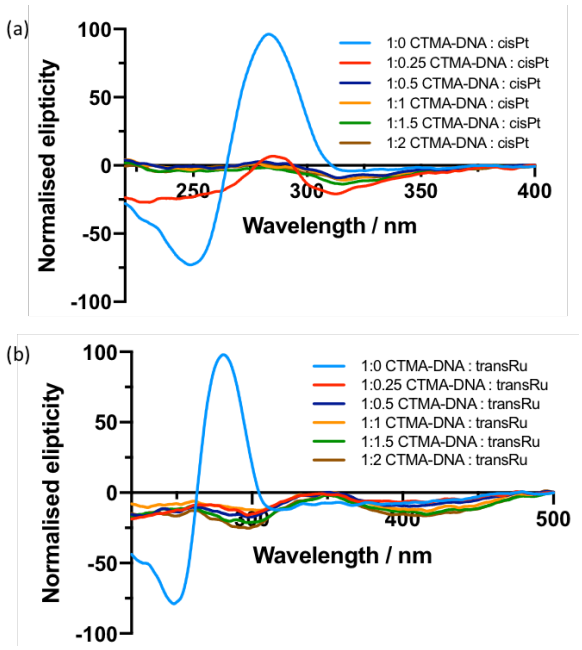

Figure 3.18 – CD measurements of an array of CTMA-DNA (1000 µM) samples in methanol with varying metal loadings (0 – 2000 µM): a – with cisplatin and b – with *trans*-[$RuCl_2DMSO_4$].

The data presented in Figure 3.18 show that the CD signal at 260 nm disappears with increase of metal loadings for both complexes. Only the unmetallised CTMA-DNA shows the familiar B-DNA structure by CD spectroscopy, whereas the signals corresponding to the metallised CTMA-DNA do not exhibit this form. This can be associated with poor solubility of the metallised CTMA-DNA samples, due to the metal complex inhibiting the binding of CTMA countercation. Overall, the study has been compromised by the function of CTMA being affected by electrostatic interactions with platinum. However, should organic solvent-soluble DNA be a requirement, solubility with lower Pt loadings may still be possible.

3.8 Conclusions

This work has demonstrated synthesis of a DNA based material precursor for fuel cell catalyst development. Moreover, the most suitable ratios of metal loadings have been successfully established through kinetic and stoichiometric studies. The metal complexes used in this work, namely cisplatin, *cis*-[$RuCl_2DMSO_4$] and *trans*-[$RuCl_2DMSO_4$] were characterised by UV/Vis and CD spectroscopy. Low metal loadings have been found to be more desirable for fuel cell catalyst development as the covalent binding mode dominates at these ratios. This mode of binding is stronger and therefore more suitable for processing using electron beam tool. High metal loading samples exhibit an unspecific binding mode, possibly consisting of electrostatic interactions, with the phosphate backbone, which would be undesirable as it is prone to cluster formation in the material.

Finally, an attempt to synthesise a metallised CTMA-DNA material was unsuccessful as high metal loadings inhibited the reaction. Future work will focus on lowering the platinum loading in the DNA material in the hope to minimise electrostatic interactions between the metal complex and DNA to achieve strong covalently bound adducts and at the same time enable formation of metallised CTMA-DNA material suitable for further processing with the electron beam tool and fuel cell catalyst fabrication.

3.9 References

1. E. Chargaff, B. Magasanik, E. Vischer, C. Green, R. Doniger and D. Elson, *J. Biol. Chem*, 1950, **186**, 51-67.
2. T. B. Singh, N. S. Sariciftci and J. G. Grote, *Adv. Polym. Sci.*, 2009, **223**, 189-212
3. Sigma-Aldrich, *DNA, sodium salt from Salmon Testes, Product Information*, 2014.
4. E. M. Heckman, J. A. Hagen, P. P. Yaney, J. G. Grote and F. K. Hopkins, *Appl. Phys. Lett.*, 2005, **87**, 211115:211111-211113.
5. V. P. Osica, T. L. Pyatigorskaya, O. F. Polyvtsev, A. T. Dembo, M. O. Klija, V. N. Vasilchenko, B. I. Venkin and B. Y. Sukharevsky, *Nucleic Acids Res.*, 1977, **4**, 1083-1096.
6. M. Morimoto, P. A. Ferchmin and E. L. Bennett, *Anal. Biochem.*, 1978, **62**, 436-448.
7. R. Ghirlando, E. J. Wachtel, T. Arad and A. Minsky, *Biochemistry*, 1992, **31**, 7110-7119.
8. M. Mindroiu, A.-M. Manea, I. Rau, J. G. Grote, H. C. L. Oliveira, A. Pawlicka and F. Kajzar, *Proc. SPIE*, 2013, **8882**, 888202-888201 - 888212.
9. Y.-W. Kwon, C. H. Lee, D.-H. Choi and J.-I. Jin, *J. Mater. Chem.*, 2009, **19**, 1353-1380.
10. J. G. Grote, E. M. Heckman, D. E. Diggs, J. A. Hagen, P. P. Yaney, A. J. Steckl, S. J. Clarson, G. S. He, Q. Zheng, P. N. Prasad, J. S. Zetts and F. K. Hopkins, *Proc. SPIE*, 2005, **5934**.
11. E. Meggers, *Curr. Opin. Chem. Biol.*, 2007, **11**, 287-292.
12. B. J. Pages, D. L. Ang, E. P. Wright and J. R. Aldrich-Wright, *Dalton Trans.*, 2015, **44**, 3505-3526.
13. E. R. Jamieson and S. J. Lippard, *Chem. Rev.*, 1999, **99**, 2467-2498.
14. C. Silvestri and J. S. Brodbelt, *Mass Spectrom. Rev.*, 2013, **32**, 247-266.
15. H. K. Liu and P. J. Sadler, *Acc. Chem. Res.*, 2011, **44**, 349-359.
16. M. Sirajuddin, S. Ali and A. Badshah, *J. Photochem. Photobiol. B*, 2013, **124**, 1-19.
17. K. Ghosh, P. Kumar and N. Tyagi, *Inorganica Chim. Acta*, 2011, **375**, 77-83.
18. G. Mestroni, E. Alessio, M. Calligaris, W. M. Attia, F. Quadrlfoglio, S. Cauci, G. Sava, S. Zorzet, S. Pacor, C. Monti-Bragadin, M. Tamaro and L. Dolzani, *Prog. Clin. Biochem. Med.*, 1989, **10**, 71.
19. E. Alessio, G. Mestroni, G. Nardin, W. M. Attia, M. Calligaris, G. Sava and S. Zorzet, *J. Am. Chem. Soc.*, 1988, **27**, 4099-4106.
20. J. M. Davey, K. L. Moerman, S. F. Ralph, R. Kanitz and M. M. Sheil, *Inorganica Chim. Acta*, 1998, **281**, 10-17.
21. S. Cauci, E. Alessio, G. Mestroni and F. Quadriliglio, *Inorganica Chim. Acta*, 1987, **137**, 19.
22. M. Coluccia, G. Sava, F. Loseto, A. Nassi, A. Boccarelli, D. Giordano, E. Alessio and G. Mestroni, *Eur. J. Cancer*, 1993, **29 A**, 1873.

23. P. Hazarika, J. Deka, S. Bhola, R. K. Bhola, C. Medhi and O. K. Medhi, *Int. J. Drug Des. Discov.*, 2012, **3**, 907-913.
24. Y. Ni, D. Lin and S. Kokot, *Anal. Biochem.*, 2006, **352**, 231-242.
25. L. S. Lerman, *J. Mol. Biol.*, 1961, **3**, 18-30.
26. W. Bauer and J. Vinograd, *J. Mol. Biol.*, 1970, **54**, 281-298.
27. S. Zhang, B. Ling, F. Qu and X. Sun, *Spectrochim. Acta A*, 2012, **97**, 521-525.
28. A. Mukherjee, *J. Phys. Chem. Lett.*, 2011, **2**, 3021-3026.
29. V. V. Kostjukov, N. M. Khomytova, A. A. H. Santiago, R. L. Ibarra, D. B. Davies and M. P. Evstigneev, *Int. J. Quantum Chem.*, 2011, **111**, 711-721.
30. C. Moucheron and A. K. D. Mesmaeker, *J. Phys. Org. Chem.*, 1998, **11**, 577-583.
31. I. Haq, P. Lincoln, D. Suh, B. Norden, B. Chowdhry and J. Chaires, *J. Am. Chem. Soc.*, 1995, **117**, 4788-4796.
32. J. K. Barton, A. T. Danishefsky and J. M. Goldberg, *J. Am. Chem. Soc.*, 1984, **106**, 2172-2176.
33. T. W. Johann and J. K. Barton, *Philos. Trans. Royal Soc. A*, 1996, **354**, 299-324.
34. A. E. Friedman, J.-C. Chambron, J.-P. Sauvage, N. J. Turro and J. K. Barton, *J. Am. Chem. Soc.*, 1990, **112**, 4960-4962.
35. S. D. Fairbanks, C. C. Robertson, F. R. Keene, J. A. Thomas and M. P. Williamson, *J. Am. Chem. Soc.*, 2019, **141**, 4644-4652.
36. K. McQuaid, J. P. Hall, L. Baumgaertner, D. J. Cardin and C. J. Cardin, *Chem. Comm.*, 2019, **55**, 9116-9119.
37. S. K. Kim and B. Nordén, *FEBS Lett.*, 1993, **315**, 61-64.
38. H. Y. Mei and J. K. Barton, *J. Am. Chem. Soc.S*, 1986, **108**, 7414-7416.
39. E. M. Heckman, R. S. Aga, A. T. Rossbach, B. A. Telek, C. M. Bartsch and J. G. Grote, *Appl. Phys. Lett.*, 2011, **98**.
40. E. M. Heckman, P. P. Yaney, J. G. Grote, F. K. Hopkins and M. M. Tomczak, *Proc. SPIE*, 2006, **6117**, 61170K-61171.
41. J. A. Hagen, W. X. Li, J. G. Grote and A. J. Steckl, *Appl. Phys. Lett.*, 2006, **88**.
42. T. B. Singh, N. S. Sariciftci, J. G. Grote and F. Hopkins, *J. Appl. Phys.*, 2006, **100**.
43. L. Wang, J. Yoshida, N. Ogata, S. Sasaki and T. Kajiyama, *Chem. Mater.*, 2001, **13**, 1273–1281.
44. R. A. Norwood, J. Thomas, N. Peyghambarian, J. Wang, L. Li, F. Ouchen and J. E. Grote, *Proc. SPIE*, 2010, **7765**.
45. K. W. Lee, K. M. Kim, J. Lee, R. Amin, B. Kim, S. K. Park, S. K. Lee, S. H. Park and H. J. Kim, *Nanotechnology*, 2011, **22**.
46. J. Dagar, M. Scarselli, M. Crescenzi and T. M. Brown, *ACS Energy Lett.*, 2016, **1**, 510-515.
47. A. R. M. Yusoff, J. Kim, J. Jang and M. K. Nazeeruddin, *ChemSusChem*, 2016, **9**, 1736-1742.
48. A. Elfwing, W. Cai, L. Ouyang, X. Liu, Y. Xia, Z. Tang and O. Inganaš, *ACS Appl. Mater. Interfaces*, 2018, **10**, 9579-9586.

49. Sigma-Aldrich, Deoxyribonucleic acid sodium salt from salmon testes, https://www.sigmaaldrich.com/catalog/product/sigma/d1626?lang=en&region=GB, (accessed 5 May, 2019).
50. M. Baldauf and W. Preidel, *J. Power Sources*, 1999, **84**, 161-166.
51. G. Felsenfeld and S. Z. Hirschman, *J. Mol. Biol.*, 1965, **13**, 407-427.
52. D. Y. Lando, I. E. Grigoryan, E. N. Galyuk, A. S. Fridman, Y. B. Dalyan and S. G. Haroutiunian, *J. Armen.*, 2013, **65**, 14-22.
53. C. N. N. s.´-Kossi, C. Descoteaux, E. Asselin, H.-A. Tajmir-Riahi and G. Berube, *DNA Cell Biol.*, 2008, **27**, 101-107.
54. J.-P. Macque and J.-L. Butour, *Eur. J. Biochem.*, 1978, **83**, 375-387.
55. A. L. Pinto and S. J. Lippard, *Biochim. Biophys. Acta*, 1985, **780**, 167-180.

Chapter 4 – Cisplatin DNA Nanostructures

4.1 Introduction

This chapter introduces the importance of precise control of structure patterning on a surface. Electron beam lithography is briefly explained along with its new sub-topic, DNA nanolithography, which exploits the structural versatility of DNA in surface patterning. In the light of DNA nanofabrication, DNA origami is mentioned to remind the reader of its potential in the nano-patterning field. Moreover, cisplatin is considered here as a viable source of platinum atoms to couple to a DNA framework. The work described herein focuses on discrete DNA duplexes, DNA structures and arrays which have the potential to act as scaffold for the precise placement of metal for application in fuel cell catalysis.

4.1.1 Nanofabrication using Electron Beam

The ultimate goal of nanotechnology lies in the ability to precisely assemble matter at the atomic level.[1] The development of scanning tunnelling microscopy (STM) and later scanning tunnelling electron microscopy (STEM) has helped in visualising such matter. However it was noticed while working with these microscopes, exposure to the electron beam induce changes in the material under study.[2, 3] While this was initially perceived as undesirable, nonetheless it opened up new possibilities for manipulating matter at the single atom level and producing alterations in a highly controlled way.[1]

Lithography is a process of producing patterns on a substrate.[4] In electron beam lithography (EBL), beams of electrons are used to generate the pattern. Other types

of lithography include photolithography which uses light to produce patterns or imprint lithography which uses a mould to imprint the pattern. The advantages of e-beam lithography over other techniques are high resolution and versatile pattern formation.[5] This technique can use project printing scheme for pattern formation or direct writing. The most common approach is direct writing owing to its superior resolution and the lack of need for expensive projection optics and masks. For this reason, it has been a technique of choice in cutting-edge nanofabrication of special products, prototyping and in R&D applications.[6] The most popular way of adding material to the substrate in direct writing EBL is the lift-off process (Figure 4.1).[5] In this process, the resist coating is exposed to the electron beam. The nanostructure pattern is developed and removed by use of a solvent. The desired nanostructure material is then deposited either by the use of an e-gun or via the evaporation process. In the final step, the unwanted resist material is washed away by soaking in a solvent bath.

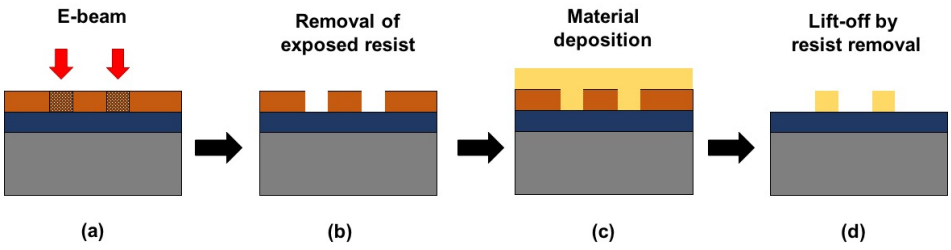

Figure 4.1 – Schematic of a direct writing EBL lift-off process: (a) e-beam resist exposure generating the desired pattern, (b) removal of exposed resist, (c) deposition of desired material, (d) removal of remaining resist and unwanted material, adapted from Tseng *et al*.[5]

Recently, the term DNA nanolithography became popular and involves a combination of traditional lithography with DNA self-assembly as a way of making nanoscale patterns. This approach uses DNA as a mask and follows a physical vapour deposition process which allows metal to be deposited through these masks and retain the shape of the masks.[7] For example, a 1D DNA double crossover array was used as such a mould in a study by Deng and Mao.[8] The DNA structure was first assembled on a mica surface and covered with a thermally evaporated gold film. Finally, an epoxy mixture was added between the gold layer and a glass slide. After separation of the gold film from the mica surface, a negative replica of the DNA structures was exposed. In another study by Jin *et al.*,[9] DNA origami of a predefined structure was absorbed onto a graphene surface with an adhesion layer (1-pyrenenethylamine), followed by seeding with silver and coating with gold. The metal-coating of the DNA material was employed to ensure its survival in the subsequent etching process which removed the unprotected graphene, transferring the DNA template structure onto it.

Finally, a study by Liu group proved that it is possible to preserve the nanoscale shape of DNA structures by a shape-conserving carbonisation of the biomaterial (Figure 4.2).[10] A DNA nanostructure, in this case a DNA Origami Triangle, was deposited on a silicon substrate and coated with Al_2O_3 by atomic layer deposition. Next, a carbonisation process followed which involved incubation of the nanostructures at 800 − 1000 °C for 3 − 5 min under H_2 atmosphere and high pressure. The last step consisted of the removal of the protective Al_2O_3 layer via H_3PO_4 etching. This work

successfully converted a soft DNA material into a more robust one, which can be used for high temperature solid state chemistries and similar applications.

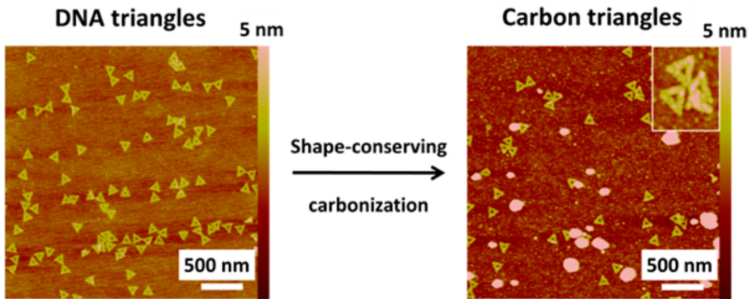

Figure 4.2 – AFM topographic images of shape-conserved carbon triangles (right) from DNA triangles (left). *Reproduced with permission from Zhou et al.*[10] *Copyright 2016 American Chemical Society.*

4.1.2 DNA origami in Nanofabrication

The ability to precisely control metal placement on the nanoscale would enable progress in artificial photosynthesis applications as well as development of devices for nanoelectronics and catalysis.[11] DNA offers a great potential in this regard due to its high programmability and versatile structure as well as various ways in which it can interact with metals.

Seeman and co-workers were the first group to pioneer the formation of 2D DNA assemblies, as discussed in Chapter 1.2. Since then, these 2D DNA frameworks (Figure 4.3) were explored for various applications including organisation of proteins[12] and gold nanoparticles[13]. Chapter 1.2 introduced DNA origami, a novel method for assembling DNA nanostructures using a long DNA strand which can be

folded using staple strands to give rise to nanoscale shapes and patterns.[14] This method employs the use of M13 mp 18 genomic DNA and the addition of over 200 short oligonucleotides, so called staple strands, to hold the assembly in place.

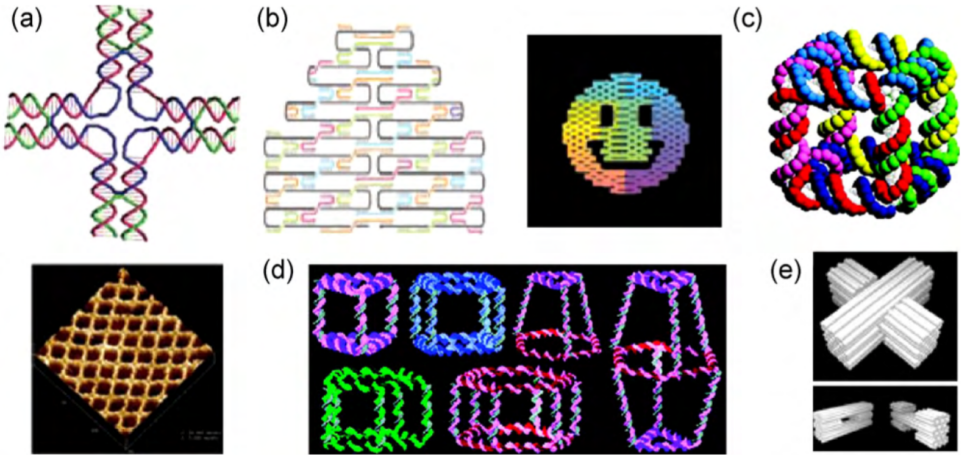

Figure 4.3 – 2D and 3D DNA objects: (a) Extended 2 D sheets, (b) Rothemund method to make DNA origami assemblies, (c) topological cube, (d) Face-centered polyhedral, (e) 3D DNA origami.

Reproduced with permission from Yang et al.[11] Copyright 2010 Elsevier B.V.

Following Rothemund's introduction of DNA origami, many studies have emerged to exploit potential applications that this scaffold presents. In a study by Liu *et al.*, DNA origami was explored for nanoelectronic circuit fabrication by a two-step process involving seeding the template with silver and then plating with gold via an established automated process.[15]

DNA origami has a potential use in single molecule detection as shown by Ke *et al*. [16] In this study, nucleic acid probe tiles were developed from DNA origami, bearing 20-mer DNA probes which can hybridise to the target RNA enabling its detection in

solution by atomic force microscopy.[16] In another study by Voigt *et al.*, single-molecule chemical reactions were performed on a DNA origami scaffold for the first time.[17] Rinker *et al*. investigated the incorporation of multiple-affinity ligands into DNA origami and proved that distance-depended multivalent binding effects can be studied this way.[18]

As discussed in Chapter 1.2., the use of DNA origami has also been shown to organise other materials. For example, protein organisation was studied by Kuzyk *et al.*, where they exploited two methods for protein assembly; via a prefabricated template for streptavidin assembly and a simultaneous assembly of origami and protein.[19] Single-walled carbon nanotubes are materials that can be arranged using the DNA origami method as described by Maune *et al*. The researchers found that the nanotubes attached to templates with good efficiency, specificity and with the desired orientation.[20] Pal *et al*. studied the organisation of silver nanoparticles on the origami surface and found that their aggregation in high salt concentration solutions could be avoided.[21]

4.1.3 Cisplatin as a platinum source with placement control

As discussed in Chapter 1, cisplatin binds to the purine bases on DNA. Although the cisplatin-DNA reaction is not 100% site-specific in targeting adjacent guanines exclusively, the simplicity of this reaction as well as the strong covalent mode of binding deem it favourable for industrial fabrications. This would be even more true if such metal-DNA adducts could be purified to give single site-specific products. This

was actually proven to be possible by Poklar *et al.,*[22] when a 20-mer poly-CT DNA oligonucleotide bearing just two adjacent guanines was synthesised and reacted with cisplatin to form a mono-platinated adduct, which subsequently was found to form a stable duplex (Figure 4.4).

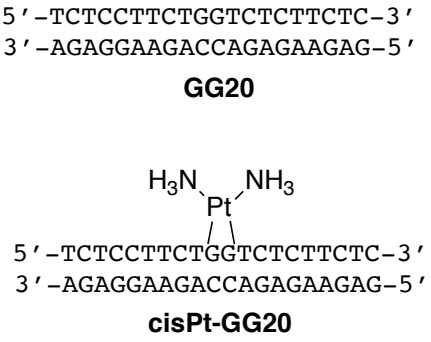

Figure 4.4 – Sequences of the unmodified 20-mer DNA duplex (GG20) and its platinated counterpart (cis-Pt-GG20), adapted from Breslauer *et al.*[22]

This study shows the effective purification of the cisplatin-DNA oligonucleotide by ion exchange HPLC, yielding a pure adduct able to hybridise with a complementary strand to form a duplex, which could form despite the crosslink being present prior to hybridisation.[22] Further characterisation of the cisplatin-DNA duplex showed by CD spectroscopy a partial shift towards the A-form of duplex DNA (Figure 4.5). Its slightly lower thermal stability than the unmodified duplex was established by thermal melting and calorimetric studies.[22]

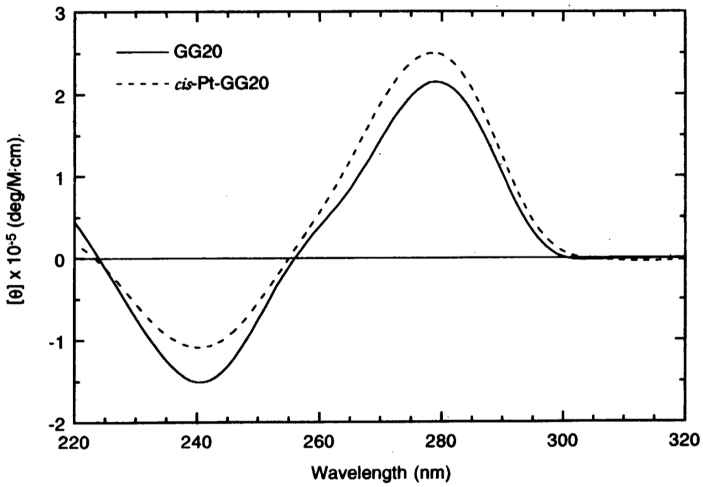

Figure 4.5 – CD spectra of the GG20 and cis-Pt-GG20 duplexes. *Reproduced with permission from Breslauer et al.*[22] *Copyright 1996 National Academy of Sciences.*

4.2 Project aims

In the previous chapter, cisplatin was found to successfully form DNA adducts but the use of ST-DNA as a substrate meant that precise placement of metal atoms was difficult to achieve. The work described in this chapter aimed to design a bottom-up approach to synthesising a novel platinum DNA material that allowed more precise metal placement control. This was to be achieved by designing specific DNA sequences for reaction with cisplatin, which would force the metal complex to bind in a specific location on a DNA strand as previously demonstrated by Poklar *et al.*[22] This DNA-metal adduct would be purified by HPLC to remove unreacted species and then characterised by tandem mass spectrometry. The final aim was to explore this DNA-metal unit for the formation of higher order structures and thus its suitability for fabrication in fuel cell catalysis applications.

4.3 Cisplatin DNA oligonucleotide adducts synthesis and purification

In order to achieve precise control of metal placement in a DNA scaffold, a bottom-up approach was chosen wherein an oligonucleotide of a known sequence reacts with cisplatin to form an adduct. This methodology is based upon well-known chemistry involving DNA and cisplatin, as detailed in Chapter 1.3. The first sequence chosen in this study was the G14 sequence (Table 4.1) based on one previously studied extensively by the Tucker group for various applications. This was then to be compared with another sequence namely a G20 strand previously designed by Poklar *et al.*[22] in their study of cisplatin intrastrand crosslinks (Table 4.1). This sequence bears the advantage of having only two adjacent GG bases, which limits the sites for cisplatin-DNA adduct formation.

Table 4.1 – Oligonucleotide sequences and their names explored in this study.

Oligonucleotide name	Oligonucleotide sequence
G14	5′–CAT TGA **GG** AGT CCA–3′
G20	5′–TCT CCT TCT **GG** TCT CTT CTC–3′

The chosen sequences were synthesised using automated solid phase synthesis (Chapter 7.2.1), purified by HPLC (Chapter 7.2.2) and characterised by mass spectrometry (Chapter 7.3.1) The results are shown in Appendix (Figure 8.2.1 & Figure 8.2.3). Further to that, they were reacted with cisplatin according to the protocol described in Chapter 7.5. These platinum-DNA adducts were then purified by HPLC (Chapter 7.5) and characterised by mass spectrometry (Chapter 7.3.1).

4.3.1 G14 strand

The platination reaction of the G14 strand yielded a mixture of adducts as indicated by mass spectrometry (Figure 4.6). These adducts were unplatinated G14, G14 plus 1 cisplatin and G14 plus 2 cisplatin moieties. This result is in agreement with the literature which found formation of 65% of GG adducts and 22% of AG adducts in cancer patients.[23] The presence of poly-cisPt adducts as well as a considerable amount of unplatinated DNA, made it necessary to isolate the desired mono-platinated adduct in order to reach the objectives of the project.

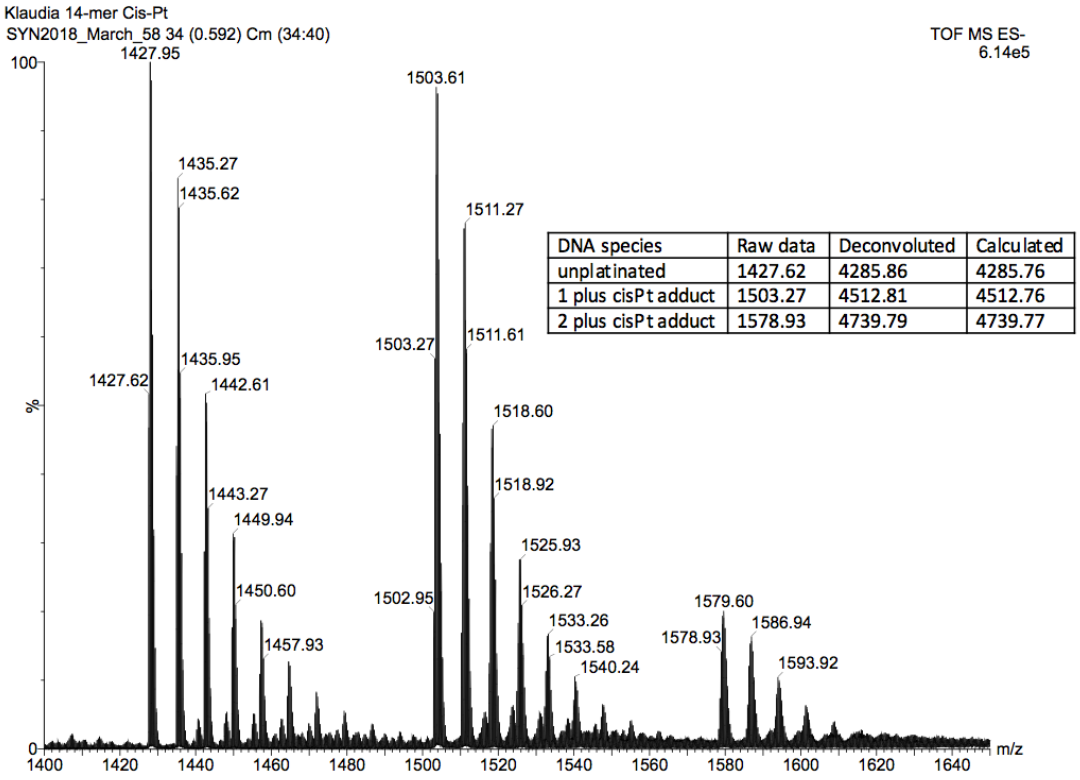

DNA species	Raw data	Deconvoluted	Calculated
unplatinated	1427.62	4285.86	4285.76
1 plus cisPt adduct	1503.27	4512.81	4512.76
2 plus cisPt adduct	1578.93	4739.79	4739.77

Figure 4.6 – ESI-MS isotopic trace of the reaction mixture of G14 strand and cisplatin, as well as its corresponding masses. Both cisplatin NH_3 groups are present in the cisplatin DNA adduct.

4.3.1.1 HPLC purification of cisPt G14 strand

Although a cisPt-DNA oligo adduct had previously been successfully isolated by Poklar *et al*.[22] using ion exchange HPLC, purifying the mono-adduct turned out not to be as straightforward as expected. Due to the lack of an available ion exchange HPLC column, and after initial consultation with chromatography experts, it was decided to use a Kinetex C18 LC column to attempt the separation.

The starting point for the HPLC method development was the method used for purification of unmodified oligonucleotide sequences, namely a 0.1 M TEAA, pH 7/ACN buffer system with a gradient of 5-18% ACN over 25 minutes at 60 °C and a flow rate 1 mL min^{-1}. A small alteration of the initial method, namely changing the gradient to 5-12 % ACN over the same time period resulted in a separation where all the species could be identified by mass spectrometry (Figure 4.7).

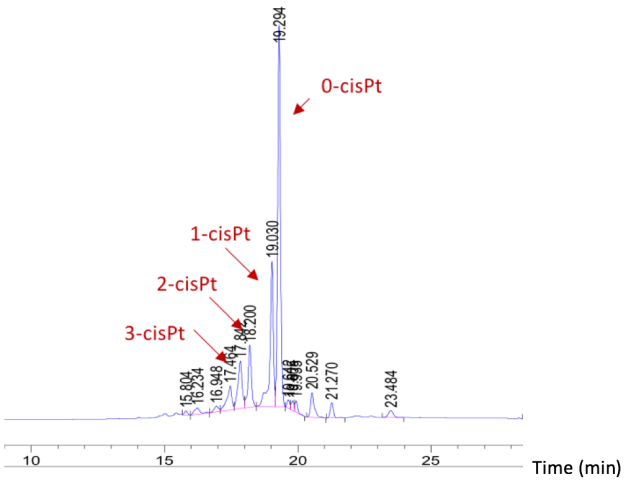

Figure 4.7 – HPLC traces of crude cisPt G14 oligonucleotide strand, monitored at 260 nm wavelength and conditions: 0.1M TEAA buffer, 5-12% (25 min) ACN, 1.0 mL min^{-1} flow rate, 60 °C, Kinetex C18 column.

Following this trial, several attempts were made to improve the separation. Both reducing and increasing the flow rate was explored, with an increase in flow rate to 1.2 mL min^{-1} giving a very small improvement (Figure 4.8a). Furthermore, lowering the final ACN concentration within the gradient method was investigated, again resulting in a small improvement (Figure 4.8b). Various temperatures were not explored, as lower temperatures increase the chances of DNA folding and at the same time making separation poorer. Higher temperatures were not explored due to the unknown thermal stability of the complex. Different columns such as a Thermo DNA Pac column and a Clarity RP column gave no further improvements. The best separation found using the TEAA buffer system is shown in Figure 4.8c.

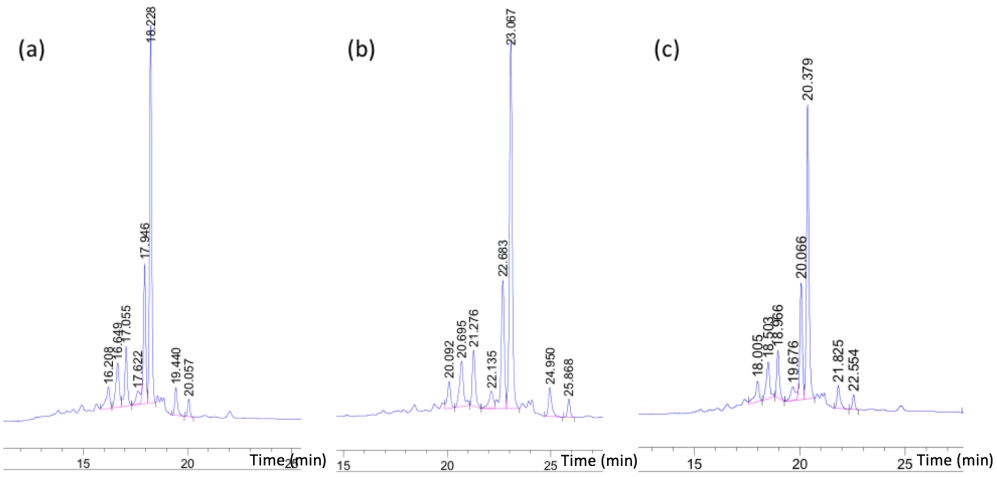

Figure 4.8 – HPLC traces of G14 cisPt mixture using Kinetex C18 column, monitored at 260 nm wavelength and conditions: 0.1 M TEAA, pH 7 /ACN buffer at 60 ^{o}C (a) 5-12% ACN (25 min), 1.2 mL min^{-1} flow rate; (b) 5-10% ACN (25 min), 1.2 mL min^{-1} flow rate; (c) 5-11% ACN (25 min), 1.2 mL min^{-1} flow rate.

This study made it clear that the only other way to obtain an improved separation was to explore different buffer systems. After a second consultation with

chromatography experts and a literature search,[24] a hexylamine/ hexafluoroisopropanol (HFIP/HA) buffer system was explored. The results of this study are presented in Figure 4.9.

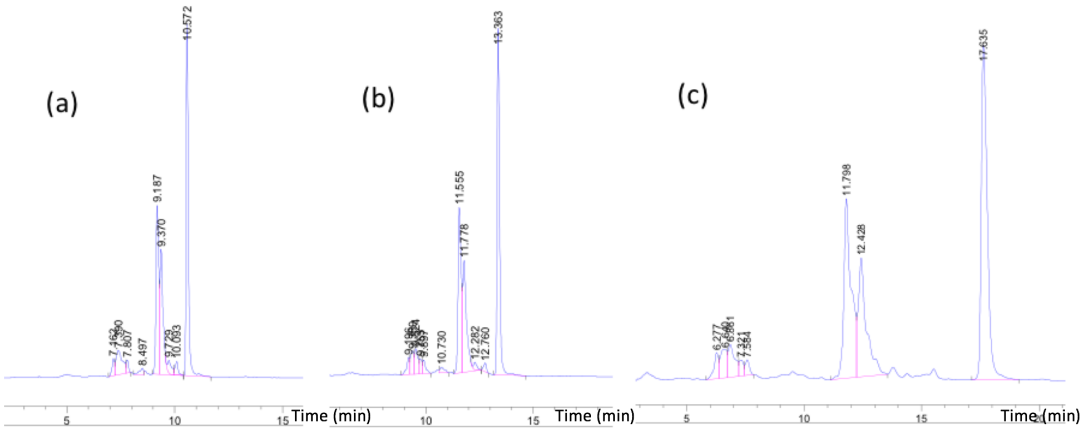

Figure 4.9 – HPLC traces of G14 cisPt mixture, monitored at 260 nm wavelength and conditions: 50 mM HFIP, 15mM HA buffer, pH:7, 1.0 mL min^{-1} flow rate, 60°C, Kinetex C18 column (a) 20-40% ACN over 20 minutes; (b) 15-35% ACN over 20 minutes; (c) 20-25 % ACN (20 min), 25 % ACN (5 min).

This buffer system showed a considerable improvement in the separation of the unmodified DNA G14 strand from its platinated adducts. However, the difference in retention time between the mono- and bis- platinated adducts decreased, merging the two peaks and resulting in a worse situation than that achieved with TEAA buffer. Therefore, it was decided to purify the mono-platinated adduct using the method presented in Figure 4.8c and in so doing, limit the injection volume to a minimum in order to maintain the separation. It was found possible to purify enough mono-platinated adduct material for further testing by performing multiple injections, with fractions collected automatically. The HPLC trace of the purified product and its mass spectrometry trace is presented in Figure 4.10.

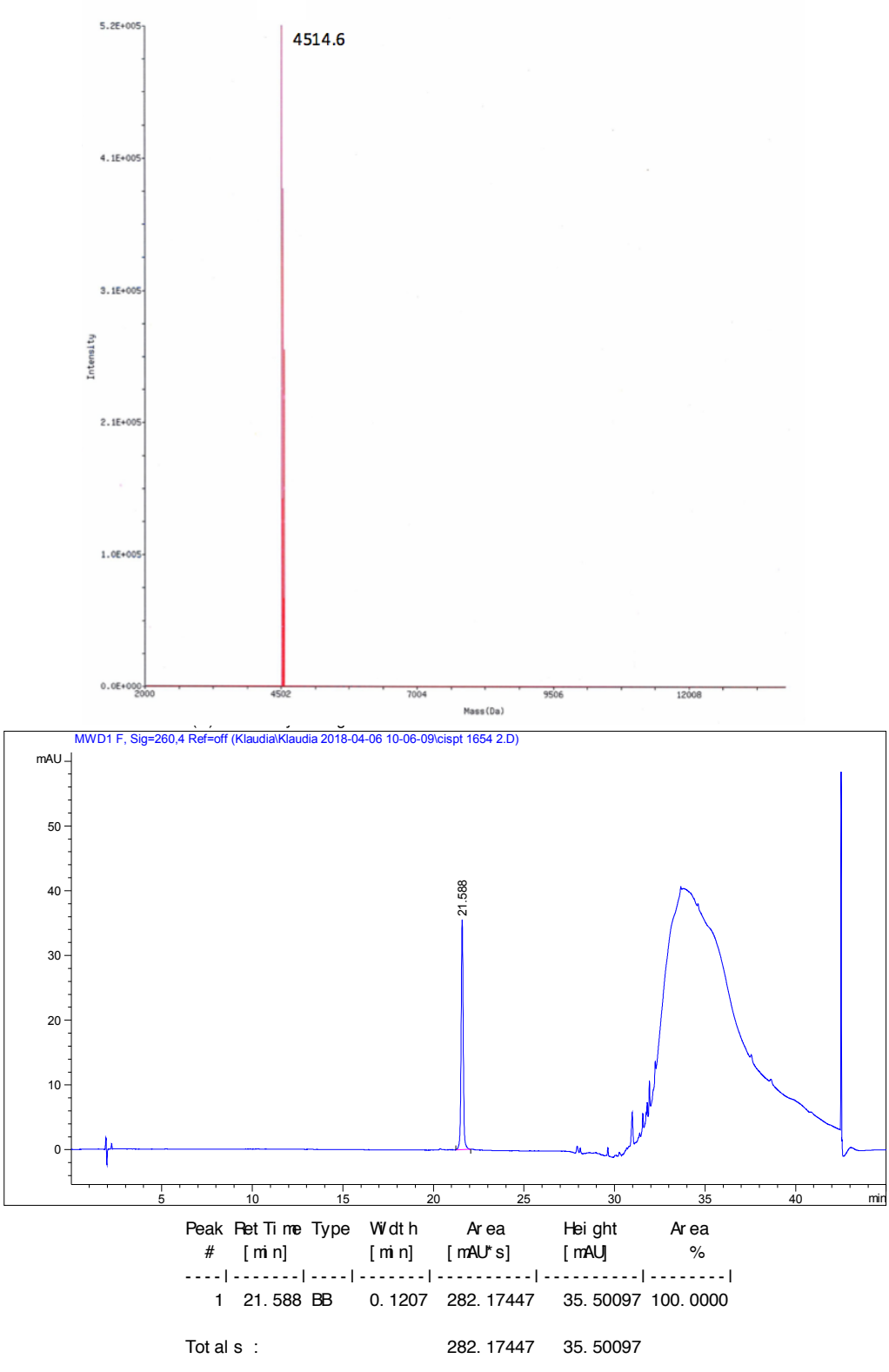

Peak #	Ret Time [min]	Type	Width [min]	Area [mAU*s]	Height [mAU]	Area %
1	21.588	BB	0.1207	282.17447	35.50097	100.0000
Totals :				282.17447	35.50097	

Figure 4.10 – ESI-MS and RP HPLC data of the purified cisPt G14 probe and eluted into MilliQ water, showing the purity of the sample. This strand was purified using Kinetex C18 column, 0.1 M TEAA, pH 7 /ACN buffer at 60 °C 5-11 % ACN (25 min), 1.2 mL min^{-1} flow rate and monitored at 260 nm. The baseline distortion between 30-45 min is due to the impurities from the organic solvent traced back to the manufacturer. Blank data provided in Appendix, Figure 8.2.32.

4.3.1.2 Tandem mass spectrometry analysis of cisPt G14 strand

As outlined earlier, the ability to precisely control metal placement within a DNA strand was one of the main objectives of this project. In order to provide direct evidence for the position of cisplatin within the G14 oligonucleotide sequence, tandem mass spectrometry was employed as this technique has proven efficient in studying related oligonucleotide systems in the literature.[25]

The first step was to identify the oligonucleotide species within the G14 cisplatin mixture (Figure 4.7). The relevant masses were then inputted to the quadrupole radiofrequency to filter out any irrelevant masses entering the collision cell for MS/MS analysis. Next, scanning and fine tuning the range of collision energies followed, which was necessary to promote sufficient collision induced dissociation (CID) fragmentation of the molecule. The data collected were analysed using ChemDraw to identify the fragments from either the 5' or 3' end of the molecule. The raw fragmentation data for the mono-adduct is shown in Figure 4.11.

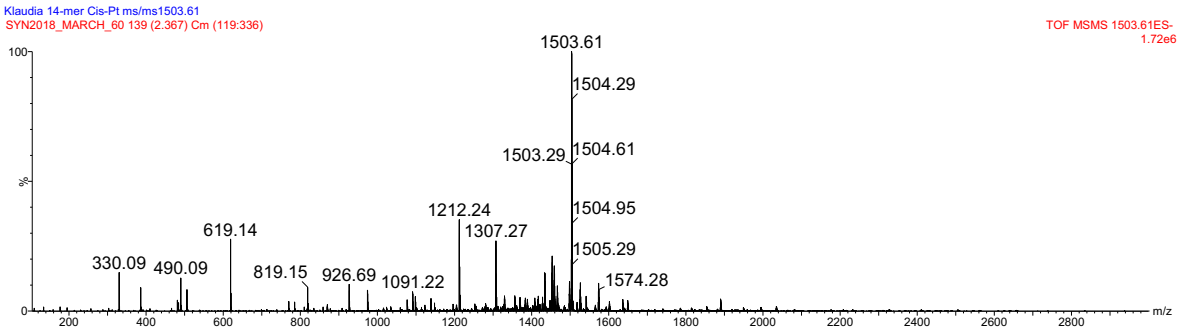

Figure 4.11 – ESI-MS/MS spectrum showing fragmentation profile of cisplatin G14 mono-adduct.

Fragmentation provided data for cisplatin-containing DNA fragments and the ones lacking cisplatin. Naturally, the presence of data corresponding to the G-cisPt-G fragment would give direct evidence for the cisPt binding preferentially to the two adjacent GG bases and at the same time confirming the literature findings. However, such data was not found, possibly due to ion suppression. An alternative approach was undertaken wherein the identification of the following fragmentation products (shown in red): 5'-CATTGAG-cisPt-GAGTCCA-3' and 5'-CATTGAG-cisPt-GAGTCCA-3' was attempted, which would give evidence for cleavage at the G bases. Such evidence was indeed found and is presented in Figure 4.12.

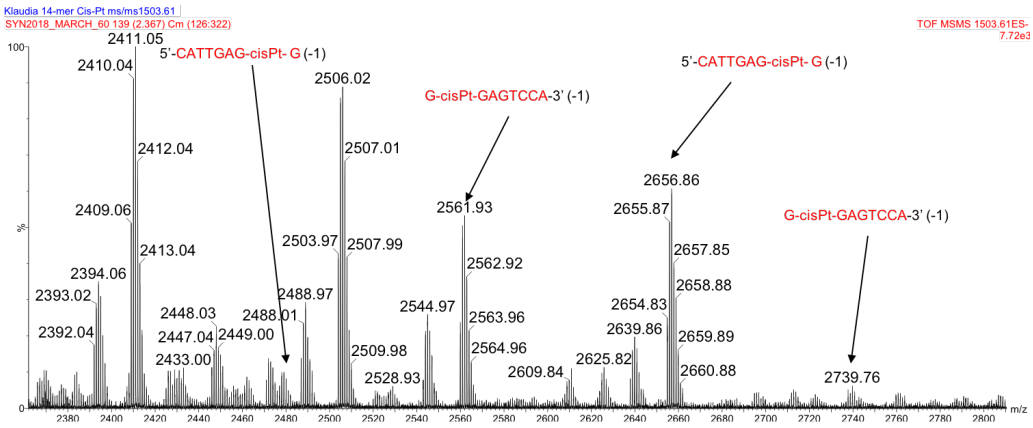

Observed mass (m/z)	Charge state	DNA Fragments with cisPt isotope patterns
2654.83	-1	5'-CATTGAG-cisPt-GAGTCCA-3'
2559.94	-1	5'-CATTGAG-cisPt-GAGTCCA-3'
2737.75	-1	5'-CATTGAG-cisPt-GAGTCCA-3'
2477.07	-1	5'-CATTGAG-cisPt-GAGTCCA-3'

Figure 4.12 – ESI-MS/MS spectrum showing DNA fragments of the G14 strand with cisPt isotope patterns. Fragmentation products shown in red.

4.3.2 G20 strand

As expected platination of the G20 strand yielded only two products, namely the unplatinated adduct and the mono-platinated, as confirmed by mass spectrometry

(Figure 4.13). This is due to the absence of additional guanine and adenine bases in the molecule. Such a system ensures that no side products are formed, which makes purification easier.

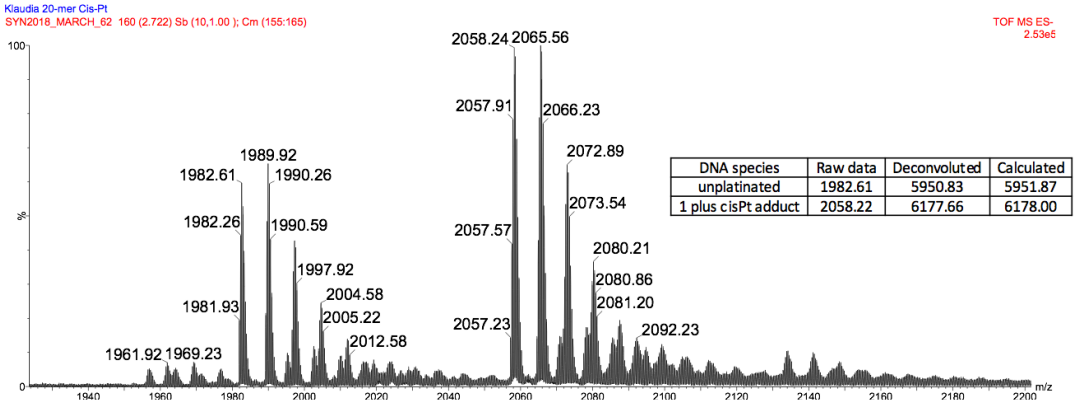

Figure 4.13 – ESI-MS isotopic trace of the reaction mixture of G20 strand and cisplatin, as well as its corresponding masses. Both cisplatin NH_3 groups are present in the cisplatin DNA adduct.

4.3.2.1 HPLC purification of cisPt G20 strand

The method development for isolation of the cisPt-G14 mono-adduct gave some insight into developing a method for the cisPt-G20 mono-adduct. Since there were no poly-adducts of cisplatin formed in the cisPt-G20 mixture, the co-elution of the platinated adducts was not an issue. This meant that the HA / HFIP buffer system for separation of unplatinated DNA from the platinated adduct was the method to use. It was done using a Kinetex C18 column, 50 mM HFIP, 15 mM HA buffer, pH:7, at 1 mL min^{-1} flow rate and 60 ^{o}C, with a gradient 20-40% ACN over 25 minutes (Figure 4.14a). A small modification to the gradient for this method yielded an even better separation, as shown in Figure 4.14b.

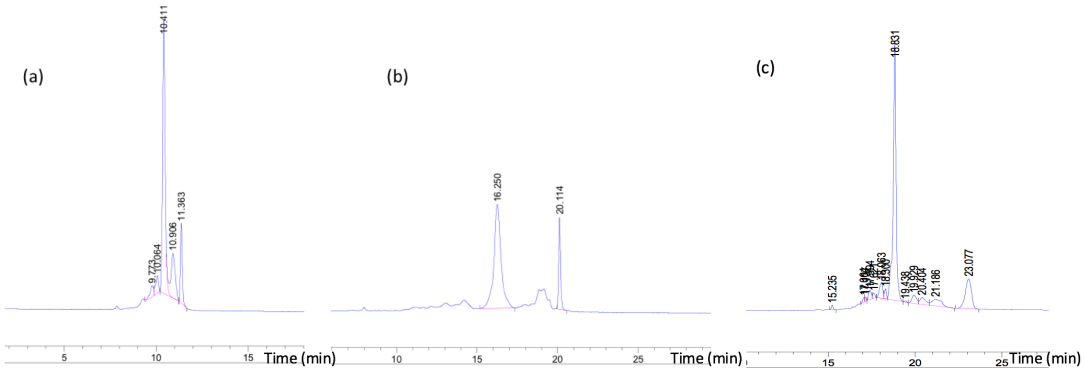

Figure 4.14 - HPLC traces of the cisPt-G20 mixture, monitored at 260 nm wavelength and conditions: 50 mM HFIP, 15 mM HA buffer, pH:7, 1.0 mL min^{-1} flow rate, 60 ^{o}C, Kinetex C18 column (a) 20-40% ACN over 20 minutes; (b) 20% -25% (5 min), 25% (15 min), 25-30% (5 min) & 30% (10 min) ACN over 30 minutes; (c) 20-45% (20 min), 45-50% (5 min), 50% (5 min) methanol over 30 minutes.

A way to further improve the separation was explored by replacing acetonitrile with methanol (Figure 4.14c). The gradient had to be adjusted due to the decrease in polarity of the solvent, which meant that more of it was needed in the ratio, to allow the DNA to travel through the column.

It can be seen therefore, from the HPLC traces in Figure 4.14 that the use of methanol further improved the separation of the two peaks. Moreover, the mono-adduct peak became sharper and more defined, allowing for scale-up.

Indeed, scaling up to a semi-preparative column was next explored, however the system suffered high pressure problems which later were subsequently ascribed to potential aggregation of unreacted cisplatin molecules on the column. This system was therefore abandoned. However, fortunately significant amounts of product for

further testing were collected using the analytical system. The HPLC trace of the purified product and its mass spectra are presented in Figure 4.15.

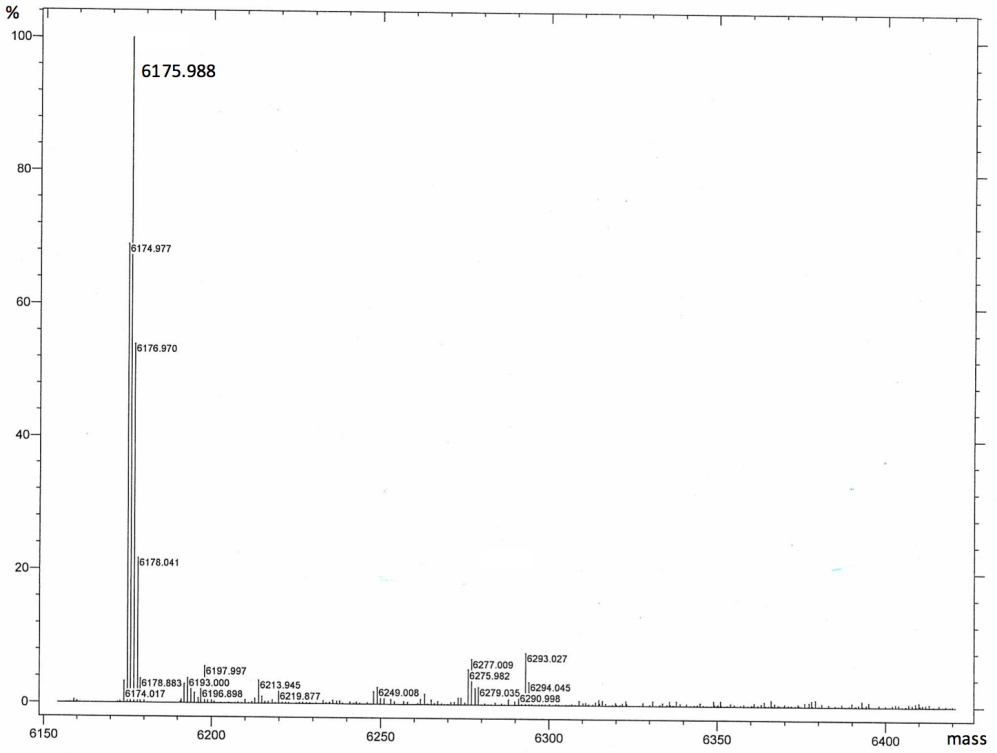

Peak #	Ret Time [min]	Type	Width [min]	Area [mAU*s]	Height [mAU]	Area %
1	20.428	BV R	0.2302	1020.06006	66.79096	100.0000
Totals :				1020.06006	66.79096	

Figure 4.15 – ESI-MS and RP HPLC data of the purified cisPt-G20 probe and eluted into MilliQ water, showing the purity of the sample. This strand was purified using 50 mM HFIP, 15 mM HA buffer, pH:7, 1.0 mL min^{-1} flow rate, 60 ^{o}C, Kinetex C18 column, with gradient 20-45% (20 min), 45-50% (5 min), 50% (5 min) methanol and monitored at 260 nm.

4.3.2.2 Tandem mass spectrometry analysis of cisPt-G20 strand

In order to confirm the position of cisplatin in the G20 strand, tandem mass spectrometry was once again employed to study this system. The fragmentation profile is presented in Figure 4.16.

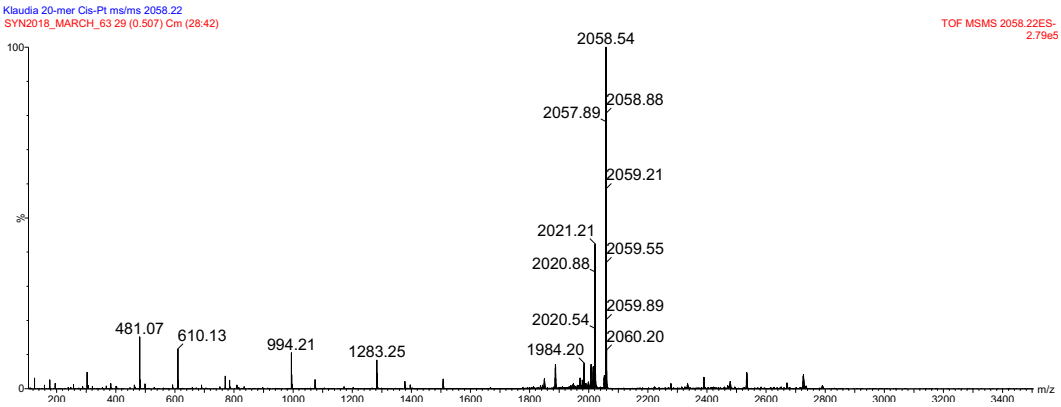

Figure 4.16 – ESI-MS/MS spectrum showing fragmentation profile of cisPt-G20 mono-adduct.

The fragmentation experiment for the cisPt-G20 mono-adduct was more challenging than for the cisplatin G14 mono-adduct. This was due to the higher molecular weight of the former as well as the presence of many overlapping fragments, due to the longer sequence than in the case of the G14 strand. Many identified fragments could come from either 5' or 3' end of the molecule (Figure 4.17).

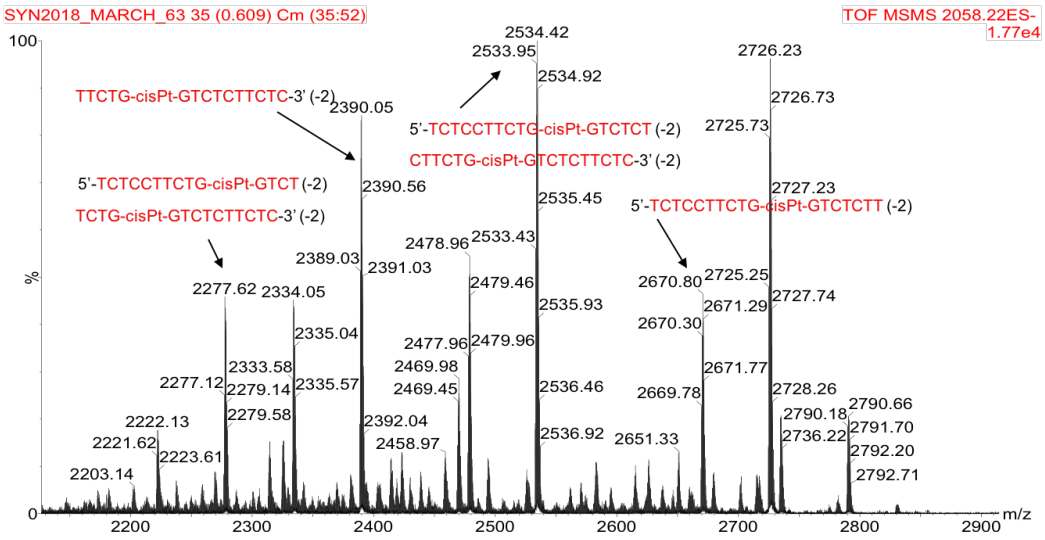

Observed mass (m/z)	Charge state	DNA Fragments with cisPt isotope patterns
2670.80	-2	5'-TCTCCTTCTG-cisPt-GTCTCTTCTC-3'
2390.05	-2	5'-TCTCCTTCTG-cisPt-GTCTCTTCTC-3'
2277.62	-2	5'-TCTCCTTCTG-cisPt-GTCTCTTCTC-3' or 5'-TCTCCTTCTG-cisPt-GTCTCTTCTC-3'
2534.42	-2	5'-TCTCCTTCTG-cisPt-GTCTCTTCTC-3' or 5'-TCTCCTTCTG-cisPt-GTCTCTTCTC-3'

Figure 4.17 – ESI-MS/MS spectrum showing DNA fragments of cisPt-G20 mono-adduct with cisplatin isotope pattern.

Again, the presence of a single G-cisPt-G fragment was not found and therefore a search for larger fragments containing cisplatin was undertaken. This resulted in a fragment containing half of the DNA strand, with cisplatin still attached to a guanine base, but lacking the sugar moiety (Figure 4.18). This was attributed to either ends of the strand and provided enough evidence to confirm that the binding position of cisplatin was at the GG pair in the middle of the strand, as anticipated.

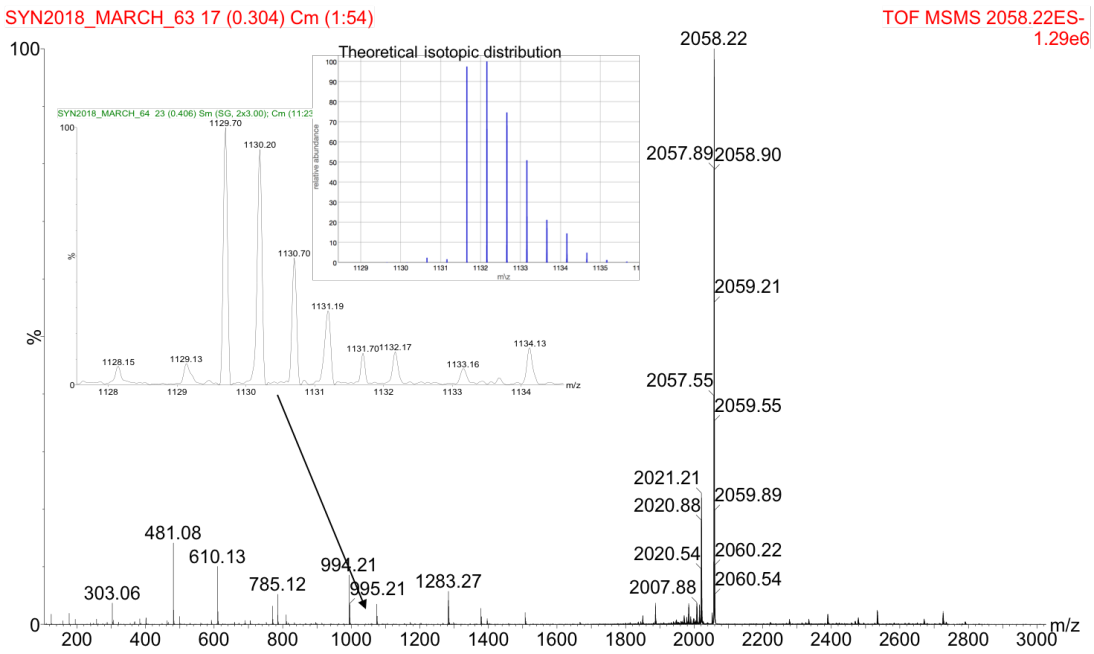

Observed mass (m/z)	Charge state	DNA Fragments with cisPt isotope patterns
1129.70	-2	5'-TCTCCTTCTG-cisPt-GTCTCTTCTC-3' or 5'-TCTCCTTCTG-cisPt-GTCTCTTCTC-3'

Figure 4.18 – ESI-MS/MS spectrum showing the cisplatin isotope pattern corresponding to the observed DNA fragment with cisPt along with its theoretical isotopic distribution.

4.4 Cisplatin DNA Duplex Formation

The ability of DNA to hybridise and form duplexes is not only a foundation of life but also of DNA nanotechnology, it being the fundamental principle by which higher order DNA structures can be designed and assembled, giving rise to endless applications. It is clear that the precise arrangement of metals would open many possibilities for nanotechnology such as nanoelectronics, catalysis or artificial photosynthesis.[11] Specific metal placement in DNA could be one way of achieving

this goal, for example by decorating preassembled DNA nanostructures, or by metal loading onto a DNA strand before assembly. The latter approach gives a higher level of specificity, but needs to be tested to assess the possibilities for building up higher ordered structures. In the study by Poklar *et al.*,[22] a strand containing an intrastrand cisplatin crosslink was tested for duplex formation and in this section, this aspect is explored further.

4.4.1 Cisplatin G14 Duplex

The addition of the cisplatin G14 strand to its complementary target strand was accomplished according to the procedure described in Chapter 7.6. The test for successful duplex formation was carried out using polyacrylamide gel electrophoresis under native conditions, as described in Chapter 7.14.1, with the results presented in Figure 4.19.

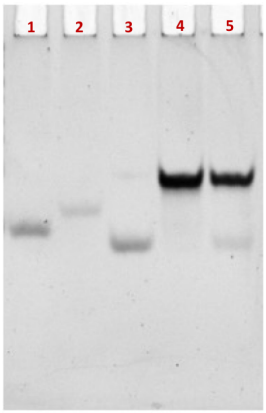

Figure 4.19 – A Diamond™ stained native 20% PAGE visualised with UV light on AlphaImager HP system, 1 x TBE buffer, 100 V, 3 h at 4 °C; Lanes: 1 – unmodified G14 probe, 2 - cisplatin G14 probe, 3 – G14 target, 4 – unmodified G14 Duplex, 5 – cisplatin G14 Duplex. Concentrations of strands were 1 µM.

The gel shows successful formation of the duplex along with the unmodified duplex control. This is evidenced by the duplex bands (lanes 4 & 5) running slower than the single strand bands (lanes 1-3). Moreover, the Diamond dye, which is used to visualise the gel, is known to intercalate more with the duplexed DNA,[26] as evidenced here by darker bands for the duplexes. Interestingly, the platinated single strand has a slower mobility than its unplatinated control, which can be explained by the adduct causing a kink in the DNA strand, which changes the helical structure, making it less linear.

Following successful hybridisation of the cisplatin G14 duplex, it was decided to study it further by UV/Vis and circular dichroism spectroscopy to determine whether there were any differences from the unmetallised control. Such a study had not previously been reported in the work by Poklar *et al*.[22] The spectroscopic measurements were performed in a 100 mM sodium phosphate and 10 mM sodium chloride buffer at pH 7 at room temperature. The results are presented in Figure 4.20.

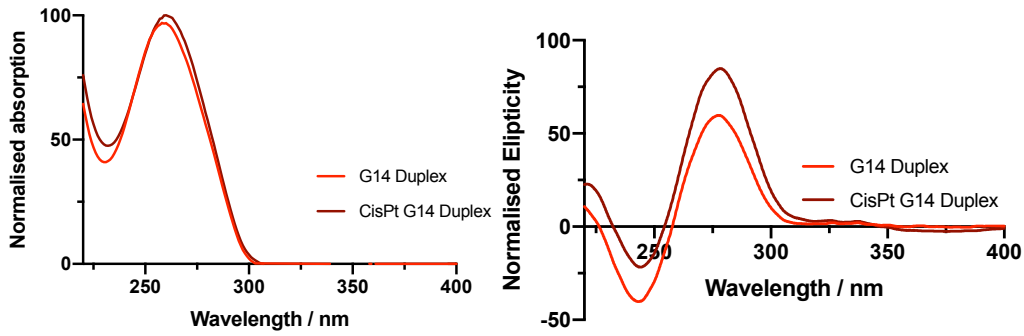

Figure 4.20 – Cisplatin G14 and G14 duplexes (10 µM) spectroscopic studies; UV/Vis spectra (left), CD spectra (right) in 10 mM sodium phosphate and 100 mM sodium chloride buffer, pH 7.0.

The spectroscopic studies follow the trend found in the literature[27] as well as in the study described in Chapter 3. The UV/Vis trace exhibits small hyperchromic and bathochromic shifts, whereas the CD results show an increase in the positive band at 280 nm and a less defined negative band at 245 nm. Both techniques confirm structural changes to the DNA duplex upon incorporation of just one cisplatin unit.

4.4.2 Cisplatin G20 Duplex

In a similar way, the cisplatin G20 Duplex was next subjected to hybridisation under standard conditions described in Chapter 7.6, with native polyacrylamide gel electrophoresis again employed to confirm the formation of the platinated duplex (Chapter 7.14.1). The results presented in Figure 4.21 also show successful formation of cisplatin G20 duplex, as evidenced by the lower mobility bands corresponding to the duplexes (lanes 4 & 5) which are darker in colour due to the nature of the intercalating dye.

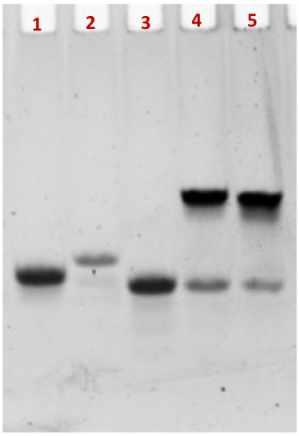

Figure 4.21 – A Diamond™ stained native 20 % PAGE visualised with UV light on AlphaImager HP system, 1 x TBE buffer, 100 V, 3 h at 4 °C; Lanes: 1 – unmodified G20 probe, 2 - cisplatin G20 probe, 3 – G20 target, 4 – unmodified G20 Duplex, 5 – cisplatin G20 Duplex. Concentrations of strands were 1 µM.

Following this, UV/Vis and CD spectroscopic techniques were once again employed to study the samples, with the results presented in Figure 4.22. The results of this study correspond to the ones achieved in the study of the G14 duplexes described earlier.

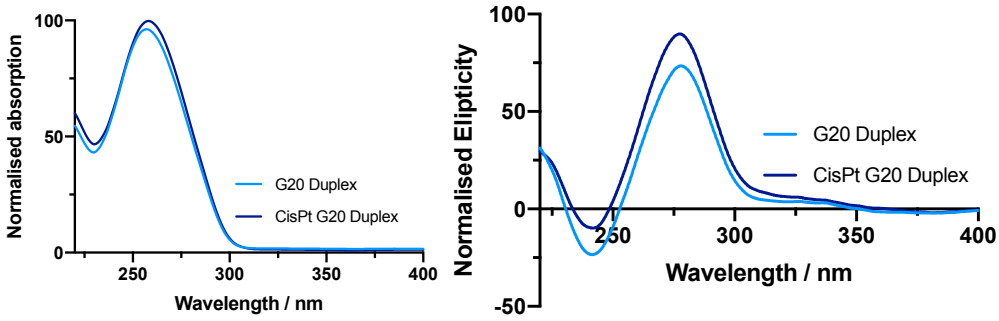

Figure 22 – CisPt-G20 and G20 duplexes (10 µM) spectroscopic studies; UV/Vis spectra (left), CD spectra (right) in 10 mM sodium phosphate and 100 mM sodium chloride buffer, pH 7.0.

4.5 Cisplatin DNA Origami Nanostructure

Given the successful formation of cisplatin duplexes, the synthesis of higher order DNA nanostructures was next considered. Inspired by Paul Rothemund's Origami Triangle[14] and the study by Gopinath *et al*.,[28] a design for a platinum decorated DNA Origami Triangle was originated. It includes a DNA Origami Triangle built from an M13 mp 18 genomic DNA and assembled with 200 oligonucleotide staples. 15 out of the 200 staples have a polyA extension, which allows docking of a complementary polyT sequences in 15 positions of the DNA Origami Triangle (Figure 4.23a). The polyT strand, having two additional guanine bases at its 3' end, would allow cisplatin adduct formation so that the DNA Origami Triangle would be loaded with platinum

at specific locations (Figure 4.23b). It is important to note that the cisplatin-containing docking strands do not take part in the DNA Origami triangle formation, but are merely attached onto the origami via its staple extensions.

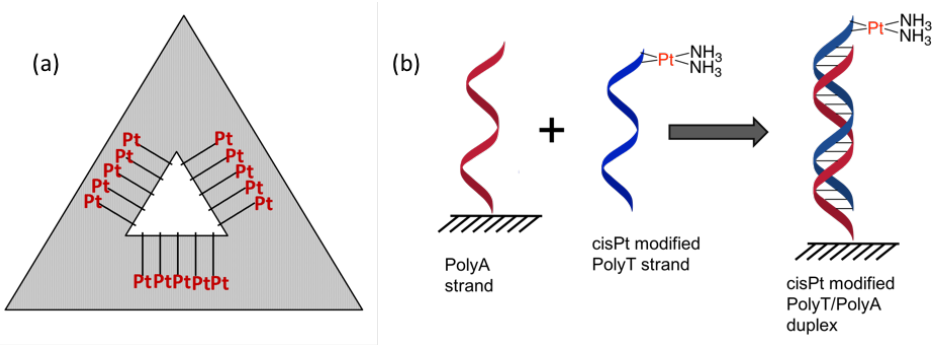

Figure 4.23 – Schematic representation of the design of cisplatin modified DNA Origami Triangle: (a) cisplatin DNA Origami Triangle, (b) hybridization of the polyA strand, anchored within the DNA origami via staples, with a cisPt modified polyT strand.

4.5.1 Synthesis and characterisation of cisPt polyT strand

Solid phase DNA synthesis was once again employed to synthesise the polyT-GG strand as well as its complementary polyA strand (Table 4.2) according to the procedures described in Chapter 7.2.1, Chapter 7.2.2 and Chapter 7.3.1. The oligonucleotides were purified by reversed phase HPLC and characterised by mass spectrometry (Appendix). Following this, the polyT-GG strand was reacted with cisplatin according to the standard procedure detailed in Chapter 7.5. This reaction gave a surprisingly good yield, as shown by the HPLC trace of the crude product in Figure 4.24. The biggest fraction was confirmed to be the desired adduct by mass spectrometry.

Table 4.2 – Sequences of PolyT-GG and PolyA oligonucleotides.

Oligonucleotide name	Oligonucleotide sequence
PolyT-GG	5′–TTT TTT TTT TTT TTT TTT TT GG–3′
PolyA	5′–AAA AAA AAA AAA AAA AAA AA–3′

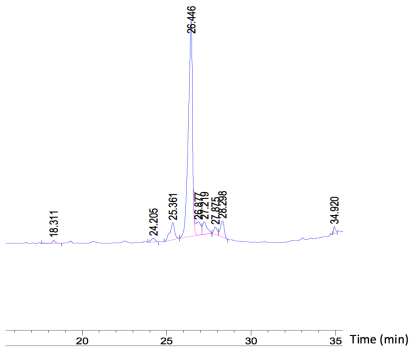

Figure 4.24 – HPLC trace of cisPt polyT-GG strand, monitored at 260 nm wavelength and conditions: 50 mM HFIP, 15 mM HA buffer, pH: 7, 1.0 mL min^{-1} flow rate, 60 ^{o}C, Kinetex C18 column, with gradient 20-45% (20 min), 45-50% (5 min), 50% (5 min) methanol.

The high yield of the mono-platinated polyT-GG adduct may be explained by the terminal location of the two guanine bases, which allows better access for the cisplatin to bind, compared to their internal location in G20 or G14 sequences.

4.5.2 Cisplatin polyT duplex formation

Before incorporation of the cisPt polyT-GG strand into the DNA Origami, it was decided to first test it for duplex formation. This was once again accomplished by hybridisation of the strand with its complementary (PolyA) using the conditions of the DNA Origami assembly described in Chapter 7.6 and subsequently running native PAGE (Figure 4.25).

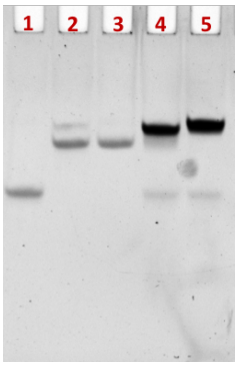

Figure 4.25 – A Diamond™ stained native 20 % PAGE visualised with UV light on AlphaImager HP system, 1xTBE buffer, 100 V, 3 h at 4 °C; Lanes: 1 – poly A, 2 – PolyT-GG, 3 – cisPt polyT-GG, 4 – Origami Duplex, 5 – cisplatin Origami Duplex. Concentrations of strands were 1 µM.

Gel electrophoresis results presented in Figure 4.25 show unfamiliar behaviour for the polyT strands in lanes 2 and 3, which being single strands were expected to travel more down the gel. Nevertheless, the much stronger intensity of the bands in lanes 4 and 5 indicate that the cisplatin origami duplex could indeed form.

To further test the unusual behaviour of the origami duplex and its cisplatin derivative, UV/Vis spectroscopy and circular dichroism spectroscopy were employed. The results of this study are presented in Figure 4.26.

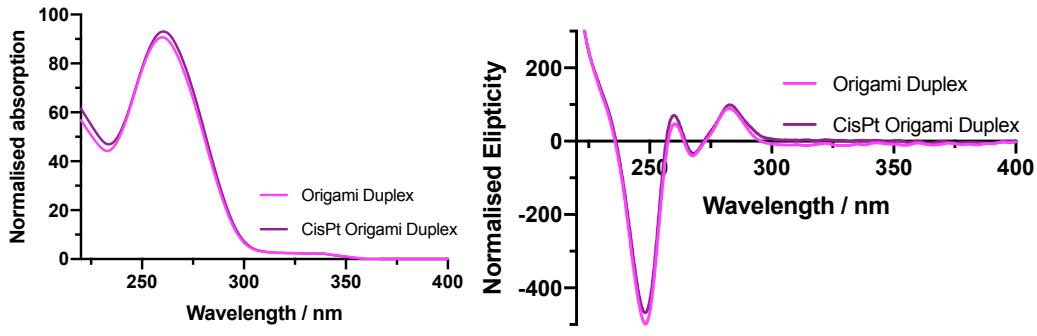

Figure 4.26 - Cisplatin Origami and Origami duplexes (10 µM) spectroscopic studies; UV/Vis spectra (left), CD spectra (right) in 10 mM sodium phosphate and 100 mM sodium chloride buffer, pH 7.0.

The UV/Vis study reveals that the pattern seen earlier with cisplatin duplexes is not so apparent here, which can be explained by the lack of a kink, due to the cisplatin binding guanines at the 3' and that does not take part in base pairing. The CD results show two positive bands at 260 nm and 280 nm as well as one negative band at 248 nm. This is a known phenomenon for polyT - polyA duplexes as shown in Chapter 2, Figure 2.12 and the literature.[29-31]

4.5.3 Self-assembly and characterisation of cisPt DNA Origami Triangle

Self-assembly of the cisplatin DNA Origami Triangle was accomplished according to the standard method described in Chapter 7.7.1 and purified by PEG precipitation according to the procedure developed by Stahl *et al.*[32], which was employed to remove excess staples used in the assembly. Following purification, the DNA Origami pellet was re-suspended in a magnesium rich buffer (5 mM Tris, 1 mM EDTA, 5 mM $MgCl_2$, 5 mM NaCl, pH 8) to maintain the structure of the DNA Origami Triangle. In order to determine successful formation of the cisplatin DNA Origami Triangle, agarose gel electrophoresis was employed according to the standard protocol detailed in Chapter 7.7.2 (Figure 4.27).

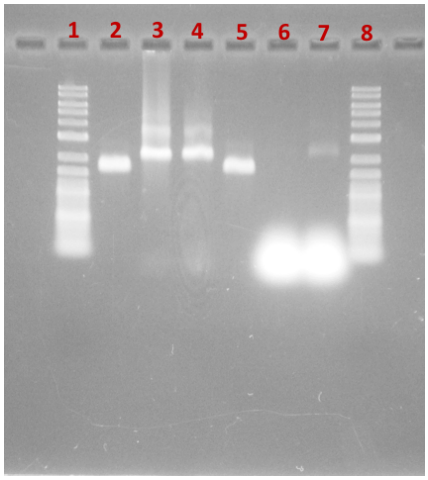

Figure 4.27 – Gel Electrophoresis of cisplatin DNA Origami Triangle (39 nM) using 1% Agarose, 1xTAE and 10 mM $MgCl_2$, 60 V, 2 h, at room temperature, stained with GelRed and visualised with UV light on AlphaImager HP system; lane 1&8 – DNA ladder; lane 2&5 – M13 mp18 ssDNA; lane 3 – unmodified DNA Origami Triangle; lane 4 – cisplatin DNA Origami Triangle; lane 6&7 – excess staples.

Results shown in Figure 4.27 show successful formation of the cisplatin DNA Origami Triangle in lane 4, as evidenced by the slower mobility band in contrast to the M13 genomic DNA alone. However, it is impossible to state whether the cisplatin polyT-GG strands were attached to the nanostructure, since they are docked onto the assembly via the staple extension as discussed earlier. Another technique used to study DNA Origami assemblies is Atomic Force Microscopy (AFM) imaging. However in this case, AFM imaging was considered not versatile enough to determine whether the cisplatin polyT-GG strands were hybridised within this nanostructure. An alternative technique is STEM (Scanning Transmission Electron Microscopy) imaging, which can detect individual atoms in a sample. This or another suitable imaging technique, could be employed to study this nanostructure in the future.

4.6 Cisplatin Holliday junction array assembly

Another approach to create a scaffold for precise metal placement using DNA nanostructure design was inspired by the work of Malo *et al.,*[33] who assembled 2D DNA arrays, as detailed in Chapter 1.2. However, adding platinum onto the already formed structure would not provide the required specificity of metal placement. Therefore, the monomeric strands would have to be platinated first. However, in order to create cisplatin modified assemblies based on this design, it was necessary to vary the DNA sequences in this nanostructure. This was due to the separation challenge arising from the formation of multiple cisplatin DNA adducts in DNA sequences containing multiple guanine and adenine bases. Therefore, it was decided to vary the sequence of the shortest strand in the design and to remove all additional guanine bases as well as adenine bases. In this way, the newly designed oligonucleotide would only bind to one cisplatin molecule in a specific predefined location within its structure, which would then be taken for the assembly of the Holliday junction. This methodology is illustrated in Figure 4.28.

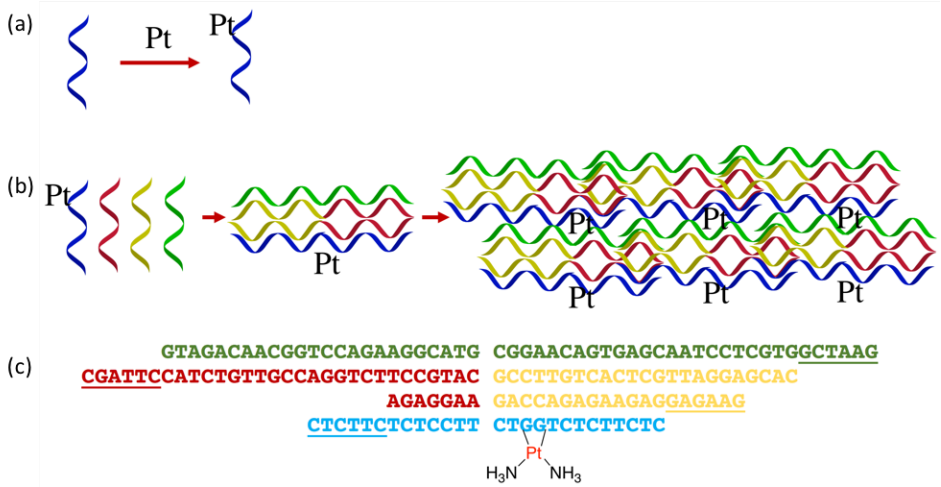

Figure 4.28 – Schematic illustration of the design of the cisplatin modified Holliday junction assembly; (a) Platination of an oligonucleotide monomer; (b) Assembly of the platinated Holliday junction assembly array; (c) Cisplatin Holliday junction monomer with its sequences.

4.6.1 Synthesis and purification of cisPt Holliday junction monomer

Following the solid phase synthesis and purification of the monomers (Appendix) for Holliday junction array assembly, the blue strand containing just two adjacent guanine bases was used for a platination reaction according to the standard protocol described in Chapter 7.5. The reaction mixture was then tested by analytical HPLC (Figure 4.29). The HPLC trace of the crude cisPt DNA adduct shows two main peaks corresponding to the unplatinated and mono-platinated DNA. The mono adduct elutes faster and the peak seems to be slightly smaller than the one corresponding to the unplatinated DNA. This was expected as the platination site was in the middle of the sequence. The cisPt Holliday junction blue strand was purified by HPLC and characterised by mass spectrometry (Appendix).

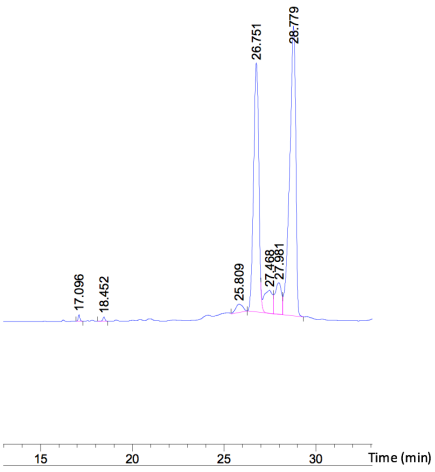

Figure 4.29 - HPLC trace of cisPt Holliday junction blue strand, monitored at 260 nm wavelength and conditions: 50 mM HFIP, 15 mM HA buffer, pH: 7, 1.0 mL min^{-1} flow rate, 60 ^{o}C, Kinetex C18 column, with gradient 20-45% (20 min), 45-50% (5 min), 50% (5 min) methanol.

4.6.2 Assembly and characterisation of cisPt Holliday junction array

Self-assembly of the cisplatin modified Holliday junction array was supported by the thermal annealing study by Malo *et al.*[33] and the method detailed in Chapter 7.9. The annealing procedure, which lasts 72 h, not only forms the individual Holliday junction structures but also joins them together via so called “overhangs” which are six DNA bases on each of the four strands complementary to the next unit. The latter process is thermodynamically favourable but takes longer to reach completion, hence a long annealing time is required.

The characterisation of the cisplatin Holliday junction is not straightforward. Gel electrophoresis cannot be employed as the assembly is in a form of indefinite array.

Thermal melting has been previously used by Malo *et al.*[33] to characterise the array assembly. In this study, thermal denaturation was accomplished by monitoring the change in fluorescence of the intercalated dye (SYBR® green) in the DNA with change in temperature, resulting in melting curves of Relative Fluorescence Units (RFU) as a function of temperature. Detailed procedure of this study is described in Chapter 7.13.2 and the results are presented in Figure 4.30.

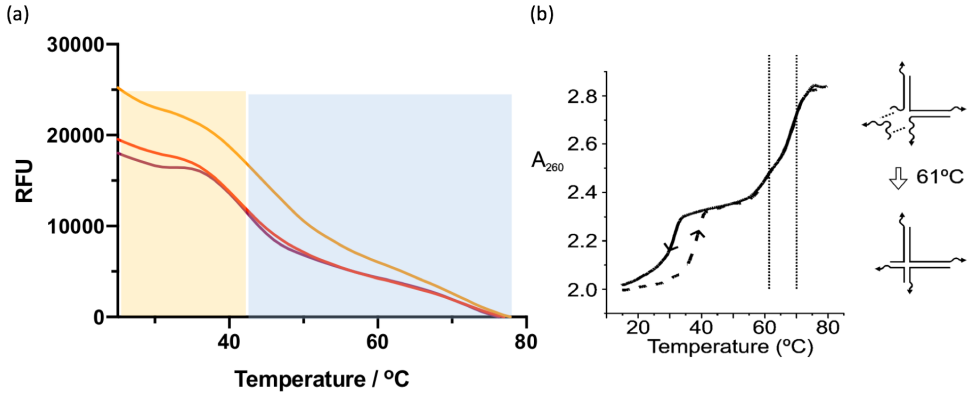

Figure 4.30 – (a) Thermal melting curve of cisPt Holliday junction array (5 µM) in 10 mM $MgCl_2$/ 5 mM Tris-Cl/ 20 mM Tris acetate/ 1 mM EDTA, 2% Triton-100 buffer, pH 7; consisting of 3 repeats. (b) The literature results of unmodified Holliday junction array are shown here for comparison. *Reprinted with permission from Malo et al.*[33] *Copyright 2009 American Chemical Society.*

It can be easily noted that the melting curve has two transition areas highlighted in yellow and blue. The lower transition temperature (yellow) suggests that the individual assemblies within the Holliday junction are being detached from one another by breaking the "overhangs", whereas the higher transition temperature (blue) indicates the subsequent disassembly of these individual structures. The results seem to be in agreement with the literature (Figure 4.30).[33]

As outlined in the Origami Triangle work, ideally other imaging techniques would also be employed to give direct evidence for assembly formation. Therefore, AFM or STEM will be employed as part of the future work.

4.7 Cisplatin G20 duplex for assembly on gold surfaces

Another approach for precise spacing of metal atoms on a surface by using DNA is to exploit the thiol-gold binding interaction. The chemistry of thiols and gold surfaces is well known.[34, 35] Thiol modified DNA can be therefore used to coat a gold surface with defined spacing. The methodology of the work presented in this chapter uses a thiol-modified single strand with the aim to hybridise a cisplatin-containing complementary strand to it, thus coating the gold surface with equally spaced platinum atoms (Figure 4.31).

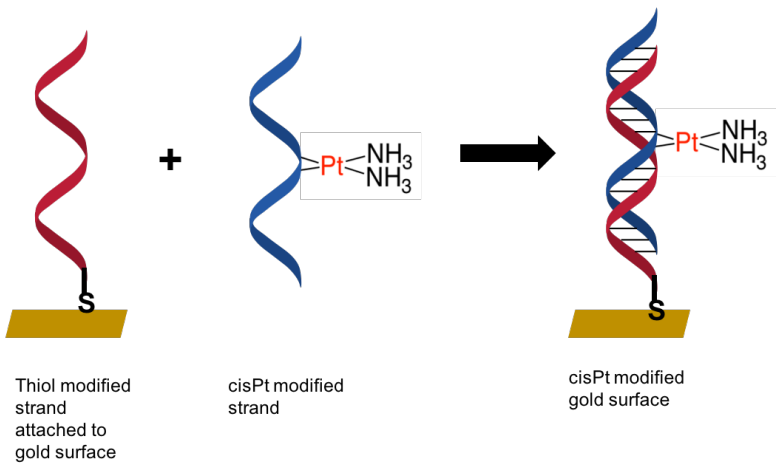

Figure 4.31 – Schematic representation of the undertaken methodology for coating gold surface with cisplatin modified DNA.

4.7.1 Synthesis and characterisation of cisPt modified thiol-modified DNA Duplex

Once again solid phase synthesis (Chapter 7.2.1) was employed to synthesise a thiol-modified DNA oligonucleotide, which was subsequently purified by RP-HPLC following the standard procedure (Chapter 7.2.2) and characterised by mass spectrometry (Chapter 7.3.1). The results are presented in the Appendix, Figure 8.2.5. The complementary Pt-containing strand was used from the study described in Section 4.3.2. The sequences of oligonucleotide strands used in this study are shown in Table 4.3.

Table 4.3 - Sequences of cisPt Lippard and complementary thiol Lippard oligonucleotides.

Oligonucleotide name	Oligonucleotide sequence
Thiol G20 target	5'–GAG AAG AGA CC AGA AGG AGA–thiol–3'
cisPt-G20 probe	5'–TCT CCT TCT **GG(cisPt)** TCT CTT CTC–3'

Upon successful hybridisation of the thiol modified G20 complementary strand and its cisPt-G20 probe (according to the standard procedure detailed in Chapter 7.5), it was necessary to test the assembled duplex prior to the surface studies. Once again, native gel electrophoresis (Chapter 7.14.1) was employed for this purpose, with the results shown in Figure 4.32.

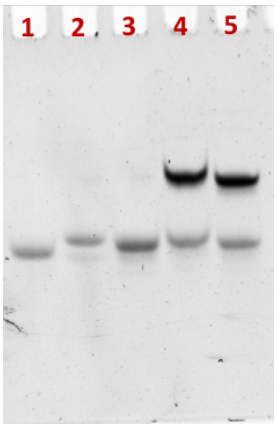

Figure 4.32 - A Diamond^{TM} stained native 20 % PAGE visualised with UV light on AlphaImager HP system, 1 x TBE buffer, 100 V, 3 h at 4 ^{o}C; Lanes: 1 – unmodified G20 probe, 2 - cisplatin G20 probe, 3 – Thiol G20 target, 4 – unmodified Thiol G20 Duplex, 5 – cisplatin Thiol G20 Duplex. Concentration of the strands were 10 µM.

Results presented in Figure 4.32 confirm formation of the thiol-modified cisplatin G20 duplex, as indicated by the slower mobility bands (lanes 4 & 5) as well as its darker appearance due to the intercalating dye. All the single strands in lanes 1-3 run faster and appear lighter.

Following successful formation of the duplexes as indicated by gel electrophoresis, it was decided to test the duplexes by UV/Vis and circular dichroism spectroscopies, with the results presented in Figure 4.33.

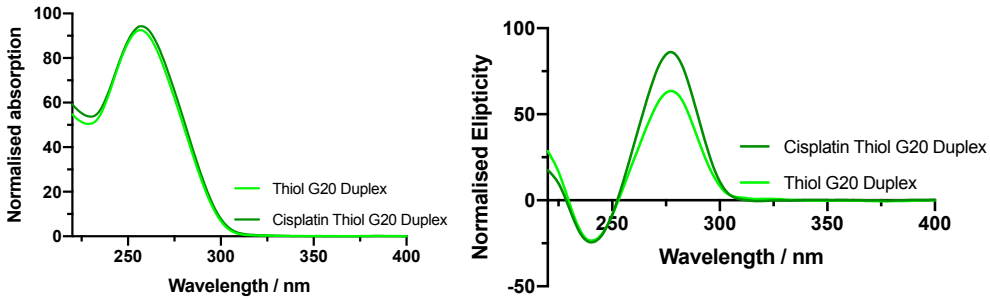

Figure 4.33 - Cisplatin Thiol G20 and Thiol G20 duplexes (10 µM) spectroscopic studies; UV/Vis spectra (left), CD spectra (right) in 10 mM sodium phosphate and 100 mM sodium chloride buffer, pH 7.0.

Results of the CD spectroscopic studies presented above confirm the familiar pattern of cisplatin modified duplexes. Future work will focus on self-assembled monolayer (SAM) formation on a surface and undertaking microscopy imaging studies. However, only a small hyperchromic and bathochromic shift is observed in the UV/Vis spectrum and a more intense band at 280 nm observed in the CD spectrum.

4.8 Thermal Melting Study

Thermal melting studies of the duplexes explored in this chapter were undertaken following a standard protocol described in Chapter 7.13.2. It was necessary to determine the stability of the cisplatin duplexes and at the same time their suitability for further testing. The results of this study are presented in Table 4.4.

Table 4.4 – Predicted and experimental results of melting temperature of the duplexes explored in Chapter 4.

Thermal melting run	G14 Duplex (°C)	CisPt G14 Duplex (°C)	G20 Duplex (°C)	CisPt G20 Duplex (°C)	Thiol G20 Duplex (°C)	CisPt Thiol G20 Duplex (°C)	Origami Duplex (°C)	CisPt Origami Duplex (°C)
Predicted	53	-	63	-	63	-	56.6	-
1	59	51	66	61	69.5	65.5	66	66.5
2	59	58	66	61	69.5	65.5	66	66.5
3	63	nd	69	63	69	65	66.5	66.5
σ	2.3	4.9	1.7	1.2	0.3	0.3	0.3	0

The thermal melting results show a significant difference between the predicted (IDT Oligo Analyser Tool)[36] and measured melting temperatures. This is due to the SYBR Green dye binding to DNA and increasing the thermal melting temperature as reported in the literature.[37] The difference can be anywhere between 6-10 °C for 20 µM dye concentration. If this discrepancy is accounted for, the unmodified duplex melting temperatures fall in the correct range of the calculated melting temperatures.

The melting temperature of cisplatin duplex is shown to be lower than the unmodified duplex. This is true for cisplatin G14 (by 8 °C) as well as for cisplatin G20 and cisplatin Thiol G20 (by 5 °C & 4 °C respectively). The cisplatin Origami duplex has the same melting temperature as its unmodified version since the cisplatin is bound to the two guanine bases at the end of the oligo, which do not contribute to duplex formation. It can be seen from the results that the shorter duplex (G14 - 14 mer) is more affected by the presence of cisplatin showing a much lower melting

temperature (difference of 8 ^{o}C) as opposed to the longer duplex (G20 – 20 mer) where the melting temperature difference is 4-5 ^{o}C. It can be concluded that while the presence of cisplatin lowers the melting temperature of a DNA strand making it less stable, its stability is well above room temperature, which allows such systems to be employed for the purpose of synthesising materials for fuel cell catalysis.

4.9 Conclusions

This project has demonstrated a successful design and synthesis of a DNA-based material with precise metal loading for fuel cell catalyst development. This was first achieved with a short oligo containing only 14 bases. High Performance Liquid Chromatography was employed to successfully isolate the mono-platinated DNA adduct and tandem mass spectrometry was used to pinpoint the precise location of the cisplatin moiety bound to the DNA strand. A sequence with only two adjacent guanine bases was next selected in order to limit the amount of poly-platinated DNA adducts and at the same time, increase the chances of a better yield and easier purification. The study of the cisplatin duplexes in this chapter confirmed the literature findings concerning their stability and allowed their exploitation for higher order nanostructure assemblies. DNA Origami was the first nanostructure explored for docking cisplatin and was accomplished by extending 15 staple strands and hybridising cisplatin modified complementary strands onto them. The second nanostructure explored for platinum scaffold was a Holliday junction array. In this study, one of the four sequences was bound to cisplatin and assembled into a

nanostructure after successful purification. Finally, the last approach to achieve equally spaced platinum groups on a surface was accomplished by making a thiol-modified probe for attachment to a gold surface. It can be summarised that cisplatin can indeed serve as an efficient metal source and DNA can be easily used as a scaffold for the precise metal placement of platinum atoms for future applications in nanotechnology and catalysis.

4.10 References

1. O. Dyck, M. Ziatdinov, D. B. Lingerfelt, R. R. Unocic, B. M. Hudak, A. R. Lupini, S. Jesse and S. V. Kalinin, *Nat. Rev.*, 2019, **4**, 497-507.
2. R. F. Egerton, P. Li and M. Malac, *Micron.*, 2004, **35**, 399-409.
3. N. Jiang, *Rep. Prog. Phys.*, 2016, 016501.
4. R. A. Lawson and A. P. G. Robinson, in *Frontiers of Nanoscience*, Elsevier Ltd., 2016, vol. 11, ch. 1, pp. 1-90.
5. A. A. Tseng, K. Chen, C. D. Chen and K. J. Ma, *IEEE Trans. Electron. Packag.*, 2003, **26**, 141-150.
6. M. A. McCord and M. J. Rooks, ed. Bellingham, WA: SPIE Optical Engineering, 1997, ch. 2, pp. 139–249.
7. B. Shen, K. Tapio, V. Linko, M. A. Kostiainen and J. J. Toppari, *Nanomaterials*, 2016, **6**, 1-22.
8. Z. Deng and C. Mao, *Angew. Chem. Int. Ed.*, 2004, **43**, 4068-4070.
9. Z. Jin, W. Sun, Y. Ke, C.-J. Shih, G. L. C. Paulus, Q. H. Wang, B. Mu, P. Yin and M. S. Strano, *Nat. Commun.*, 2013, **4**, 1-9.
10. F. Zhou, W. Sun, K. B. Ricardo, D. Wang, J. Shen, P. Yin and H. Liu, *ACS Nano.*, 2016, **10**, 3069−3077.
11. H. Yang, K. L. Metera and H. F. Sleiman, *Coord. Chem. Rev.*, 2010, **254**, 2403-2415.
12. H. Yan, S. H. Park, G. Finkelstein, J. H. Reif and T. H. LaBean, *Science*, 2003, **301**, 1882-1884.
13. Y. Y. Pinto, J. D. Le, N. C. Seeman, K. Musier-Forsyth, T. A. Taton and R. A. Kiehl, *Nano Lett.*, 2005, **12**, 2399-2402.
14. P. W. K. Rothemund, *Nature*, 2006, **440**, 297-302.
15. J. Liu, Y. Geng, E. Pound, S. Gyawali, J. R. Ashton, J. Hickey, A. T. Woolley and J. N. Harb, *ACS Nano*, 2011, **5**, 2240-2247.
16. Y. Ke, S. Lindsay, Y. Chang, Y. Liu and H. Yan, *Science*, 2008, **319**, 180-183.
17. N. V. Voigt, T. Tørring, A. Rotaru, M. F. Jacobsen, J. B. Ravnsbæk, R. Subramani, W. Mamdouh, J. Kjems, A. Mokhir, F. Besenbacher and K. V. Gothelf, *Nat. Nanotechnol.*, 2010, **5**, 200-203.
18. S. Rinker, Y. Ke, Y. Liu, R. Chhabra and H. Yan, *Nat. Nanotechnol.*, 2008, **3**, 418-422.
19. A. Kuzyk, K. T. Laitinen and P. Torma, *Nanotechnology*, 2009, **20**, 235305-235310.
20. H. T. Maune, S. P. Han, R. D. Barish, M. Bockrath, W. A. Goddard, P. W. K. Rothemund and E. Winfree, *Nat. Nanotechnol.*, 2010, **5**, 61-66.
21. S. Pal, Z. Deng, B. Ding, H. Yan and Y. Liu, *Angew. Chem. Int. Ed.*, 2010, **49**, 2700-2704.
22. N. Poklar, D. S. Pilch, S. J. Lippard, E. A. Redding, S. U. Dunham and K. J. Breslauer, *Proc. Natl. Acad. Sci.*, 1996, **93**, 7606-7611.
23. E. R. Jamieson and S. J. Lippard, *Chem. Rev.*, 1999, **99**, 2467-2498.
24. L. Gong, *Rapid Commun. Mass Spectrom.*, 2015, **29**, 2402-2410.

25. S. Studzińska, *Talanta*, 2018, **176**, 329-343.
26. Promega, *Journal*, 2013, 8.
27. M. Sirajuddin, S. Ali and A. Badshah, *J. Photochem. Photobiol. B*, 2013, **124**, 1-19.
28. A. Gopinath and P. W. K. Rothemund, *ACS Nano*, 2014, **8**, 12030-12040.
29. S. R. Ok and D. W. Gruenwedel, *Z. Naturforsch.* , 1993, **48**, 488-494.
30. D. Musumeci, V. Roviello and G. N. Roviello, *Int. J. Nanomedicine*, 2018, **13**, 2613-2629.
31. M. Vorlickova, I. Kejnovska, K. Bednarova, D. Renciuk and J. Kypr, *Chirality*, 2012, **24**, 691-698.
32. E. Stahl, T. G. Martin, F. Praetorius and H. Dietz, *Angew. Chem. Int. Ed.*, 2014, **53**, 12735-12740.
33. J. Malo, J. C. Mitchell and A. J. Turberfield, *J. Am. Chem. Soc.*, 2009, **131**, 13574-13575.
34. *United States Pat.,* 1994.
35. R. G. Nuzzo and D. L. Aliara, *J. Am. Chem. Soc.*, 1983, **105**, 4481-4483.
36. I. D. Technologies, OligoAnalyzer Tool, https://www.idtdna.com/calc/analyzer, (accessed 2015-2019).
37. H. Gudnason, M. Dufva, D. D. Bang and A. Wolff, *Nucleic Acids Res.*, 2007, **35**, 1-8.

Chapter 5 – Ferrocene DNA Nanostructures

5.1 Introduction

This chapter introduces the ferrocene molecule as well as its incorporation into DNA. The benefits and applications of using a ferrocene-nucleic acid system are subsequently highlighted. Furthermore, a new approach for precise metal placement into DNA is described wherein DNA assemblies are modified with ferrocene via solid phase DNA synthesis. The synthesis and characterisation of these structures, namely a ferrocene DNA Tetrahedron (Fc-DNA-Tet) as well as ferrocene Holliday Junction (Fc-DNA-Holl) assemblies are detailed.

5.1.1 Ferrocene

Ferrocene was first synthesised by Pauson in his failed attempt to prepare fulvalene from a cyclopentadienyl Grignard reagent and $FeCl_3$.[1] However, it was only a year later that Wilkinson identified the correct 'sandwich' structure of the compound, with an X-ray structure depicting it in both staggered and eclipsed conformations (Figure 5.1).[2] It has two planar cyclopentadienyl rings, each with 6 π-electrons, that sandwich the central Fe^{2+} ion. This results in a neutral molecule with a stable 18-electron configuration.[3]

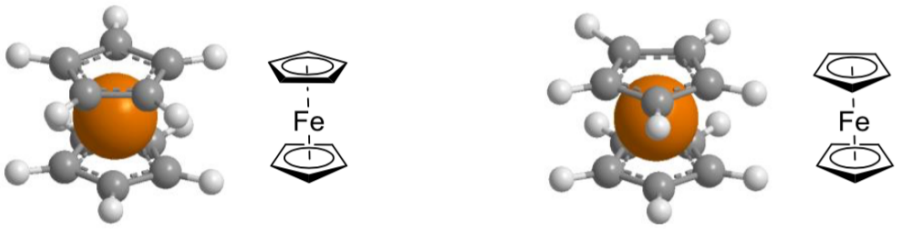

Figure 5.1 – Wilkinson's sandwich model of Ferrocene. *Reproduced with permission from J.L. Kedge.*[4] *Copyright 2017 University of Birmingham.*

Ferrocene is most commonly produced by cracking cyclopentadiene before the immediate addition of iron(II) chloride (Figure 5.2).[5] The molecule can be functionalised in a variety of ways, including by Friedel-Crafts alkylation/acylation and Vilsmeier-Haack formylation,[6] deprotonation using butylithium reagents,[7] or through treatment with organolithium reagents with use of various stereoselective groups to achieve monolithiation.[8]

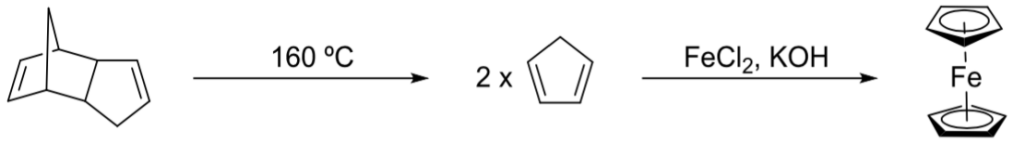

Figure 5.2 – Standard procedure employed for synthesis of Ferrocene, adapted from G. Wilkinson.[5]

The chemistry of ferrocene has revolutionised organometallic chemistry with its broad range of applications.[9] For instance, ferrocene has been successfully incorporated into polymers and studied for its use in cathodic battery materials. A study conducted by the Goodenough group used ferrocene-doped polypyrrole polymer to obtain a 2 µm thick material with 65 mA h g^{-1} at 0.2 °C, giving a favourable lowering of overpotential at high discharge rates which means improved cycling stability.[10] More recently, Ding *et al.* produced a ferrocene-based semiliquid battery which demonstrated a power density exceeding 1400 W L^{-1} and an energy density of 40 Wh L^{-1} with a stability of 80% over 500 cycles.[11] These are relatively good specifications in comparison to commercial and advanced batteries.[12]

Ferrocene has also been utilised in the formation of liquid crystals. Deschenaux *et al.* developed a dendric core substituted with six mesomorphic ferrocene units which exhibited a broad enantiotropic smectic (arranged in well-defined planes) A phase.[13] A few years later, the same group developed an optically active liquid-crystalline material using ferrocene-based vinyl monomers.[14]

Hexaferrocene stars have become very popular due to their remarkable redox, electrochemical and electrostatic behaviour (Figure 5.3).[15] These species exhibit a single cyclic voltammetry wave due to the ferrocene groups being located further away from the central benzene.[16] However, the closer the ferrocene groups are to the centre, the more significant the electrostatic factor becomes and multiple redox waves are observed.[9]

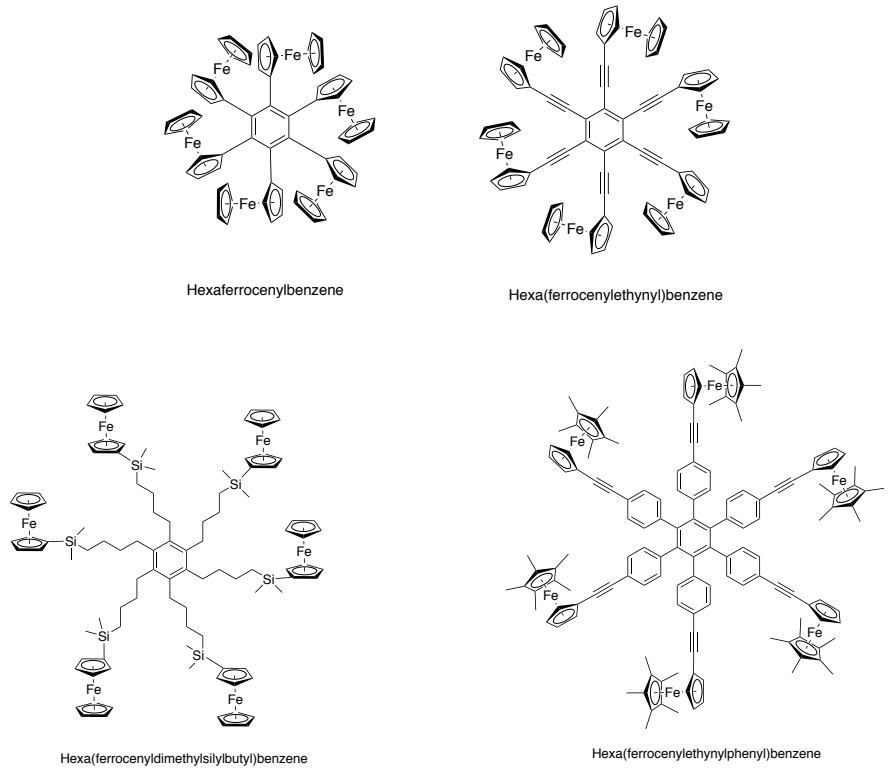

Figure 5.3 – Examples of hexaferrocene stars, adapted from D. Astruc.[9]

These various ferrocene-containing dendrons and dendrimers have found applications in redox sensing and catalysis. For instance, the Astruc group synthesised giant ferrocene-terminated dendrimers which contain up to 15000 ferrocene termini. These molecules are capable of controlled molecular movement, acting like molecular machines as they expand and contract upon reduction and oxidation, giving rise to a molecular electrochromic battery.[17] In another study, catalytically active palladium nanoparticles were stabilised by dendrimers containing triazolylferrocenyl termini.[18]

Medicine is another field to which the redox properties of ferrocene have been applied. The Turner group used ferrocene-mediated enzyme electrodes for amperometric detection of glucose in blood, wherein ferrocenium was formed at the anode and oxidises the glucose oxidase enzyme, which in turn oxidises the glucose substrate to gluconolactone.[19] Many ferrocene derivatives exhibit antitumor activities, including ferrocenium salts[20], ferrocene conjugated to biological molecules (e.g. nucleobases, peptides),[21] and ferrocenyl compounds based on selective estrogen modulators (e.g. ferrocifens,[22] ferrociphenols, ferrocenophanes).[23]

5.1.2 Ferrocene-modified Nucleic Acids

DNA biosensors that are able to detect single point variations in genetic sequences are particularly important for the sensing and screening of cancer and other genetic diseases. Ideally this is done without the need for PCR amplification of the analyte.[24]

Redox-labeled probes, in particular ferrocene-containing oligonucleotides, have been extensively studied for the electrochemical sensing of DNA.[25]

Peptide nucleic acids are DNA analogues with a pseudopeptide backbone to which nucleobases are attached. The standard procedure for the preparation of PNAs consists of monomer synthesis, as achieved by Dueholm *et al.* and subsequent assembly using a solid-phase peptide synthesis protocol.[26] The first ferrocene labeled PNA was prepared by Hess *et al.* using ferrocene carboxylic acid chloride with thymine-PNA methyl ester.[27] The ease of its fabrication via standard solid phase synthesis, as well as the proven lack of interference with DNA binding, made the ferrocene PNA conjugate a desirable marker for DNA binding and led to its application in DNA biosensing.[28]

A relevant example in this area is the ferrocene nucleic acid oligomer produced by the Tucker group, who synthesised such an oligomer containing eight ferrocene units and sixteen thymine nucleobases (Figure 5.4).[29] This was accomplished by first preparing a tetra-substituted ferrocene monomer containing a thymine base on each Cp ring and subsequently forming the oligomer using the standard solid phase synthesis via phosphoramidite chemistry.

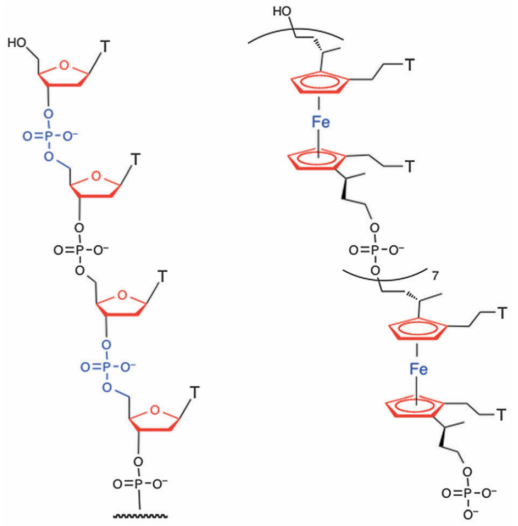

Figure 5.4 – Structure of DNA (left) and FcNA (right). *Reproduced with permission from Nguyen et al.*[29] *Copyright 2012 Royal Society of Chemistry.*

Ferrocene can be incorporated into DNA in several ways, not just as a part of the backbone. It is possible to tag ferrocene derivatives to a primary amine on the DNA, or to use a phosphoramidite derivative to incorporate it into DNA via automated solid-phase synthesis.[24] Postsynthetic modification of the DNA strand with a ferrocene derivative has also been accomplished by acylation of the 5'- and 3'-terminal amino group of the oligonucleotide by N-hydroxysuccinimide ester of ferrocenecarboxylic acid.[30]

Letsinger *et al*. found the phosphoramidite approach was easy to adopt based on previous work on the incorporation of a wide variety of other tags such as biotin, fluorescein and acridine.[31] Their strategy involved coupling of a ferrocenyl-phosphoramidite to a thymine bound to a controlled pore glass (CPG) support by standard solid-phase DNA synthesis (Figure 5.5). The synthesised ferrocene-

containing oligonucleotide was additionally modified with a thiol at its 3' end which allowed the assembly of this oligonucleotide on to a gold surface as a SAM (Self-Assembled Monolayer), forming a densely packed monolayer film. Cyclic voltammetry of this modified gold substrate exhibited a reversible wave with an $E_{1/2}$ = 220 mV corresponding to the ferrocene redox couple.[31]

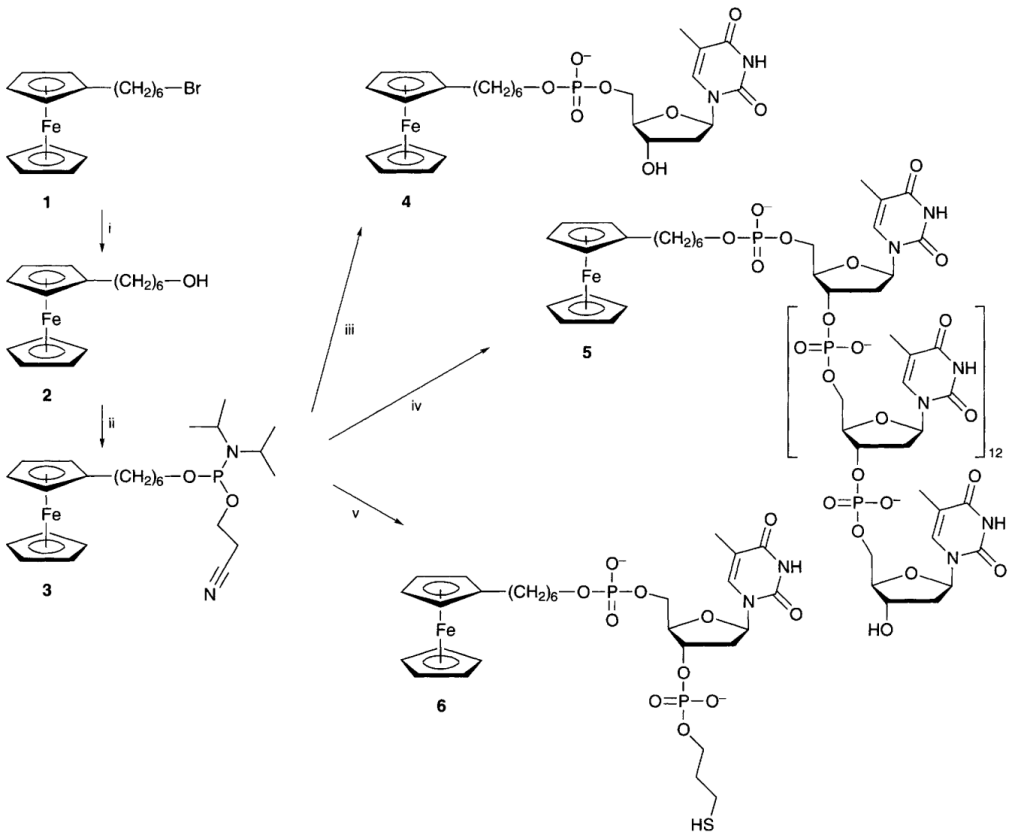

Figure 5.5 – Synthetic route to a thiol modified Ferrocene-labeled oligonucleotide, adapted from Mucic *et al*.[31]

The main applications of ferrocene-modified nucleic acids are found in biosensing.[24, 30] Biosensors are sensors with biological components and typically convert a biological response into an observable signal, with some employing redox chemistry to give an informative electrical signal.[32] The desired qualities of biosensors are

specificity, reusability and an independence of parameters such as pH or temperature.[33] Biosensors are not only comprised of DNA, but also can be enzyme- or tissue- based devices as well as immunosensors and thermal biosensors (responding to temperature).[32]

The hybridisation of a probe strand to its complementary strand to form a stable duplex is at the heart of most DNA-based biosensors.[34] The common make up of an electrochemical DNA detector comprises of a short, single stranded oligonucleotide (15-20 mer) immobilised on to the surface of an electrode (e.g. as a SAM), which upon immersion in a target DNA solution and hybridisation of the two complementary strands, causes a change in a physiochemical property of the surface layer, which can be detected (Figure 5.6).[30]

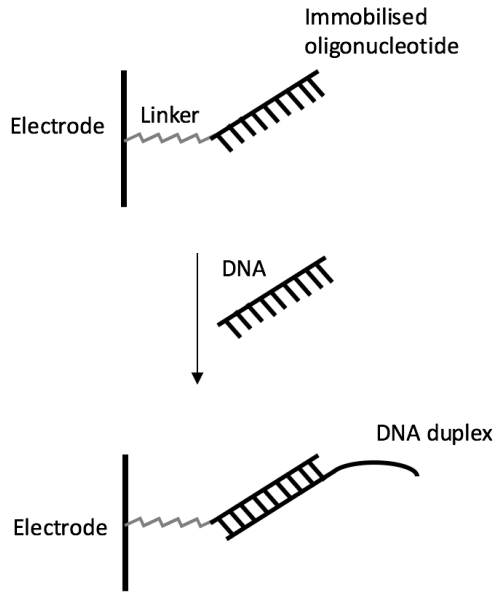

Figure 5.6 – Schematic representation of duplex formation on an electrode surface, adapted from Zatsepin *et al*.[30]

Letsinger *et al.*[31] pioneered the field of DNA gold surface electrochemistry, as mentioned earlier. Since then, the Maeda group developed a surface-based gene sensor based on ferrocene-modified DNA. However, in their example, an unmodified probe was bound to the surface and a second strand, containing ferrocene, was not immobilised. When a target strand was introduced, it hybridised to the strand on the surface as well as the ferrocene-modified strand, generating an electrochemical response (Figure 5.7).[35]

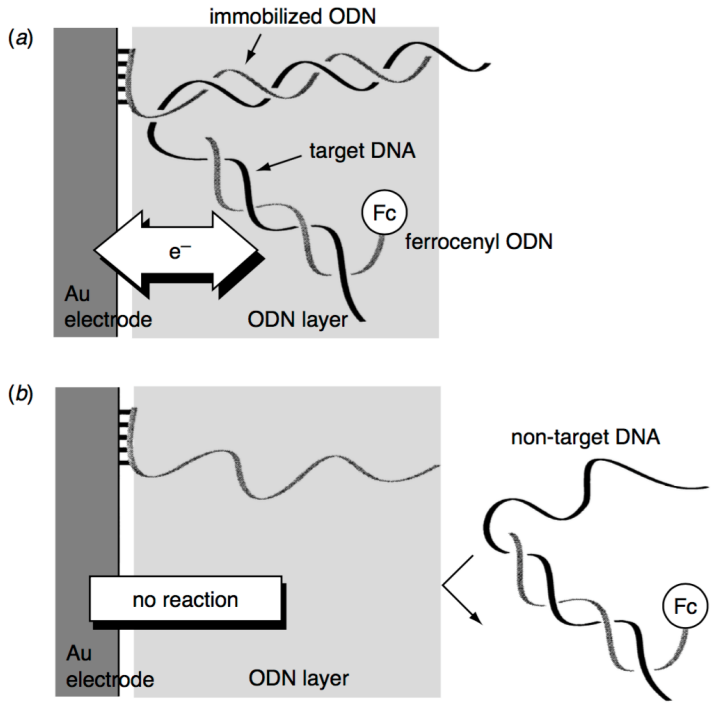

Figure 5.7 – Schematic illustration of the gene sensing system, *reproduced with permission from Ihara et al.*[35] *Copyright 1997 Royal Society of Chemistry.*

The Willner group[36] developed a ferrocene-based DNA sensor to detect viral DNA. In this study, a thiolated oligonucleotide immobilised on a gold surface had a complementary sequence to the viral DNA (M13) thus enabling the binding of the

genomic DNA from the phage to the gold surface. Subsequently, Fc-labeled UTP (uridine-5'-triphosphate) in the presence of a polymerase enzyme replicated the viral genomic DNA, incorporating the ferrocene bases in the replica. This redox-active sensor was found to mediate electron transfer between the enzyme glucose oxidase and the electrode, activating the process of glucose oxidation (Figure 5.8).[36]

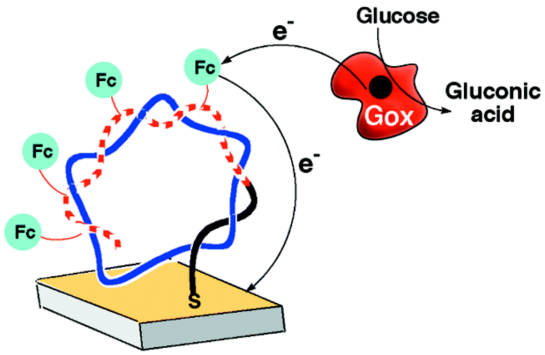

Figure 5.8 – Schematic representation of the redox active DNA sensor. *Reproduced with permission from Patolsky et al.*[36] *Copyright 2002 American Chemical Society.*

In another study by Wang *et al.*,[37] it was shown that thrombin detection could be achieved through the use of a ferrocene-labeled aptamer. This system comprised a gold electrode modified with functionalised gold nanoparticle, $(Ru(bpy)_3)^{2+}$–AuNPs), as well as a ferrocene-modified molecular beacon aptamer. Upon binding of the aptamer to thrombin, the ferrocene tag moved away from the electrode surface, resulting in an easily detectable electrochemical signal (Figure 5.9).[37]

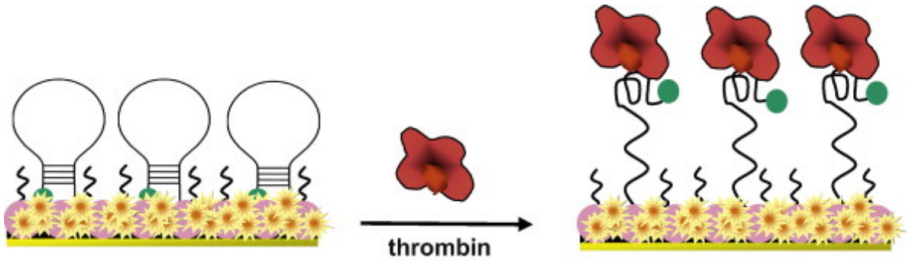

Figure 5.9 – Schematic representation of the ferrocene labeled aptamer sensor for detection of thrombin. *Reproduced with permission from Wang et al.*[37] *Copyright 2009 Elsevier B.V.*

5.2 Project aims

As described in previous chapters, the central goal of this thesis is to utilise metal-modified DNA in the design of novel materials to be used in fuel cell catalysis. Using DNA as a scaffold, metal atoms can be strategically placed at specific sites in order to achieve the most efficient metal packing for catalytic performance. If maximum catalytic efficiency can be achieved, less material can be used, reducing cost and weight. The aims of this part of the work was to explore the use of iron as a metal within the catalytic material as opposed to, or in addition to, platinum, further helping to reduce costs. This was to be achieved by the direct incorporation of a ferrocene unit into DNA strands using automated solid-phase synthesis. Subsequently, the ferrocene-modified strands would undergo self-assembly to form higher ordered structures for their potential use in the fabrication of novel fuel cell catalysts.

5.3 Ferrocene phosphoramidite approach to metal placement

The ferrocene phosphoramidite route was chosen to achieve precise control over metal placement in the DNA scaffold, as previously it had been studied within the group for applications in electrochemical sensing.[29] It is important to note that the ferrocene modification in this study was inserted directly into the sugar phosphate backbone by replacing two sugar units and one phosphate unit of a DNA (Figure 5.10). This is due to the well-established fact that the length of the ferrocene unit is comparable to the two adjacent base pairs in a DNA molecule.[29]

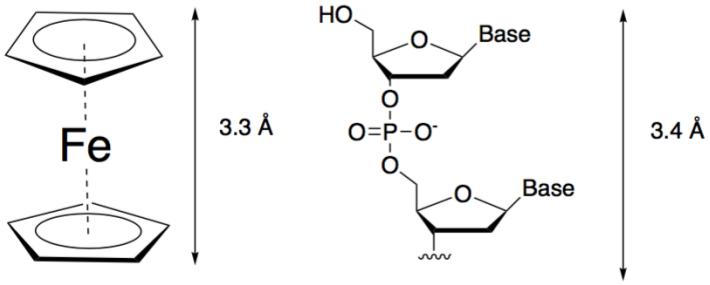

Figure 5.10 – Comparison of the length of the ferrocene unit (left) and two sugar units in the B form of DNA, adapted from Nguyen *et al*.[29]

5.4 Ferrocene-modified DNA Tetrahedron (Fc-DNA-Tet)

Originally, it was decided to compose a simple discrete DNA nanostructure containing ferrocene units distributed at specific locations. This project was inspired by the work of Goodman *et al*.[38] who synthesised a DNA tetrahedron using four 55-mer long oligonucleotides in a single-step annealing process (Figure 5.11). Each

strand is divided into three parts, with each part separated by two bases 'hinges', that remain unhybridised to allow the desired folding of the structure to occur.

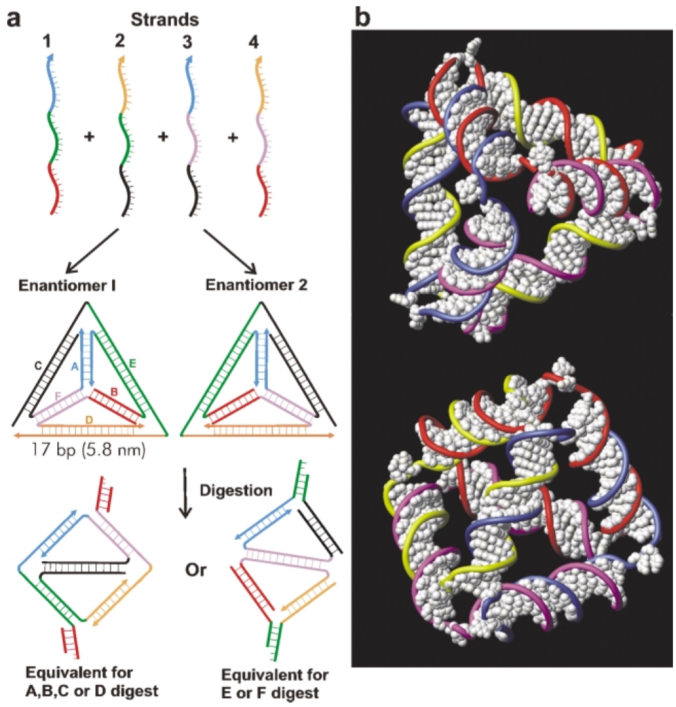

Figure 5.11 – DNA tetrahedron; (a) Synthetic scheme with the two possible enantiomers. (b) Computational model of the DNA tetrahedron. *Reproduced with permission from Goodman et al.*[38] *Copyright 2004 Royal Society of Chemistry.*

In this study, it was decided to incorporate one ferrocene unit into each of the four vertices of the DNA tetrahedron (Table 5.1) via automated solid-phase DNA synthesis (Figure 5.12). The ferrocene units would be located at the hinges, specifically in between the two bases that remain unhybridised during tetrahedron assembly. This was to ensure that enough flexibility would be retained at each of the vertices to accommodate an angle of 60° between adjacent edges. This approach created another way of spacing metal atoms within a DNA structure in a precise manner. As

far as we are aware, the synthesis of a ferrocene-modified tetrahedron would be unprecedented. The unmodified sequences were also to be made as a control (see Appendix).

Table 5.1 – DNA sequences of the Ferrocene modified Tetrahedron.

Strand	Oligonucleotide sequence
T-1	5′–ACATTCCTAAGTCTGAAAFcCATTACAGCTTGCTACACGAGAAG AGCCGCCATAGTA–3′
T-2	5′–TATCACCAGGCAGTTGACFcAGTGTAGCAAGCTGTAATAGATGC GAGGGTCCAATAC–3′
T-3	5′–TCAACTGCCTGGTGATAAFcAACGACACTACGTGGGAATCTACT ATGGCGGCTCTTC–3′
T-4	5′–TTCAGACTTAGGAATGTGFcCTTCCCACGTAGTGTCGTTTGTAT TGGACCCTCGCAT–3′

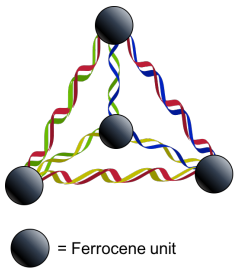

Figure 5.12 – Schematic representation of the ferrocene modified DNA tetrahedron.

5.4.1 Synthesis of Ferrocene-modified DNA Tetrahedron

The project begun by synthesising the ferrocene phosphoramidite (Figure 5.13) which was accomplished by Harry Dixon.[39] Following synthesis, it was incorporated into the four DNA tetrahedron strands (Table 5.1) via solid-phase DNA synthesis, with one modification in each strand.

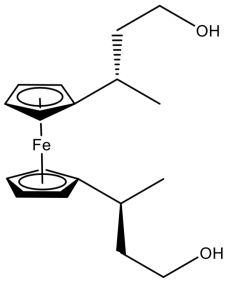

Figure 5.13 – Structure of FcHH (ss) modification incorporated into the DNA oligonucleotide strands. The ferrocene monomer synthesised by Harry Dixon.[39]

Several attempts were made to purify the ferrocene modified strands using HPLC. However, this proved to be very challenging due to the length of the oligonucleotides and the ferrocene modification making the chromatographic separation even more challenging, resulting in co-eluted peaks of n, n-1, n-2 etc., as confirmed by mass spectrometry. Figure 5.14 shows one of the attempts of Fc modified oligonucleotide separation using HPLC.

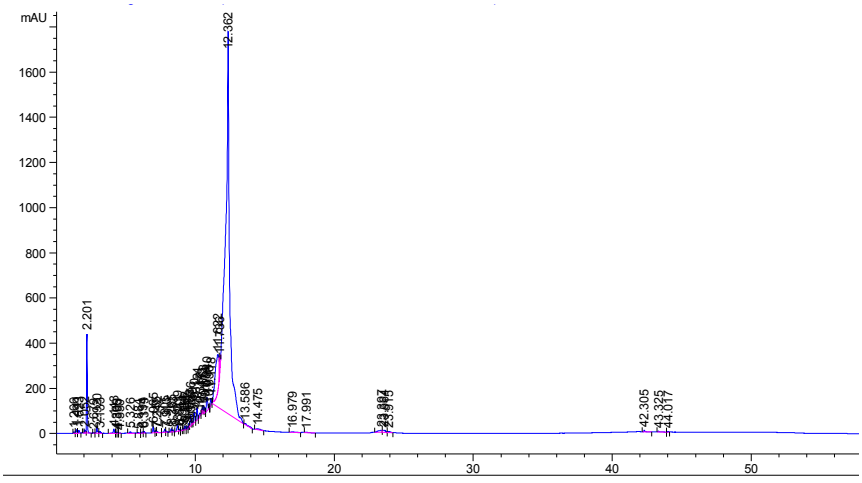

Figure 5.14 – Representative HPLC trace of an attempt of method development for Fc modified oligonucleotides. Conditions: Clarity RP HPLC column, 50 mM HFIP, 15 mM HA buffer, pH:7, 1.0 flow rate, 60^{o}C with a gradient 60% methanol over 10 minutes, 60-64% methanol over 2 minutes, 64% methanol over 10 minutes, 64-66% methanol over 2 minutes, 66-100% methanol over 6 minutes.

Therefore based on the literature[40] as well as advice from other DNA nanotechnology research groups, it was decided to use denaturing polyacrylamide gel electrophoresis instead for purification of the strands. This was accomplished using the protocol described in Chapter 7.2.3.

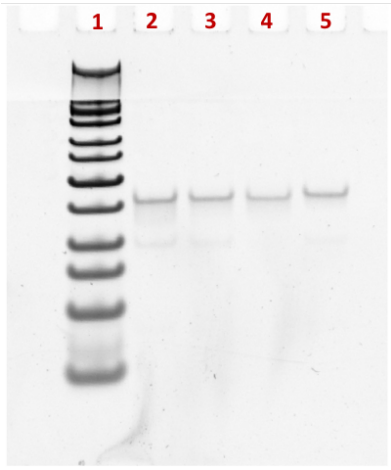

Figure 5.15 – A Diamond™ stained denaturing PAGE (stacking gel with resolving 15% polyacrylamide) visualised with UV light on AlphaImager HP system, 100V, 3h at room temp. Lane 1- 300 bp Ultra Low Range DNA Ladder; 2- Fc-T1 strand; 3- Fc-T2 strand; 4- Fc-T3 strand; 5- Fc-T4 strand. Concentrations of strands were 1 µM.

Denaturing gel electrophoresis studies show that the ferrocene-modified oligonucleotides could be achieved in high purity (Figure 5.15). These strands and their unmodified counterparts, were characterised by mass spectrometry with the expected masses being obtained (Appendix). The concentration was measured again by employing the Beer-Lambert law (Chapter 7.3.2). The ferrocene modified tetrahedron structures were then assembled by employing the buffer system and annealing time as established by the Turberfield group[38] and as described in Chapter

7.10. The assembly of the DNA tetrahedron had to be performed at low concentrations 15 nM - 100 nM. This was due to the resulting DNA misfolds at higher concentrations and generation of aggregates (multiple bands in native PAGE) which decreased the yield of the desired product. This adjustment to the original protocol was made after initial experiments involving the unmodified DNA tetrahedron assembled at high concentrations (Figure 5.16) as well as upon receiving advice from collaborators. In order to yield enough product for further experiments, it was necessary to produce the nanostructure in low concentrations and in large volumes (1-2 mL) and then concentrate the solution with a micro-centrifuge filter as described in Chapter 7.10.

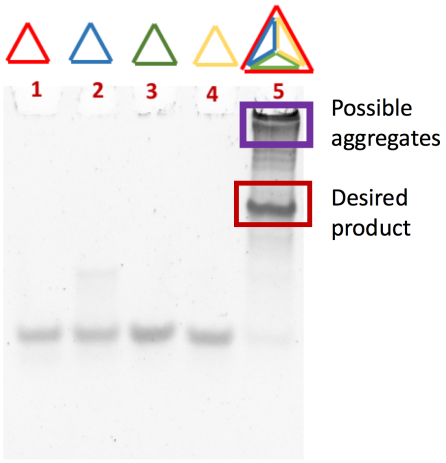

Figure 5.16 – A Diamond™ stained native 8% PAGE of DNA tetrahedron assembled at 1µM and visualised with UV light on AlphaImager HP system, 1 x TAMg buffer, 100 V, 1.5h at 4°C. Lanes 1–4: unmodified T-1, T-2, T-3, T-4 respectively; Lane 5: full assembly of unmodified DNA tetrahedron, showing possible aggregation.

5.4.2 Characterisation of ferrocene-modified DNA Tetrahedron

Native polyacrylamide gel electrophoresis was employed to verify the formation of the ferrocene-modified DNA tetrahedron, following the procedure detailed in Chapter 7.14.1. A range of hybridisation combinations were explored in order to confirm its successful formation, Figure 5.17.

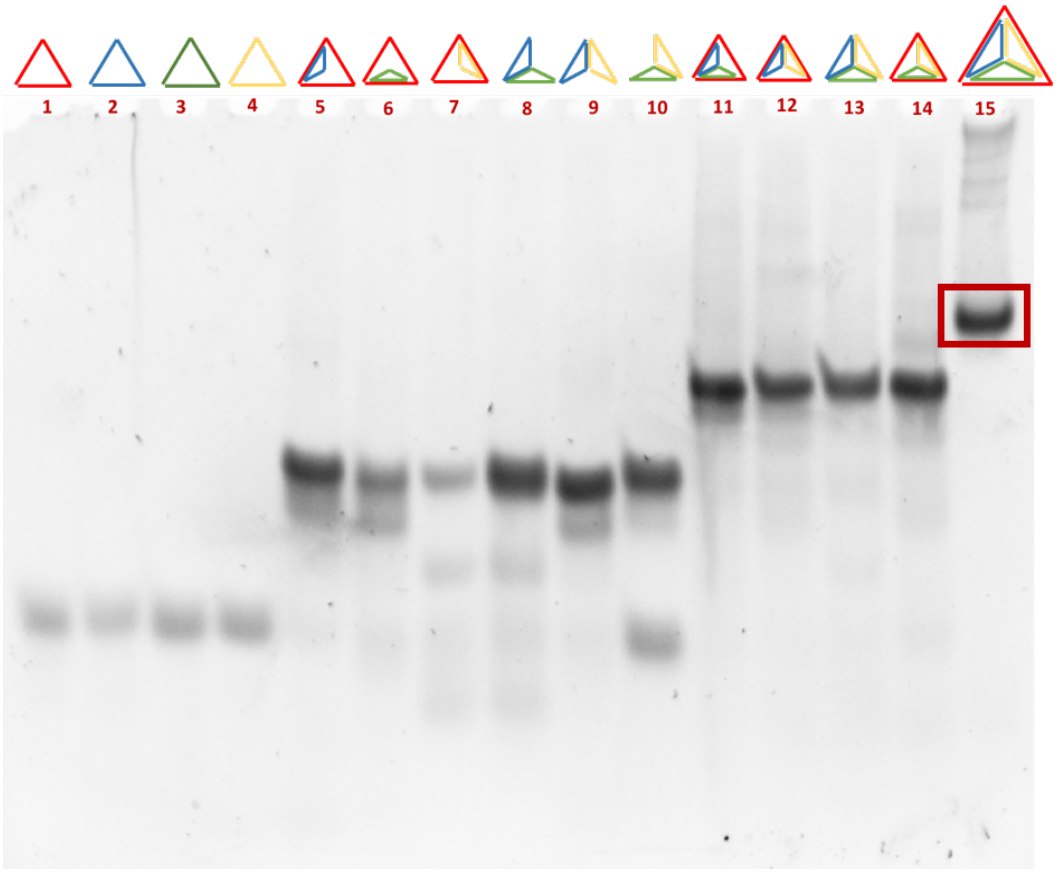

Figure 5.17 – A Diamond™ stained native 8 % PAGE visualised with UV light on AlphaImager HP system, 1xTAMg buffer, 100 V, 1.5h at 4°C. Lanes 1–4: T-1, T-2, T-3, T-4 respectively; Lane 5: Fc-T1, Fc-T2; Lane 6: Fc-T1, Fc-T3; Lane 7: Fc-T1, Fc-T4; Lane 8: Fc-T2, Fc-T3; Lane 9: Fc-T2, Fc-T4; Lane 10: Fc-T3, Fc-T4; Lane 11: Fc-T1, Fc-T2, Fc-T3; Lane 12: Fc-T1, Fc-T2, Fc-T4; Lane 13: Fc-T2, Fc-T3, Fc-T4; Lane 14: Fc-T1, Fc-T3, Fc-T4; Lane 15: full assembly of ferrocene-modified DNA tetrahedron. Concentrations of strands were 0.5 µM.

By exploring all possible combinations of the four DNA strands, it is possible to unambiguously state that the successful formation of the ferrocene modified DNA tetrahedron assembly has been accomplished, as is indicated by the lowest mobility band in lane 15, Figure 5.17. The result can be compared with the unmodified DNA tetrahedron gel results in Figure 5.16, as well as the literature results.[38] This proves that the combination of equimolar quantities of the oligonucleotide strands (Fc-T1 – Fc-T4) yields the desired product. This was not taken for further purification due to the satisfactory purity determined by gel electrophoresis.

Another technique used to study this system is AFM, however no conclusive data has been gathered so far. The difficulty of working with this system lies in the fact that the assembly has to be formed at low concentrations (15 nM or 100 nM). As outlined above, higher concentrations applied in the annealing step result in the formation of misfolded structures of higher molecular weight. This fact alone inhibits efficient production of the ferrocene DNA tetrahedron on a large scale. An alternative method for production of this assembly, for instance using buffer exchange, could generate higher yields.

5.5 Ferrocene modified Holliday Junction (Fc-DNA-Holl)

Successful results with the ferrocene-modified DNA tetrahedron study led to intend in exploring larger array-based systems. This was inspired by the work of Malo *et al.*,[41] who assembled 2D DNA arrays as detailed in Chapter 1.2.2.1. It was decided to

modify two strands in a four-way Holliday junction assembly with ferrocene units in such a way that each discrete Holliday junction would contain two ferrocene units positioned approximately in the middle of the structure (Figure 5.18). The ferrocene-modified strands, along with the unmodified oligonucleotides, would then form extended assemblies through the use of overhangs ('sticky ends'). The sequences are shown in Figure 5.19.

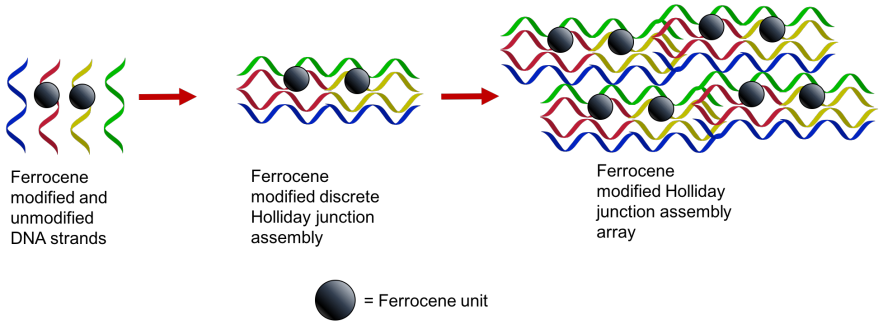

Figure 5.18 – Schematic illustration of the design of the Ferrocene modified Holliday junction assembly.

Strand	Oligonucleotide sequence
HJ-1	5'-CTAACTACATGCCTTFcGGACCGTTGTCTAC-3'
HJ-2	5'-GCGATGAGCAGGATAGTTAG-3'
HJ-3	5'-CACGAGGATTGCFcACTGTTCCGTCCTGCTCATCGC-3'
HJ-4	5'-GTAGACAACGGTCCAGAAGGCATGCGGAACAGTGAGCAATCCTCGTG-3'
HJA-1	5'-CTAACTACATGCCTTFcGGACCGTTGTCTACCTTAGC-3'
HJA-2	5'-GCGATGAGCAGGATAGTTAGAGTATC-3'
HJA-3	5'-CACGAGGATTGCFcACTGTTCCGTCCTGCTCATCGCGATACT-3'
HJA-4	5'-GTAGACAACGGTCCAGAAGGCATGCGGAACAGTGAGCAATCCTCGTGGCTAAG-3'

Ferrocene modified Holliday Junction Discrete:

5'-GTAGACAACGGTCCAGAAGGCATGCGGAACAGTGAGCAATCCTCGTG-3'
3'-CATCTGTTGCCAGGFcTTCCGTACGCCTTGTCAFcCGTTAGGAGCAC-5'
5'-CTAACTATCCTGCTCATCGC-3'
3'-GATTGATAGGACGAGTAGCG-5'

Ferrocene modified Holliday Junction Array:

5'-GTAGACAACGGTCCAGAAGGCATGCGGAACAGTGAGCAATCCTCGTGGCTAAG-3'
3'-CGATTCCATCTGTTGCCAGGFcTTCCGTACGCCTTGTCAFcCGTTAGGAGCAC-5'
5'-CTAACTATCCTGCTCATCGCGATACT-3'
3'-CTATGAGATTGATAGGACGAGTAGCG-5'

Figure 5.19 – Ferrocene-modified Holliday junction and Holliday junction array sequences (overhangs are underlined) and appearance upon assembly.

5.5.1 Synthesis of the ferrocene-modified duplex

The tetrahedron work had used a chiral ferrocene. However, in order to make the monomer synthesis easier and cheaper, it was decided to use an achiral derivative (Figure 5.20) for the Holliday junction work. However, first it was decided to examine the behaviour of this ferrocene unit in a duplex strand and to compare the results with the cisplatin-modified duplexes detailed in Chapter 4. Therefore, the sequences for the duplex formation were taken from Lippard work on cisplatin intrastrand duplexes described by Poklar *et al*.[42] The synthesis of the ferrocene phosphoramidite of the diol (Figure 5.20) was accomplished by Lily Baily following the established literature.[43, 44] It was then incorporated in the normal way into a DNA strand (Table 5.2) via automated solid-phase DNA synthesis (Chapter 7.2.1). A complementary strand (G20 target) was also synthesised, along with an unmodified G20 probe which replaced the ferrocene unit with two guanine bases, to act as a control.

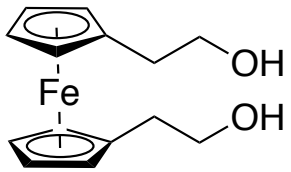

Figure 5.20 – Structure of FcHH (ss) modification incorporated into the DNA oligonucleotide strands. The ferrocene monomer was synthesized by Lily Baily.[45]

Table 5.2 – Sequences of the DNA oligonucleotides synthesized for the study of the duplex. Fc indicates ferrocene modification.

Oligonucleotide name	Oligonucleotide sequence
Fc G20 probe	5′–TCT CCT TCT Fc TCT CTT CTC–3′
G20 target	5′–GAG AAG AGA CC AGA AGG AGA–3′
G20 probe	5′–TCT CCT TCT GG TCT CTT CTC–3′

Following successful synthesis of the DNA oligonucleotides, they were purified by reversed-phase HPLC (Chapter 7.2.2) and characterised by mass spectrometry (Chapter 7.3.1). The results are presented in the Appendix, Figures 8.2.3, 8.2.4 & 8.2.14. The oligo concentration was measured via the standard procedure (Chapter 7.3.2) and calculated via the Beer-Lambert law, using a molar extinction coefficient for the ferrocene moiety as 3300 L Mol^{-1} cm^{-1}. Assembly of the ferrocene modified duplex and unmodified duplex control was accomplished according to the standard procedure and outlined in Chapter 7.6.

5.5.2 Characterisation of ferrocene-modified duplex

The first technique employed to study the ferrocene-modified duplex was native polyacrylamide gel electrophoresis. This was performed as stated in the standard protocol outlined in Chapter 7.14.1, and the results of this study are presented in Figure 5.21. The presence of new bands in lanes 4 and 5 indicate the successful formation of the ferrocene duplex as well as the unmodified duplex control. The higher mobility bands (lanes 1-3) correspond to single strands, which travel faster down the gel. There is not complete duplex formation under these conditions, as indicated by the appearance of the higher mobility bands in lanes 4 and 5.

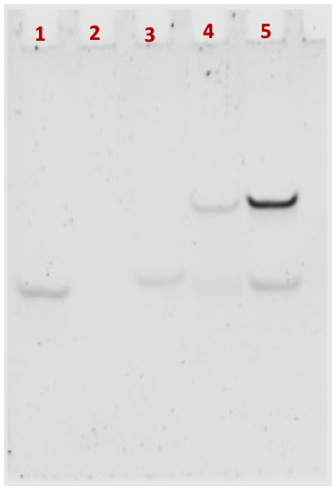

Figure 5.21 - A Diamond™ stained native 20% PAGE visualised with UV light on AlphaImager HP system, 1 x TBE buffer, 100 V, 3h at 4°C; Lanes: 1 – G20 target, 2 - Ferrocene G20 probe, 3 – G20 probe, 4 – Ferrocene G20 Duplex, 5 – G20 Duplex. Concentrations of strands were at 1 µM.

Interestingly, the expected band in lane 2 was not apparent following the staining step. This is attributed to the presence of ferrocene in the sample which affects the interaction with the Diamond dye, inhibiting it from being successfully imaged.

Next, spectroscopic techniques were employed in order to study the structure of the ferrocene duplex. UV/Vis spectroscopy and CD spectroscopy were used and the samples were measured in the standard buffer conditions (10 mM sodium phosphate and 100 mM sodium chloride buffer of pH 7 at room temperature). The results obtained are presented in Figure 5.22.

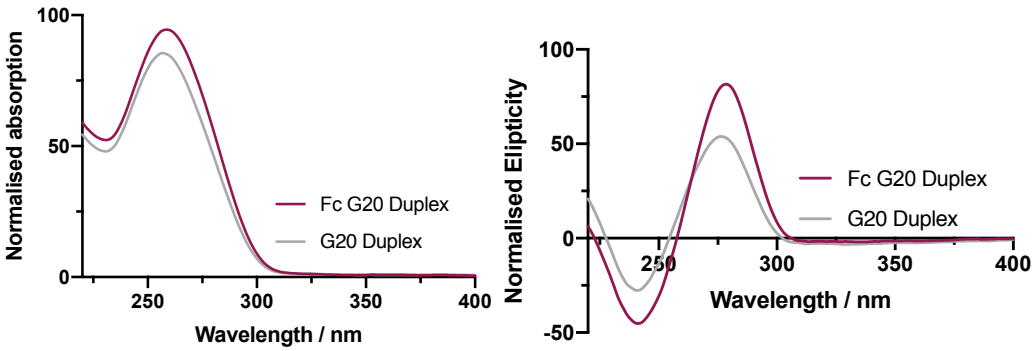

Figure 5.22 - Ferrocene G20 and G20 duplexes (10 µM) spectroscopic studies; UV/Vis spectra (left), CD spectra (right) in 10 mM sodium phosphate and 100 mM sodium chloride buffer, pH 7.0.

The UV/Vis spectrum study shows a small hyperchromic and bathochromic shift for the ferrocene modified duplex, indicating a slight disruption in structure caused by the ferrocene. This is consistent with the literature which shows that the absorbance intensity of hybridised DNA decreases (band at 260 nm) as the number of hydrogen bonding base-pair increases.[46] The ferrocene duplex contains two bases less than the unmodified duplex and therefore it exhibits a higher UV/Vis absorbance.

The circular dichroism results show the expected formation of B-DNA for both duplexes. An increase of the 280 nm band and a more defined band at 245 nm are evident in the ferrocene-modified duplex. These small changes suggest that ferrocene modification does not have a significant impact on the helicity of the modified DNA duplex.

The final technique used to characterise the ferrocene duplex was thermal melting. This technique was employed to establish the duplex stability and was accomplished

using the standard technique detailed in Chapter 7.13.2. The results are shown in Table 5.3.

Table 5.3 - Predicted and experimental results of melting temperature of the ferrocene and unmodified duplexes (10 µM) in 10 mM sodium phosphate and 100 mM sodium chloride buffer, pH 7.0.

Thermal melting run	Unmodified duplex	Ferrocene duplex
Predicted	63	-
1	69.0	47.0
2	69.0	47.0
3	69.5	47.5
σ	0.3	0.3

The discrepancy between the calculated and experimental melting temperature value is due to the interaction of the intercalating dye with the DNA, as described in Chapter 4 and the literature.[47] The melting temperature of the ferrocene duplex is lower than the unmodified duplex by 22 ^{o}C. This can be explained by the fact that there are two fewer base pairs in the ferrocene modified duplex than in the unmodified one. Nonetheless, the stability of the ferrocene modified duplex is satisfactory for potential applications at room temperature.

5.5.3 Synthesis of ferrocene-modified Holliday junction

Following the successful study of the ferrocene duplexes, it was possible to undertake the synthesis of ferrocene-modified Holliday junction nanostructures. Once again, solid-phase DNA synthesis was employed to synthesise the four oligonucleotide strands of the Holliday junction structure, with the red and the

yellow strands (Figure 5.19) having one ferrocene unit incorporation in each (Chapter 7.2.1). The four strands with the so-called “sticky ends” for the ferrocene-modified Holliday junction array were also synthesised in the same way. Each strand was purified by the reversed-phase HPLC (Chapter 7.2.2) and characterised by mass spectrometry (Chapter 7.3.1). The concentration was measured again by employing the Beer-Lambert law, with the Epsilon value for ferrocene unit being 3300 L mol^{-1} cm^{-1} (Chapter 7.3.2). The ferrocene modified Holliday junction structures as well as the array form were assembled using the procedures described in Chapter 7.8 & Chapter 7.9. The array structures were formed under an extended annealing time (72 hours) to allow for the thermodynamics of the reaction to pull the overhangs together to form the array.

5.5.4 Characterisation of discrete ferrocene-modified Holliday junction

The first technique employed to study the formation of the assembly was native polyacrylamide gel electrophoresis, following the procedure described in Chapter 7.14.1. The results are presented in Figure 5.23.

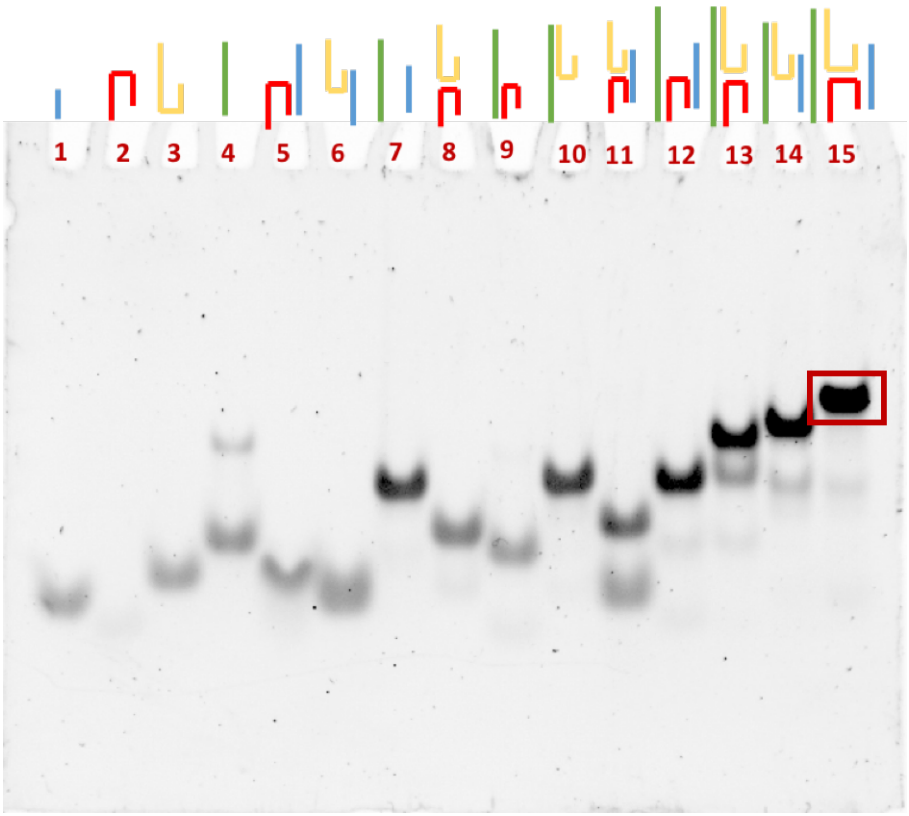

Figure 5.23 - A Diamond™ stained native 8% PAGE visualised with UV light on AlphaImager HP system, 1 x TAMg buffer, 100 V, 1.5h at 4°C. Lanes 1–4: HJ-1, HJ-2, HJ-3, HJ-4 respectively; Lane 5: HJ-1, HJ-2; Lane 6: HJ-1, HJ-3; Lane 7: HJ-1, HJ-4; Lane 8: HJ-2, HJ-3; Lane 9: HJ-2, HJ-4; Lane 10: HJ-3, HJ-4; Lane 11: HJ-1, HJ-2, HJ-3; Lane 12: HJ-1, HJ-2, HJ-4; Lane 13: HJ-2, HJ-3, HJ-4; Lane 14: HJ-1, HJ-3, HJ-4; Lane 15: full assembly of unmodified Holliday junction. DNA concentrations: 1 µM.

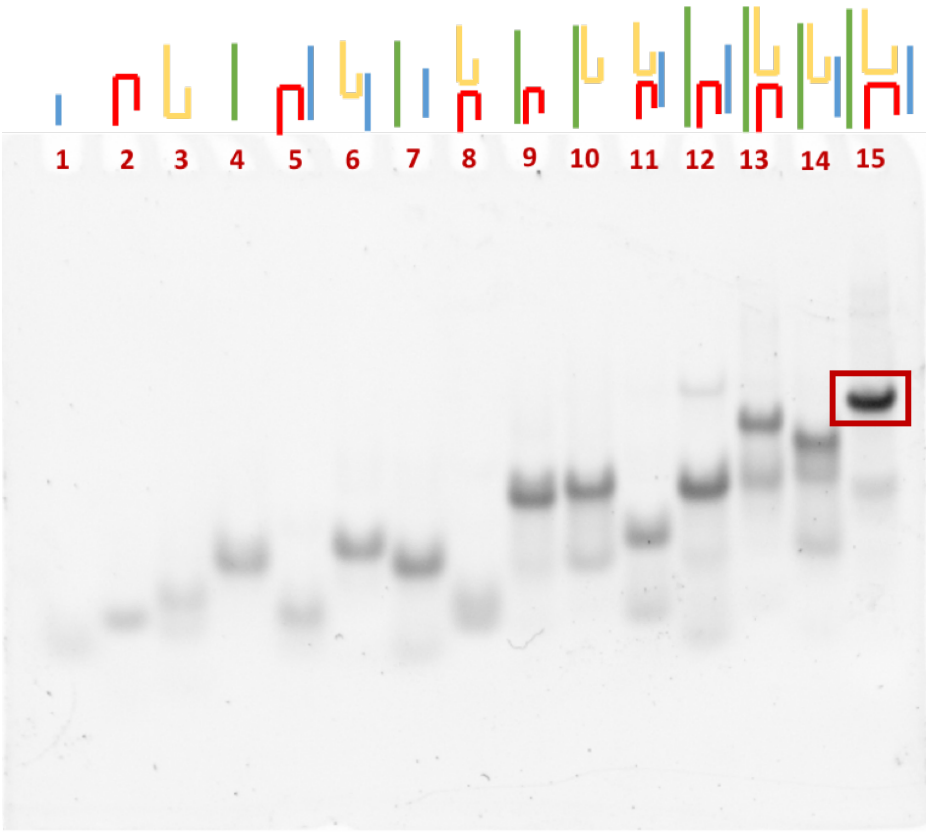

Figure 5.24 - A Diamond™ stained native 8% PAGE visualised with UV light on AlphaImager HP system, 1 x TAMg buffer, 100 V, 1.5h at 4°C. Lanes 1–4: HJ-1, HJ-2, HJ-3, HJ-4 respectively; Lane 5: HJ-1, HJ-2; Lane 6: HJ-1, HJ-3; Lane 7: HJ-1, HJ-4; Lane 8: HJ-2, HJ-3; Lane 9: HJ-2, HJ-4; Lane 10: HJ-3, HJ-4; Lane 11: HJ-1, HJ-2, HJ-3; Lane 12: HJ-1, HJ-2, HJ-4; Lane 13: HJ-2, HJ-3, HJ-4; Lane 14: HJ-1, HJ-3, HJ-4; Lane 15: full assembly of ferrocene modified Holliday junction. DNA concentrations: 1 µM.

It can be clearly seen from the results presented in Figure 5.23 that the ferrocene modified Holliday junction has been successfully assembled. This is evidenced by the lowest mobility in Lane 15, which compares well with the literature[41] and the unmodified system (Figure 5.24). Diamond stain, which is used to visualise the gel, is known to intercalate with the hybridised DNA to a larger extent,[48] resulting in darker and more defined bands. This means that the strongest band in lane 15 is a fully hybridised structure. Lane 12 contains a faint shadow, with the mobility comparable

to that of the full assembly. This might be explained by a possible “forking” of the structure, resulting in slowing its mobility down the gel. This band however, being very faint, can be neglected and regarded as merely a misfold.

Following the gel electrophoresis study, spectroscopic techniques were employed in order to study the ferrocene-modified Holliday junction. UV/Vis spectroscopy and CD spectroscopy were used and the samples were measured in the standard buffer conditions (annealing buffer: 10 mM $MgCl_2$/ 5 mM Tris-Cl/ 20 mM Tris acetate/ 1 mM EDTA buffer of pH 7 at room temperature). The results obtained are presented in Figure 5.25.

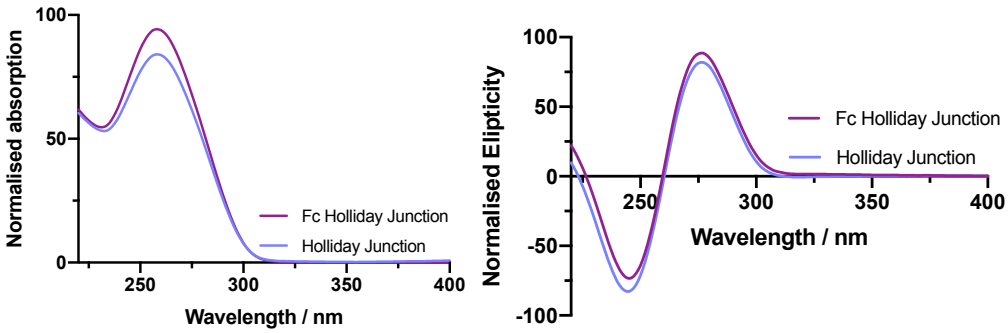

Figure 5.25 - Ferrocene Holliday Junction (10 µM) and unmodified Holliday junction (10 µM) spectroscopic studies; UV/Vis spectra (left), CD spectra (right) in 10 mM $MgCl_2$/ 5 mM Tris-Cl/ 20 mM Tris acetate/ 1 mM EDTA buffer, pH 7.0.

The UV/Vis spectra show the familiar hyperchromic shift for the ferrocene modified assemblies, but with the bathochromic shift less apparent. The CD spectra show an increase of intensities of the band at 280 nm and a less defined band at 245 nm. Once again, it can be concluded that the ferrocene containing system retains the B-DNA form but with a slight destabilisation in the structure.

Finally, thermal melting was employed to determine the stability of the ferrocene-modified assemblies. The experiments were conducted according to the established procedure detailed in Chapter 7.13.2, with the results presented in Table 5.4.

Table 5.4 - Predicted and experimental results of melting temperature of the ferrocene and unmodified Holliday Junction structures (10 µM), in 10 mM $MgCl_2$/ 5 mM Tris-Cl/ 20 mM Tris acetate/ 1 mM EDTA buffer, pH 7.

Thermal melting run	Unmodified Holliday Junction	Ferrocene Holliday Junction
1	74.5	66
2	75.5	66
3	75	66
σ	0.5	0

The thermal melting temperature of the ferrocene modified Holliday junction is lower than the unmodified structure by 9 ^{o}C. This can be explained due to the lack of hydrogen bonding at the ferrocene modification in two out of the four strands in the structure, with adenine and guanine being the opposite bases in both positions within the nanostructure. Nonetheless, the stability of the ferrocene Holliday junction structure was deemed satisfactory for the desired applications, being clearly stable at room temperature.

5.5.5 Characterisation of ferrocene-modified Holliday junction array

Upon successful characterisation of the discrete ferrocene Holliday junction assembly, it was necessary to determine whether the array structure could be formed via the “sticky ends” as found in the literature.[41] In order to characterise such

array assemblies thermal melting is employed. In this study, thermal denaturation was accomplished by monitoring the change in fluorescence of the intercalated dye (SYBR® green) in the DNA with change in temperature, resulting in melting curves of Relative Fluorescence Units (RFU) as a function of temperature. Detailed procedure of this study is described in Chapter 7.13.2, with the results presented in Figure 5.26.

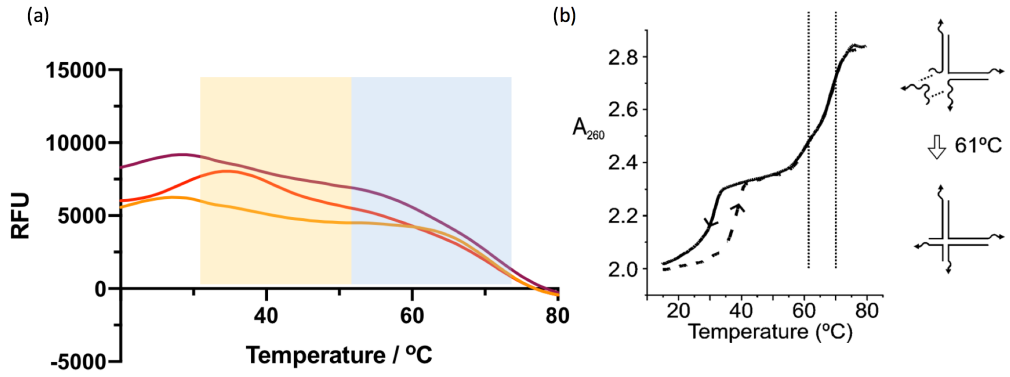

Figure 5.26 - Thermal melting curve of ferrocene-modified Holliday junction array (5 µM) in 10 mM $MgCl_2$/ 5 mM Tris-Cl/ 20 mM Tris acetate/ 1 mM EDTA, 2% Triton-100 buffer, pH 7; consisting of 3 repeats. The literature results of unmodified Holliday junction array are shown on the right here for comparison. *Reprinted with permission from Malo et al.*[41] *Copyright 2009 American Chemical Society.*

Two transition areas can be identified. The lower transition temperature (yellow) corresponds to the sticky ends being detached from one another whereas the higher transition temperature (blue), corresponds to the individual Holliday junction structures disassembling upon heating. The higher transition temperature (blue region) corresponds with the thermal melting data found for the discrete structures in Table 4. The melting curves seem to relate to the unmodified versions found in the literature (Figure 5.26).[41] However, thermal melting results alone are not enough to determine array formation. AFM imaging would be a suitable technique to

characterise this system and will be employed as part of the future work along with electrochemistry experiments.

5.6 Conclusions

The successful employment of ferrocene in higher ordered DNA frameworks has been demonstrated in this study. This has been achieved by applying standard automated solid-phase DNA synthesis to two phosphoramidite derivatives of ferrocene. Structures employed in this study were ferrocene modified duplexes, a discrete Holliday junction assembly, a Holliday junction array and a DNA Tetrahedron. The ferrocene-containing assemblies were verified by native polyacrylamide gel electrophoresis, confirmed by the lower mobility bands and matched unmodified runs. Moreover, spectroscopic techniques (UV/Vis and CD) were used to probe the structures of the assembly which consisted of B-DNA. Finally, thermal melting studies were employed to test the stability of the ferrocene containing structures, as well as to determine the formation of the Holliday junction arrays. In conclusion, ferrocene can be effectively employed as a source of iron atoms not only in duplex structures but also in extended arrays. As such the approach may present many opportunities for the application of such modified DNA structures where metal atoms are required at precise locations. In the future, additional work will be conducted to utilise electrochemistry for characterisation of these structures.

5.7 References

1. T. J. Kealy and P. L. Pauson, *Nature*, 1951, **168**, 1039-1040.
2. G. Wilkinson, M. Rosenblum, M. C. Whiting and R. B. Woodward, *J. Am. Chem. Soc.*, 1952, **74**, 2125-2126.
3. O. E. Fischer and W. Pfab, *Z. Naturforsch. B Chem. Sci.*, 1952, **7**, 377-379.
4. J. L. Kedge, University of Birmingham, 2017.
5. G. Wilkinson, *Org. Synth.*, 1963, **4**, 473.
6. R. B. Woodward, M. Rosenblum and M. C. Whiting, *J. Am. Chem. Soc.*, 1952, **74**, 3458-3459.
7. M. Roemer and C. A. Nijhuis, *Dalton Trans.*, 2014, **43**, 11815-11818.
8. V. Mamane, *Tetrahedron: Asymmetry*, 2010, **21**, 1019-1029.
9. D. Astruc, *Eur. J. Inorg. Chem.*, 2017, 6-29.
10. K. Park, S. B. Schougaard and J. B. Goodenough, *J. Adv. Mater.*, 2007, **19**, 848-851.
11. Y. Ding, Y. Zhao and G. Yu, *Nano Lett.*, 2015, **15**, 4108-4113.
12. Y. Zhao, Y. Ding, Y. Li, L. Peng, H. R. Byon, J. B. Goodenougha and G. Yu, *Chem. Soc. Rev.*, 2015, **44**, 7968-7996.
13. R. Deschenaux, E. Serrano and A.-M. Levelut, *Chem. Comm.*, 1997, **16**, 1577-1578.
14. J. Brettar, T. Bürgi, B. Donnio, D. Guillon, R. Klappert, T. Scharf and R. Deschenaux, *Adv. Funct. Mater.*, 2005, **16**, 260-267.
15. E. Peris, *Coord. Chem. Rev.*, 2004, **248**, 279-297.
16. S. Nlate, J. Ruiz, J.-C. Blais and D. Astruc, *Chem. Comm.*, 2000, 417-418.
17. C. Ornelas, J. Ruiz, C. Belin and D. Astruc, *J. Am. Chem. Soc.*, 2009, **131**, 590-601.
18. A. K. Diallo, C. Ornelas, L. Salmon, J. R. Aranzaes and D. Astruc, *Angew. Chem. Int. Ed.*, 2007, **46**, 8644-8648.
19. A. E. G. Cass, G. Davis, G. D. Francis, H. A. O. Hill, W. J. Aston, I. J. Higgins, E. V. Plotkin, L. D. L. Scott and A. P. F. Turner, *Anal. Chem.*, 1984, **56**, 667-671.
20. P. Köpf-Maier, H. Köpf and E. W. Neuse, *J. Cancer Res. Clin. Oncol.*, 1984, **108**, 336-340.
21. A. A. Simenel, E. A. Morozova-Lubov, V. S. Svetlana, I. Zykova, V. V. Kachala-Larissa, A. Ostrovskaya, N. V. Bluchterova and M. M. Fomina, *Appl. Organomet. Chem.*, 2009, **23**, 219-224.
22. S. Top, A. Vessières, G. Leclercq, J. Quivy, J. Tang, J. Vaissermann, M. Huché and G. Jaouen, *Eur. J. Chem.*, 2003, **9**, 5223-5236.
23. A.-L. Lainé and C. Passirani, *Curr. Opin. Pharmacol.*, 2012, **12**, 420-426.
24. H.-B. Kraatz, *J. Inorg. Organomet. Polym. Mater.*, 2005, **15**, 83-106.
25. J.-L. H. A. Duprey and J. H. R. Tucker, *Chem. Lett*, 2014, **43**, 157-163.
26. K. L. Dueholm, M. Egholm, C. Behrens, L. Christensen, H. F. Hansen, T. Vulpius, K. H. Petersen, R. H. Berg, P. E. Nielsen and O. Buchardt, *J. Org. Chem.*, 1994, **59**, 5767-5773.

27. A. Hess and N. Metzler-Nolte, *Chem. Comm.*, 1999, 885-886.
28. J. C. Verheijen, G. A. v. D. Marel, J. H. v. Boom and N. Metzler-Nolte, *Bioconjugate Chem.*, 2000, **6**, 741-743.
29. H. V. Nguyen, Z.-Y. Zhao, A. Sallustrau, S. L. Horswell, L. Male, A. Mulas and J. H. R. Tucker, *Chem. Comm.*, 2012, **48**, 12165-12167.
30. T. S. Zatsepin, S. Y. Andreev, T. Hianik and T. S. Oretskaya, *Russ. Chem. Rev.*, 2003, **72**, 537-554.
31. R. C. Mucic, M. K. Herrlein, C. A. Mirkin and R. L. Letsinger, *Chem. Comm.*, 1996, 555-557.
32. P. Mehrotra, *J. Oral Biol. Craniofac. Res.*, 2016, **6**, 153-159.
33. D. R. Thevenot, K. Toth, R. A. Durst and G. S. Wilson, *Biosens. Bioelectron.*, 2001, **16**, 121-131.
34. J. Wang, *Biosens. Bioelectron.*, 1998, **13**, 757-762.
35. T. Ihara, M. Nakayama, M. Murata, K. Nakano and M. Maeda, *Chem. Comm.*, 1997, 1609-1610.
36. F. Patolsky, Y. Weizmann and I. Willner, *J. Am. Chem. Soc.*, 2002, **124**, 770-772.
37. X. Wang, P. Dong, W. Yun, Y. Xu, P. He and Y. Fang, *Biosens. Bioelectron.*, 2009, **24**, 3288-3292.
38. R. P. Goodman, R. M. Berry and A. J. Turberfield, *Chem. Comm.*, 2004, 1372-1373.
39. H. Dixon, *Incorporation of Ferrocene into DNA for Biological Applications*, University of Birmingham, 2018.
40. Q. Zhang, H. Lv, L. Wang, M. Chen, F. Li, C. Liang, Y. Yu, F. Jiang, A. Lu and G. Zhang, *Int. J. Mol. Sci.*, 2016, **17**, 1-16.
41. J. Malo, J. C. Mitchell and A. J. Turberfield, *J. Am. Chem. Soc.*, 2009, **131**, 13574-13575.
42. N. Poklar, D. S. Pilch, S. J. Lippard, E. A. Redding, S. U. Dunham and K. J. Breslauer, *Proc. Natl. Acad. Sci.*, 1996, **93**, 7606-7611.
43. T. Ihara, D. Sasahara, M. Shimizu and A. Jyo, *Supramol. Chem.*, 2009, **21**, 207-217.
44. M. Ismail, Ph.D., University of Birmingham, 2018.
45. L. Baily, University of Birmingham, 2019.
46. M. M. Ackerman, C. Ricciardi, D. Weiss, A. Chant and C. M. Kraemer-Chant, *J. Chem. Educ.*, 2016, **93**, 2089-2095.
47. H. Gudnason, M. Dufva, D. D. Bang and A. Wolff, *Nucleic Acids Res.*, 2007, **35**, 1-8.
48. Promega, *Journal*, 2013, 8.

Chapter 6 – Anthracene DNA Nanostructures

6.1 Introduction

This chapter begins by introducing photochromism as well as compounds which exhibit photochromic properties. It also highlights the applications of such compounds. Moreover, the incorporation of photochromic groups in DNA is discussed and their impact on the structure of the DNA double helix. Following this, the anthracene chemical structure is described and its photodimerisation is detailed, along with its applications in supramolecular chemistry. The anthracene photodimerisation literature is then reviewed as well as its potential applications in biological systems and DNA self-assembly. Finally, a new approach for anthracene photo-dimerised DNA self-assembly, namely a Three Point Star is described and characterised.

6.1.1 Photochromism

Photochromism is defined as the reversible transformation of a chemical species induced by light, leading to an isomer having a different absorption spectrum, as well as distinct chemical and physical properties.[1] Photochromism has various applications in optoelectronics, including optical switching, optical memory and nonlinear optics.[2] The most well-known example of a photochromic compound is azobenzene which, in 1937 was found to undergo *trans* to *cis* isomerisation upon exposure to UV light (300-400 nm) by Hartley *et al.*[3] (Figure 6.1). This photo-induced reaction is reversible by applying heat or light with wavelengths longer than 400 nm.

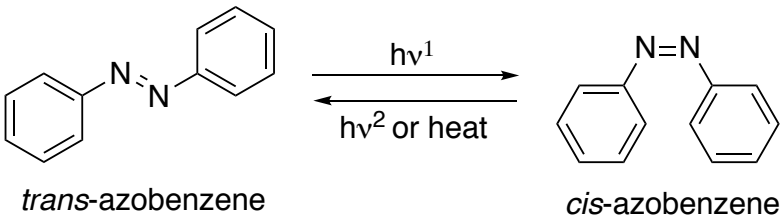

Figure 6.1 – Photo-induced *cis*/*trans* isomerisation of azobenzene.

Figure 6.2 shows further examples of photochromic compounds, for instance spiropyrans and spirooxazines which undergo photo-isomerisation to their merocyanine forms by cleavage of the C-O bond.[1] Applications of this class of compounds have been found in optical recording of data, light filters, photo-switches and multifunctional materials.[4] For example, spiropyran films containing rhodopsin have been developed for an increased level of photosignal.[5] Naphthopyrans are also an important class of photochromic compounds which have found an application in ophthalmic lenses and other plastic transparent materials due to their efficient change of colour upon UV irradiation.[6] Naturally occurring flavylium salts have also been shown to exhibit photochromic properties, with isomerisation taking place between flavylium salts and trans-chalcone, as studied by Wunscher *et al.*[7]

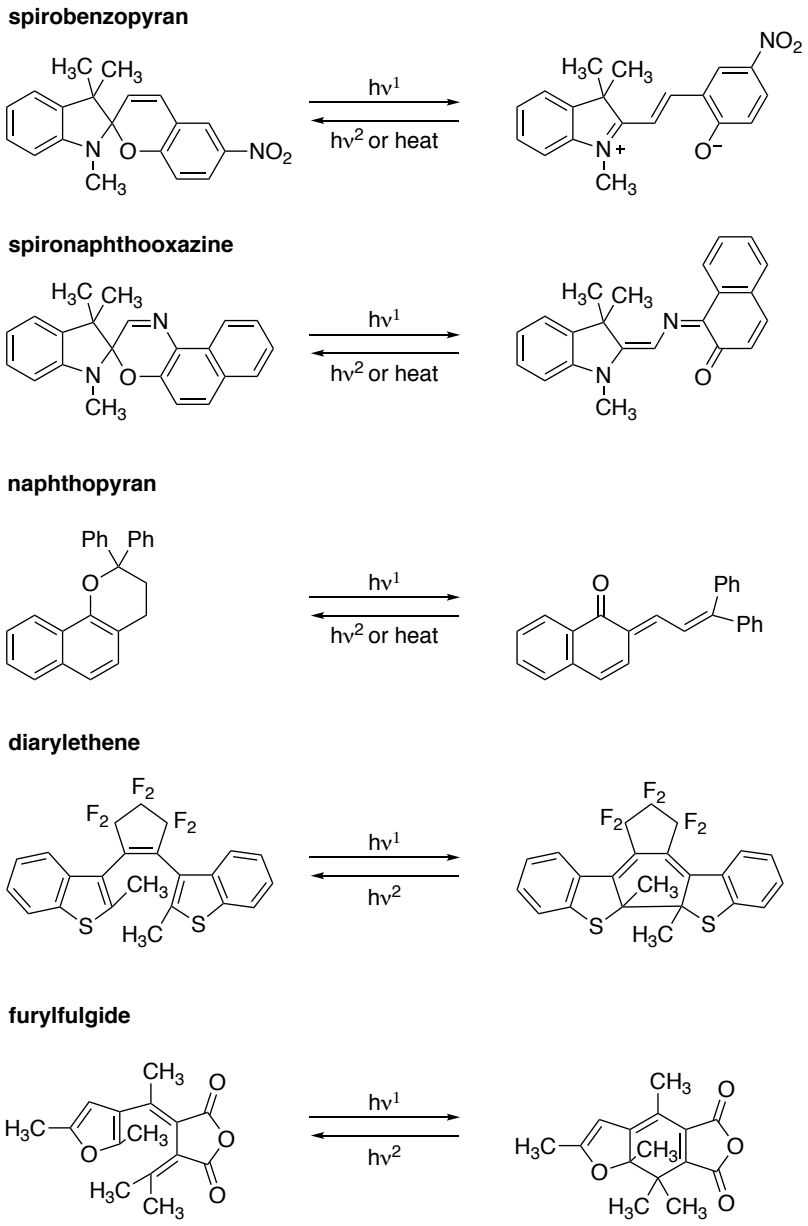

Figure 6.2 – Structures of photochromic compounds, adapted from Kobatake *et al.*[1]

Diarylethenes and fulgides belong to a photochromic category of compounds which are thermally irreversible, making them useful in applications requiring optical memory, optical switching and display.[8,9] Diarylethenes have been shown to exhibit excellent photochromic performance, namely thermal stability of up to 80 °C, giving fatigue resistance and desirable absorption spectra.

6.1.2 Photochromic groups in DNA

As the field of DNA nanotechnology has expanded along with its significance and applications,[10, 11] it has become important to investigate the possibility of incorporating photochromic groups into DNA. In order to do this without significantly destabilising the DNA duplex,[12] Kashida *et al.* utilised D-/L- threoninol to produce a wedge type insertion of azobenzene (Figure 6.3).[13]

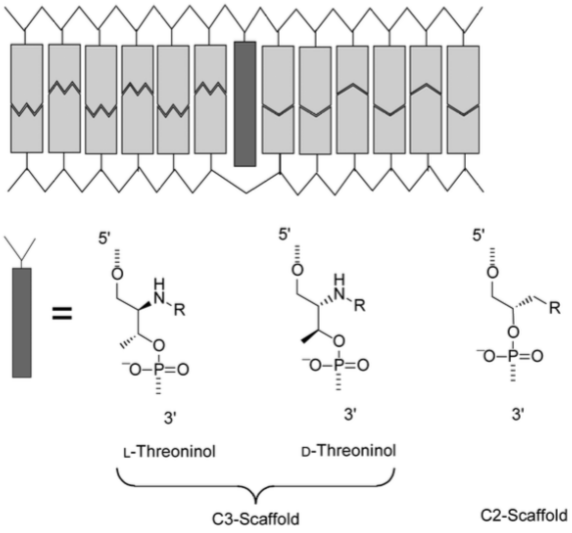

Figure 6.3 – Incorporation of D-/L- threoninol into DNA. *Reproduced with permission from Kashida et al.*[13] *Copyright 2009 Bentham Science Publishers.*

The researchers explored insertion of azobenzene via both isomers of threoninol using automated DNA synthesis. Upon duplex formation with a base-short complementary strand, the azobenzene was shown to be wedged into the cavity created by the threoninol insertion. Moreover, the D-isomer of the threoninol was found to stabilise the duplex more, which was explained by the right handed helicity of naturally occurring DNA.[13]

The effect of switching between the *trans* and *cis* forms of azobenzene on the stability of the DNA duplex was then investigated. It was found that the *trans* isomer stabilised the duplex as it was able to stack between the bases, whereas the *cis* isomer was destabilising due to steric hindrance (Figure 6.4).[13]

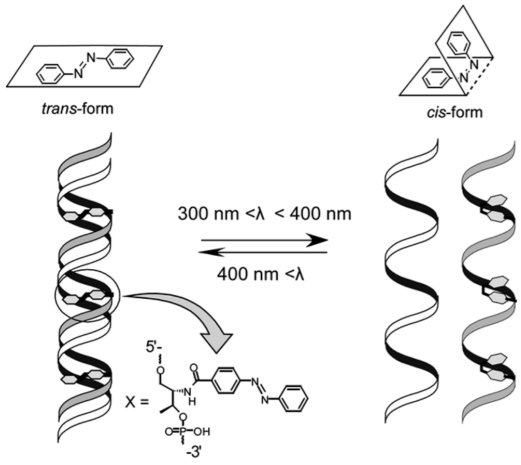

Figure 6.4 – Schematic representation of photo induced regulation of azobenzene modified DNA.

Reproduced with permission from Kashida et al.[13] Copyright 2009 Bentham Science Publishers.

Following the work of Kashida *et al.*, Maeda's group reported a new strategy for photo-regulation of DNA hybridisation through the synthesis of a photochromic nucleoside containing fluorenylvinyl group (Figure 6.5).[14] Circular dichroism studies confirmed no deviation from the usual B-DNA structure upon incorporation into a 20-mer strand. The studies focused on G-quadruplexes, with the modified guanine base incorporated into various positions of the thrombin binding aptamer. The group demonstrated successful photo-regulation of thrombin binding, thereby creating the possibility of constructing photo-controllable molecular machines using this technique.[15]

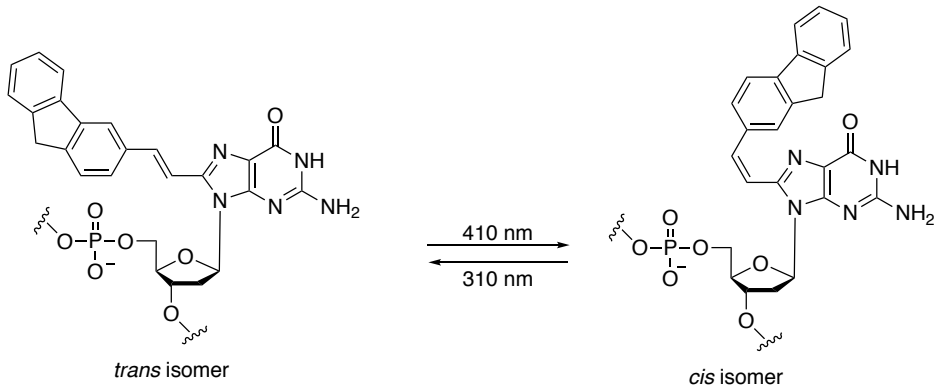

Figure 6.5 – *Cis-trans* isomerisation of 8-fluorenylvinyl-2'-deoxyguanosine by light, adapted from Ogasawara *et al.*[15]

Diarylethenes with photochromic properties have also been used to modify DNA components. A study by Singer *et al.*[16] involved modification of an adenine nucleotide with a diarylethene functional group which underwent photo-induced cyclisation (Figure 6.6). This system not only generated the highly coloured closed-ring isomer upon irradiation with UV light, but also exhibited recognition of complementary thymidine. As a result of this study, a molecular switch was developed which was able to react to both photochromic and acidichromic (by protonation with TFA) stimuli independently.[16]

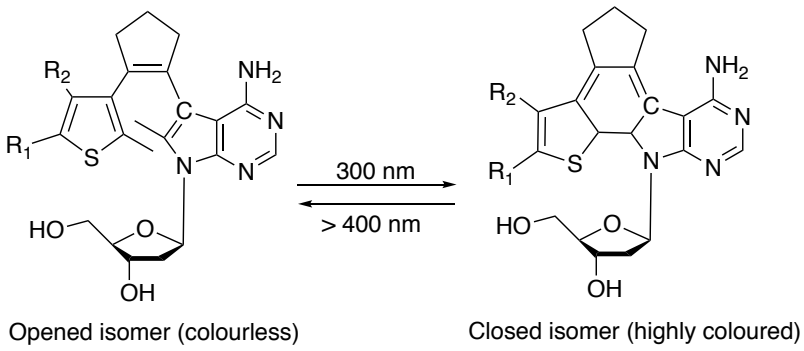

Figure 6.6 – Photo-isomerisation reaction of the diarylethene modified adenine nucleotide, adapted from Singer *et al.*[16]

In another study by the Jäschke group, a novel diarylethene DNA photoswitch was developed by post-synthetically reacting iodo-modified oligonucleotide with the photochromic group via Suzuki-Miyuara cross-coupling.[17] The results showed highly reversible photoswitching and high thermal stability of the diarylethene when part of DNA, with a negligible UV-induced change in the DNA conformation.[17]

6.1.3 Anthracene

Anthracene is an organic compound composed of three fused benzene rings with interesting photophysical and photochemical properties.[18, 19] This colourless compound exhibits a blue fluorescence under UV light. Anthracene photodimerisation is one of the oldest known reactions involving light, which was first observed in 1869.[20] It occurs upon excitation at 365 nm and in the presence of another anthracene, resulting in a 4π+4π photocycloaddition involving two covalent bond formations to create a photo-dimer (Figure 6.7).[21]

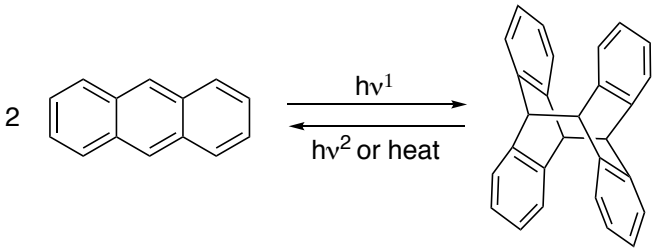

Figure 6.7 – Photochemical dimerisation reaction of anthracene.

Anthracene derivatives have been employed in many systems due to their desirable physical and chemical properties.[22] For instance, it has been used in synthesis of functional polymeric materials such as the one reported by Goto *et al.*[23] who

prepared a mesoporous organosilica from 9,10-bis(trialkoxysilyl)-anthracene via sol-gel condensation. In another study by Selinger, anthracene was used to make the first pH-responsive fluorescent sensor.[24] The VanZyl group synthesised molecular tweezers that bound electron-poor aromatic guests and, with the use of rigid spacers, enforced a syn-coplanar orientation of the anthracene chromophores.[25]

Anthracene is a desirable subunit for creating various covalent structures.[22] Linear anthracene structures can be prepared from anthraquinones and 9-lithioanthracenes[26] and from 2,6-anthrylene via Suzuki-Miyaura coupling[27]. Anthracene can also be used to create branched structures as demonstrated by Tamao group, who used three or more anthracene fluorophores to produce a fluoride chemosensor.[28] Similarly, anthracene has been used to generate conjugated macrocycles (Figure 6.8).[29] For example, a macrocycle made with 9,10-diethynyl-anthrylenes and m-ethynyl-phenylene was made with an inner diameter of 1.6 nm.[30] Another study by Miki *et al.*[31] demonstrated macrocycle formation through reductive aromatisation of dihydroanthrylene. A triangular macrocycle was produced by Chen *et al.*[32] and so-called Molecular Eyeglasses, consisting of twin-macrocycles, were designed by the Ohe group[33].

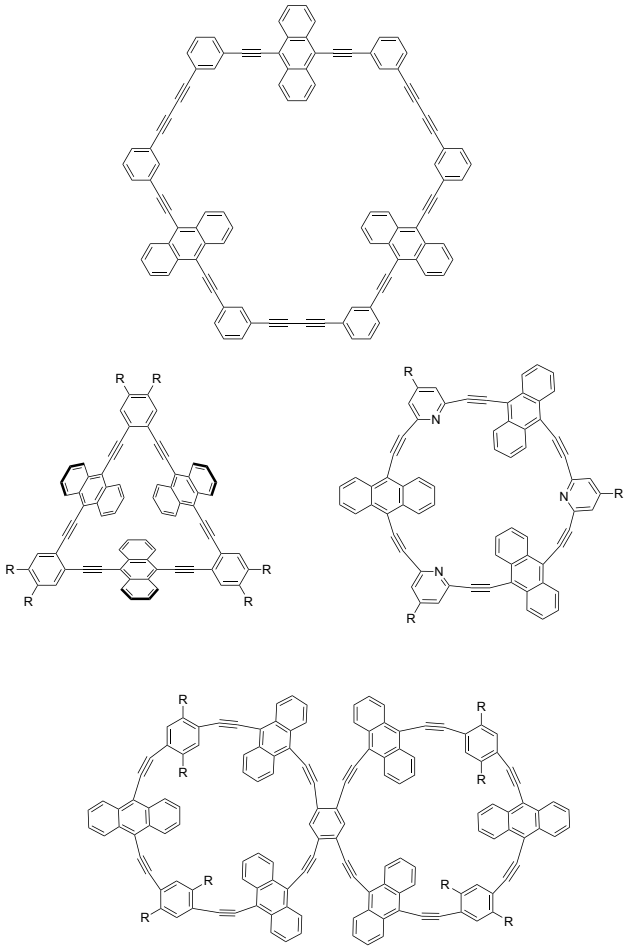

Figure 6.8 – Examples of 9,10-Anthrylene-acetylene macrocycles, adapted from Yoshizawa *et al.*[22]

Anthracene has been able to enrich supramolecular chemistry with its properties. The Raymond group was the first to synthesise anthracene-modified coordination cages.[34] Upon addition of Ti (IV) or Ga (III) into the 2,6-anthrylene biscatechol ligands, an M_2L_3 triple helicate formed, which then transformed into an M_4L_6 tetrahedral capsule (Figure 6.9a).[35] In another study by Tidmarsh *et al.*,[36] a large octanuclear cage was developed from anthracene with attached bidentate pyrazolyl-pyridines and flexible methylene hinges.

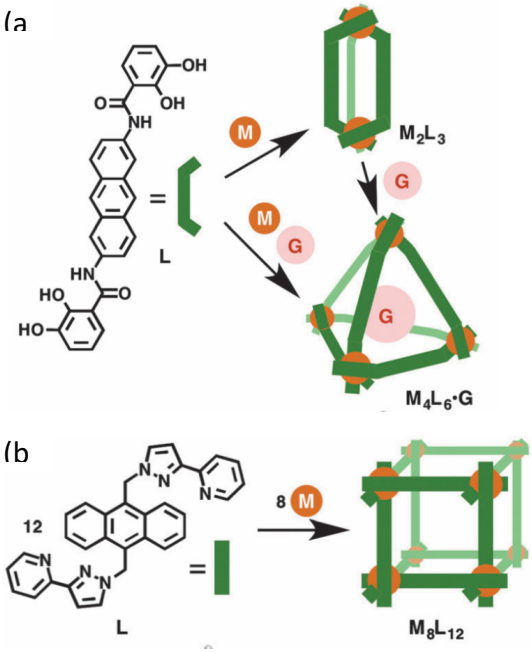

Figure 6.9 – (a) Synthesis scheme of the M_2L_3 helicate and M_4L_6 tetrahedral capsule; (b) Synthesis scheme of octanuclear coordination cages. *Reproduced with permission from Yoshizawa et al.*[22] *Copyright 2013 Royal Society of Chemistry.*

6.1.4 Anthracene-modified DNA oligonucleotides

The well-established and inherent photo-induced dimerisation properties of anthracene have led to exploration of its use in coupling reactions, for instance in polymers to create block co-polymers, as shown by Goldbach *et al.*[37] Another example of such an approach is in DNA ligation, due to the great interest in exploring the effect of joining ends of DNA together through non-enzymatic means. Photoligation presents many advantages to this process such as low cost, the no need for additives and the ability to control a reaction using a specific wavelength.[38]

Ihara and coworkers[38] pioneered in the field of anthracene DNA photoligation by attaching an anthracene group at the end of an array of oligonucleotides and probing

it for photodimerisation. This design had to ensure close proximity of the anthracenes and special alignment for the photodimerisation reaction to occur. The photoadducts were identified by mass spectrometry and HPLC analysis. Moreover, the group was able to isolate the adducts and test them using a thermal melting study which showed an increased stability upon photo-dimer formation by 13.6^{o}C.[38]

The aforementioned proof of concept study led the group to explore this area in more detail in various systems such as in formation of hairpins and DNA triple helices.[39] The results of their studies showed a remarkable increase in the melting point of a dimerised hairpin by 43.8 ^{o}C, greatly stabilising the structure. Furthermore, the DNA triplex formed by a Hoogsten base-pairing was shown to provide an additional third strand that was able to switch the strand to which it was bound.[39] The researchers were therefore able to achieve reactions that a ligase enzyme could not catalyse.

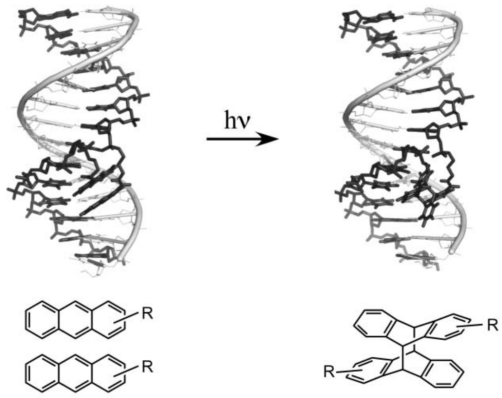

Figure 6.10 – Photo induced ligation reaction of DNA via anthracene dimerisation. *Reproduced with permission from Mukae et al.[39] Copyright 2009 Royal Society of Chemistry.*

Arslan and co-workers explored the possibility to apply anthracene dimerisation to SNP (single nucleotide polymorphism) sensing and were able to study the effect of the mismatch position on the photochemical ligation reaction. As expected, the presence of mismatches caused a reduction in the efficiency of the photodimerisation reaction, meaning that if two different bases were at the polymorphism location in the ligation site, the varying rate of the photoligation reaction would result in SNP detection.[40]

The Tucker group[41] incorporated two anthracene monomers into an oligonucleotide strand to investigate the effect of photodimerisation on duplex formation. The results showed successful formation of an intra-strand dimer (Figure 6.11) upon exposure to a 365 nm light, as indicated by HPLC and mass spectrometry. Moreover, thermal reversion studies were subsequently undertaken and resulted in the photodimer fully reverting back to the open undimerised form. Thermal melting, circular dichroism and gel electrophoresis studies were conducted which revealed that the stability of a duplex formed between the anthracene-modified strand and a complementary unmodified sequence could be controlled by light. Ultimately, it was shown that this anthracene DNA system exhibited a gated switching, in that upon addition of one strand photochromism was inhibited, however addition of a competing strand unlocked the system, allowing photodimerisation to re-occur.[41] Recent work on a related aptamer system demonstrated photo-switched thrombin binding and catalysis.[42]

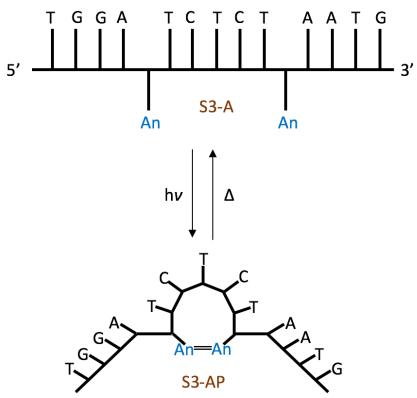

Figure 6.11 – Intrastrand photochromic system with a Head-to-Tail anthracene photo-dimer, adapted from Manchester *et al.*[41]

In a related study by Bullen *et al.*[43] an anthracene photodimerisation system was explored in conjunction with a peptide-DNA assembly. Each of the two peptides were modified with anthracene and DNA target strands were synthesised. Four different scenarios were investigated to probe for peptide dimer formation (Figure 6.12). The first one showed no dimer formation upon photo-irradiation of the two anthracene-modified peptides alone. The second one explored a non-specific DNA sequence to assist the dimer formation, however there was no dimer formed upon photo-irradiation. Even a half-target sequence was explored for assisting the dimer formation but unsuccessfully. Only the final scenario involving a full target sequence allowed for successful dimer formation.[43] The dimerisation was tested using fluorescence and SDS PAGE which concluded that this system could be used for formation of peptide dimers. However, the need for the DNA to assist this dimer was required in order to allow the anthracene molecules to come into close proximity for the photo-reaction to take place.

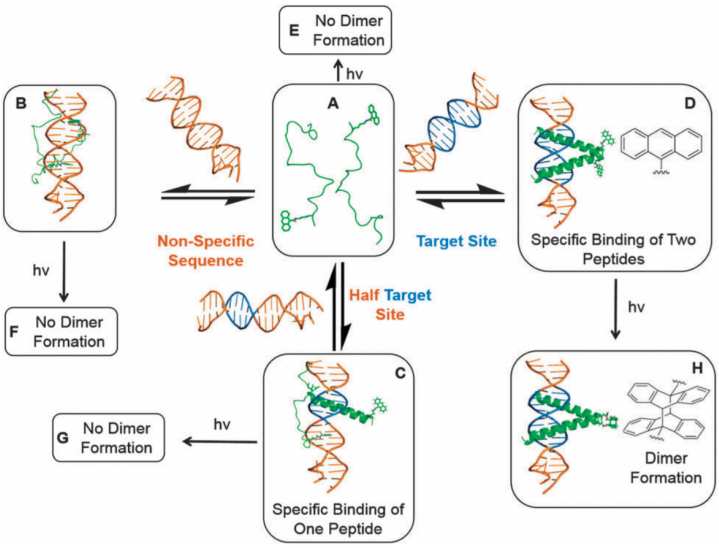

Figure 6.12 – Four approaches to the sequence-selective photodimerisation of anthracene modified peptide, *reproduced from Bullen et al.*[43] *Copyright Creative Commons Attribution 3.0.*

Another study by Pasternak *et al.*[44] showed a successful photoligation of DNA using an anthracene modified 2'-amino-LNA nucleotide. 9-Methylanthracene 2'-amino-LNA phosphoramidite was synthesised and incorporated into the oligonucleotides via automated solid phase DNA synthesis. The photoligation experiments involved linking two anthracene modified monomers, which was verified by UV/Vis spectroscopy as well as ion exchange HPLC.[44]

In yet another study by Ackermann *et al.*,[45] anthracene modified oligonucleotides were used to self-assemble dsDNA nanocircles. This was accomplished by hybridising a bis-anthracene modified 21-mer strand into a 168-mer dsDNA nanocircle containing a complementary strand. This system was studied by AFM microscopy to confirm the unspecific assembly of DNA circles.[45] This study has proven the

possibility of using intercalation of anthracene as a means of assembling higher order structures from subunits.

Anthracene has also been used to make a two-dimensional polymer assembled from a DNA network and covalently linked by means of anthracene photodimerisation.[46] This was accomplished by synthesising a branched oligonucleotide with a benzene core and three identical self-complementary oligonucleotides (Figure 6.13). This was shown to result in a 2D superstructure which brings the anthracene molecules close together, allowing for the dimerisation to take place and ultimately form a 2D polymer. This material was studied by AFM imaging as well as UV/Vis spectroscopy to verify the anthracene conversion into dimers.[46]

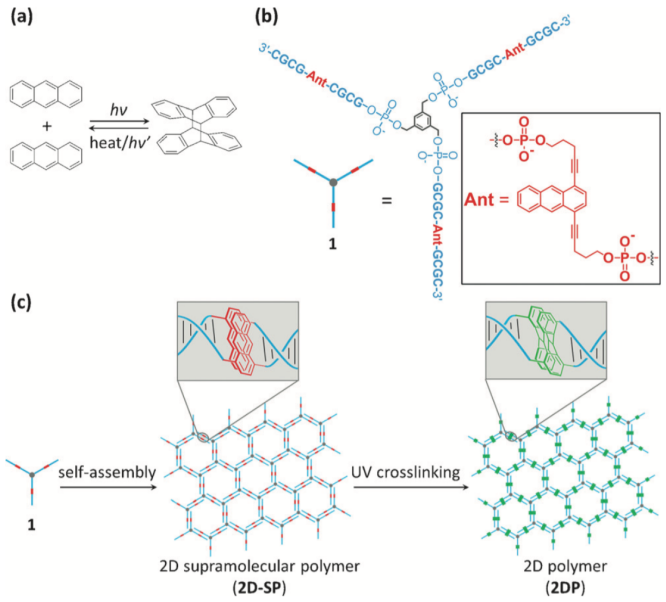

Figure 6.13 – Self-assembly of a 2D polymer; (a) anthracene dimerisation, (b) anthracene modified building block, (c) Formation of a 2D polymer. *Reproduced with permission from Yu et al.*[46] *Copyright 2017 John Wiley and Sons.*

6.2 Project aims

The aim of this project was to produce a discrete and robust DNA self-assembly mediated by anthracene photodimerisation that would be able to withstand denaturing conditions. This was to be accomplished by employing a known self-assembled DNA structure, namely a Three Point Star (3PS) and functionalising two of the three oligonucleotide building block units with two anthracene molecules in each strand. The specific locations of the anthracene molecules would ensure the successful photocyclisation necessary to covalently link the assembly and thus making it stable to denaturing conditions. Denaturing polyacrylamide gel electrophoresis would be employed to verify the stability of the structure.

6.3 Design of the Anthracene Three Point Star

The design of the Three Point Star DNA assembly was inspired by the work of Avakyan *et al.*[47] who explored assembling DNA arrays on supported lipid bilayers for cellular recognition, plasmonics or light harvesting applications. The Three Point Star assembly is shown in Figure 6.14, and consists of a template strand (S1) of a specific sequence and two complementary sequences (S2 & S3) which bind to an internal template in three positions. The assembly is formed by combining the three strands S1:S2:S3 in a ratio 1:3:3.

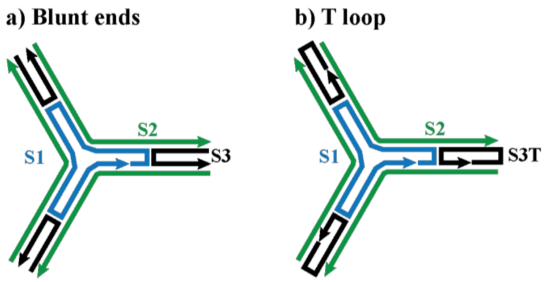

Figure 6.14 – Schematic structure of the Three Point Star assembly: (a) discrete assembly with blunt ends, (b) unit of an array with T loop ends. *Reproduced with permission from the Supplementary Information of Avakyan et al.*[47] *Copyright 2017 American Chemical Society.*

The work presented in this chapter is the result of a collaborative project with the Sleiman group and aims to reinforce the structure developed by Avakyan *et al*. with covalent adducts formed by anthracene photo-dimers (Chapter 6.4). This was done by incorporating anthracene units into the S2 and S3 strands in such a way that each anthracene tag in the S2 strand could pair up and form a photo-crosslink with an anthracene in the S3 strand (Figure 6.15).

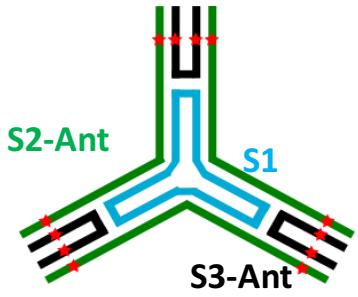

Figure 6.15 – Schematic structure of the Anthracene Three Point Star (3PS) assembly with antharecene modification shown in red.

6.3.1 Synthesis of anthracene phosphoramidite

The anthracene phosphoramidite **6,** as shown in Scheme 1, was the target molecule since it provides the desired functionality to the oligonucleotide and is compatible

with automated DNA synthesis (Chapter 2.1). The process of synthesising this anthracene molecule (**6**) and incorporating it into DNA strands has already been developed within the Tucker group and was used again for this study.[48] All intermediate products in the scheme (Scheme 6.1) were characterised using ^{1}H NMR, ^{13}C NMR and mass spectrometry with ^{31}P NMR additionally used to characterise the phosphoramidite target molecule **6**.

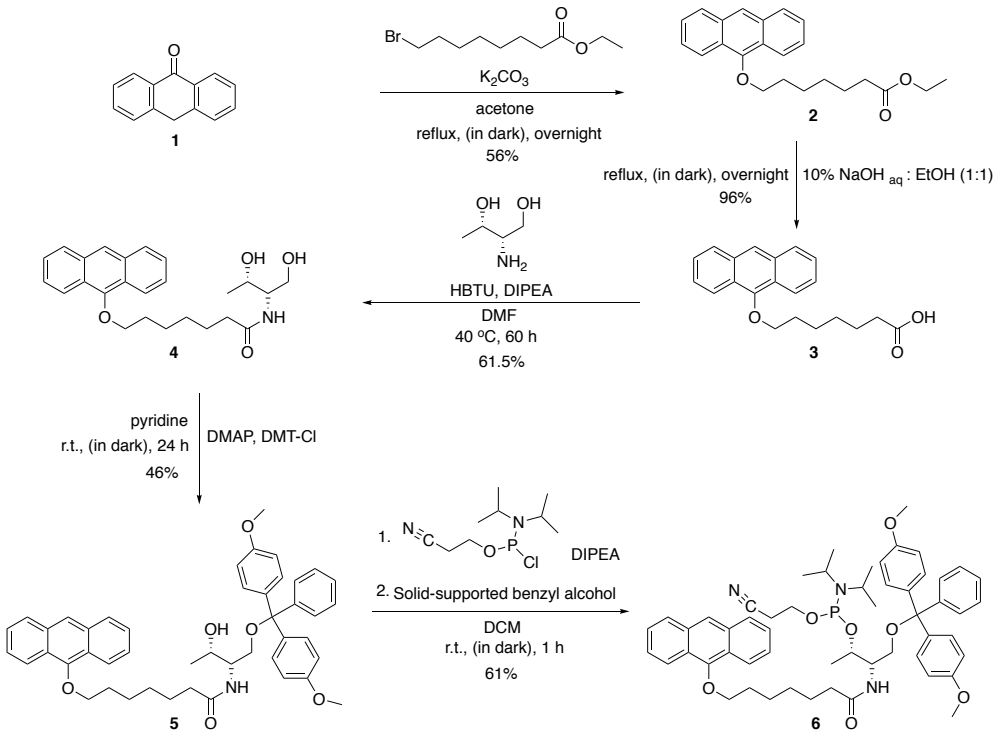

Scheme 6.1 – Synthetic scheme of anthracene phosphoramidite (6) from anthrone (1).

As the compounds were sensitive to both light and water, the reactions were carried out in the dark and under an inert atmosphere. The target molecule **6** was used immediately for the DNA synthesis in order to ensure the best coupling efficiency.

6.3.2 Assembly of anthracene Three Point Star

The relevant DNA oligonucleotide sequences containing the anthracene tag were synthesised via automated DNA synthesis (Chapter 7.2.1) and then purified using RP-HPLC (Chapter 7.2.2) and analysed by mass spectrometry (Chapter 7.3.1). The unmodified sequences were supplied by Avakyan *et al.*[47] All the sequences used in this study are presented in Table 6.1.

Table 6.1 - Unmodified and Anthracene modified Three Point Star assembly sequences.

Strand	Oligonucleotide sequence
S1	5′–AGGCACCATCGTAGGTTTCTTGCCAGGCACCATCGTA GGTTTCTTGCCAGGCACCATCGTAGGTTTCTTGCC–3′
S2	5′–ACTATGCAACCTGCCTGGCAAGCCTACGATGGACACGGTAACG–3′
S3	5′–CGTTACCGTGTGGTTGCATAGT–3′
S2-Ant	5′–ACTA**Ant**GCAACCTGCCTGGCAAGCCTACGATGGACACGG**Ant** AACG–3′
S3-Ant	5′–CGTT**Ant**CCGTGTGGTTGC**Ant**TAGT–3′

The sequences were then assembled into the desired Three Point Star assembly according to a standard protocol described in Chapter 7.12.1. Due to the design of the assembly, it was important to find an optimum ratio of the S1 strand to the S2 and S3 in order to yield the most product. This was found to be 1:4:4 (S1:S2:S3 respectively) as opposed to the 1:3:3 for the unmodified assembly (see Section 6.6).

6.3.3 Photocyclisation of the anthracene Three Point Star

Successful annealing of the assembly allowed for the anthracene molecules contained within the DNA strands to come into close proximity for the photocyclisation reaction to take place. The photo-irradiation of the samples was originally accomplished using a 365 nm wavelength lamp in the Sleiman lab in McGill

(Montreal). However, this protocol was later improved by addition of a 365 nm bandpass filter (Edmundoptics) and degassing of the solution prior to irradiation to further minimise the possibility of DNA degradation. The details of both protocols are described in Chapter 7.12.2.

6.4 Thermal melting studies

Thermal melting gives a good indication of DNA duplex stability. This technique was employed here to study the stability of the anthracene 3PS assembly and to compare it with the unmodified structure. The details of the thermal melting protocol are given in Chapter 7.13.2 and the results are presented in Figure 6.16.

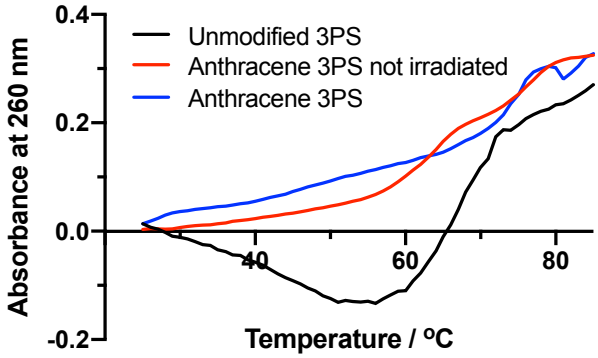

Figure 6.16 – Thermal melting curves of: unmodified 3PS assembly (S1:S2:S3 = 1:3:3), anthracene 3PS assembly before photocyclisation (S1:S2:S3 = 1:4:4), and anthracene 3PS assembly after 30 minute photocyclisation (S1:S2:S3 = 1:4:4). Concentration of the S1 strand was 375 nM. The buffer system was 1 x TAMg.

The results presented in Figure 6.16 show two transition temperatures: 66.7 ^{o}C and 71.5 ^{o}C for the unmodified assembly and similarly two transition temperatures: 64.3 ^{o}C and 77.6 ^{o}C for the anthracene modified assembly. This result is partially

consistent with the literature[49] which states that intercalation of anthracene stabilises DNA duplexes. Interestingly, the photo-irradiated anthracene modified assembly shows only one transition temperature of 76.6 ^{o}C. The lack of a lower transition temperature suggests that the shorter sequences bound by anthracene crosslinks after photocyclisation are held together strongly and the full assembly only comes apart when the heat starts to denature the photo-dimers, giving rise to only one melting temperature.

6.5 Atomic Force Microscopy imaging

AFM imaging in liquid mode was accomplished in the Sleiman group by Pongphak Chidchob (Chapter 2.7). The success of this technique relies upon successful anchoring of the DNA assemblies upon the mica surface, which is used as a support for the sample to be imaged. Nickel cations are used to balance the negative charge of the mica and the negative charge of the DNA phosphate backbone. Another challenge upon imaging in liquid mode is that the DNA structure tends to drift off from the imaged surface square while the image capture is in process, resulting in failed images. Some of the best images acquired are presented in Figure 6.17.

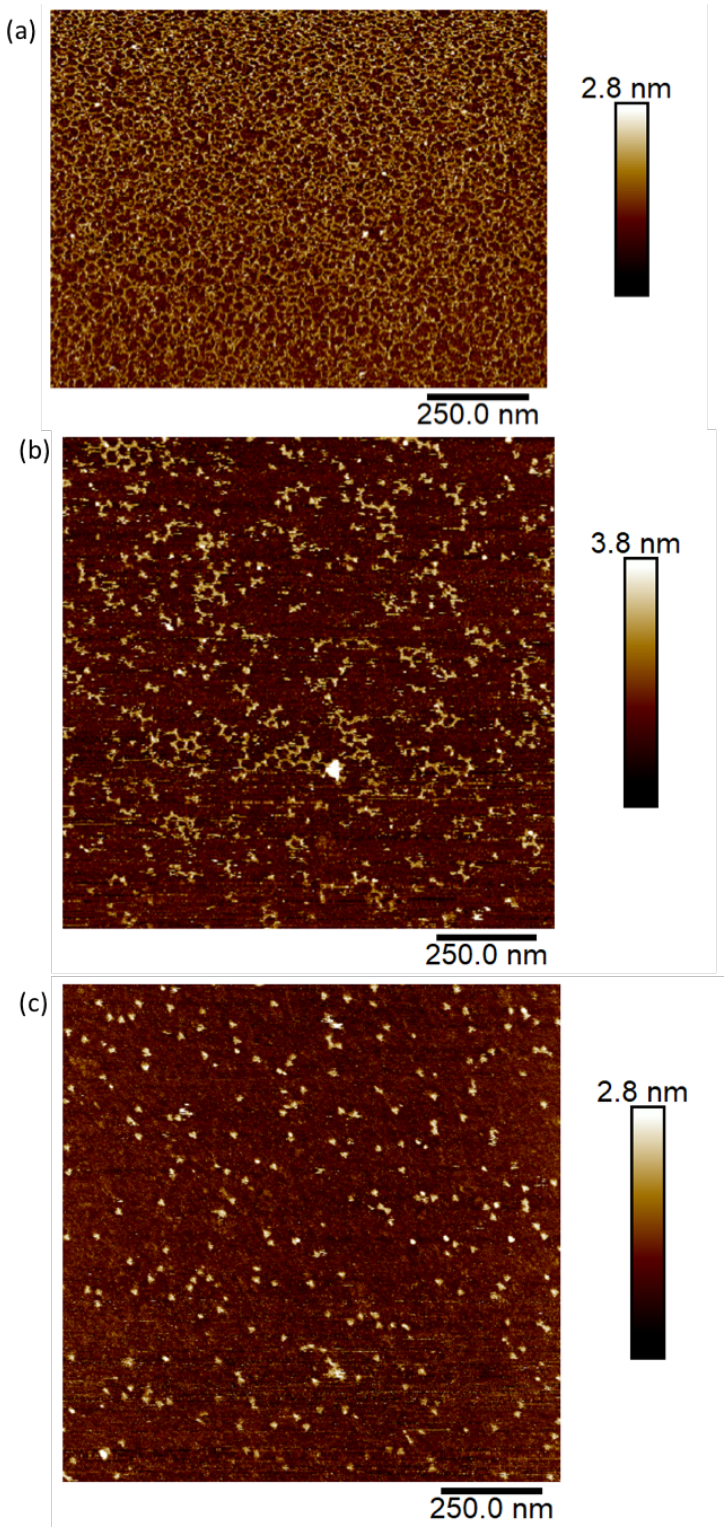

Figure 6.17 – AFM images of (a) unmodified 3PS assembly (S1:S2:S3 = 1:3:3), (b) anthracene 3PS assembly (S1:S2:S3 = 1:4:4), (c) anthracene 3PS assembly (S1:S2:S3 = 1:4:4) after 30 minute photo-irradiation.

The unmodified 3PS assembly shows a densely packed grid-like structure on the mica support (Figure 6.17a). The structures are uniform and well-defined. However, the anthracene modified 3PS assembly shows many broken structures with defects (Figure 6.17b). Upon photo-irradiation, the assembly seems to collapse entirely, appearing as spherical structures (Figure 6.17c). One explanation for this might be that the UV radiation was damaging the sample. This was later resolved by introducing the bandpass filter and degassing the solution. However, AFM images for these samples under these conditions were not obtained due to time constraints.

6.6 Polyacrylamide Gel Electrophoresis

Polyacrylamide gel electrophoresis is the most common technique used for characterisation of higher order DNA assemblies. This separation technique allows for identification of DNA species based on their size.[50] Described in this section, gel electrophoresis was used to characterise the Anthracene 3PS assembly and test its robustness against denaturing conditions. Native polyacrylamide gel electrophoresis (Chapter 7.14.1) was first employed to determine an optimum ratio of the S1 strand to the S2 and S3 in order to yield the most product. It was important to do this as the photocyclisation reaction could only be employed on the annealed assembly. The protocol for the native PAGE is presented in Chapter 7.14.1 and the results are shown in Figure 6.18.

1	DNA ladder
2	S3-Ant
3	S2-Ant
4	S1
5	S1+S2-Ant **(1:1)**
6	S1+S2-Ant **(1:2)**
7	S1+S2-Ant **(1:3)**
8	S1+S2-Ant **(1:4)**
9	S1+S2-Ant+S3-Ant **(1:3:1)**
10	S1+S2-Ant+S3-Ant **(1:3:2)**
11	S1+S2Ant+S3-Ant **(1:3:3)**
12	S1+S2-Ant+S3-Ant **(1:4:1)**
13	S1+S2-Ant+S3-Ant **(1:4:2)**
14	S1+S2-Ant+S3-Ant **(1:4:3)**
15	S1+S2-Ant+S3-Ant **(1:4:4)**
16	S1+S2+S3 **(1:3:3)** (unmodified)

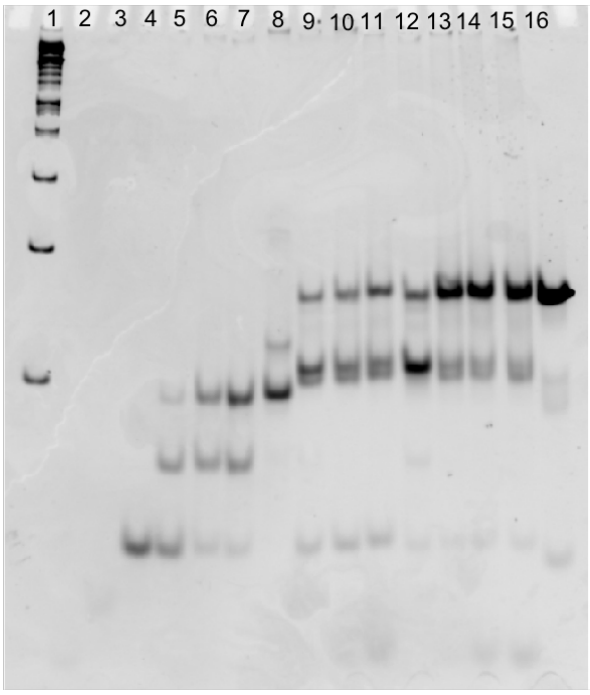

Figure 6.18 - A Diamond™ stained native 6% PAGE visualised with UV light on Bio-Rad system, 1 x TAMg buffer, 250 V, 2.5 h at 4 °C; combination gel of increasing ratios of S2 and S3 strand. Concentration of the S1 strand was 375 nM.

The results show that the optimum ratio for the Anthracene 3PS assembly appears to be the S1:S2:S3 = 1:4:4 (Lane 15), whereas the ratio adopted for the unmodified assembly was S1:S2:S3 = 1:3:3 (Lane 16). This 1:4:4 ratio was employed in all the experiments undertaken on the Anthracene 3PS because it yields the most product as evident by the strongest band (Lane 15) in relation to the 1:3:3 ratio present in Lane 11. Lanes 2 and 3 are not visible as they run off the gel.

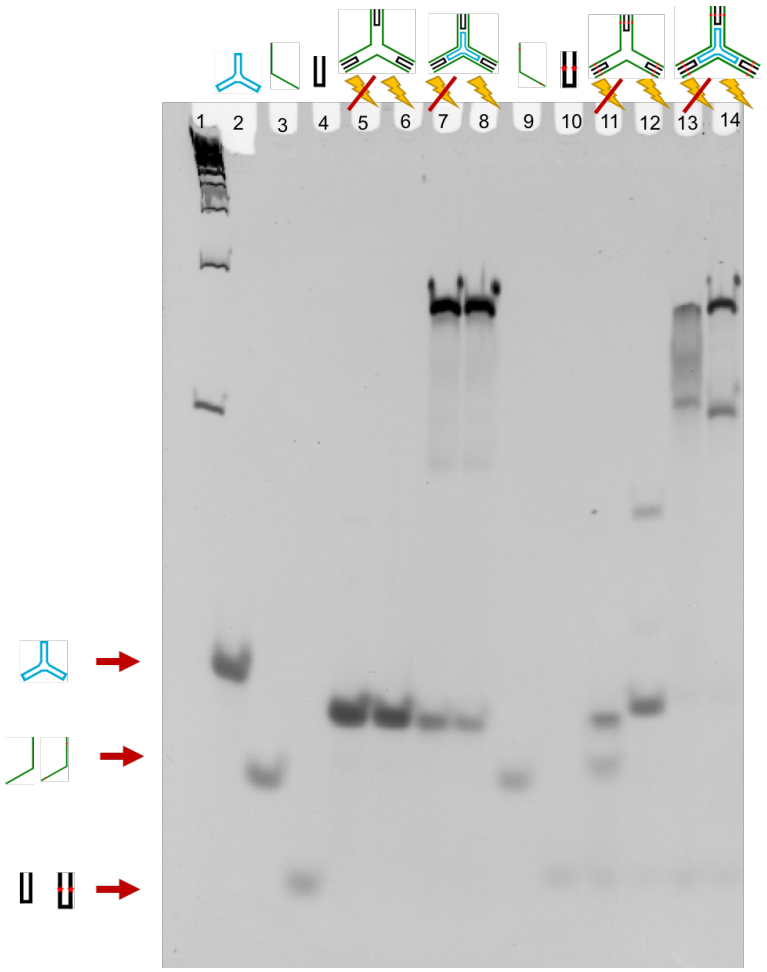

Figure 6.19 - A Diamond™ stained native 6% PAGE of anthracene 3PS assembly (1:4:4) photo-irradiated for 30 minutes without the 365 nm filter, visualised with UV light on Bio-Rad system, 1 x TAMg buffer, 250 V, 2.5 h at 4 °C. Concentration of the S1 strand was 375 nM.

A second gel experiment was then undertaken on assemblies that had been exposed to photo-irradiation for 30 minutes (Figure 6.19). Successful anthracene 3PS assembly formation is evidenced by the low mobility bands present in lanes 13 and 14. These lanes correspond to the unmodified assembly in lanes 7 & 8 which are comparable to the literature results.[47] It is important to note that the photo-irradiated sample bands do not differ from the non-irradiated ones under these native conditions although it is interesting to note that the modified systems give a

sharper band in lane 14 after photo-irradiation. Overall these results indicate that the anthracene 3PS assembly has been successfully formed.

Following this experiment, it was decided to test the anthracene 3PS assembly under denaturing conditions to establish whether the assembly could stay intact under these conditions due to the formation of photo-crosslinks. This was done by employing denaturing PAGE protocol, (detailed in Chapter 7.14.2) with the results presented in Figure 6.20.

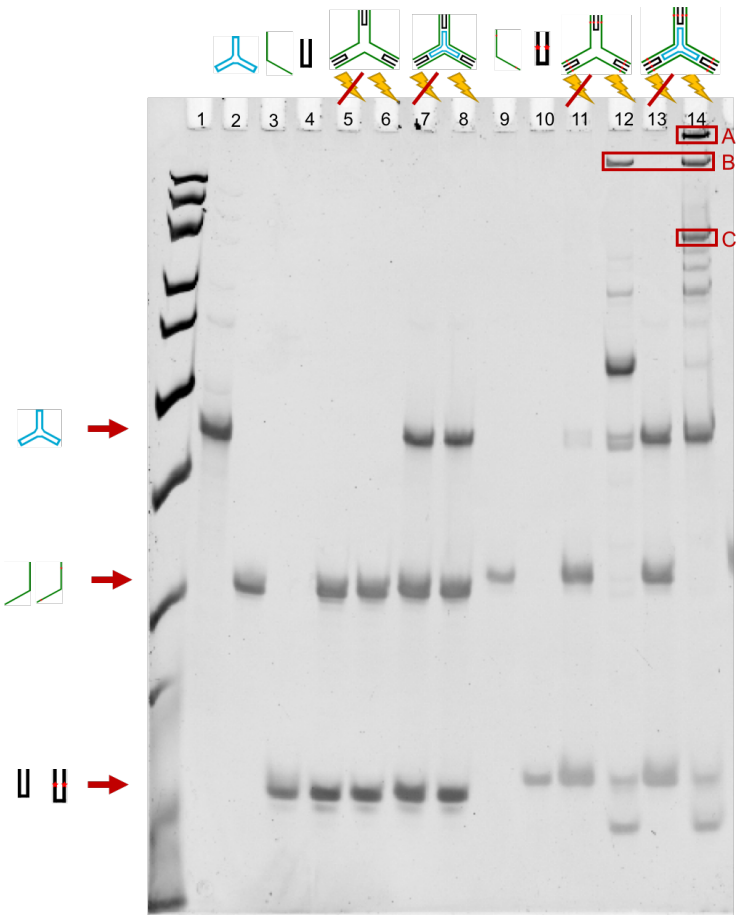

Figure 6.20 - A Diamond™ stained denaturing 15% PAGE of anthracene 3PS assembly (1:4:4) photo-irradiated for 30 minutes without the 365 nm filter, visualised with UV light on Bio-Rad system, 1 x TBE buffer, 250 V for 30 min, 500 V for 1 h, 7 M Urea. Concentration of the S1 strand was 375 nM.

Urea is a well-known denaturing agent, mainly used for preparative polyacrylamide gel electrophoresis used in DNA purification.[51] It is also common practice to use formamide in this process, which is normally added directly to the sample and incubated before loading onto the gel. In this study, successful denaturation can be seen by there being three bands corresponding to each of the components of the unmodified 3PS assembly in lane 7. The anthracene modified assembly also denatures under these conditions (lane 13). Interestingly however, the photo-irradiated anthracene 3PS assembly shows low mobility bands (lane 14), suggesting that the dimerisation reaction was at least partially successful and that higher order DNA structures were maintained despite the denaturing conditions. This can be attributed to covalent bonds forming between the anthracene molecules embedded within the S2 and S3 DNA strands. The unmodified assembly was photo-irradiated as a negative control to confirm that light had no effect on the unmodified DNA structure (lane 8). Moreover, it was interesting to investigate the role of the central S1 strand in the 3PS structure and the assembly that was formed without it (lane 5, 6, 11, 12). Interestingly, one higher order structure (labelled B) was evident upon prior photo-irradiation as seen in lane 12, similar to the assembly with the S1 strand (lane 14). This led to the hypothesis that the template strand S1 might not be necessary for formation of the full assembly. This also suggests that the highest band (labelled A) contains the S1 template trapped within the structure. Further experiments would be needed to confirm this.

There was another band in the gel in Figure 6.20 that caused concern, namely the highest mobility band at the bottom of the gel in lanes 12 and 14. It appears that the band corresponding to the unbound S3 strand had split into two upon photo-irradiation, which suggested a possible light-triggered degradation. It was therefore decided to improve the photocyclisation protocol (Chapter 7.12.2) by incorporation of a bandpass filter and degassing the solutions prior to the reaction.

The second study of the anthracene 3PS assembly was accomplished according to the improved photocyclisation protocol detailed in Chapter 7.12.2. Native PAGE was once again employed to verify successful formation of the anthracene 3PS assembly according to the established protocol described in Chapter 7.14.1. The results are presented in Figure 6.21.

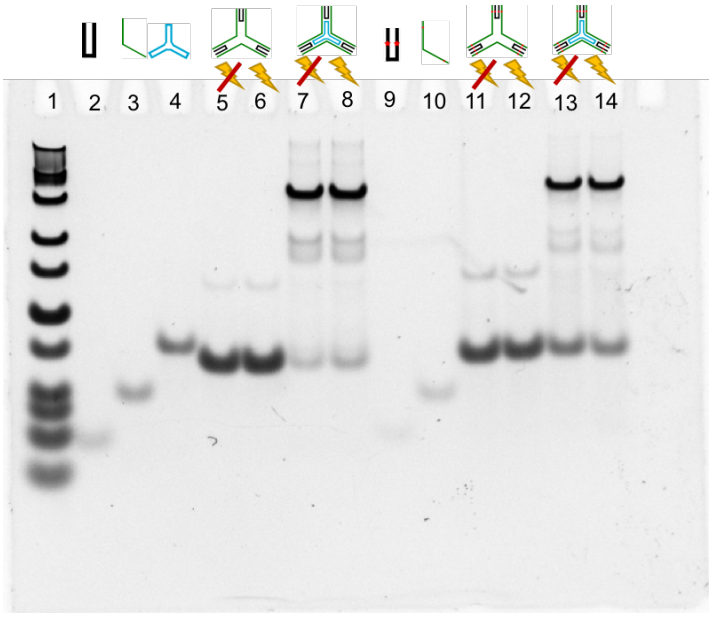

Figure 6.21 - A Diamond™ stained native 8% PAGE of anthracene 3PS assembly (1:4:4) photo-irradiated for 3 h with the 365 nm filter, visualised with UV light on AlphaImager HP system, 1 x TAMg buffer, 100 V, 1.5 h at 4 °C. Concentration of the S1 strand was 375 nM.

Once again, successful anthracene 3PS assembly formation is evident in lanes 13 and 14. These bands are comparable to the unmodified assembly bands (lanes 7 and 8) in that they migrate at the same speed down the gel (Figure 6.21). Again, photo-irradiation does not seem to bring about major differences under these native conditions. Moreover, the full assembly is not formed without the S1 (template) strand as seen in lanes 5, 6, 11 and 12. However, the possibility of hybridisation between S2 and S3 strands cannot be eliminated. In fact, the presence of lower mobility bands in lanes 5, 6, 11 and 12 do suggest such behaviour.

The improved photocyclisation protocol (Chapter 7.12.2) allowed for a better control of the dimerisation reaction. Initially, three hours of 365 nm wavelength light exposure was employed. However, denaturing PAGE showed faint bands corresponding to dimerised products. Therefore, remaining amounts of samples, were subjected to photo-irradiation for up to 12 h. The reaction was monitored at 3 h intervals and the results of this study are presented in Figure 6.22.

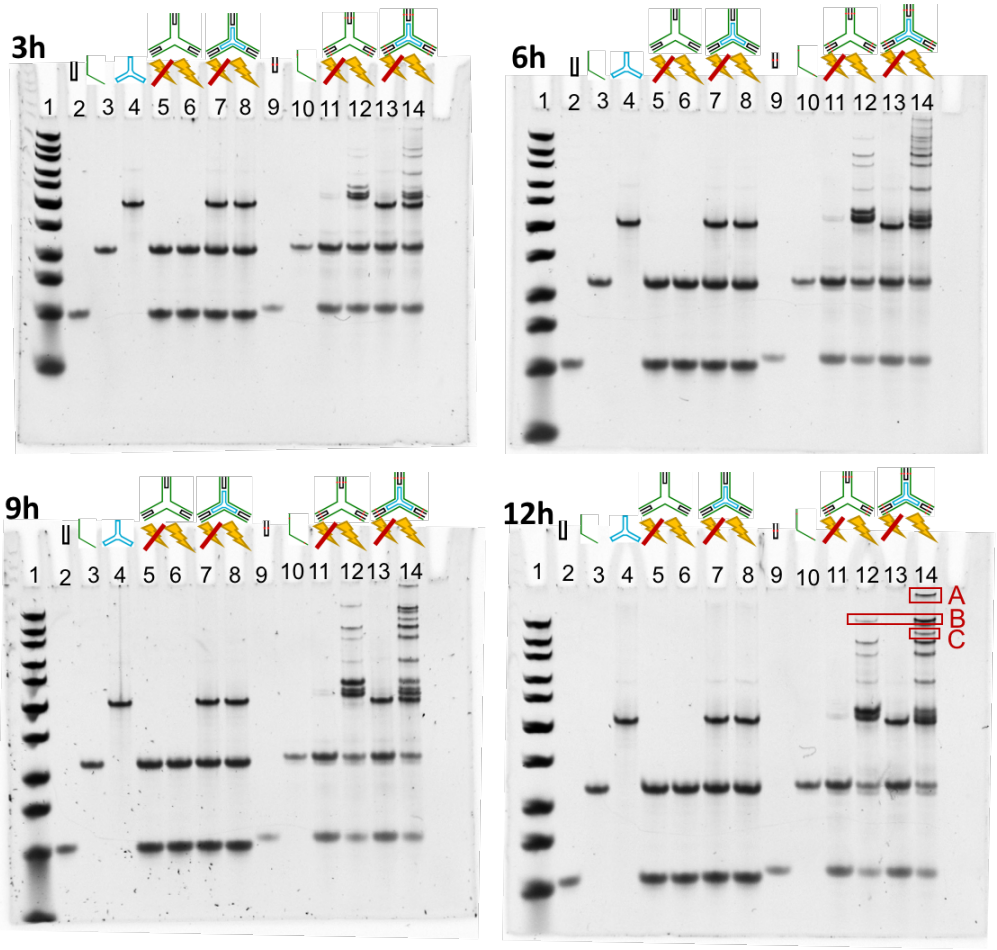

Figure 6.22 - A Diamond™ stained denaturing 15% PAGE of anthracene 3PS assembly (1:4:4) photo-irradiated for 3, 6, 9 and 12 h with the 365 nm filter, visualised with UV light on AlphaImager HP system, 1 x TBE buffer, 50 V for 30 min, 100 V for 1 h 40 min, 7 M urea. Concentration of the S1 strand was 375 nM.

It can be clearly seen from the results in Figure 6.22 that the photocyclisation reaction takes place but is considerably slower under these conditions. However, the possible degradation bands due to photo-irradiation seen in Figure 6.20 are now absent, which suggests that degradation of DNA was successfully prevented by the improved protocol. As seen previously however, the unmodified 3PS assembly falls apart under denaturing conditions into its components, regardless of the use of light

(lanes 5, 6, 7, 8). The unexposed anthracene modified 3PS assembly also gets denatured under this conditions (lane 13). In contrast, the photo-irradiated anthracene 3PS assembly (lane 14) shows multiple lower mobility bands, the strength of which increases with the irradiation time. This is also true for the anthracene assembly annealed without the S1 (template) strand (lane 12). However, the template strand does seem to play a role in the formation of the full anthracene 3PS assembly, as evidenced by the lowest mobility band A in lane 14, which is clearly absent in lane 12. It can therefore be stated with certainty that the photo-cyclised anthracene 3PS assembly retains higher order structures under denaturing conditions. However, it is impossible to confirm whether the full assembly is retained under these conditions. This is because the photo-cyclisation reactions of which up to six are possible, do not go to completion in 12 hours which was the maximum time frame explored in this study. This means that not all of the six positions in one assembly are necessarily formed. Unfortunately, ESI mass spectrometry was unable to verify the formation of the full assembly. CID-MS seems more promising for this system, however it was impossible to test this due to the instrument incompatibility. Another technique would have to be employed to confirm the successful retention of the full anthracene 3PS assembly under denaturing conditions.

6.7 Conclusions

This study has demonstrated successful formation of a novel anthracene modified DNA assembly that has the potential to withstand denaturing conditions. This has been achieved by employment of a Three Point Star DNA structure and incorporating anthracene molecules into its components via solid phase DNA synthesis. Further to this, the structure was exposed to 365 nm light in order to facilitate the formation of intermolecular covalent adducts between the anthracene molecules. The resultant structure was characterised by thermal melting, AFM imaging as well as native and denaturing PAGE. Successful formation of higher order structures resistant to denaturing conditions was confirmed. However, it was not possible to unambiguously prove the retention of the main Anthracene 3PS structure under these conditions.

6.8 References

1. S. Kobatake and M. Irie, *Annu. Rep. Prog. Chem., Sect. C: Phys. Chem.*, 2003, **99**, 227-313.
2. G. H. Brown, *Photochromism*, Wiley-Interscience, New York, 1971.
3. G. S. Hartley, *Nature*, 1937, **140**, 281.
4. B. S. Lukyanov and M. B. Lukyanova, *Chem. Heterocyc. Com.*, 2005, **41**, 281-311.
5. J. Min, J.-W. Choi, W. H. Lee and U. R. Kirn, *Biosens. Bioelectron.*, 1998, **13**, 1151.
6. *United States Pat.,* 1992.
7. H. Wünscher, G. Haucke and P. Czerney, *J. Photochem. Photobiol.*, 2002, **152**, 61-71.
8. M. Irie, *Chem. Rev.*, 2000, **100**, 1685-1716.
9. Y. Yokoyama, *Chem. Rev.*, 2000, **100**, 1717-1739.
10. N. C. Seeman, *Annu. Rev. Bioph. Biom.*, 1998, **27**, 225-248.
11. A. V. Pinheiro, D. Han, W. M. Shih and H. Yan, *Nat. Nanotechnol.*, 2011, **6**, 763-772.
12. T. S. Zatsepin, M. J. Gait and T. S. Oretskaya, *IUBMB Life*, 2004, **56**, 209-214.
13. H. Kashida, X. Liang and H. Asanuma, *Curr. Org. Chem.*, 2009, **13**, 1065-1084.
14. S. Ogasawara and M. Maeda, *Angew. Chem. Int. Ed.*, 2008, **47**, 8839-8842.
15. S. Ogasawara and M. Maeda, *Angew. Chem. Int. Ed.*, 2009, **48**, 6671-6674.
16. M. Singer and A. Jaschke, *J. Am. Chem. Soc.*, 2010, **132**, 869-878.
17. H. Cahova and A. Jäschke, *Angew. Chem. Int. Ed.*, 2013, **52**, 3186-3190.
18. D. O. Cowan and R. L. Drisko, Plenum Press, New York, 1976, ch. 2.
19. H. D. Becker, *Chem. Rev.*, 1993, **93**, 145-172.
20. H. Bouas-Laurent, A. Castellan, J.-P. Desvergne and R. Lapouyade, *Chem. Soc. Rev.*, 2000, **29**, 43-55.
21. H. Bouas-Laurent, A. Castellan, J.-P. Desvergne and R. Lapouyade, *Chem. Soc. Rev.*, 2001, **30**, 248-263.
22. M. Yoshizawa and J. K. Klosterman, *Chem. Soc. Rev.*, 2014, **43**, 1885-1898.
23. Y. Goto, N. Mizoshita, O. Ohtani, T. Okada, T. Shimada, T. Tani and S. Inagaki, *Chem. Mater.*, 2008, **20**, 4495-4498.
24. B. K. Selinger, *Aust. J. Chem.*, 1977, **9**, 2087-2090.
25. S. C. Zimmerman and C. M. VanZyl, *J. Am. Chem. Soc.*, 1987, **109**, 7894-7896.
26. M. Baumgarten, U. Müller, A. Bohnen and K. Müllen, *Angew. Chem. Int. Ed.*, 1992, **31**, 448-451.
27. K. Ito, T. Suzuki, Y. Sakamoto, D. Kubota, Y. Inoue, F. Sato and S. Tokito, *Angew. Chem. Int. Ed.*, 2003, **42**, 1159-1162.
28. S. Yamaguchi, S. Akiyama and K. Tamao, *Organometallics*, 1998, **17**, 4347-4352.

29. M. Iyoda, J. Yamakawa and M. J. Rahman, *Angew. Chem. Int. Ed.*, 2011, **50**, 10522-10553.
30. I. T. M. Kazuaki, T. Shinji, *Chemistry Lett.*, 2010, **39**, 288-290.
31. K. Miki, M. Fujita, Y. Inoue, Y. Senda, T. Kowada and K. Ohe, *J. Org. Chem.*, 2010, **75**, 3537-3540.
32. S. Chen, Q. Yan, T. Li and D. Zhao, *Org. Lett.*, 2010, **12**, 4784-4787.
33. K. Miki, T. Matsushita, Y. Inoue, Y. Senda, T. Kowada and K. Ohe, *Chem. Comm.*, 2013, **49**, 9092-9094.
34. D. L. Caulder and K. N. Raymond, *Acc. Chem. Res.*, 1999, **32**, 975-982.
35. M. Scherer, D. L. Caulder, D. W. Johnson and K. N. Raymond, *Angew. Chem. Int. Ed.*, 1999, **38**, 1588-1592.
36. I. S. Tidmarsh, T. B. Faust, H. Adams, L. P. Harding, L. Russo, W. Clegg and M. D. Ward, *J. Am. Chem. Soc.*, 2008, **130**, 15167-15175.
37. J. T. Goldbach, T. P. Russell and J. Penelle, *Macromolecules*, 2002, **35**, 4271-4276.
38. T. Ihara, T. Fujii, M. Mukae, Y. Kitamura and A. Jyo, *J. Am. Chem. Soc.*, 2004, **126**, 8880-8881.
39. M. Mukae, T. Ihara, M. Tabara and A. Jyo, *Org. Biomol. Chem.*, 2009, **7**, 1349-1354.
40. P. Arslan, T. Ihara, M. Mukae and A. Jyo, *Anal. Sci.*, 2008, **24**, 173-176.
41. J. Manchester, D. M. Bassani, J.-L. H. A. Duprey, L. Giordano, J. S. Vyle, Z.-Y. Zhao and J. H. R. Tucker, *J. Am. Chem. Soc.*, 2012, **134**, 10791-10794.
42. A. Ali, G. A. Bullen, B. Cross, T. R. Dafforn, H. A. Little, J. Manchester, A. F. A. Peacock and J. H. R. Tucker, *Chem. Comm.*, **39**, 5627-5630.
43. G. A. Bullen, J. H. R. Tucker and A. F. A. Peacock, *Chem. Comm.*, 2015, **51**, 8130-8133.
44. K. Pasternak, A. Pasternak, P. Gupta, R. N. Veedu and J. Wengel, *Bioorg. Med. Chem.*, 2011, **19**, 7407-7415.
45. D. Ackermann, G. Rasched, S. Verma, T. L. Schmidt, A. Heckelc and M. Famulok, *Chem. Comm.*, 2010, **46**, 4154-4156.
46. H. Yu, D. T. L. Alexander, U. Aschauer and R. Häner, *Angew. Chem. Int. Ed.*, 2017, **56**, 5040-5044.
47. N. Avakyan, J. W. Conway and H. F. Sleiman, *ACS*, 2017, **139**, 12027-12034.
48. J.-L. H. A. Duprey, Doctor of Philosophy, Birmingham, 2010.
49. K. Yamana, R. Aota and H. Nakano, *Tetrahedron Lett.*, 1995, **36**, 8427-8430.
50. N. Education, Gel Electrophoresis, https://www.nature.com/scitable/definition/gel-electrophoresis-286, 2019).
51. T. Maniatis and A. Efstratiadis, *Methods Enzymol.*, 1980, **65**, 299-305.

Chapter 7 – Experimental

7.1 Materials

Sigma Aldrich (Gillingham, UK) and Fisher Scientific (Loughborough, UK) were the main suppliers of all reagents and materials used within this thesis unless otherwise stated. All reagents used for DNA synthesis were purchased from Link Technologies Ltd (Bellshill, UK), except for DCM (Life Technologies, Paisley, UK), TCA (Sigma Aldrich, Gillingham, UK) and acetonitrile (Rathburn Chemicals Ltd, Scotland, UK). Further purification of the purchased reagents was not conducted.

7.2 Oligonucleotide synthesis and purification

7.2.1 Synthesis

All DNA oligonucleotides were synthesised via a phosphoramidite method[1] (Chapter 2) on an Applied Biosystems 394 DNA/RNA synthesiser on a 1.0 µmol scale. This is with the exception of 3 unmodified strands in Chapter 6 namely S1, S2 and S3 strands which were supplied pure by collaborators at McGill University. Anthracene and ferrocene phosphoramidites were incorporated into the relevant DNA sequences using the same procedure. All phosphoramidites were made up to a 0.1 M concentration prior to the DNA synthesis. Automatic DNA oligonucleotide synthesis is a cyclic process which is performed in 6 steps. The oligonucleotide is being made on a CPG (controlled-pore glass resin) where the first base at the 3' end has been pre-attached by the manufacturer.

1) CPG resin is washed with acetonitrile at the start of the cycle.

2) Solution of 3% trichloroacetic acid in dichloromethane is used to deprotect the DMT group at the 5’ OH.
3) 0.1 M solution of the next phosphoramidite in the sequence was activated using 0.5 M ethylthiotetrazole (ETT) and coupled for a duration of 25 seconds.
4) Capping of any unreacted DNA is accomplished using tetrahydrofuran (THF)/ pyridine/ 10% acetic anhydride at 70:15:15 ratio and 10% methyl imidazole in THF.
5) Phosphite-triester is oxidised to phosphotriester using 0.02 M iodine THF/ pyridine/ water at 70:15:15 ratio.
6) The final step is executed after all the phosphoramidites in the sequence had been coupled. The DNA was cleaved from the resin using 30% ammonium hydroxide solution for 90 minutes. Removal of protective groups was done by heating the cleaved DNA oligonucleotide in ammonium hydroxide solution at 65 ^{o}C for 6 hours.

It is a common practice to store synthesised oligonucleotide sequences dry at -18 ^{o}C, therefore the ammonia solution had been removed *in vacuo* prior to storage.

7.2.2 Purification by RP-HPLC

All oligonucleotides synthesised using the automated DNA synthesis in house were purified using Reversed-Phase High Performance Liquid Chromatography (RP-HPLC) using a Phenomenex Clarity Oligo RP 5 µm 250 x 10 mm column on an Agilent Technologies 1260 Infinity System. The only exceptions were four ferrocene

modified DNA tetrahedron sequences which were purified using denaturing PAGE as detailed in Section 7.2.3. The crude DNA oligonucleotide sample was re-dissolved in 1 mL of MilliQ water and loaded on the column. The elution times were monitored by UV detector with a 260 nm wavelength and additionally with a 360 nm wavelength for the anthracene modified sequences. After collection, samples were dried *in vacuo* and re-dissolved in 1 mL of MilliQ water.

Some of the RP-HPLC gradient methods have been previously developed by the Tucker group and served here directly for purification purposes or as a useful starting point in development of new methods. The flow rate used in all purifications was set to 3 mL min^{-1} and the temperature of the column to 60 ^{o}C. Buffer D was the buffer of choice and contained 0.1 M triethyl ammonium acetate (TEAA) in HPLC grade H_2O. All unmodified oligonucleotides were purified using a method called Short Oligo of gradient 5 – 18 % Acetonitrile in Buffer D over a period of 30 minutes. A DMT-ON method was used for oligonucleotides containing two anthracene modifications and consisted of gradient of 15 - 60 % acetonitrile over a period of 30 minutes. A method used for a ferrocene modified DNA oligonucleotide was FcNA Anth method of gradient 15 – 25 % acetonitrile over 30 minutes; and for a ferrocene modified oligonucleotide longer than 35 bases was Extended Fc Short Oligo method of gradient 5 – 18 % acetonitrile over 40 minutes. All methods contained a washing step of 100 % Acetonitrile over 10 minutes and a column equilibration which returned to the time 0 buffer system for 5 minutes.

Table 7.1 – Summary of HPLC methods employed in this thesis.

Method	Gradient (ACN content)	Time	Temperature	Flow rate
Short Oligo	5 – 18 %	30 min	60 °C	3 mL min^{-1}
DMT-ON	15 – 60 %	30 min	60 °C	3 mL min^{-1}
FcNA Anth	15 – 25 %	30 min	60 °C	3 mL min^{-1}
Extended Fc Short Oligo	5 – 18 %	40 min	60 °C	3 mL min^{-1}

Following HPLC purification of oligonucleotides, the samples were desalted using a size- exclusion Sephadex NAP-10 column (GE Healthcare). This was accomplished by loading 1 mL of sample onto the column and eluting it with 1.5 mL of MilliQ water. Subsequently, the purity of oligonucleotides was confirmed by analytical RP-HPLC system using the same Agilent instrumentation equipped with a Phenomenex Clarity 5 µm Oligo-RP LC 250 x 4.6 mm column and a flow rate of 1 mL min^{-1}. All samples were considered pure if the purity was above 95% and were suitable for further experiments.

7.2.3 Purification by denaturing PAGE

Denaturing polyacrylamide gel electrophoresis (PAGE) was performed to purify four ferrocene modified DNA Tetrahedron sequences used in Chapter 5. This type of gel was performed vertically with a 15 % gel containing 7.5 mL of 40 % acrylamide, 7 M Urea (5.04 g) as a denaturing agent with 4 mL of 5 x TBE (0.5 M Tris base, 0.5 M Boric Acid, 10 mM EDTA), topped up to 20 mL total volume and polymerised with 10 % APS (150 µL) and TEMED (15 µL). The mixture was transferred into a 1 mm gel rack

with a well comb and allowed to set for 10 minutes. Samples containing 150 - 250 µM DNA (200 µL) were mixed with formamide (200 µL) and incubated for 15 minutes prior to loading into the wells, 10 µL in each well. Low molecular weight marker (5 µL) was run alongside the sample. The electrophoretic run was undertaken for 1 h and 10 minutes at 100 V in electrophoresis buffer 1 x TBE (0.1 M Tris base, 0.1 M boric acid, 2 mM EDTA). The gel was visualised under a UV lamp by a shadow on a silica plate and the strongest band corresponding to the product was excised with a scalpel.

The excised gel slabs were crushed with a spatula and 3 mL of MilliQ water was added for every 0.5 mL of gel. The samples were frozen at -80 ^{o}C by placing the Eppendorf vials in liquid nitrogen and immediately afterwards reheated to 90 ^{o}C and incubated at that temperature for 5 minutes. Thus treated samples were left on a shaker overnight. The following day, gel extraction was carried out. The gel residue was filtered off and rinsed with MilliQ water. The eluted DNA was dried *in vacuo* and desalted twice using NAP-25 columns (GE Healthcare).[2]

7.3. Oligonucleotide characterisation

7.3.1. Characterisation by Mass Spectrometry

DNA oligonucleotide characterisation was performed using negative mode electrospray ionisation mass spectrometry (ESI-MS). Ten microliters of purified oligonucleotide sample at a concentration of about 100 µM in MilliQ water were

analysed using a Waters XEVO G2-XS system with a Time of Flight (TOF) detector and additionally passed through an LC-MS system Acquity UPLC with a C18 1.7 µm column prior to mass spectrometry characterisation. The deconvolution of the raw data was accomplished using Promass (Novatia) with a ZNova algorithm. Oligonucleotide molecular mass prediction was done via an online tool IDT OligoAnalyser.[3]

7.3.2 Oligonucleotide concentration determination

Concentrations of DNA were determined using a Shimadzu BioSpec Nano UV/Vis/NIR Spectrophotometer by measuring the absorbance at 260 nm. The molar extinction coefficients of the respective oligonucleotides were calculated using the IDT OligoAnalyzer tool[3], using the nearest neighbour method. The extinction coefficients for anthracene modification was $\varepsilon^{\lambda 260}$=51444 L mol^{-1} cm^{-1}, for ferrocene was $\varepsilon^{\lambda 260}$=3300 L mol^{-1} cm^{-1} and for cisplatin was $\varepsilon^{\lambda 260}$=24000 L mol^{-1} cm^{-1}. Whereas the extinction coefficient for ST-DNA was $\varepsilon^{\lambda 260}$=6600 L mol^{-1} cm^{-1}.

7.4 Synthesis and characterisation of ST-DNA metal complexes

7.4.1 Synthesis of ST-DNA metal complexes

ST-DNA was obtained in a dry form of sodium salt. The material was placed in a Sterilin tube and dissolved in MilliQ water by stirring vigorously overnight. Sonication

was applied for 9 minutes in 10 seconds on, 20 seconds off intervals.[4] The concentration was measured according to the protocol described in Section 7.3.2. Subsequent dilution to a concentration of around 16,000 µM was carried out which served as a stock solution for preparation of 1000 µM samples. Cisplatin was obtained from Sigma Aldrich and dissolved in MilliQ water to a concentration of 8300 µM to serve as a stock solution. Ruthenium complexes: *trans*-$RuCl_2DMSO_4$ and *cis*-$RuCl_2DMSO_4$, were synthesised and characterised by Georgina Leck.[5] The stock solutions of ruthenium complexes were made up in MilliQ water to a concentration of 2500 µM. Stock samples of ST-DNA and cisplatin were combined and diluted to a desired concentrations detailed in Chapter 3.3. The DNA metal complex samples were vortexed, placed in the dark and incubated at 37 ^{o}C overnight. The prepared samples were directly taken for UV/Vis and CD measurements without changing the concentrations or buffering system.

7.4.2 Synthesis of CTMA-DNA metal complexes

The metal complex (cisplatin, *trans*-$RuCl_2DMSO_4$ and *cis*-$RuCl_2DMSO_4$) reaction with ST-DNA was accomplished according to the procedure in Section 7.4.1. The metal-DNA samples of desired concentrations were mixed with the aqueous solution of cetyltrimethyl ammonium chloride (1000 µM) in a volumetric ratio of 1:1.[6] The samples were left on a shaker overnight to allow for the precipitate to appear. The following day, samples were centrifuged for 10 minutes at 13000 RPM and the solvent was removed by pipetting. The pellets were washed with MilliQ water 3

times. The water residue in the samples was removed *in vacuo*. Samples were re-dissolved in methanol to the original volume by placing on a shaker overnight. Some loss of material was expected but not monitored. The prepared samples were directly taken for UV/Vis and CD measurements without changing the concentrations nor buffering system.

7.5 Synthesis and purification of cisplatin oligonucleotides

The oligonucleotide of a desired sequence and concentration of 100 µM was incubated with an equimolar amount of cisplatin in MilliQ water in the dark at 37 ^{o}C overnight. The prepared sample was then purified using RP-HPLC on an Agilent Technologies 1260 Infinity System equipped with a Phenomenex Kinetex 5 µm EVO C18 250 x 4.6 mm column. The gradient method for this purification as well as conditions and buffer systems are discussed in Chapter 4, where the appropriate sequence specific methods are developed. The injection volumes varied from 5 - 100 µL depending on separation. The elution times were monitored by UV detector at 260 nm. The fractions from multiple injections were collected automatically using a fraction collector, combined, dried *in vacuo*, re-dissolved in 1 mL and desalted using NAP-10 column (GE Healthcare) detailed in Section 7.2.2. The desalted samples were frequently further concentrated by lyophilisation.

7.6 Formation of DNA Duplex

A stoichiometric mixture (10 µM) of two complementary oligonucleotides was heated rapidly to 90 ^{o}C and subsequently cooled from 90 ^{o}C to 4 ^{o}C over approximately 5 minutes in annealing buffer (10 mM sodium phosphate pH 7.0, 100 mM NaCl in MilliQ water). The sequences and duplexes formed of appropriate DNA duplexes are discussed in Chapters 4 and 5.

7.7 DNA Origami Triangle

7.7.1 Self-assembly and purification of DNA Origami Triangle

The protocols for DNA Origami Triangle assembly[7] and purification[8] were adapted from the literature. The folding reaction was prepared in 50 µL volume PCR tube. The reaction mixture consisted of 1 x Tris-EDTA, $MgCl_2$ buffer (10 mM Tris, 1 mM EDTA, 12.5 mM $MgCl_2$, pH 8.35), origami staple stock (unmodified sequences, DNA-PAINT, poly-A sequences) of 100 µM concentration of each strand, Poly-TGG-cisPt of 100 µM and 250 ng μL^{-1} of M13 mp 18 ssDNA. The reaction mixture was incubated at 90 ^{o}C for 5 minutes and then cooled to 20 ^{o}C with a rate of 0.2 ^{o}C per minute using Bio Rad Thermocycler. The purification of the DNA Origami Triangle was accomplished by mixing the folded reaction mixture with PEG purification buffer (15% PEG 8000, 505 mM NaCl, 20 mM $MgCl_2$) in a 1:1 volumetric ratio. The sample was centrifuged at 16000 RPM for 30 minutes at 4 ^{o}C. Supernatant was removed and the pellet was re-suspended in 30 µL of Target Buffer (5mM Tris, 1 mM EDTA, 5 mM $MgCl_2$, 5 mM NaCl, pH 8). Concentration of DNA Origami Triangle was determined

by measuring the absorbance at 260 nm on a Shimadzu BioSpec Nano UV/Vis/NIR Spectrophotometer, by applying the extinction coefficient of $\varepsilon^{\lambda max}$=123,735,380 L mol^{-1} cm^{-1}.

7.7.2 Agarose gel electrophoresis of DNA Origami Triangle

Agarose gel electrophoresis was run to verify assembly formation of DNA Origami Triangle. This gel was performed horizontally with 1% w/v agarose running gel. The gel was composed of 0.8 g agarose in 80 mL of 0.5 x buffer (20 mM Tris base, 10 mM Acetic acid, 0.5 mM EDTA, 5 mM $MgCl_2$). The mixture was microwaved for 1 minute until the solid dissolved and transferred into a gel rack equipped with a well comb. The gel was allowed to set for 30 minutes. Samples of DNA Origami Triangle, M13 mp 18 ssDNA as well as supernatant from the purification were loaded into the wells. Electrophoresis was undertaken for 2 hours at 60 V in electrophoresis buffer (40 mM Tris base, 20 mM Acetic acid, 1 mM EDTA, 10 mM $MgCl_2$) and stirred half way to remove magnesium salt residue depositing on the electrode. The gel was post stained with GelRed (Thermo Scientific) stain for 30 minutes and imaged using Alpha Imager HP (Alpha Innotech).

7.8 Assembly of DNA Holliday junction

The Holliday junction assembly was inspired by the literature.[9] A mixture of four synthetic oligonucleotides (Chapter 5) having concentration of 10 µM each was heated rapidly to 90 ^{o}C and subsequently cooled from 90 ^{o}C to 4 ^{o}C over

approximately 5 minutes in annealing buffer[9] (10 mM $MgCl_2$, 5 mM Tris–Cl, 20 mM Tris acetate, 1 mM EDTA in MilliQ water).

7.9 Assembly of DNA Holliday junction array

The Holliday junction array assembly was inspired by the literature.[9] A mixture of four synthetic oligonucleotides (Chapter 4 and 5) having concentration of 5 µM each was heated rapidly to 90 ^{o}C and subsequently cooled from 90 ^{o}C to 14 ^{o}C over 76 hours in annealing buffer[9] (10 mM $MgCl_2$, 5 mM Tris–Cl, 20 mM Tris acetate, 1 mM EDTA, 2% Triton X-100 in MilliQ water) on a T Robot (Biometra) thermocycler and Beckman Coulter system.

7.10 Assembly of DNA Tetrahedron

The DNA Tetrahedron assembly was inspired by the literature.[10] A 1 mL mixture of four synthetic oligonucleotides (Chapter 5) having concentration of 15 nM each was heated rapidly to 90 ^{o}C and subsequently cooled from 90 ^{o}C to 4 ^{o}C over approximately 5 minutes in annealing buffer[10] (20 mM $MgCl_2$, 10 mM Tris–Cl, 1 mM EDTA in MilliQ water). The short annealing time was to prevent the formation of misfolds. The annealed DNA Tetrahedron sample was subsequently concentrated using a 30 kD Amicon Ultra 0.5 mL centrifugal filter (Millipore) to 357 nM.

7.11 Synthesis of anthracene phosphoramidite

The protocol for anthracene phosphoramidite synthesis was followed without changes from the thesis of Jean-Louis Duprey.[11]

7.11.1 Synthesis of ethyl 7-(anthracen-9-yloxy)heptanoate

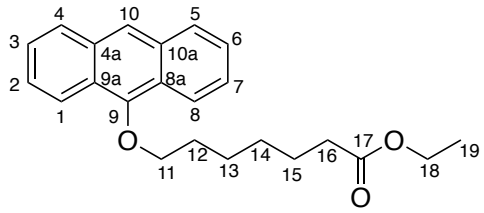

Equimolar amounts of anthrone (5 g, 0.026 mol) and potassium carbonate (3.56 g, 0.026 mol) were dissolved in $Ar_{(g)}$ degassed acetone (200 mL). The mixture was stirred in the absence of light under inert atmosphere for 15 minutes. Ethyl-7-bromoheptanoate (5 mL, 0.026 mol) was added to the mixture and the reaction was refluxed overnight in the dark under an inert atmosphere. The following morning, the solution was filtered off and the solvent removed *in vacuo*. The resultant orange solid was dissolved in DCM (100 mL), washed with water (50 mL), dried over $MgSO_4$ and filtered. Silica column was used for purification and the solvent system was 10% ethyl acetate in hexane. The product was orange solid (5.03 g, 0.014 mol, 56%).

^{1}H NMR (300 MHz, $CDCl_3$) δ 8.27 (d, J = 6.8 Hz, 2H, H_1), 8.20 (s, 1H, H_{10}), 7.98 (d, J = 6.7 Hz, 2H, H_4), 7.49 – 7.42 (m, 4H, H_2 and H_3), 4.20 – 4.11 (m, 4H, CH_2CH_3, OCH_2 H_{11}), 2.35 (t, J = 7.5 Hz, 2H, $O(CH_2)_5CH_2CO$), 2.09 – 2.01 (m, 2H, OCH_2CH_2), 1.78 – 1.64 (m, 4H, $O(CH_2)_2CH_2CH_2$), 1.53 – 1.45 (m, 2H, $O(CH_2)_4CH_2$), 1.26 (t, J = 7.1 Hz, 3H, CH_2CH_3).

^{13}C NMR (400 MHz, $CDCl_3$) δ C 173.9 (C_{17}=O), 151.5 (C_9), 132.5 (2xC_{4a}), 128.5 (2xC_4),

125.6 (2xC_2), 125.2 (2xC_3), 124.8 (2xC_{9a}), 122.5 (C_{10}), 122.1 (2xC_1), 76.1 (C_{11}), 60.4 (CH_2CH_3), 34.5 (C_{16}), 30.6 (C_{12}), 29.3 (C_{15}), 26.1 (C_{13}), 25.1 (C_{14}), 14.4 (CH_2CH_3).

m/z (ES MS) calcd for $C_{22}H_{24}O_3Na$ ($M+Na^+$) 373.1 found 373.1

7.11.2 Synthesis of 7-(Anthracen-9-yloxy)heptanoic acid

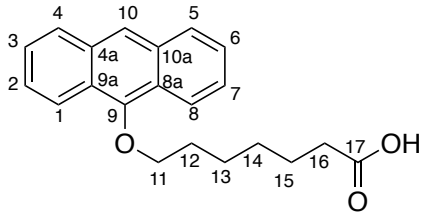

Ethyl 7-(anthracen-9-yloxy)heptanoate (5 g, 0.014 mol) was dissolved in 200 mL of 10% NaOH : EtOH (1:1). The solution was refluxed overnight in the dark under an inert atmosphere. The solvent was removed *in vacuo* and another 400 mL of water was added to the aqueous mixture. Hydrochloric acid (conc.) was added dropwise until creamy precipitate appeared. The solid was filtered off and dried in air. The yield of the product was 4.43 g (0.014 mol, 96%).

^{1}H NMR (300 MHz, $CDCl_3$) δ 8.3 (d, J = 9.3 Hz, 2H, H_1), 8.2 (s, 1H, H_{10}), 8.0 (d, J = 7.3 Hz, 2H, H_4), 7.5 – 7.4 (m, 4H, H_2 and H_3), 4.2 (t, J = 6.6 Hz, 2H, $OCH_2(CH_2)_5CO$ H_{11}), 2.4 (t, J = 7.4 Hz, 2H, $O(CH_2)_5CH_2CO$ H_{16}), 2.1 – 2.0 (m, 2H, $OCH_2CH_2(CH_2)_3CO$ H_{12}), 1.8 – 1.7 (m, 4H, $O(CH_2)_2CH_2CH_2CH_2CO$, H_{13}), 1.6 – 1.5 (m, 2H, $O(CH_2)_4CH_2$ H_{14}). ^{13}C NMR (400 MHz, $CDCl_3$) δ 179.9 (C_{17}=O), 151.5 (C_9), 132.5 (2xC_{4a}), 128.6 (2xC_4), 125.6 (2xC_2), 125.2 (2xC_3), 124.8 (2xC_{9a}), 122.5 (C_{10}), 122.1 (2xC_1), 76.1 (C_{11}), 34.2 (C_{16}), 30.6 (C_{12}), 29.2 (C_{15}), 26.1 (C_{13}), 24.8 (C_{14}).

m/z (ES MS) calcd for $C_{21}H_{22}O_3Na$ ($M-H+Na^+$) 345.4 found 373.2

7.11.3 Synthesis of 7-(anthracen-9-yloxy)-N-((2S,3S)-1,3-dihydroxybutan-2-yl)heptanamide

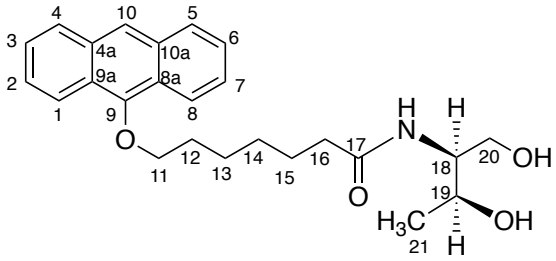

7-(Anthracen-9-yloxy)heptanoic acid (4.43 g, 0.014 mol) was dissolved in DMF (20 mL). Equimolar amount of HBTU (5.21 g, 0.014 mol) was added and stirred under an inert atmosphere in the dark for 15 min. Equimolar quantities of D-threoninol (1.45 g, 0.014 mol) and DIPEA (2.27 mL, 0.014 mol) were added. The mixture was left to continue stirring in the dark at 40 ^{o}C for 40 h under an inert atmosphere. The solution was diluted with 30 mL methanol and 60 mL DCM, washed with water (50 mL) three times and dried with magnesium sulphate. The solvent was removed *in vacuo* and the purification was done on a silica column with the solvent system of 1-5% MeOH in DCM. The product was a pale yellow solid and yielded 3.4595 g (0.0084 mol, 62%). ^{1}H NMR (400 MHz, $CDCl_3$) δ 8.3 (d, J = 9.9 Hz, 2H, H_1), 8.2 (s, 1H, H_{10}), 8.0 (d, J = 9.6 Hz, 2H, H_4), 7.5 – 7.4 (m, 4H, H_2 and H_3), 6.4 (d, J = 7.8 Hz, 1H, N*H*), 4.2 – 4.1 (m, 3H, O$CH_2CH_2CH_2O$ H_{11} and CH_3CHOH H_{19}), 3.9 – 3.8 (m, 1H, C*H*NH H_{18}), 3.8 – 3.8 (m, 2H, $CHCH_2OH$ H_{20}), 3.5 (s, 1H, CHO*H*), 2.3 (t, J = 7.5 Hz, 2H, CH_2CO H_{16}), 2.0 (q, J = 14.7, 6.6 Hz, 2H, $CH_2CH_2CH_2CH_2CH_2CO$ H_{12}), 1.8 (q, 2H, CH_2CH_2CO H_{15}), 1.6 (m, 2H, $CH_2CH_2CH_2CH_2CO$ H_{13}), 1.5 (q, J = 8.9, 8.4 Hz, 2H, $CH_2CH_2CH_2CO$ H_{14}), 1.2 (d, J = 6.4 Hz, 3H, CH_3CHOH H_{21}). ^{13}C NMR (300 MHz, $CDCl_3$) δ 174.8 (C_{17}=O), 151.3 (C_9), 132.5

(2xC_{4a}), 128.5 (2xC_4), 125.5 (2xC_2), 125.2 (2xC_3), 124.7 (2xC_{9a}), 122.4 (C_{10}), 122.1 (2xC_1), 76.0 (C_{11}), 67.7 (C_{19}), 64.1 (C_{20}), 55.1 (C_{18}), 36.8 (C_{16}), 30.6 (C_{12}), 29.3 (C_{13}), 26.1 (C_{15}), 25.9 (C_{14}), 20.4 (C_{21}). m/z (ES MS) calcd for $C_{25}H_{31}O_4Na$ ($M+Na^+$) 432.215 found 432.2147

7.11.4 Synthesis of 7-(Anthracen-9-yloxy)-N-((2S,3S)-1-(bis(4-methoxyphenyl)(phenyl)methoxy)-3-hydroxybutan-2-yl)heptanamide

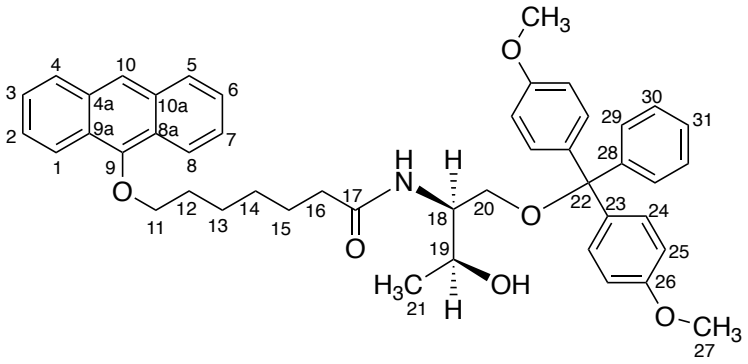

7-(anthracen-9-yloxy)-N-((2S,3S)-1,3-dihydroxybutan-2-yl)heptanamide (3.4565 g, 0.0084 mol) was dissolved in pyridine (30 mL, 0.37 mol). Equimolar amount of DMT-Cl (2.86 g, 0.0084 mol) and 0.15 x moles of DMAP (0.1546 g, 0.0012 mol) were added and stirred in the dark for 24 h under an inert atmosphere. The product was extracted with DCM (2 x 50 mL). Pyridine was washed with water (50 mL) three times. The mixture was dried with magnesium sulphate, filtered and the solvent removed *in vacuo*. Silica column was used to purify the product, with the

solvent system of 40 % hexane, 59 % ethyl acetate and 1 % TEA. The product yielded pale yellow crystalline solid of 2.7328 g (0.0038 mol, 45 %).

^{1}H NMR (300 MHz, $CDCl_3$) δ 8.3 – 8.3 (m, 1H, H_{10}), 8.2 (s, 2H, H_1), 8.0 – 8.0 (m, 2H, H_4), 7.5 – 7.4 (m, 6H, H_2, H_3, H_{29}), 7.3 – 7.2 (m, 6H, H_{24} and H_{30}), 7.2 (t, J = 7.2 Hz, 1H, H_{31}), 6.8 (d, J = 8.8 Hz, 4H, H_{25}), 6.1 (d, J = 8.7 Hz, 1H, N*H*), 4.2 – 4.1 (m, 2H, OCH_2CO H_{11}), 4.0 – 3.9 (m, 2H, NHC*H*CHOH H_{18}, NHCHC*H*OH H_{19}), 3.8 (s, 6H, OCH_3 H_{27}), 3.1 – 3.1 (m, 3H, CH_2ODMT H_{20} and CHCO*H*), 2.3 (t, 2H, CH_2CO H_{16}), 2.1 – 2.0 (m, 2H, CH_2CH$_2$CH$_2$CH$_2$CH$_2$CO H_{12}), 1.6 – 1.5 (m, 4H, CH_2CH$_2$CH$_2$CH$_2$CO H_{13} and CH_2CH$_2$CO H_{15}), 1.3 (q, 2H, CH_2CH$_2$CH$_2$CO H_{14}), 1.1 (d, J = 6.3 Hz, 3H, CH_3CHOH H_{21}).

^{13}C NMR (400 MHz, $CDCl_3$) δ 173.5 (C_{17}=O), 158.8 (2xC_{26}), 151.6 (C_9), 144.5 (C_{28}), 135.7 (2xC_{23}), 132.6 (2xC_{4a}), 130.1 (4xC_{24}), 128.6 (2xC_4), 128.2 (2xC_{29}), 128.1 (2xC_{30}), 127.2 (C_{31}), 125.6 (2xC_2), 125.2 (2xC_3), 124.9 (2xC_{9a}), 123.2 (2xC_1) 122.6 (C_{10}), 113.5 (4xC_{25}), 87.0 (C_{22}), 76.1 (C_{11}), 69.0 (C_{19}), 65.6 (C_{20}), 55.4 (2xC_{27}), 53.4 (C_{18}), 37.0 (C_{16}), 30.7 (C_{12}), 29.5 (C_{13}), 26.3 (C_{15}), 26.0 (C_{14}), 20.1 (C_{21}). m/z (ES MS) calcd for $C_{46}H_{49}O_6N$ ($M+Na^+$) 734.3458 found 734.3470

7.11.5 Synthesis of (2S,3S)-3-(7-(anthracen-9-yloxy)heptanamido)-4-(bis(4-methoxyphenyl)(phenyl)methoxy)butan-2-yl (2-cyanoethyl) diisopropylphosphoramidite

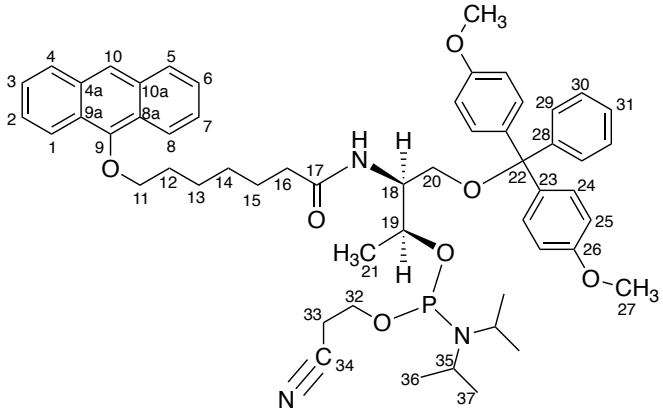

7-(Anthracen-9-yloxy)-N-((2S,3S)-1-(bis(4-methoxyphenyl)(phenyl)methoxy)-3-hydroxybutan-2-yl)heptanamide (1 g, 0.0014 mol) was dissolved in anhydrous DCM (50 mL). DIPEA (0.726 mL, 0.0042 mol) was added to the stirring solution in the dark and 2-Cyanoethyl-diisopropylchlorophosphoramidite (0.38 mL, 0.0017 mol) was added dropwise. The reaction was stirred for 1 h in the dark under an inert atmosphere. The solution was quenched by adding 1 mL of methanol and left to stir for another 15 minutes in the dark. The solution was diluted with DCM (50 mL), filtered and washed twice with a 2 M aqueous solution of sodium carbonate (50 mL) and once with brine (50 mL). The solution was then dried with magnesium sulphate. The product was purified using an activated basic alumina column with a solvent system of 49 % hexane, 50 % ethyl

acetate and 1 % TEA. The product yielded a yellow powdery solid 0.1332 g (0.00015 mol, 61 %).

^{1}H NMR (400 MHz, CD_3CN) δ 8.3 (s, 1H, H_{10}), 8.3 – 8.2 (m, 2H, H_1), 8.0 – 8.0 (m, 2H, H_4), 7.5 – 7.4 (m, 4H, H_3 and H_4), 7.3 – 7.2 (m, 6H, H_2 and H_{24}), 7.2 – 7.2 (m, 3H, H_{30} and H_{31}), 6.8 – 6.8 (m, 4H, H_{25}), 6.2 (d, J = 8.8 Hz, 1H, N*H*), 4.2 – 4.1 (m, 4H, O$CH_2CH_2CH_2$ H_{11}, C*H*NH H_{18}, CHC*H*OP H_{19}), 3.5 – 3.4 (m, 4H, POCH_2 H_{32} and PNC*H* H_{35}), 3.1 – 3.0 (m, 2H, CH_2ODMT H_{20}), 2.5 (t, J = 6.0 Hz, 2H, CH_2CN H_{33}), 2.2 (t, J = 3.6 Hz, 2H, CH_2CO H_{16}), 2.0 – 1.9 (m, 2H, C$H_2CH_2CH_2CH_2CH_2$CO H_{12}), 1.7 – 1.6 (m, 4H, C$H_2CH_2CH_2CH_2$CO H_{13} and CH_2CH_2CO H_{15}), 1.5 (dd, 3H, C$H_2CH_2CH_2$CO H_{14}), 1.2 – 1.0 (m, 12H, CH_3 H_{36}), 1.0 (t, J = 6.7, 3.5 Hz, 3H, CH_3CHOP H_{21}).

^{31}P NMR (122 MHz, CD_3CN) δ 147.6, 146.9. m/z (ES^+ MS) calcd for $C_{55}H_{66}O_7NaP$ ($M+Na^+$) 934.4536 found 934.4573.

7.12 Anthracene Three Point Star

7.12.1. Self-assembly of anthracene Three Point Star

The anthracene Three Point Star assembly was inspired by the literature.[12] A mixture of three oligonucleotides S1:S2:S3 in a molar ratio of 1:4:4 (375 nM : 1.5 µM : 1.5 µM) was heated rapidly to 95 °C and incubated for 5 minutes, subsequently cooled from 80 °C to 4 °C with a 5 minute hold at each 1.0 degree in 1 x TAMg annealing buffer (40 mM Tris-Cl, 26 mM $MgCl_2$, 25 mM acetic acid, pH 8.0). The annealing process was accomplished on a T Robot (Biometra) thermocycler and Beckman Coulter system.

7.12.2 Photocyclisation of anthracene Three Point Star

The photocyclisation reaction of the anthracene Three Point Star assembly was conducted after the annealing had taken place successfully. The solutions containing the assembly were degassed with argon for approximately 30 seconds. The degassed samples in PCR tubes were placed on a watch glass and immobilised. A 365 nm bandpass filter (Edmund Optics) with a 10 nm bandwidth was placed on top of the samples and surrounded with foil. A UV lamp (Spectroline) was placed on top in alignment with the samples and the filter. The entire apparatus was placed in a cold room at 4 ^{o}C. Irradiations were conducted in 3 hours' intervals up to 12 h.

7.13 Spectroscopy studies

7.13.1 UV/Vis absorption study

The UV/Vis experiments conducted in Chapter 3 were carried out using a Jasco J-810 spectropolarimeter (Jasco, Japan) using a 1 cm path length QS quartz cuvette. Baseline was subtracted from the sample spectra by measuring the absorbance of the buffer, the sample was dissolved in. The instrument parameters were as follows: Range - 220–400 nm, Response 1.0 s, Data pitch – 1.0 nm, Scanning mode - Continuous, Scan speed – 100 nm/min, Band width - 1.00 nm, and Accumulation - 3.

The UV/Vis experiments carried out in Chapter 4 and 5 were accomplished on a Shimadzu BioSpec Nano. Data sets were baseline corrected by subtracting the buffer absorbance. The scan range was 200-800 nm. The concentrations were made up to

10 µM. The buffering system for the duplex assemblies was 100 mM NaCl, 10 mM sodium phosphate, pH 7, whereas for the Holliday junction assemblies 10 mM $MgCl_2$, 5 mM TrisCl, 20 mM Tris acetate, 1 mM EDTA, pH 7.

7.13.2 Thermal denaturation study

Thermal melting experiments carried out in Chapter 4 and 5 were accomplished on a CamSpec, M550 Double Beam Scanning UV/Visible Spectrophotometer. The samples were made up to 10 µM. The buffering system for duplex assemblies was 100 mM NaCl, 10 mM sodium phosphate, pH 7; for the Holliday junction assemblies 10 mM $MgCl_2$, 5 mM TrisCl, 20 mM Tris acetate, 1 mM EDTA, pH 7; and for Holliday junction array assemblies was 10 mM $MgCl_2$, 5 mM TrisCl, 20 mM Tris acetate, 1 mM EDTA, 2% Triton, pH 7. One microliter of SsoAdvanced universal SYBR® green supermix (Bio-rad) was added to 19 µL of each 10 µM DNA assembly sample. The thermal denaturation experiments of DNA duplexes and Holliday junction assemblies were accomplished by heating the samples from 20 ^{o}C – 90 ^{o}C and cooled from 90 ^{o}C – 20 ^{o}C at a rate of 1 ^{o}C min^{-1}. Thermal denaturation experiment of Holliday junction array assemblies was accomplished by heating the samples from 20 ^{o}C – 80 ^{o}C and cooled from 80 ^{o}C – 20 ^{o}C at a rate of 0.1 ^{o}C min^{-1}. The monitored wavelength was 260 nm. Melting temperature values were calculated from the maxima of the negative first derivative of the melting curve.

Thermal melting experiments conducted in Chapter 6 were accomplished on an Agilent Cary500 UV/Vis Spectrophotometer using a 10 cm path length Q quartz

cuvette, by monitoring 260 nm wavelength. The concentrations of the samples were as follows: S1 – 375 nM, S2 and S3 – 1.5 µM each. The buffer system was 1xTAMg (40 mM Tris-Cl, 26 mM $MgCl_2$, 25 mM acetic acid, pH 8). The samples were heated from 25 ^{o}C – 95 ^{o}C, with temperature increase of 1 ^{o}C min^{-1}.

7.13.3 Circular Dichroism study

The CD experiments conducted in Chapter 3, 4 and 5 were carried out using a Jasco J-1500 spectropolarimeter (Jasco, Japan) using a 1 cm path length QS quartz cuvette. The parameters of measurements were as follows: Response time of 1.0 s, data pitch of 1.0 nm, bandwidth of 1.00 nm and a scanning speed of 100 nm min^{-1} with 3 accumulations. Data sets were baseline corrected. Samples in Chapter 3 were made up to their respective concentrations detailed in Chapter 3 and Section 7.4. Samples in Chapter 4 and 5 were made up to 10 µM. The buffering system for the duplex assemblies was 100 mM NaCl, 10 mM sodium phosphate, pH 7, whereas for the Holliday junction assemblies 10 mM $MgCl_2$, 5 mM TrisCl, 20 mM Tris acetate, 1 mM EDTA, pH 7.

7.14 Characterisation by PAGE

7.14.1 Native PAGE

Native polyacrylamide gel electrophoresis was performed vertically with a 20 % running gel for all duplex assemblies (Chapter 4 and 5) and 8 % for ferrocene tetrahedron (Chapter 5), Holliday junction (Chapter 5), anthracene 3PS (Chapter 6).

The running gel of duplex assemblies was comprised of 40% acrylamide solution (5 mL) added to 2 mL of 5 x TBE buffer (0.5 M Tris base, 0.5 M Boric Acid, 10 mM EDTA), 3 mL of MilliQ water and polymerised with 10% APS (75 µL) and TEMED (7.5 µL). The running gel of ferrocene tetrahedron, Holliday junction and anthracene 3PS assemblies was comprised of 40% acrylamide solution (2 mL) added to 1 mL of 10 x TAMg buffer (400 mM Tris-Cl, 260 mM $MgCl_2$, 250 mM acetic acid, pH 8) and 7 mL of MilliQ water and polymerised with 10% APS (75 µL) and TEMED (7.5 µL). The mixture was transferred into a 1 mm gel rack with a well comb and allowed to set for 10 minutes. Pre-annealed samples containing 0.5-1 µM DNA were mixed with 30% glycerol in 5:1 volumetric ratio and loaded into the wells. GeneRuler Ultra Low Range DNA ladder (Thermo Scientific) was run alongside the samples. Electrophoresis was undertaken at 4 ^{o}C for 3 h (for all duplex assemblies) or 1 h 30 min (for ferrocene tetrahedron, Holliday Junction and anthracene 3PS assemblies) at 100 V in electrophoresis buffer 1 x TBE (0.1 M Tris base, 0.1 M Boric Acid, 2 mM EDTA) for duplex assemblies and 1 x TAMg (40 mM Tris-Cl, 26 mM $MgCl_2$, 25 mM acetic acid, pH 8) for ferrocene tetrahedron, Holliday Junction and anthracene 3PS assemblies. The gel was stained with Diamond (Promega) stain for 10 minutes and visualised using AlphaImager HP (Alpha Innotech).

7.14.2 Denaturing PAGE

Denaturing polyacrylamide gel electrophoresis was performed vertically with a 15 % running gel for anthracene 3PS assemblies (Chapter 6) and 15 % running gel with 4 % stacking gel for ferrocene tetrahedron strands (Chapter 5). The running gel for

both experiments was comprised of 40% acrylamide solution (2 mL) added to 2 mL of 5 x TBE buffer (0.5 M Tris base, 0.5 M Boric Acid, 10 mM EDTA), 2.52 g Urea (7 M), 3 mL of MilliQ water and polymerised with 10% APS (75 µL) and TEMED (7.5 µL). The stacking gel was comprised of 40% acrylamide solution (0.53 mL) added to 2 mL of 5 x TBE buffer (0.5 M Tris base, 0.5 M Boric Acid, 10 mM EDTA), 3 mL of MilliQ water and polymerised with 10% APS (75 µL) and TEMED (7.5 µL). The resolving mixture was transferred into a 1 mm gel rack with a well comb and allowed to set for 10 minutes (for anthracene 3PS assemblies). For the ferrocene tetrahedron strands gel, the resolving mixture was transferred into a 1 mm gel rack, filling it to about 75 %, water was added carefully on the top of the unset gel solution and allowed to set for 10 minutes. The stacking gel mixture was then transferred onto the resolving gel, equipped with a comb and allowed to set for 20 minutes. Samples containing 4 µL of 250 nM (ferrocene tetrahedron strands) 10 µL of 375 nM – 1.5 µM DNA (anthracene 3PS assemblies) were mixed with formamide in 1:1 volumetric ratio and incubated for 15 minutes prior to loading into the wells, 5 µL in each well. 3 µL of GeneRuler Ultra Low Range DNA ladder (Thermo Scientific) was run alongside the samples. The electrophoretic run was undertaken for 3 h at 100 V in electrophoresis buffer 1 x TBE (0.1 M Tris base, 0.1 M Boric Acid, 2 mM EDTA). The gel was stained with Diamond (Promega) stain for 10 minutes and visualised using AlphaImager HP (Alpha Innotech).

7.15 References

1. T. Brown and T. J. Brown, Nucleic Acids Book 2013, https://www.atdbio.com/content/17/Solid-phase-oligonucleotide-synthesis, (accessed 25/07/2019).
2. J. Pollard, Purification of oligonucleotides using denaturing polyacrylamide gel electrophoresis, https://molbio.mgh.harvard.edu/szostakweb/protocols/denaturepage/index.html, (accessed 2015-2019).
3. I. D. Technologies, OligoAnalyzer Tool, https://www.idtdna.com/calc/analyzer, (accessed 2015-2019).
4. Diagenode, Standard protocols DNA shearing for Bioruptor Pico, https://www.diagenode.com/files/protocols/Standard_protocols_for_DNAShearing.pdf, (accessed 2015-2019).
5. G. Leck, *Metal Modified DNA Assemblies, DNA Origami and their Potential Use in Fuel Cell Catalysis*, University of Birmingham, 2017.
6. E. Hebda, M. Jancia, F. Kajzar, J. Niziol, J. Pielichowski, I. Rau and A. Tane, *Mol. Cryst. Liq. Cryst.*, 2012, **556**, 309-316.
7. A. Gopinath and P. W. K. Rothemund, *ACS Nano*, 2014, **8**, 12030-12040.
8. E. Stahl, T. G. Martin, F. Praetorius and H. Dietz, *Angew. Chem. Int. Ed.*, 2014, **53**, 12735-12740.
9. J. Malo, J. C. Mitchell and A. J. Turberfield, *J. Am. Chem. Soc.*, 2009, **131**, 13574-13575.
10. R. P. Goodman, R. M. Berry and A. J. Turberfield, *Chem. Comm.*, 2004, 1372-1373.
11. J.-L. H. A. Duprey, Doctor of Philosophy, Birmingham, 2010.
12. N. Avakyan, J. W. Conway and H. F. Sleiman, *ACS*, 2017, **139**, 12027-12034.

8 - Appendix

8.1 Mass Spectrometry and Reversed–phase High Performance Liquid Chromatography

Table 8.1 – DNA oligonucleotide calculated masses, sequences and codes used within this Thesis.

Name	Number	Molecular Mass	Sequence
G14 Probe	1687	4287.8	5′-CAT TGA GGAG TCC A-3′
G14 Target	1688	4238.8	5′-TGG ACT CCT CAA TG-3′
cisPt G14 Probe	1687 cisPt	4516.8	5′-CAT TGA GG **(cisPt)** AGT CCA-3′
G20 Probe	1676	5951.9	5′-TCT CCT TCT GGT CTC TTC TC-3′
G20 Target	1677	6282.2	5′-GAG AAG AGA CCA GAA GGA GA-3′
Thiol G20 Target	524 (sigma)	6612.3	5′-GAG AAG AGA CCA GAA GGA GA-thiol-3′
cisPt-G20 Probe	1676 cisPt	6180.9	5′-TCT CCT TCT GG **(cisPt)** TCT CTT CTC-3′
PolyT-GG	2021	6984.6	5′-TTT TTT TTT TTT TTT TTT TTT GG-3′
PolyA	2023	6515.4	5′-AAA AAA AAA AAA AAA AAA AAA-3′
cisPt PolyT-GG	2021 cisPt	7213.6	5′-TTT TTT TTT TTT TTT TTT TTG G**(cisPt)**-3′
HJA*-1	2077	11340.4	5'-AGA GGA ACA TGC CTT CTG GAC CGT TGT CTA CCT TAG C-3'
HJA*-2	2079	7732	5'-CTC TTC TCT GGT CTT CCT CTC TTC TC-3'
HJA*-3	2078	13046.5	5'-CAC GAG GAT TGC TCA CTG TTC CGG ACC AGA GAA GAG GAG AAG-3'
HJA*-4/ HJA-4	2076	16449.7	5'-GTA GAC AAC GGT CCA GAA GGC ATG CGG AAC AGT GAG CAA TCC TCG TGG CTA AG-3'
cisPt HJA*-2	2079 cisPt	7961	5'-CTC TTC TCT GG**(cisPt)**TCT TCC TCT CTT CTC-3'
Fc-G20 Probe	2096	5655.01	5′-TCT CCT TCT **Fc** TCT CTT CTC-3′
HJ-1	2090	9164.57	5'-CTA ACT ACA TGC CTT **Fc** GGA CCG TTG TCT AC-3'
HJ-2	2087	6243.05	5'-GCG ATG AGC AGG ATA GTT AG-3'
HJ-3	2091	10704.87	5'-CAC GAG GAT TGC **Fc** ACT GTT CCG TCC TGC TCA TCG C-3'

HJ-4	2101	14565.44	5'-GTA GAC AAC GGT CCA GAA GGC ATG CGG AAC AGT GAG CAA TCC TCG TG-3'
HJA-1	2088	10991.92	5'-CTA ACT ACA TGC CTT **Fc** GGA CCG TTG TCT ACC TTA GC-3'
HJA-2	2098	8095.36	5'-GCG ATG AGC AGG ATA GTT AGA GTA TC-3'
HJA-3	2089	12557.17	5'-CAC GAG GAT TGC **Fc** ACT GTT CCG TCC TGC TCA TCG CGA TAC T-3'
Fc-T1	1841	17241.51	5′-ACA TTC CTA AGT CTG AAA **Fc** CAT TAC AGC TTG CTA CAC GAG AAG AGC CGC CAT AGT A-3′
Fc-T2	1842	17393.61	5′-TAT CAC CAG GCA GTT GAC **Fc** AGT GTA GCA AGC TGT AAT AGA TGC GAG GGT CCA ATA C-3′
Fc-T3	1843	17271.51	5′-TCA ACT GCC TGG TGA TAA **Fc** AAC GAC ACT ACG TGG GAA TCT ACT ATG GCG GCT CTT C-3′
Fc-T4	1844	17250.41	5′-TTC AGA CTT AGG AAT GTG **Fc** CTT CCC ACG TAG TGT CGT TTG TAT TGG ACC CTC GCA T-3′
T1	1547	16880	5′-ACA TTC CTA AGT CTG AAA CAT TAC AGC TTG CTA CAC GAG AAG AGC CGC CAT AGT A-3′
T2	1548	17032.1	5′-TAT CAC CAG GCA GTT GAC AGT GTA GCA AGC TGT AAT AGA TGC GAG GGT CCA ATA C-3′
T3	1562	16910	5′-TCA ACT GCC TGG TGA TAA AAC GAC ACT ACG TGG GAA TCT ACT ATG GCG GCT CTT C-3′
T4	1563	16888.9	5′-TTC AGA CTT AGG AAT GTG CTT CCC ACG TAG TGT CGT TTG TAT TGG ACC CTC GCA T-3′
S1	-	22083.3	5′-AGG CAC CAT CGT AGG TTT CTT GCC AGG CAC CAT CGT AGG TTT CTT GCC AGG CAC CAT CGT AGG TTT CTT GCC-3′
S2	-	13206.6	5′-ACT ATG CAA CCT GCC TGG CAA GCC TAC GAT GGA CAC GGT AAC G-3′
S3	-	6772.4	5′-CGT TAC CGT GTG GTT GCA TAG T-3′
S2-Ant	1759	13479.2	5′-ACT A **Ant** GCA ACC TGC CTG GCA AGC CTA CGA TGG ACA CGG **Ant** AAC G-3′
S3-Ant	1761	7027.0	5′-CGT T **Ant** CCG TGT GGT TGC **Ant** TAG T-3′

8.2 Mass Spectrometry and Reversed–phase High Performance Liquid Chromatography

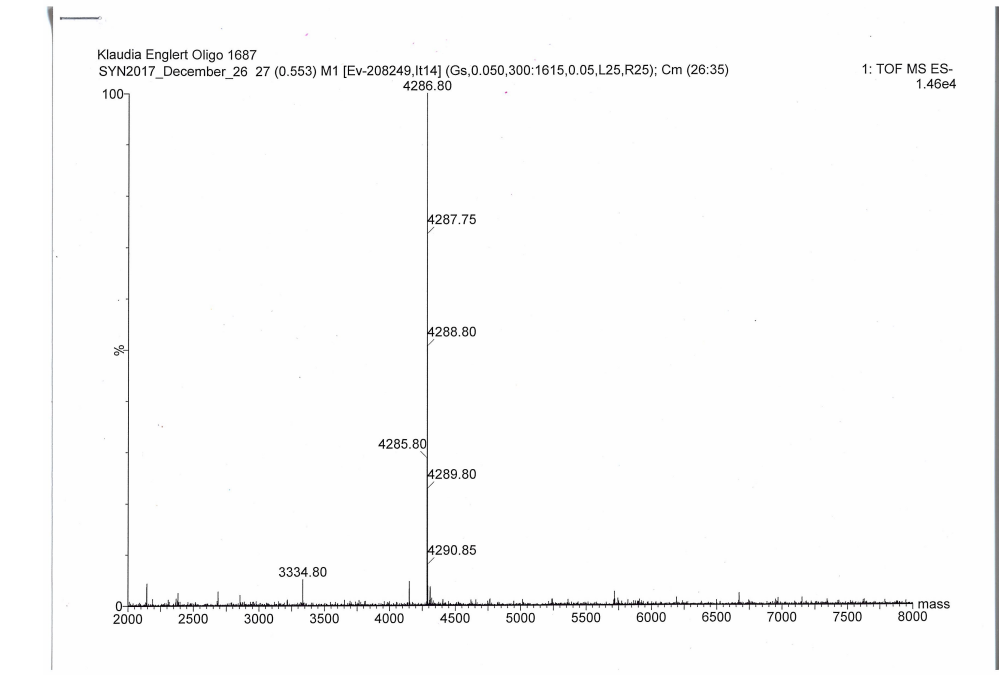

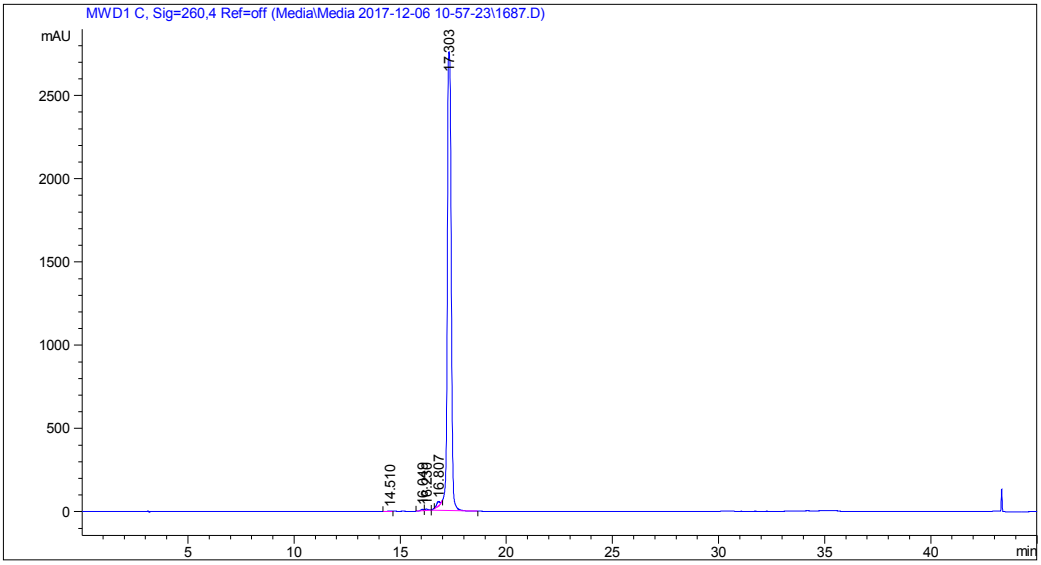

Peak #	Ret Time [min]	Type	Width [min]	Area [mAU*s]	Height [mAU]	Area %
1	14.510	BV	0.1940	30.20939	2.44780	0.0833
2	16.049	BV	0.1471	73.12758	7.54150	0.2017
3	16.230	VB	0.1527	90.81232	8.36022	0.2505
4	16.807	BV E	0.1624	289.71552	26.74547	0.7992
5	17.303	VB R	0.2035	3.57671e4	2754.21631	98.6652
Totals :				3.62510e4	2799.31130	

Figure 8.2.1 – ESI-MS and RP HPLC data of the purified G14 probe and eluted into MilliQ water. This strand was purified using the Short Oligo method (Chapter 7.2.2) and absorption was monitored at 260 nm.

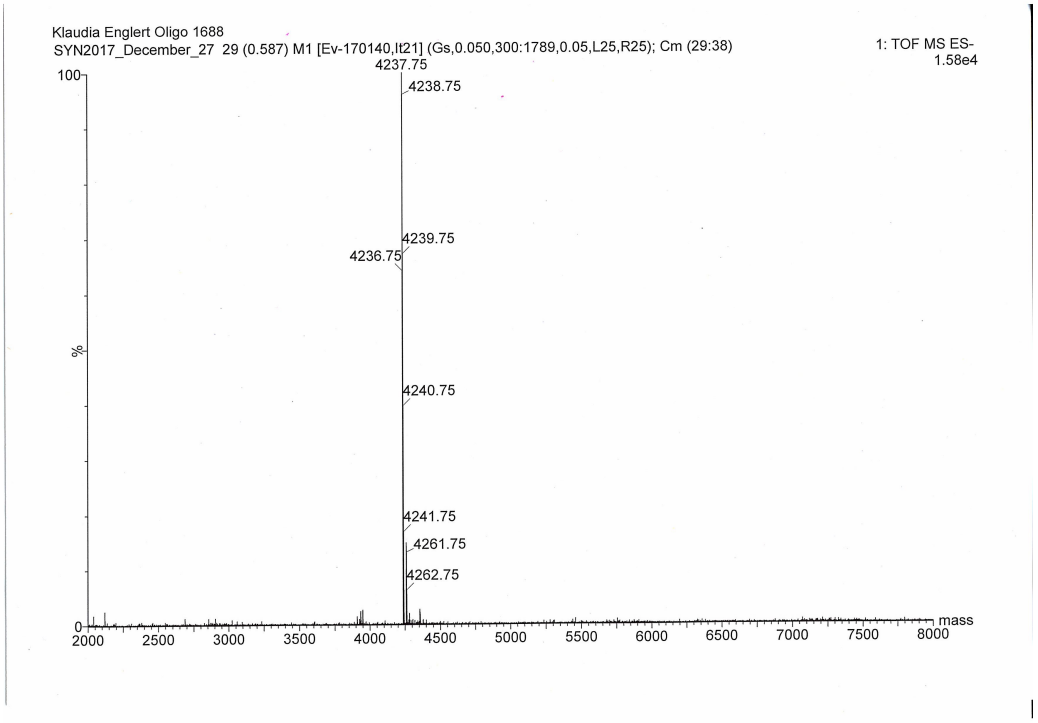

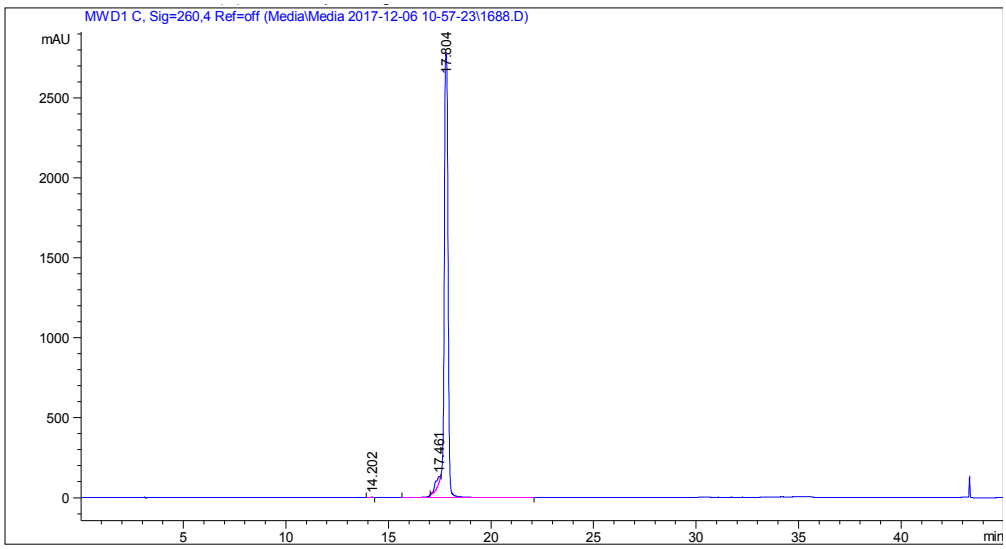

Peak #	Ret Time [min]	Type	Width [min]	Area [mAU*s]	Height [mAU]	Area %
1	14.202	BV	0.1432	23.31700	2.44525	0.0605
2	17.461	VV E	0.2780	864.49304	39.70393	2.2448
3	17.804	VB R	0.2102	3.76225e4	2774.83789	97.6946
Totals :				3.85103e4	2816.98707	

Figure 8.2.2 – ESI-MS and RP HPLC data of the purified G14 target and eluted into MilliQ water. This strand was purified using the Short Oligo method (Chapter 7.2.2) and absorption was monitored at 260 nm.

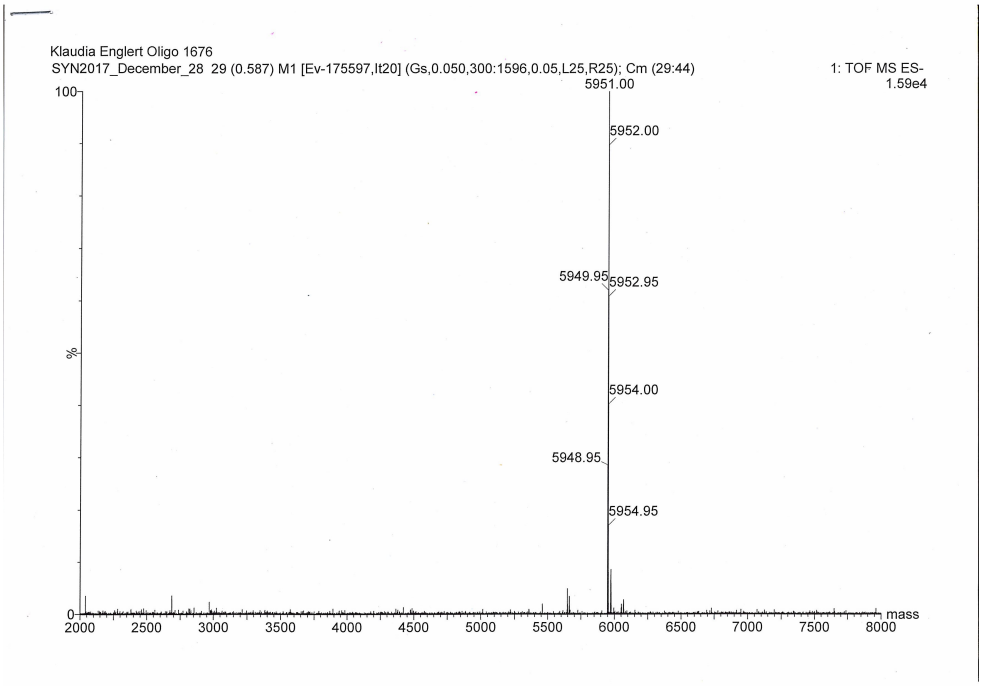

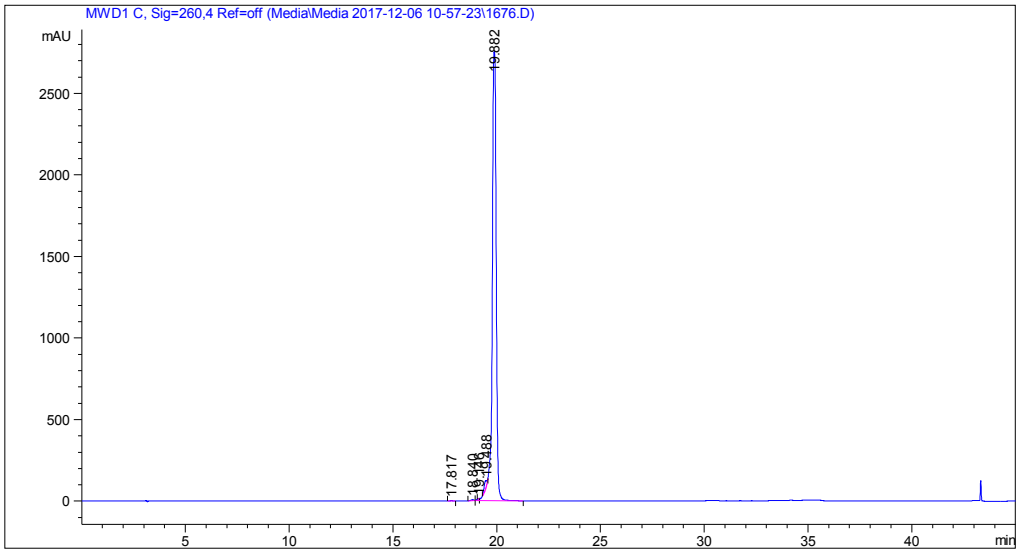

Peak #	Ret Time [min]	Type	Width [min]	Area [mAU*s]	Height [mAU]	Area %
1	17.817	VB	0.1533	20.58050	1.98019	0.0543
2	18.840	BB	0.1534	41.15581	4.31113	0.1087
3	19.146	BV E	0.0871	10.91972	2.23041	0.0288
4	19.488	VV E	0.1570	448.05252	43.20572	1.1830
5	19.882	VB R	0.2084	3.73531e4	2751.43628	98.6251
Totals :				3.78738e4	2803.16372	

Figure 8.2.3 – ESI-MS and RP HPLC data of the purified G20 probe and eluted into MilliQ water. This strand was purified using the Short Oligo method (Chapter 7.2.2) and absorption was monitored at 260 nm.

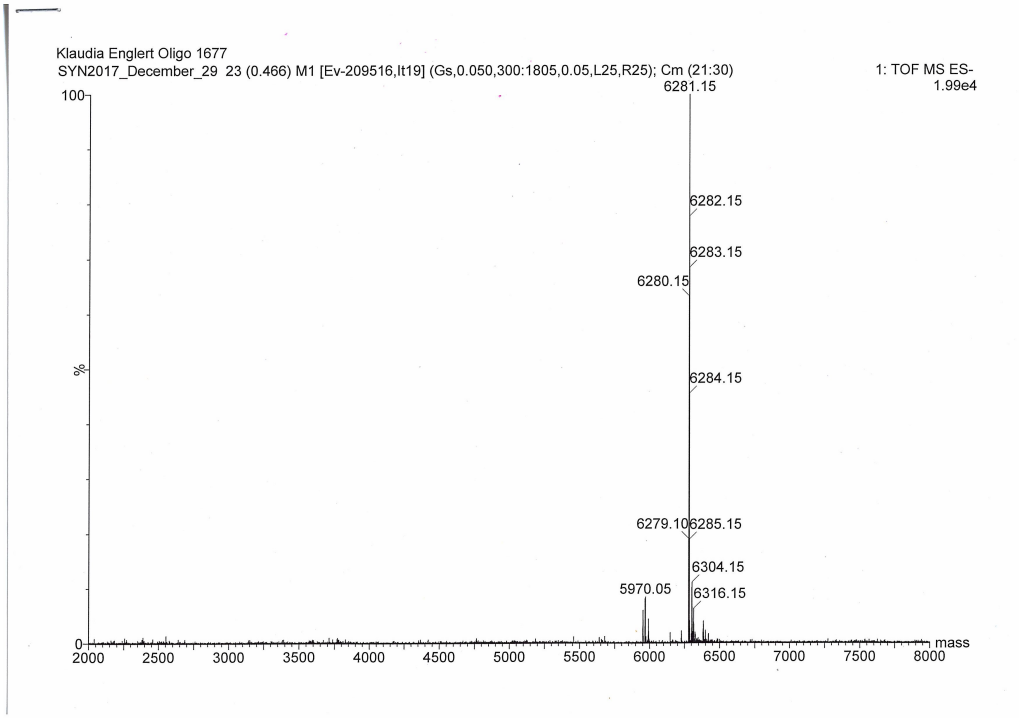

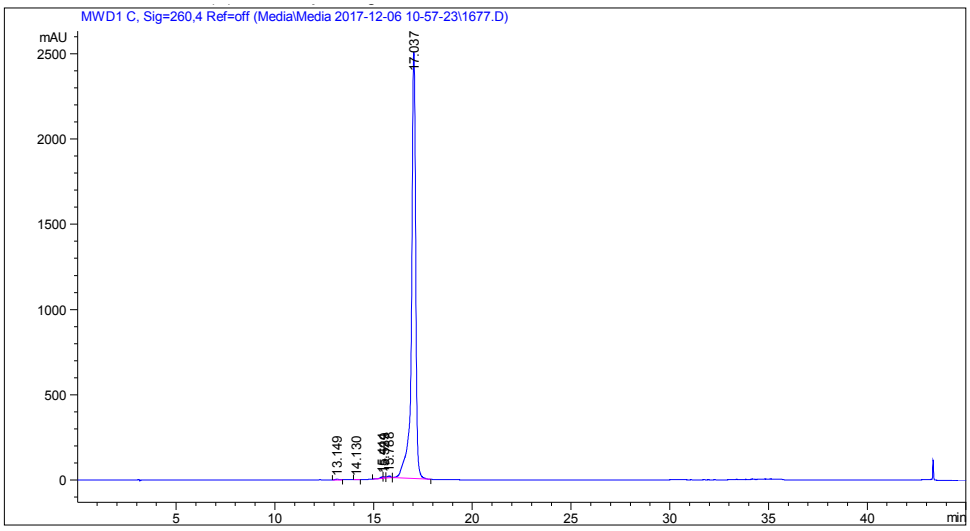

Peak #	Ret Time [min]	Type	Width [min]	Area [mAU*s]	Height [mAU]	Area %
1	13.149	BV	0.1788	53.89816	4.34181	0.1436
2	14.130	VB	0.1711	24.37810	2.20281	0.0649
3	15.444	BV	0.1502	86.97642	8.44376	0.2317
4	15.529	VV	0.1139	60.27130	7.65390	0.1606
5	15.788	VB	0.1756	129.33073	11.12808	0.3446
6	17.037	BB	0.2216	3.71791e4	2498.53101	99.0546
Totals :				3.75340e4	2532.30137	

Figure 8.2.4 – ESI-MS and RP HPLC data of the purified G20 target and eluted into MilliQ water. This strand was purified using the Short Oligo method (Chapter 7.2.2) and absorption was monitored at 260 nm.

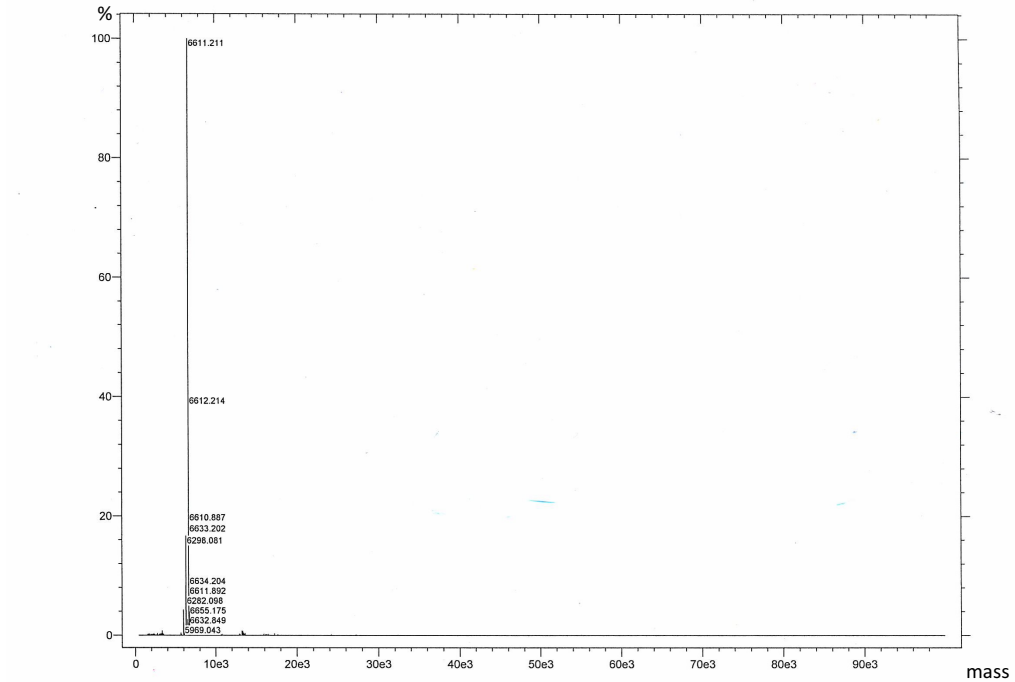

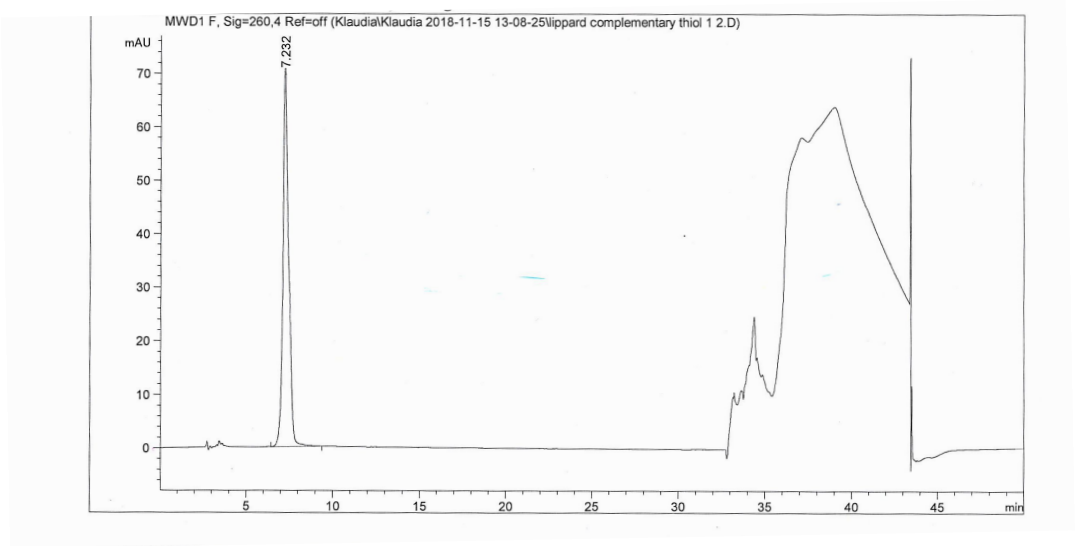

Peak #	RetTime [min]	Type	Width [min]	Area [mAU*s]	Height [mAU]	Area %
1	7.232	BB	0.3249	1617.14832	70.69635	100.0000
Totals :				1617.14832	70.69635	

Figure 8.2.5 – ESI-MS and RP HPLC data of the purified Thiol G20 target and eluted into MilliQ water. This strand was purified using the Short Oligo method (Chapter 7.2.2) and absorption was monitored at 260 nm.

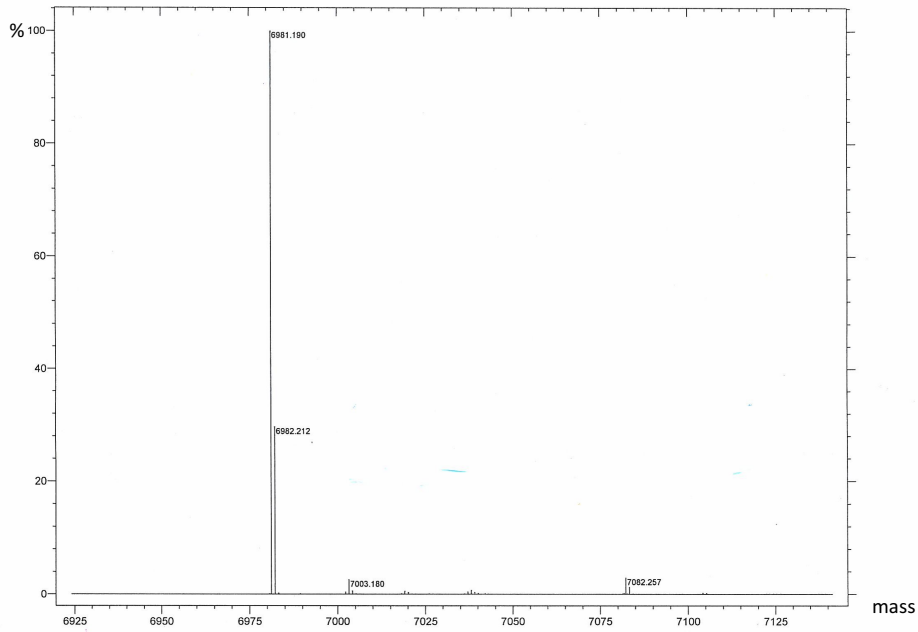

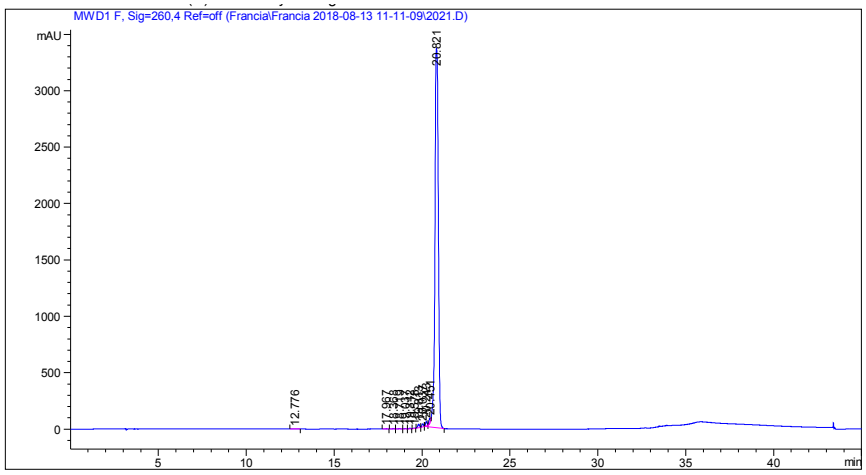

Peak #	Ret Time [min]	Type	Width [min]	Area [mAU*s]	Height [mAU]	Area %
1	12.776	BB	0.1245	19.16332	2.31705	0.0410
2	17.967	BB	0.1126	23.90079	3.21849	0.0511
3	18.368	BB	0.1093	26.98080	3.77716	0.0577
4	18.719	BV	0.1184	30.34140	3.83162	0.0649
5	19.037	VB	0.1069	25.01021	3.69712	0.0535
6	19.312	BB	0.1043	34.15051	5.22505	0.0730
7	19.578	BB	0.1071	17.51546	2.64974	0.0374
8	19.813	BB	0.1097	218.09540	31.93956	0.4662
9	20.037	BB	0.0979	164.51714	27.47050	0.3517
10	20.243	BV E	0.1002	245.51767	38.61999	0.5249
11	20.451	VV E	0.1088	267.64478	36.80193	0.5722
12	20.821	VB R	0.2126	4.57058e4	3361.20386	97.7066
Totals :				4.67786e4	3520.75208	

Figure 8.2.6 – ESI-MS and RP HPLC data of the purified PolyT-GG and eluted into MilliQ water. This strand was purified using the Short Oligo method (Chapter 7.2.2) and absorption was monitored at 260 nm.

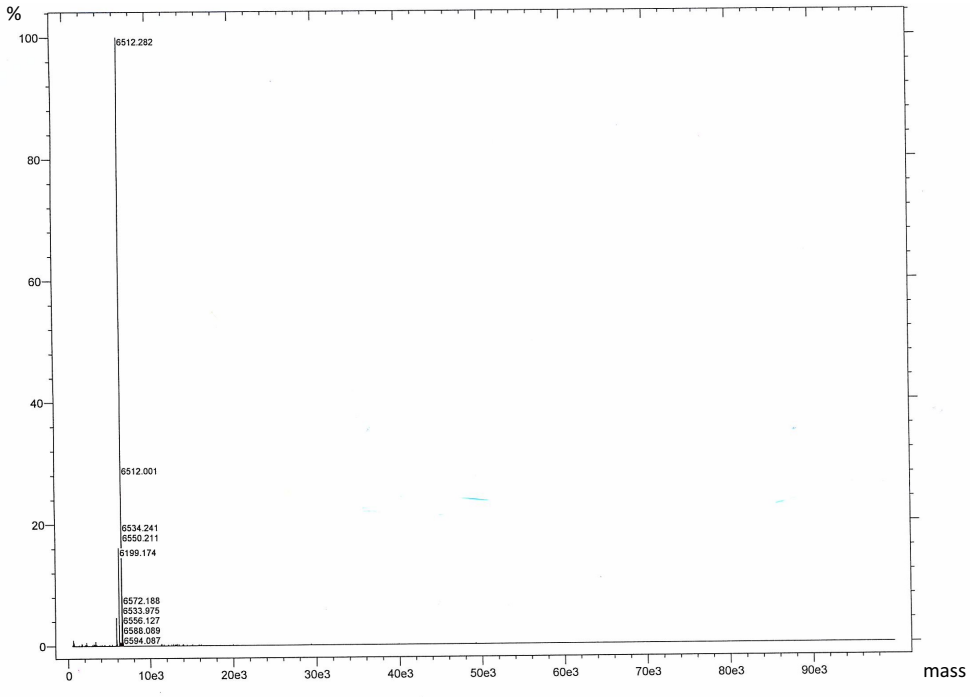

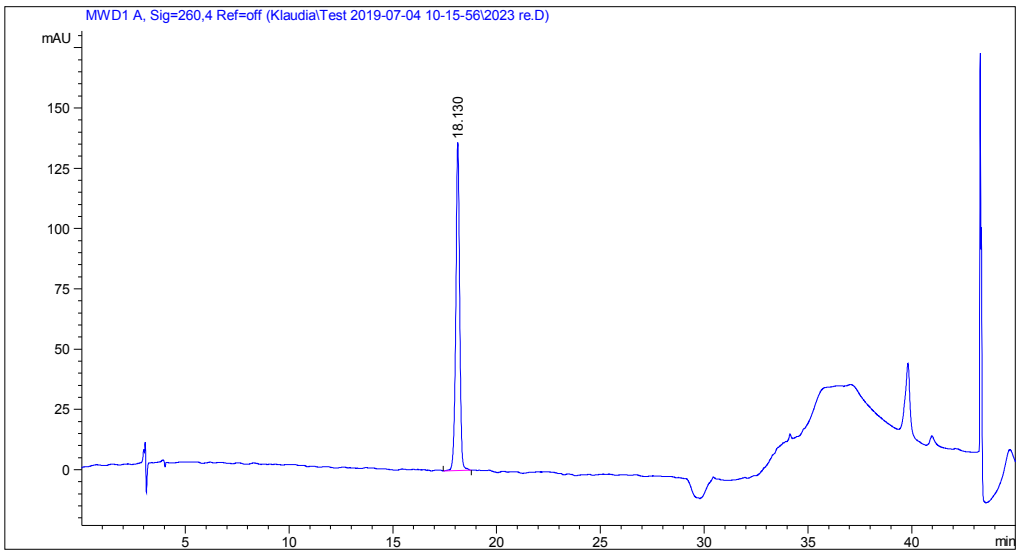

Peak #	Ret Time [min]	Type	Width [min]	Area [mAU*s]	Height [mAU]	Area %
1	18.130	BB	0.1947	1758.85022	136.14397	100.0000
Totals :				1758.85022	136.14397	

Figure 8.2.7 – ESI-MS and RP HPLC data of the purified PolyA and eluted into MilliQ water. This strand was purified using the Short Oligo method (Chapter 7.2.2) and absorption was monitored at 260 nm.

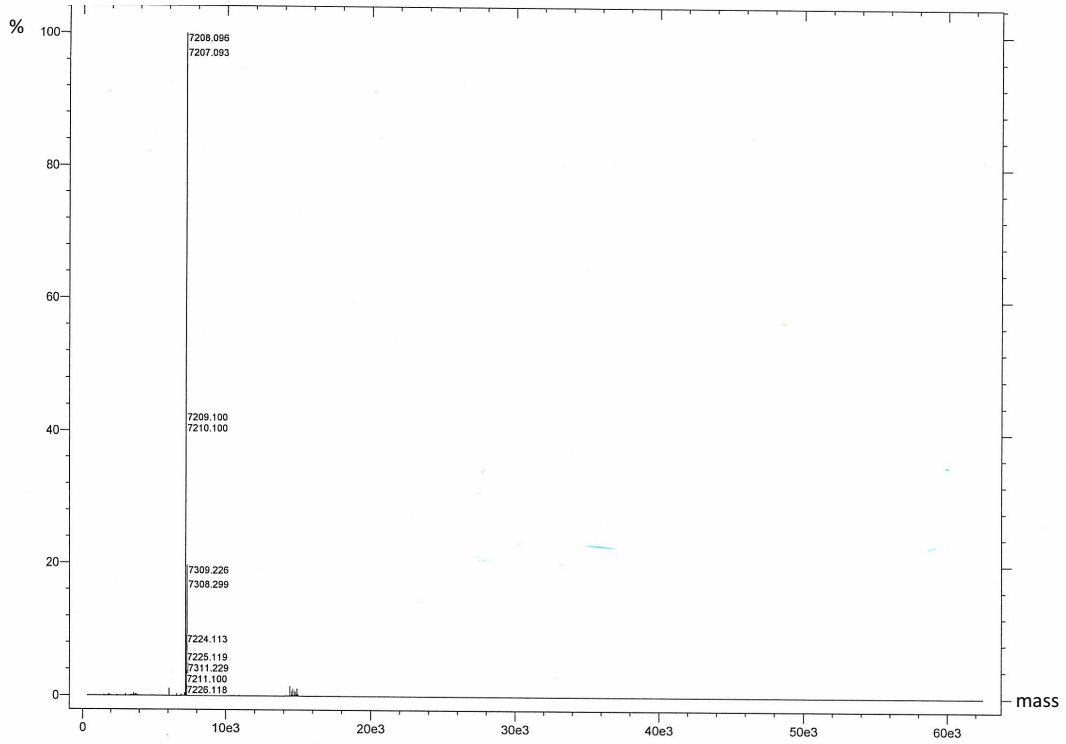

Additional Info : Peak(s) manually integrated

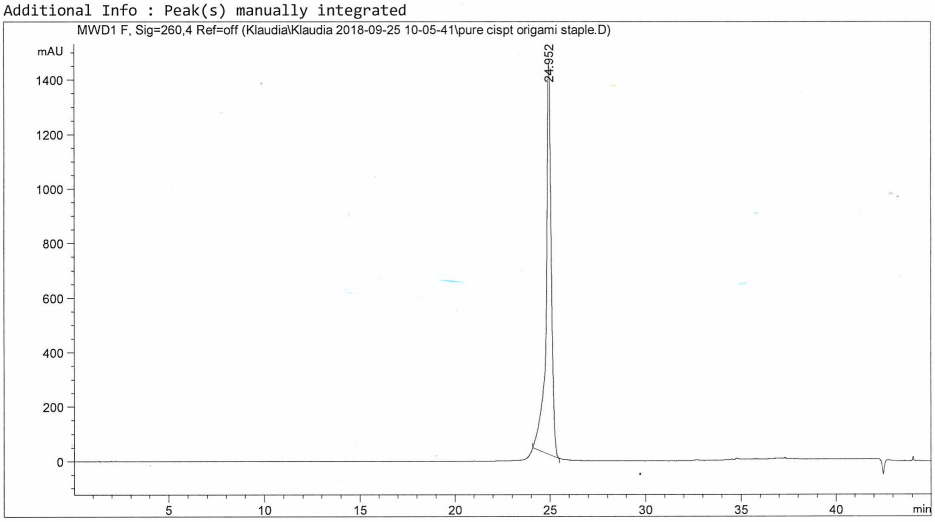

Peak #	RetTime [min]	Type	Width [min]	Area [mAU*s]	Height [mAU]	Area %
1	24.952	BB	0.2773	2.74156e4	1432.29639	100.0000
Totals :				2.74156e4	1432.29639	

Figure 8.2.8 – ESI-MS and RP HPLC data of the purified cisPt PolyT-GG and eluted into MilliQ water. This strand was purified using 50 mM HFIP, 15 mM HA buffer, pH: 7, 1.0 flow rate, 60 ^{o}C, Kinetex C18 column, with gradient 20-45% (20 min), 45-50% (5 min), 50% (5 min) methanol and absorption was monitored at 260 nm.

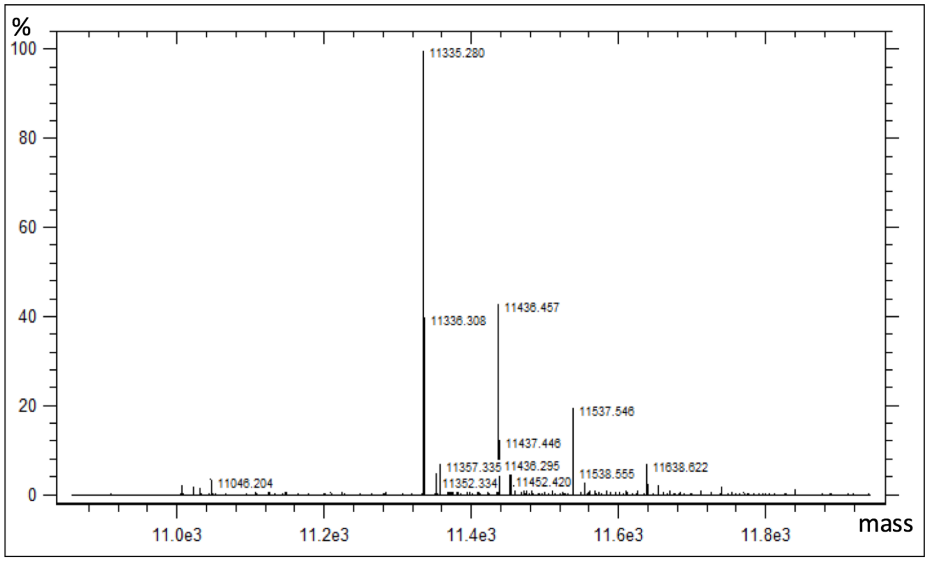

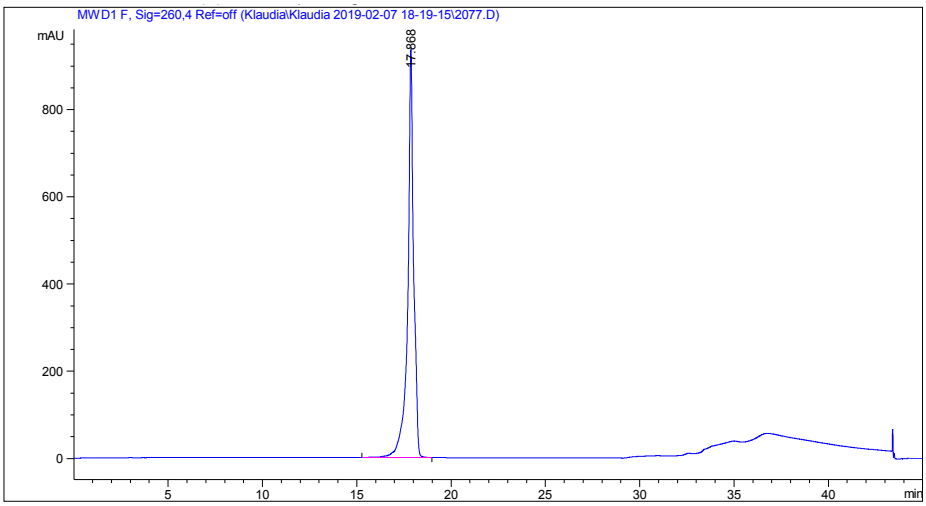

Peak #	Ret Time [min]	Type	Width [min]	Area [mAU*s]	Height [mAU]	Area %
1	17.868	VB R	0.2963	2.03815e4	935.09503	100.0000
Totals :				2.03815e4	935.09503	

Figure 8.2.9 – ESI-MS and RP HPLC data of the purified HJA*-1 and eluted into MilliQ water. This strand was purified using the Short Oligo method (Chapter 7.2.2) and absorption was monitored at 260 nm.

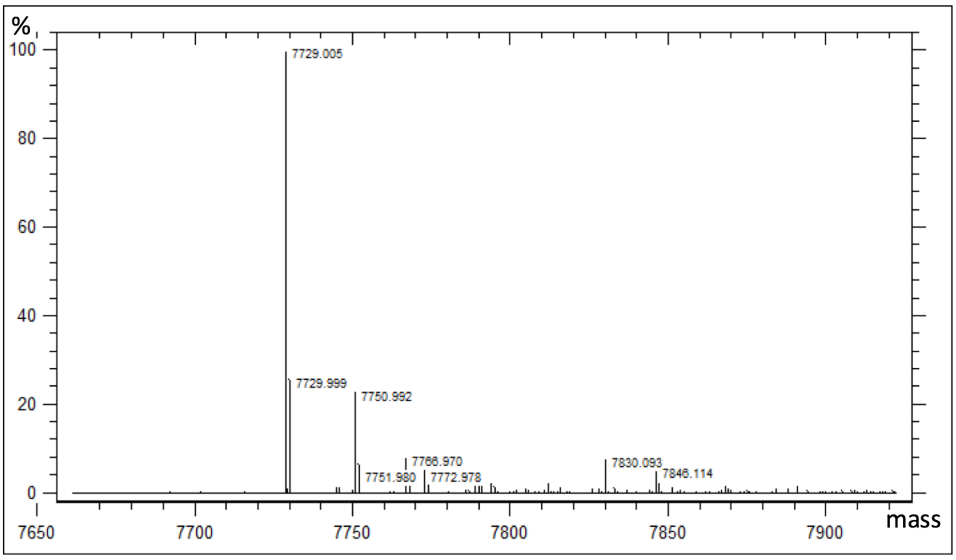

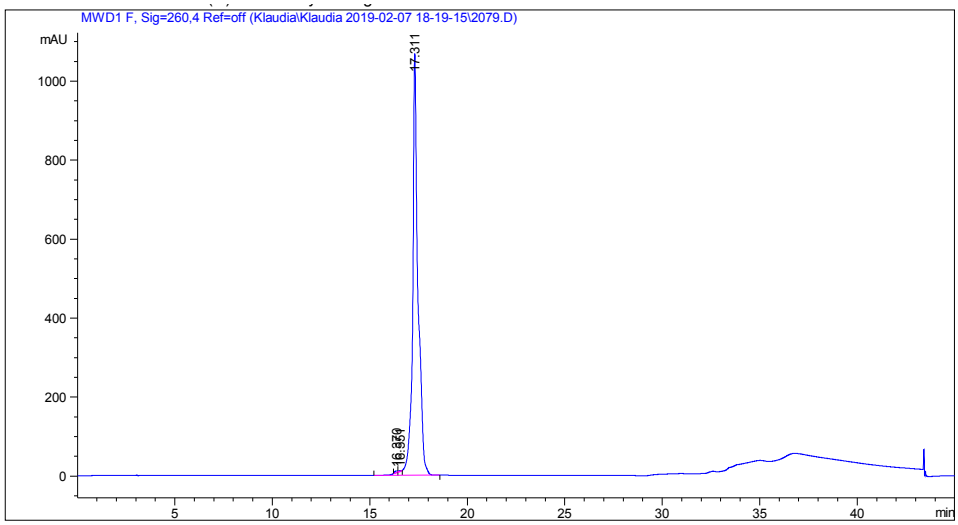

Peak #	Ret Time [min]	Type	Width [min]	Area [mAU*s]	Height [mAU]	Area %
1	16.370	BV E	0.1640	49.82689	4.84500	0.2415
2	16.551	VV E	0.1471	21.87362	2.07253	0.1060
3	17.311	VB R	0.2647	2.05580e4	1067.38147	99.6524
Totals :				2.06297e4	1074.29899	

Figure 8.2.10 – ESI-MS and RP HPLC data of the purified HJA*-2 and eluted into MilliQ water. This strand was purified using the Short Oligo method (Chapter 7.2.2) and absorption was monitored at 260 nm.

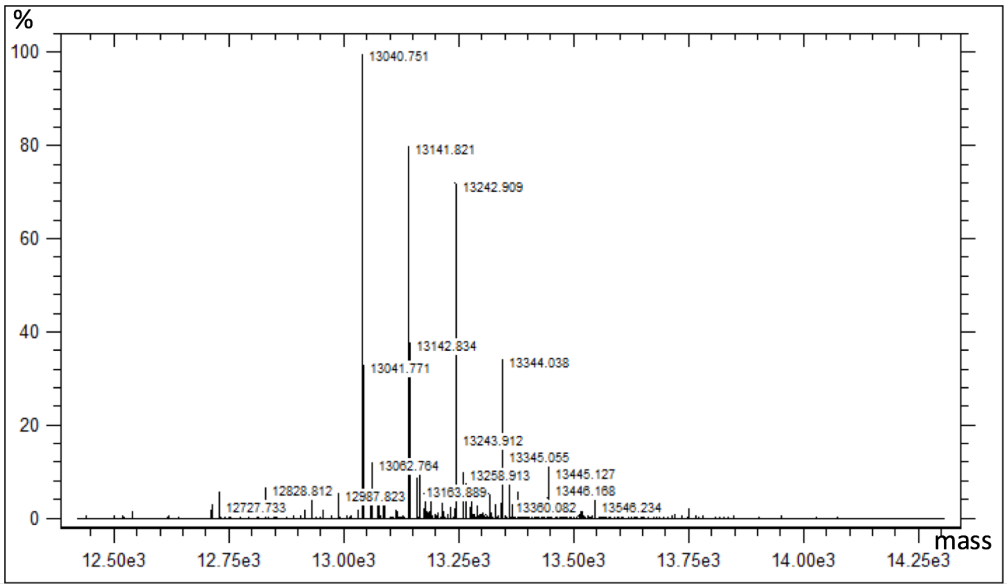

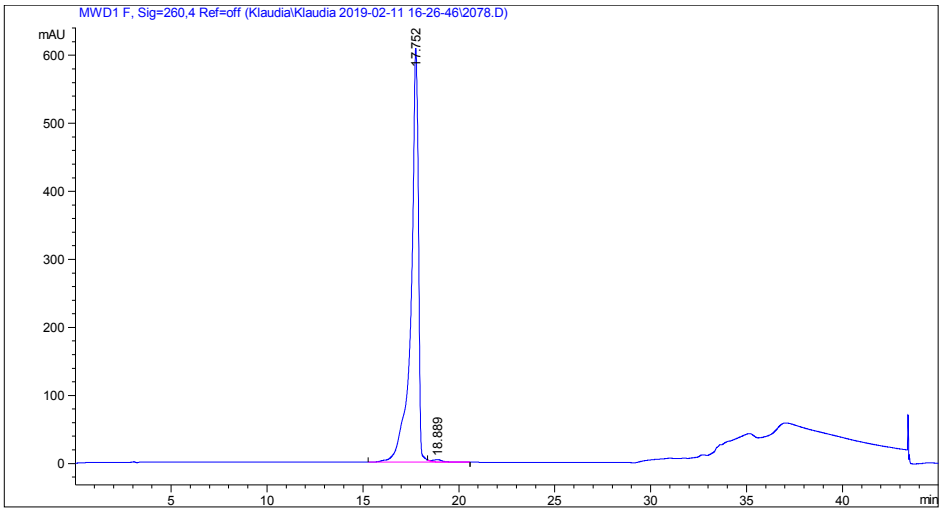

Peak #	Ret Time [min]	Type	Width [min]	Area [mAU*s]	Height [mAU]	Area %
1	17.752	BV R	0.3871	1.62305e4	608.57495	99.2324
2	18.889	VB E	0.5021	125.55582	3.50347	0.7676
Totals :				1.63560e4	612.07842	

Figure 8.2.11 – ESI-MS and RP HPLC data of the purified HJA*-3 and eluted into MilliQ water. This strand was purified using the Short Oligo method (Chapter 7.2.2) and absorption was monitored at 260 nm.

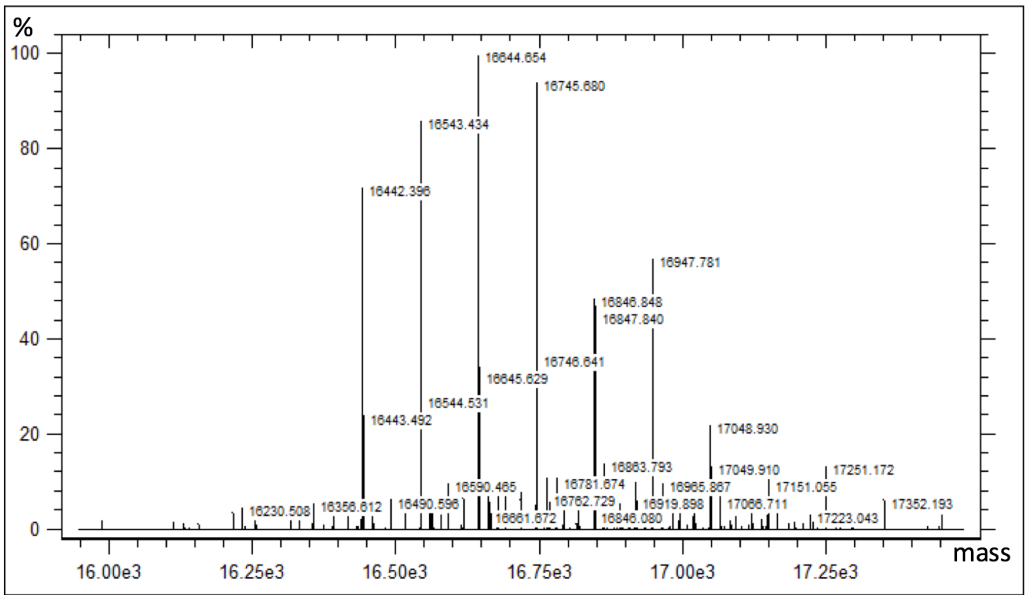

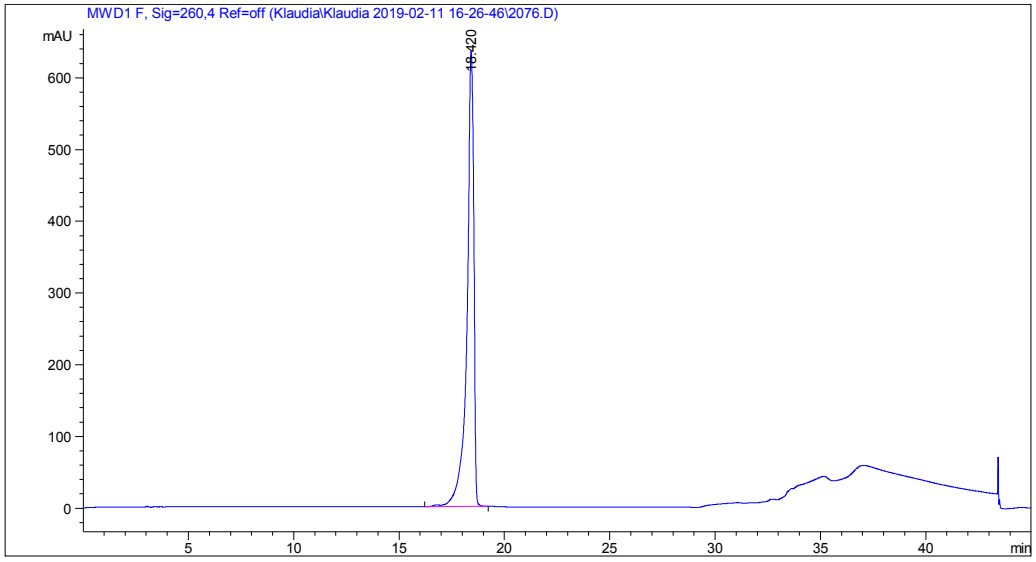

Peak #	Ret Time [min]	Type	Width [min]	Area [mAU*s]	Height [mAU]	Area %
1	18.420	VB R	0.3344	1.42576e4	633.86096	100.0000
Totals :				1.42576e4	633.86096	

Figure 8.2.12 – ESI-MS and RP HPLC data of the purified HJA*-4/HJA-4 and eluted into MilliQ water. This strand was purified using the Short Oligo method (Chapter 7.2.2) and absorption was monitored at 260 nm.

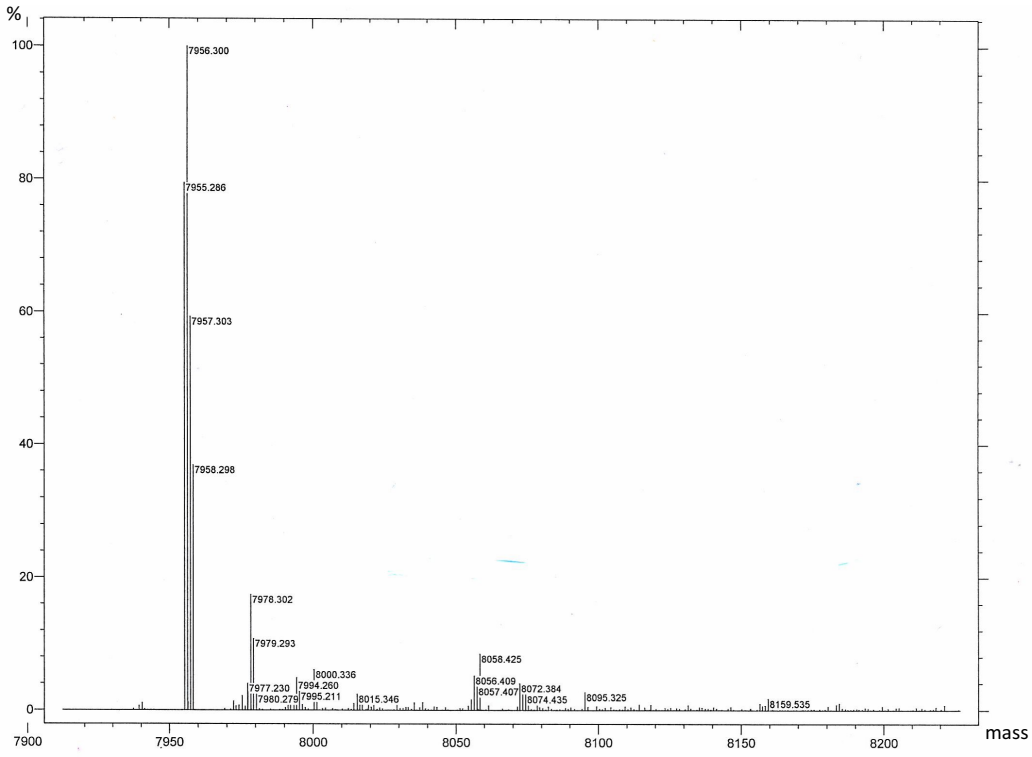

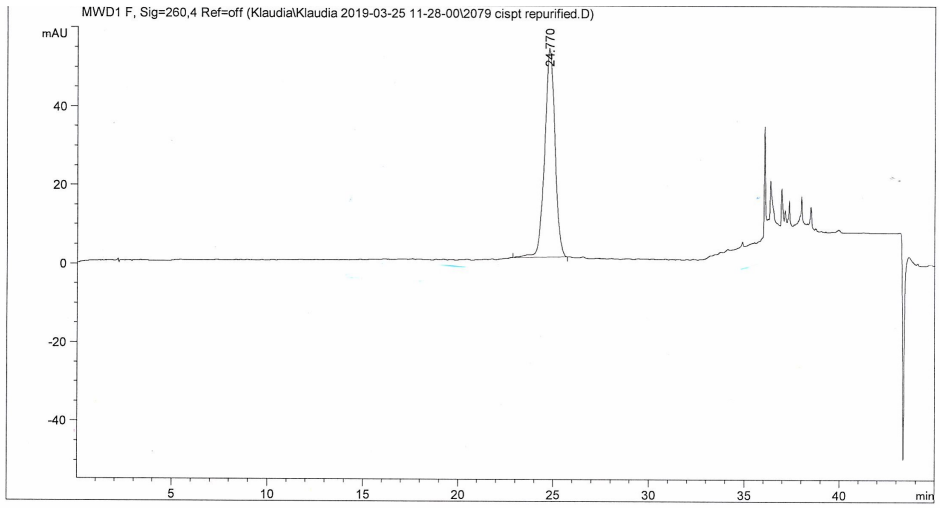

Peak #	RetTime [min]	Type	Width [min]	Area [mAU*s]	Height [mAU]	Area %
1	24.770	BB	0.5769	1994.45520	53.01543	100.0000
Totals :				1994.45520	53.01543	

Figure 8.2.13 – ESI-MS and RP HPLC data of the purified cisPt HJA*-2 and eluted into MilliQ water. This strand was purified using 50 mM HFIP, 15 mM HA buffer, pH: 7, 1.0 flow rate, 60 ^{o}C, Kinetex C18 column, with gradient 20-45% (20 min), 45-50% (5 min), 50% (5 min) methanol and absorption was monitored at 260 nm.

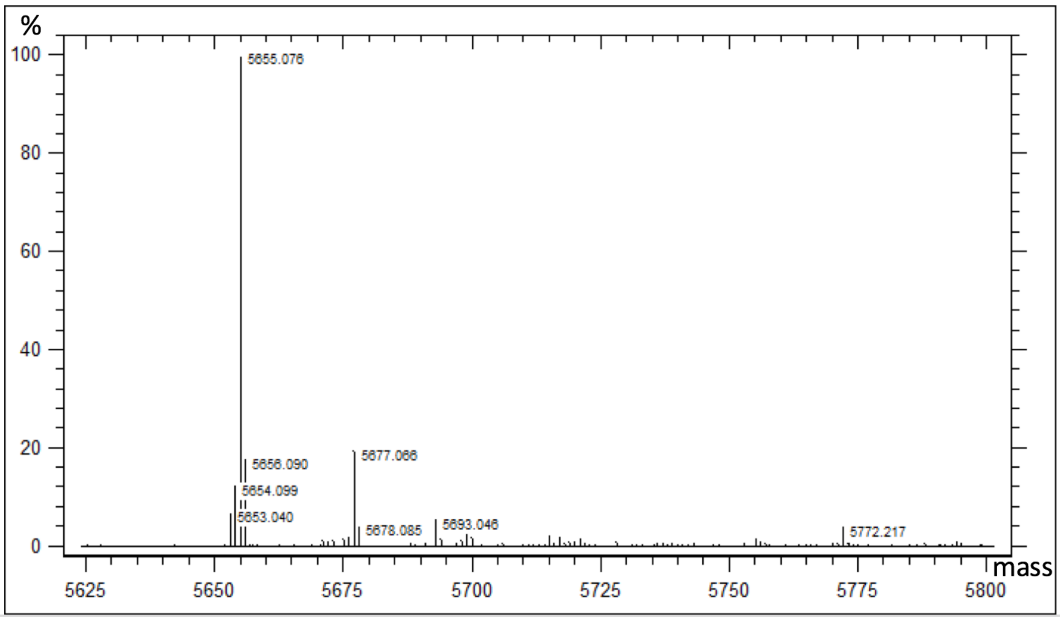

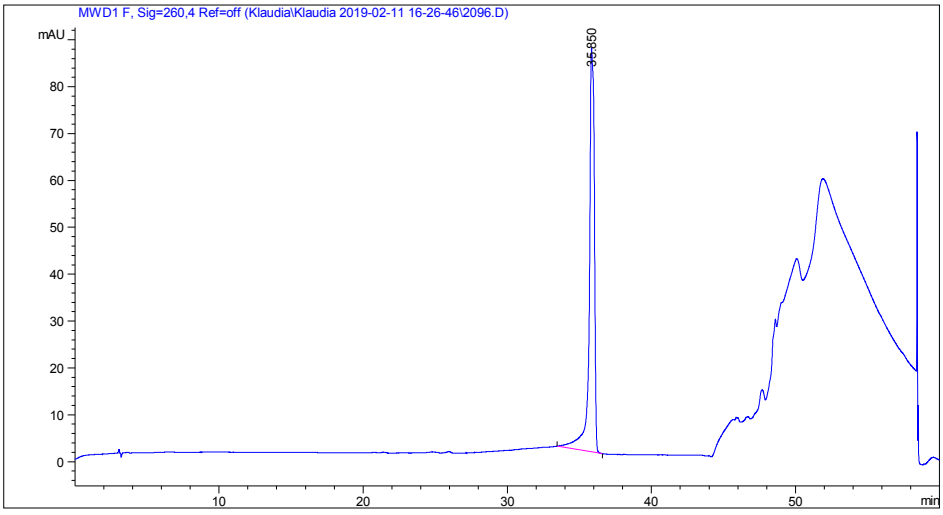

Peak #	Ret Time [min]	Type	Width [min]	Area [mAU*s]	Height [mAU]	Area %
1	35.850	BB	0.3319	2140.79541	86.14102	100.0000
Totals :				2140.79541	86.14102	

Figure 8.2.14 – ESI-MS and RP HPLC data of the purified Fc-G20 and eluted into MilliQ water. This strand was purified using the FcNA Anth method (Chapter 7.2.2) and absorption was monitored at 260 nm.

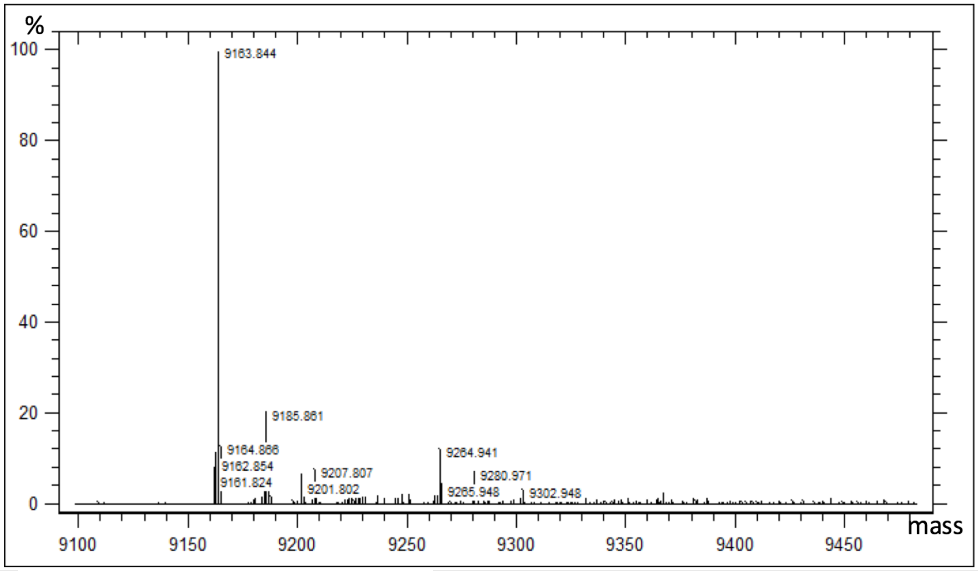

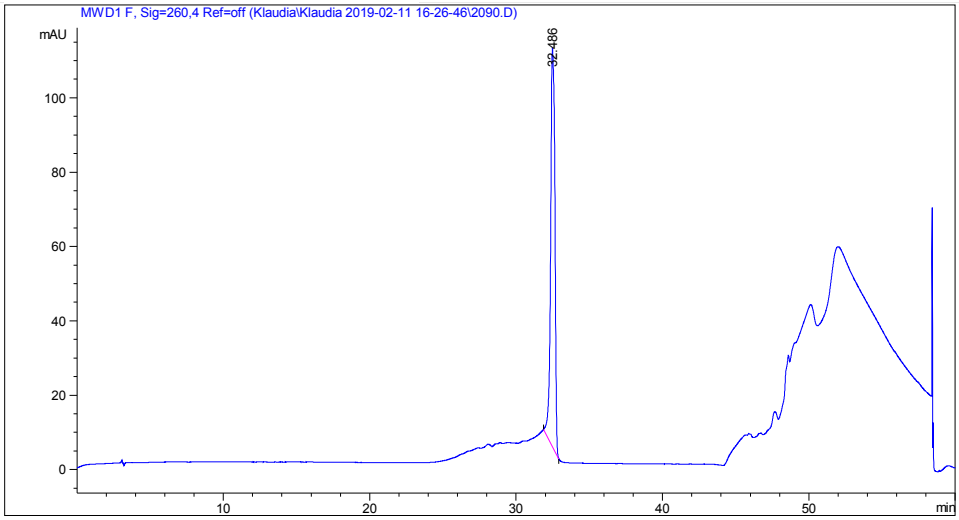

Peak #	Ret Time [min]	Type	Width [min]	Area [mAU*s]	Height [mAU]	Area %
1	32.486	BB	0.3285	2188.71777	107.08734	100.0000
Totals :				2188.71777	107.08734	

Figure 8.2.15 – ESI-MS and RP HPLC data of the purified HJ-1 and eluted into MilliQ water. This strand was purified using the FcNA Anth method (Chapter 7.2.2) and absorption was monitored at 260 nm.

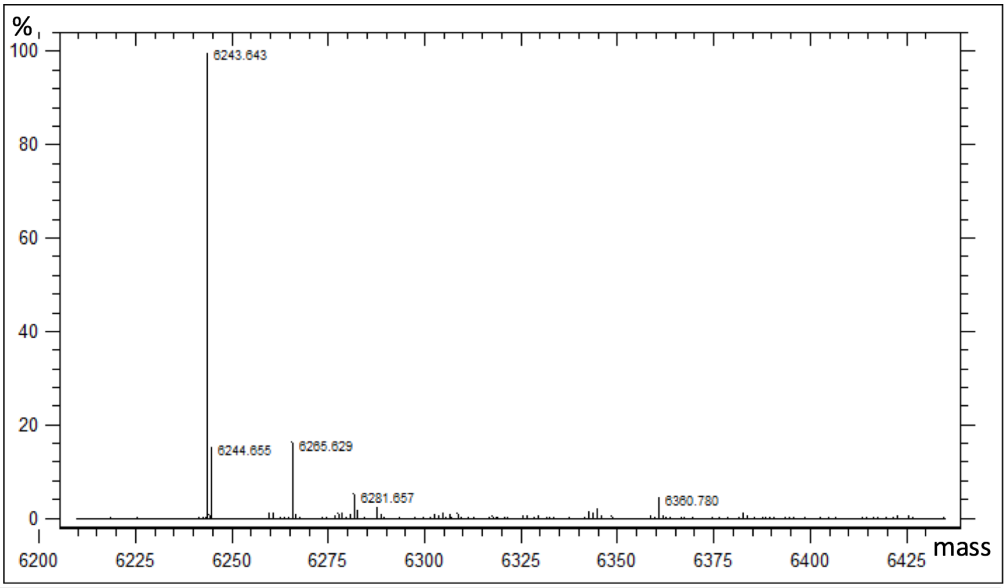

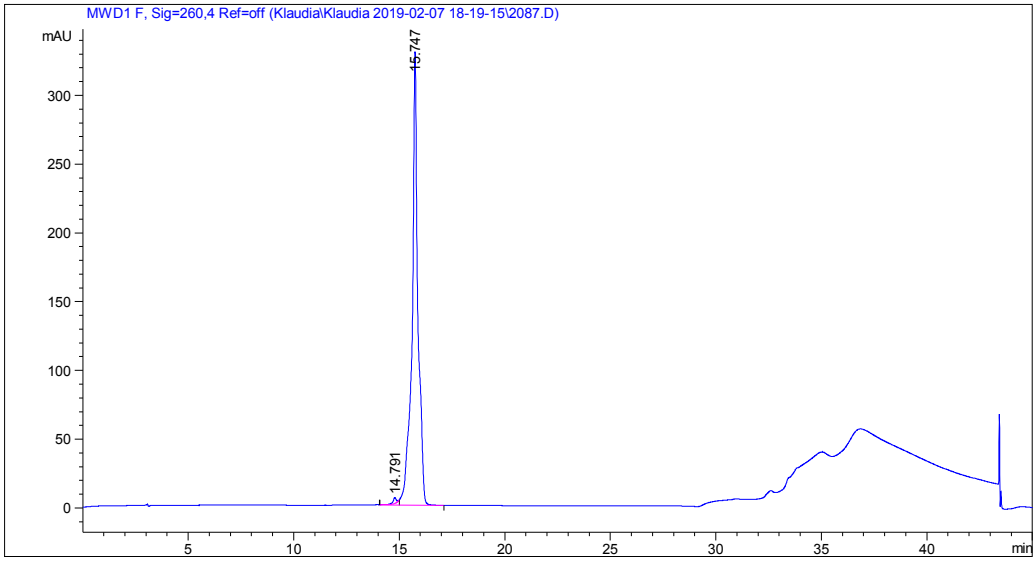

Peak #	Ret Time [min]	Type	Width [min]	Area [mAU*s]	Height [mAU]	Area %
1	14.791	BV E	0.1671	47.90399	4.13529	0.7351
2	15.747	VB R	0.2649	6469.17871	329.66241	99.2649
Totals :				6517.08270	333.79771	

Figure 8.2.16 – ESI-MS and RP HPLC data of the purified HJ-2 and eluted into MilliQ water. This strand was purified using the Short Oligo method (Chapter 7.2.2) and absorption was monitored at 260 nm.

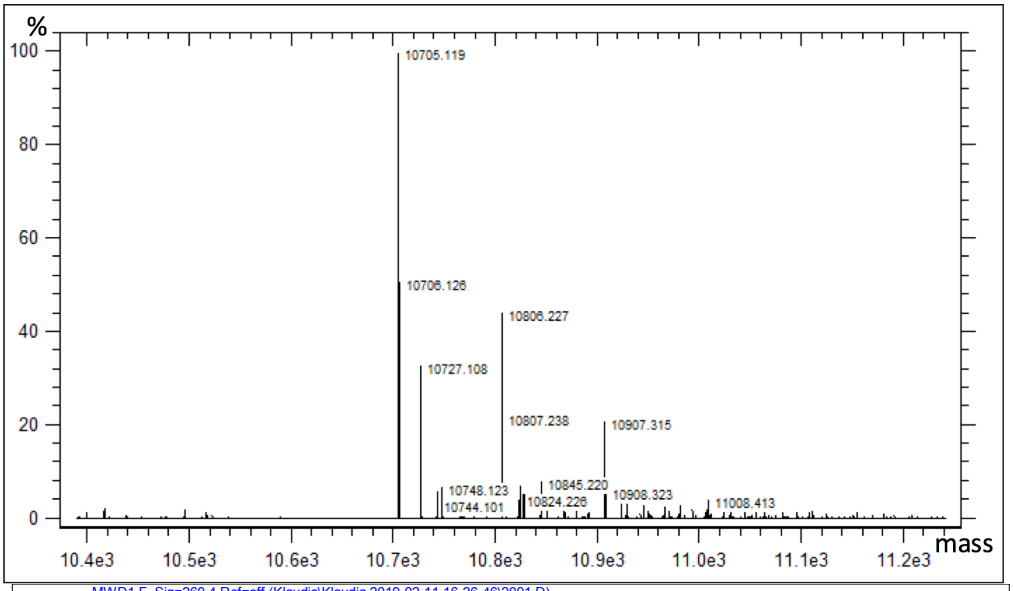

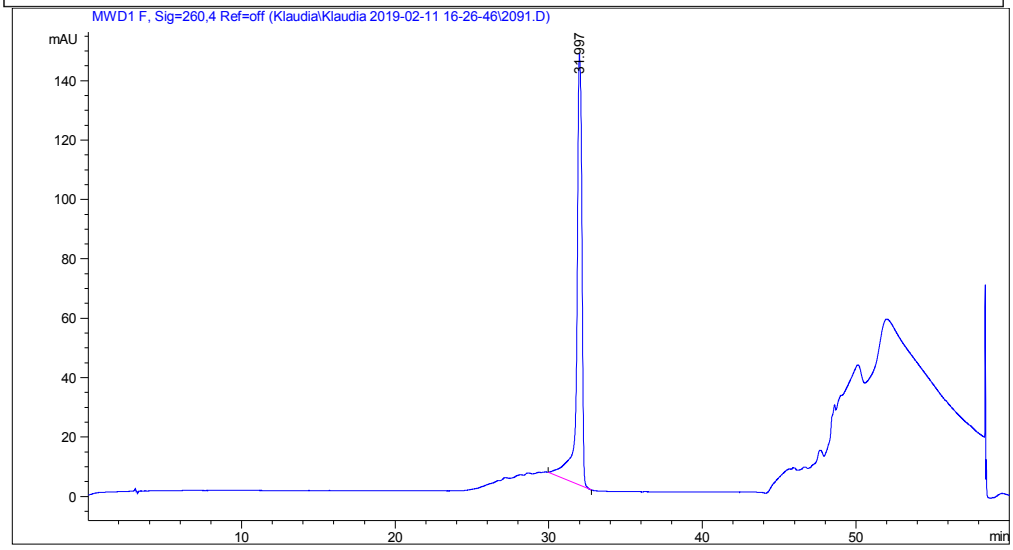

Peak #	Ret Time [min]	Type	Width [min]	Area [mAU*s]	Height [mAU]	Area %
1	31.997	BB	0.3595	3377.15552	145.11292	100.0000
Totals :				3377.15552	145.11292	

Figure 8.2.17 – ESI-MS and RP HPLC data of the purified HJ-3 and eluted into MilliQ water. This strand was purified using the FcNA Anth method (Chapter 7.2.2) and absorption was monitored at 260 nm.

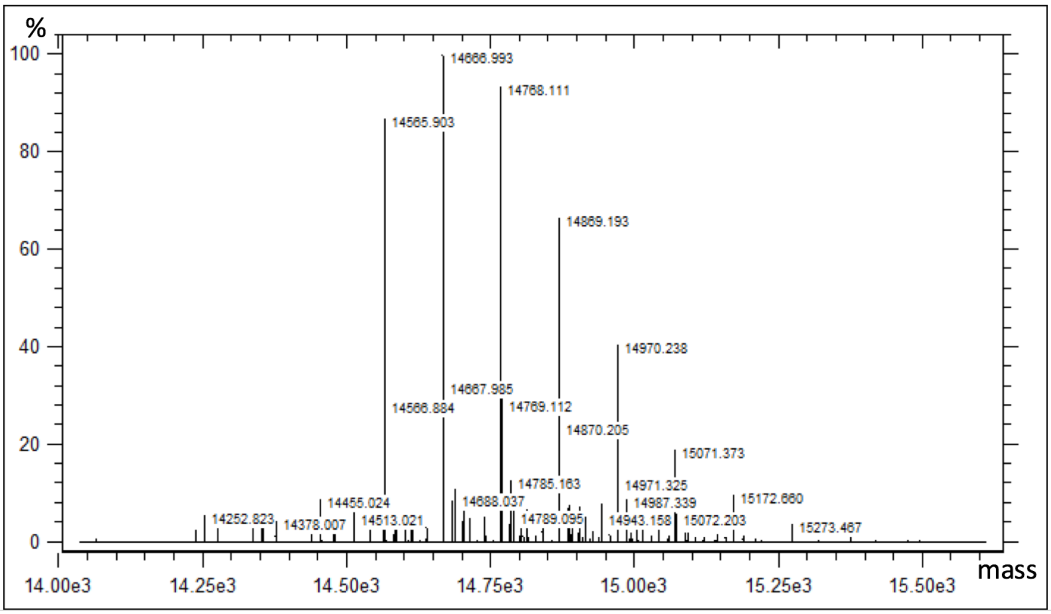

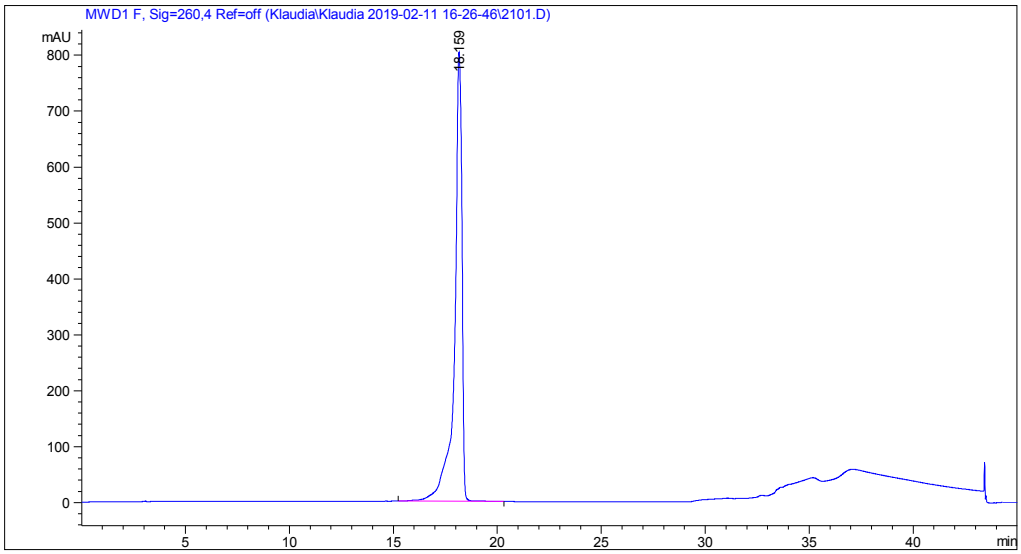

Peak #	Ret Time [min]	Type	Width [min]	Area [mAU*s]	Height [mAU]	Area %
1	18.159	BB	0.3659	1.98170e4	803.15546	100.0000
Totals :				1.98170e4	803.15546	

Figure 8.2.18 – ESI-MS and RP HPLC data of the purified HJ-4 and eluted into MilliQ water. This strand was purified using the Short Oligo method (Chapter 7.2.2) and absorption was monitored at 260 nm.

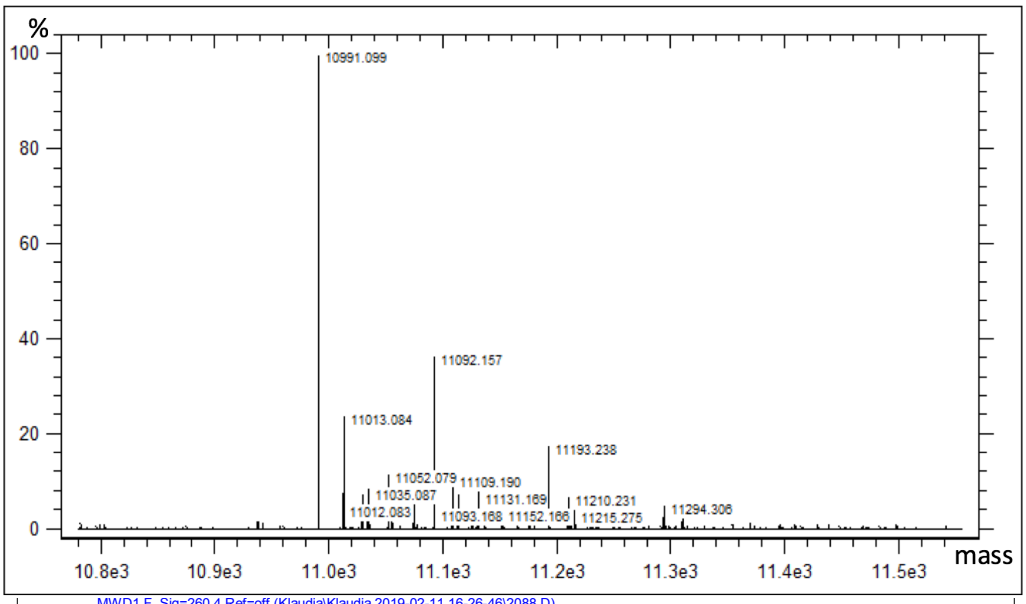

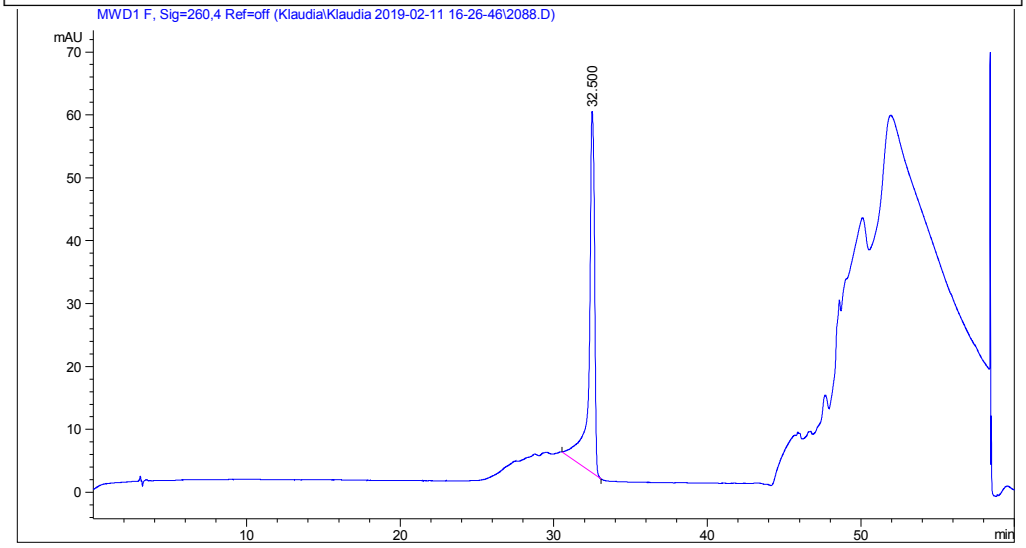

Peak #	Ret Time [min]	Type	Width [min]	Area [mAU*s]	Height [mAU]	Area %
1	32.500	BB	0.3792	1444.94666	57.48713	100.0000
Totals :				1444.94666	57.48713	

Figure 8.2.19 – ESI-MS and RP HPLC data of the purified HJA-1 and eluted into MilliQ water. This strand was purified using the Extended Fc Short Oligo method (Chapter 7.2.2) and absorption was monitored at 260 nm.

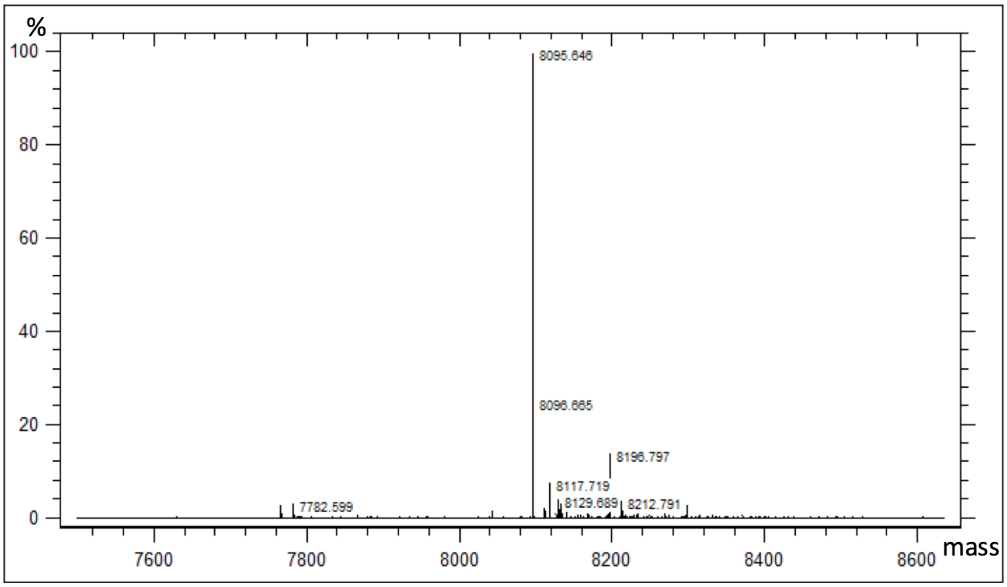

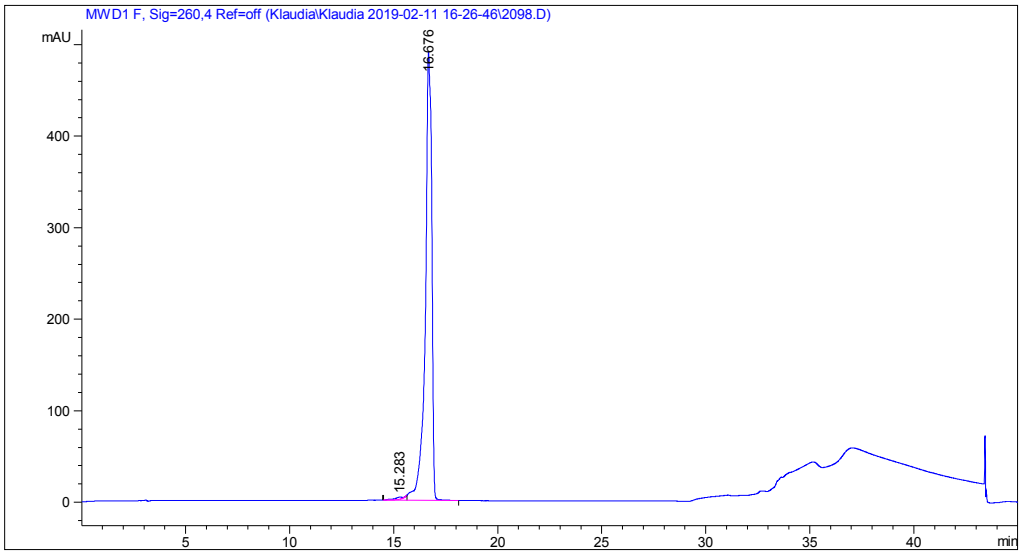

Peak #	Ret Time [min]	Type	Width [min]	Area [mAU*s]	Height [mAU]	Area %
1	15.283	BV E	0.3966	69.08689	2.23518	0.6431
2	16.676	VB R	0.2902	1.06742e4	489.85880	99.3569
Totals :				1.07433e4	492.09398	

Figure 8.2.20 – ESI-MS and RP HPLC data of the purified HJA-2 and eluted into MilliQ water. This strand was purified using the Short Oligo method (Chapter 7.2.2) and absorption was monitored at 260 nm.

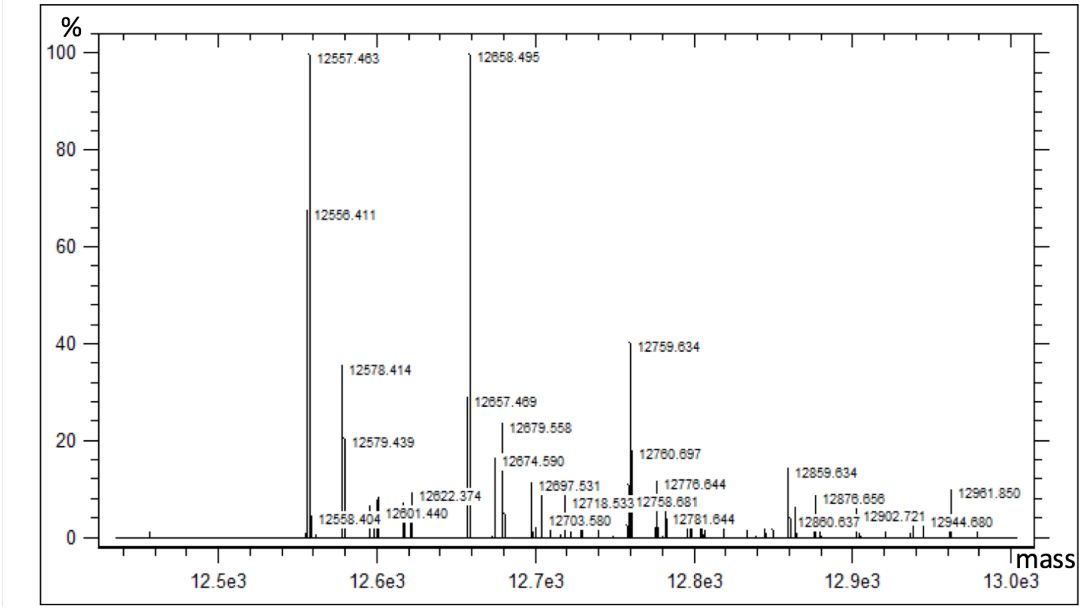

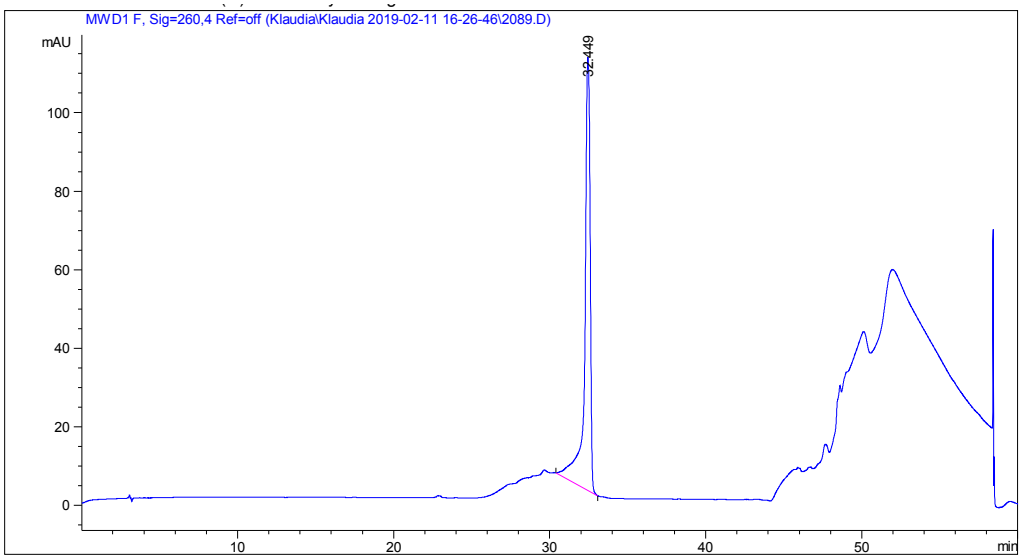

Peak #	Ret Time [min]	Type	Width [min]	Area [mAU*s]	Height [mAU]	Area %
1	32.449	BB	0.3746	2711.41504	110.38625	100.0000
Totals :				2711.41504	110.38625	

Figure 8.2.21 – ESI-MS and RP HPLC data of the purified HJA-3 and eluted into MilliQ water. This strand was purified using the Extended Fc Short Oligo method (Chapter 7.2.2) and absorption was monitored at 260 nm.

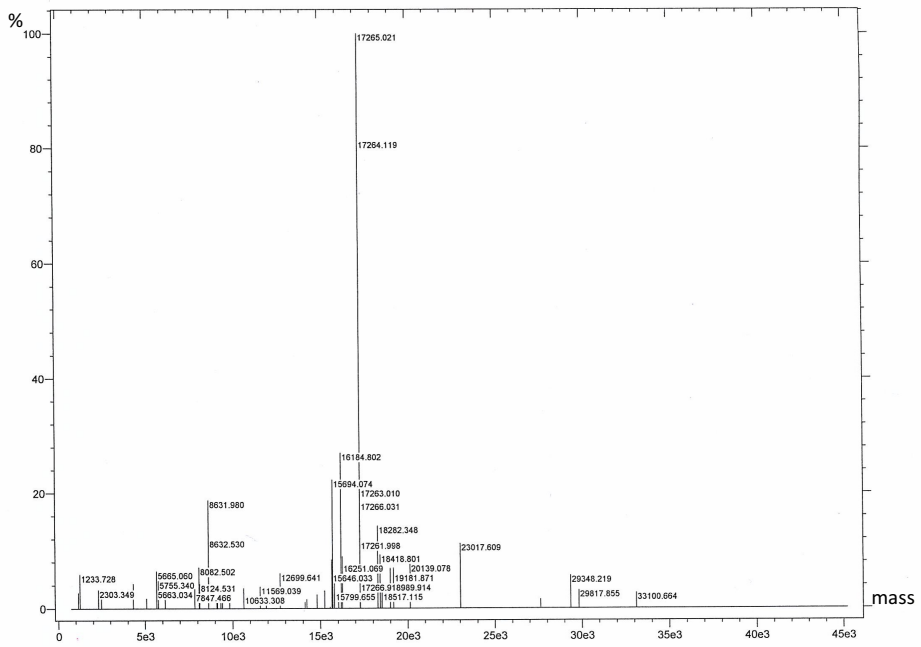

Figure 8.2.22 – ESI-MS data of the purified Fc-T1 and eluted into MilliQ water. This strand was purified using denaturing PAGE (Chapter 7.2.3) and absorption was monitored at 260 nm.

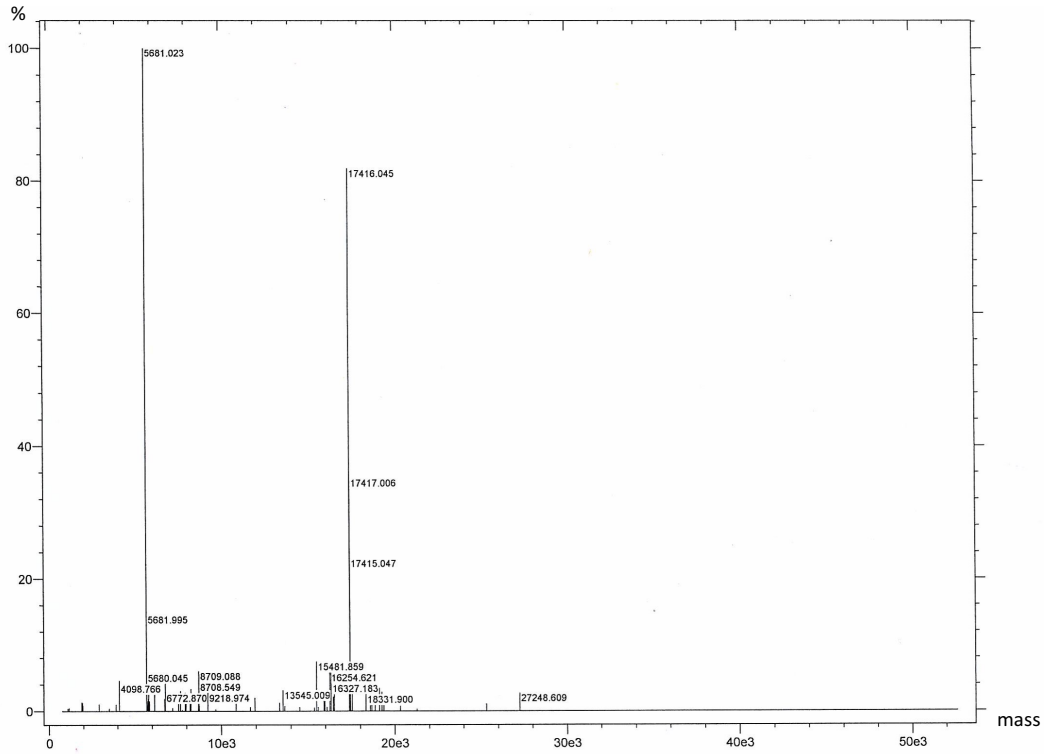

Figure 8.2.23 – ESI-MS data of the purified Fc-T2 and eluted into MilliQ water. This strand was purified using denaturing PAGE (Chapter 7.2.3) and absorption was monitored at 260 nm.

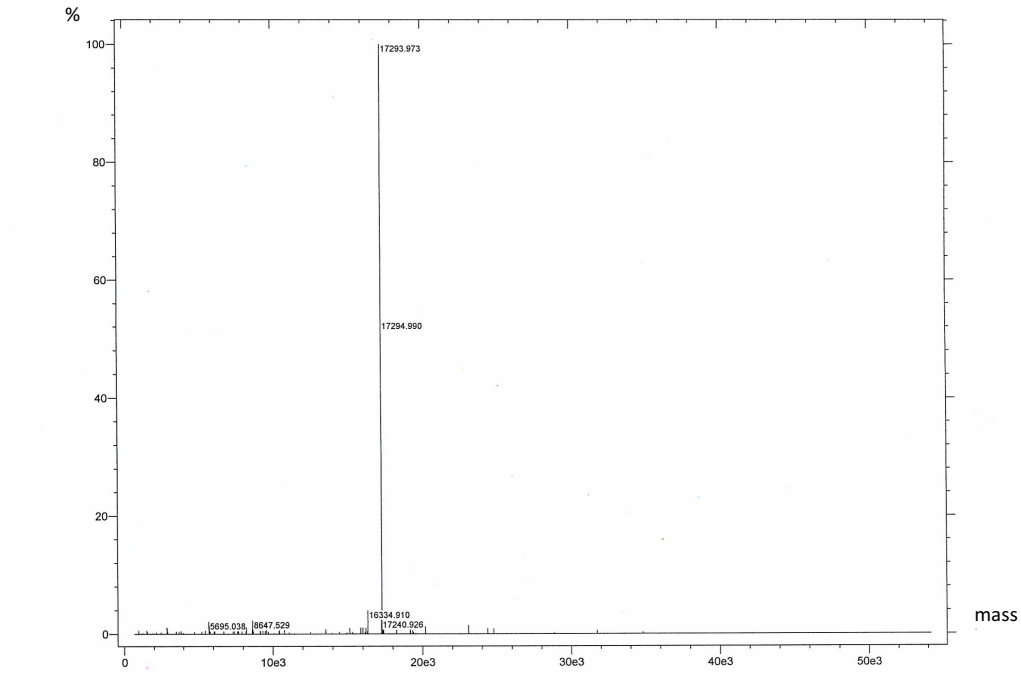

Figure 8.2.24 – ESI-MS data of the purified Fc-T3 and eluted into MilliQ water. This strand was purified using denaturing PAGE (Chapter 7.2.3) and absorption was monitored at 260 nm.

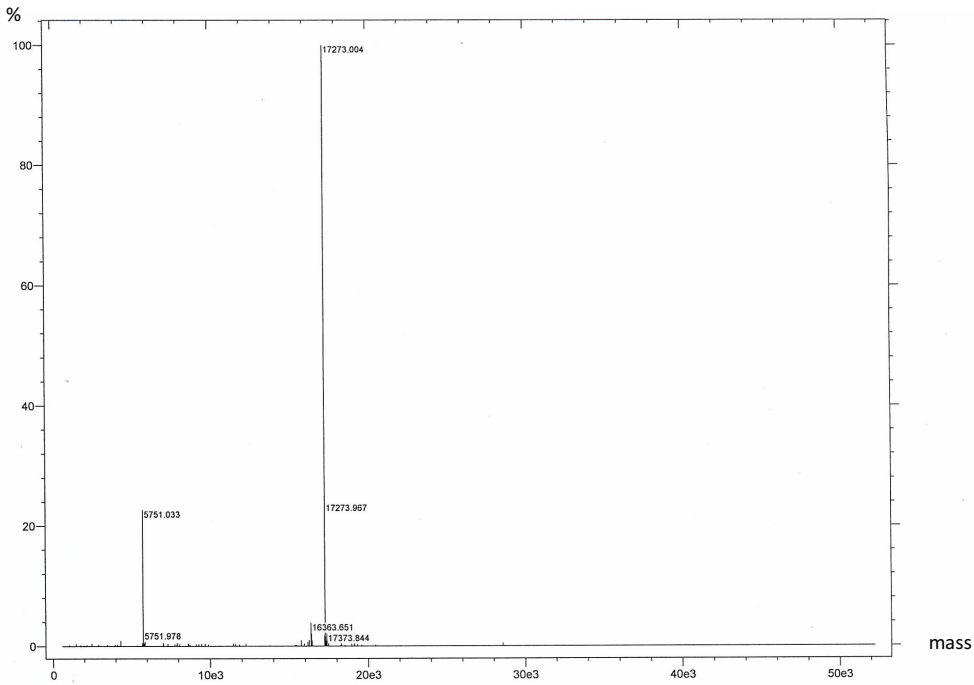

Figure 8.2.25 – ESI-MS data of the purified Fc-T4 and eluted into MilliQ water. This strand was purified using denaturing PAGE (Chapter 7.2.3) and absorption was monitored at 260 nm.

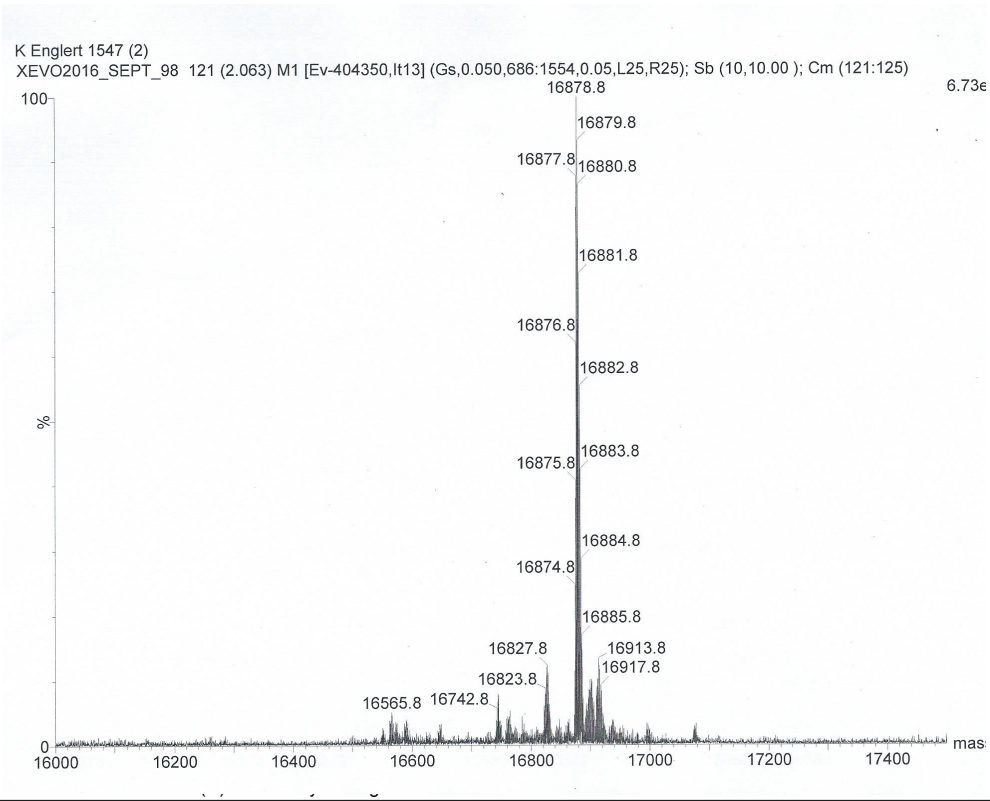

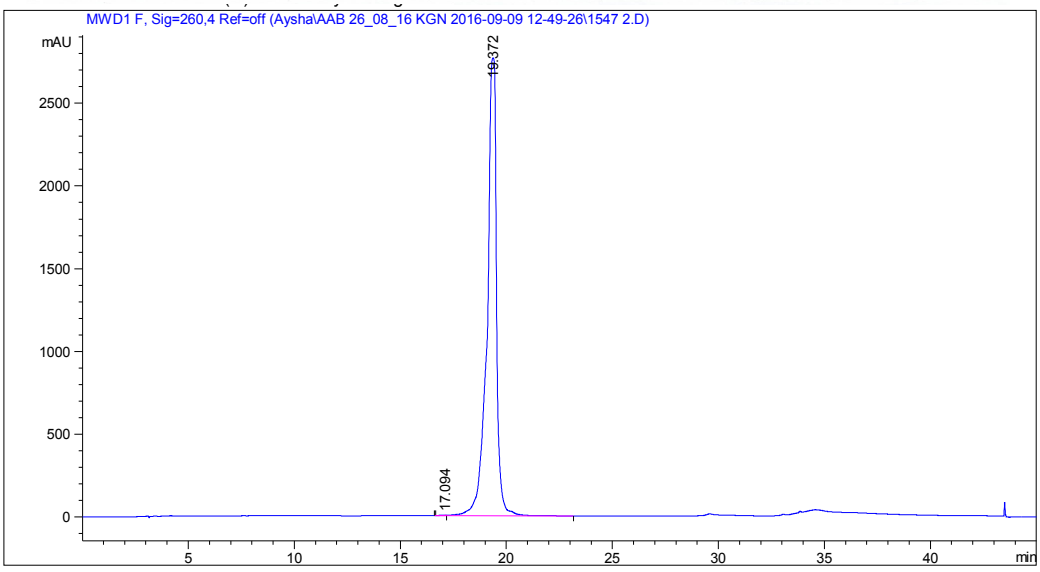

Peak #	Ret Time [min]	Type	Width [min]	Area [mAU*s]	Height [mAU]	Area %
1	17.094	BV E	0.2123	33.97973	2.22323	0.0396
2	19.372	VB R	0.4558	8.57432e4	2765.01904	99.9604

Figure 8.2.26 – ESI-MS and RP HPLC data of the purified T1 and eluted into MilliQ water. This strand was purified using the Short Oligo method (Chapter 7.2.2) and absorption was monitored at 260 nm.

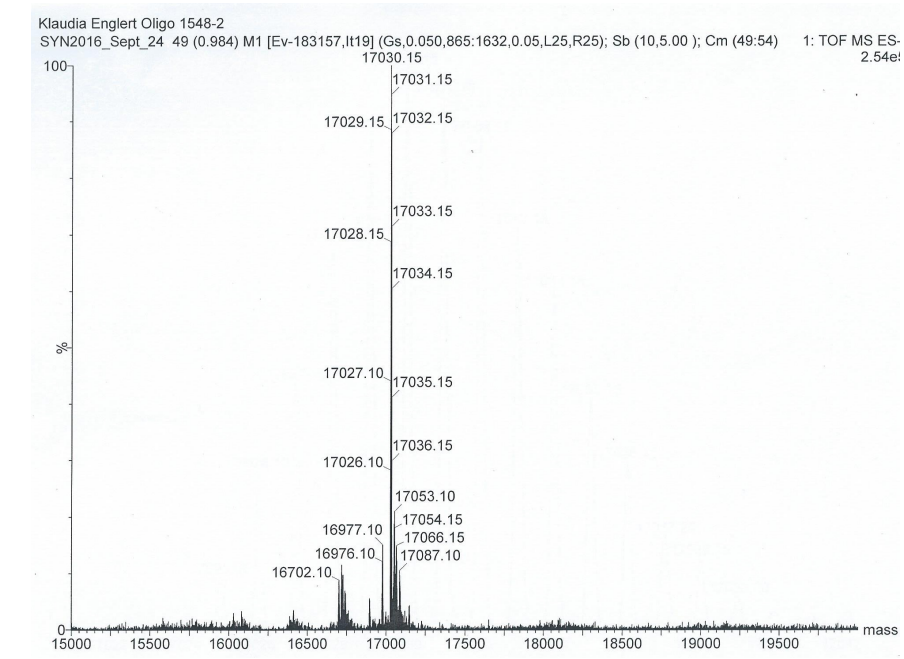

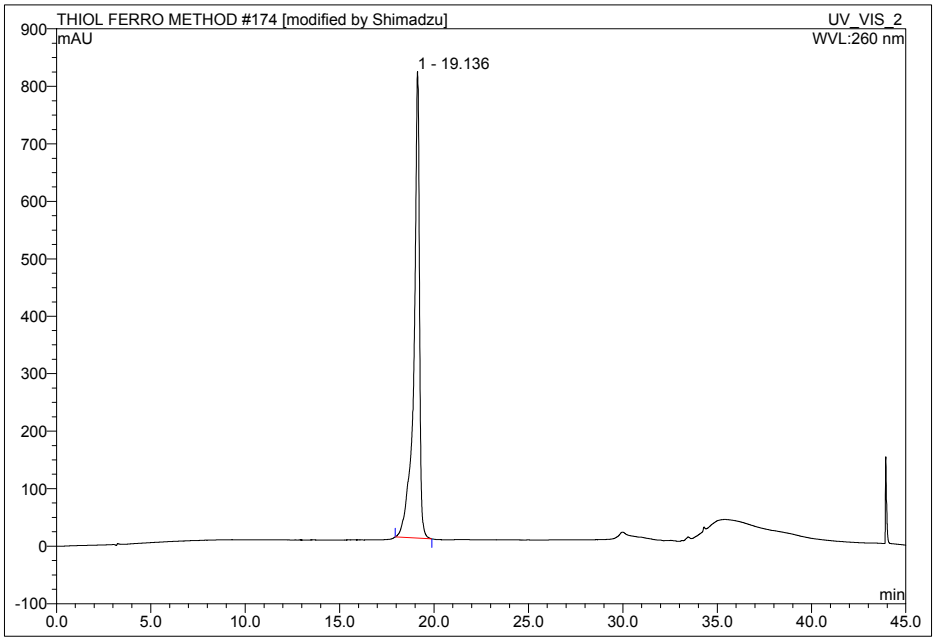

No.	Ret.Time min	Peak Name	Height mAU	Area mAU*min	Rel.Area %	Amount	Type
1	19.14	n.a.	811.476	275.945	100.00	n.a.	BMB*
Total:			811.476	275.945	100.00	0.000	

Figure 8.2.27 – ESI-MS and RP HPLC data of the purified T2 and eluted into MilliQ water. This strand was purified using the Short Oligo method (Chapter 7.2.2) and absorption was monitored at 260 nm.

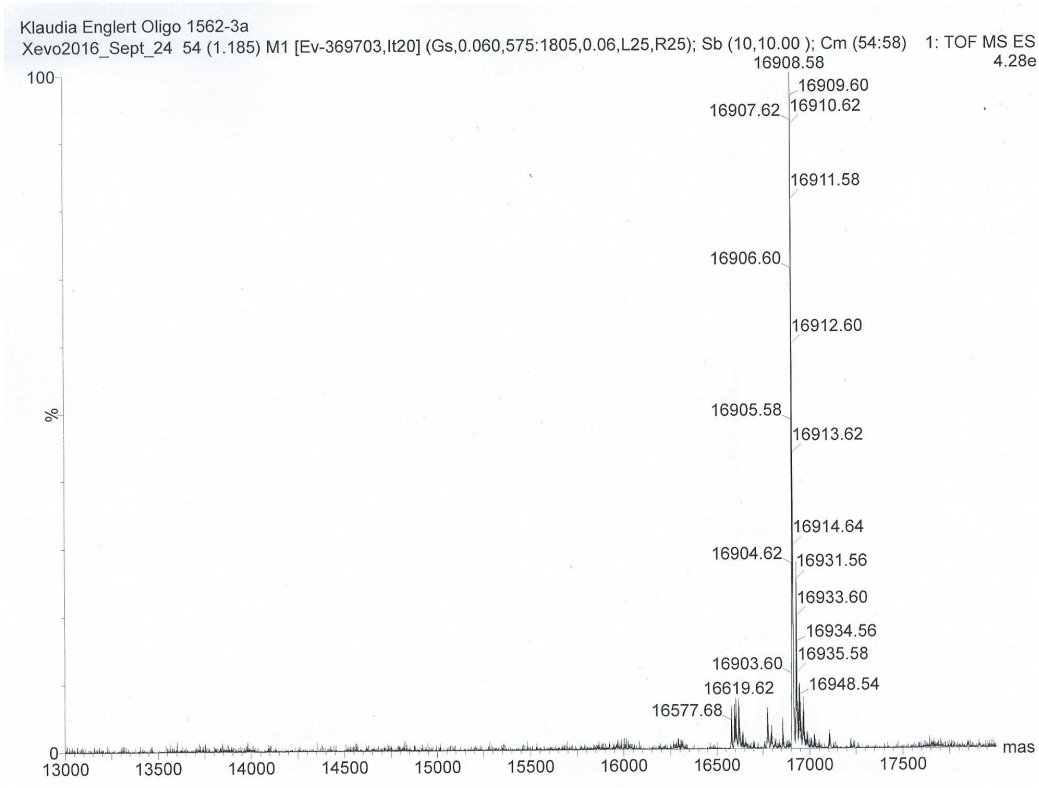

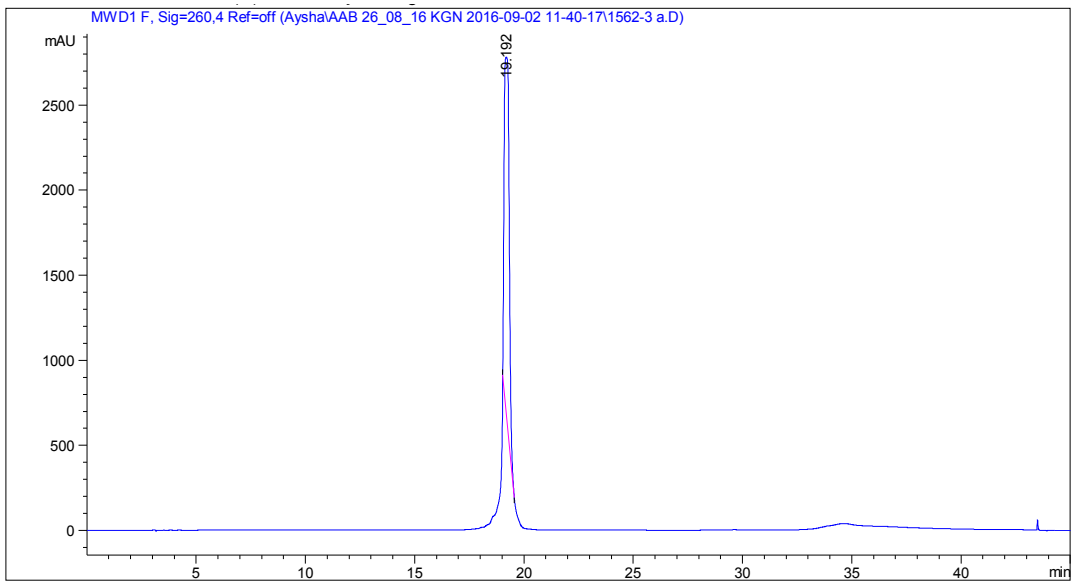

Peak #	Ret Time [min]	Type	Width [min]	Area [mAU*s]	Height [mAU]	Area %
1	19.192	BB	0.2412	3.37785e4	2082.69775	100.0000

Figure 8.2.28 – ESI-MS and RP HPLC data of the purified T3 and eluted into MilliQ water. This strand was purified using the Short Oligo method (Chapter 7.2.2) and absorption was monitored at 260 nm.

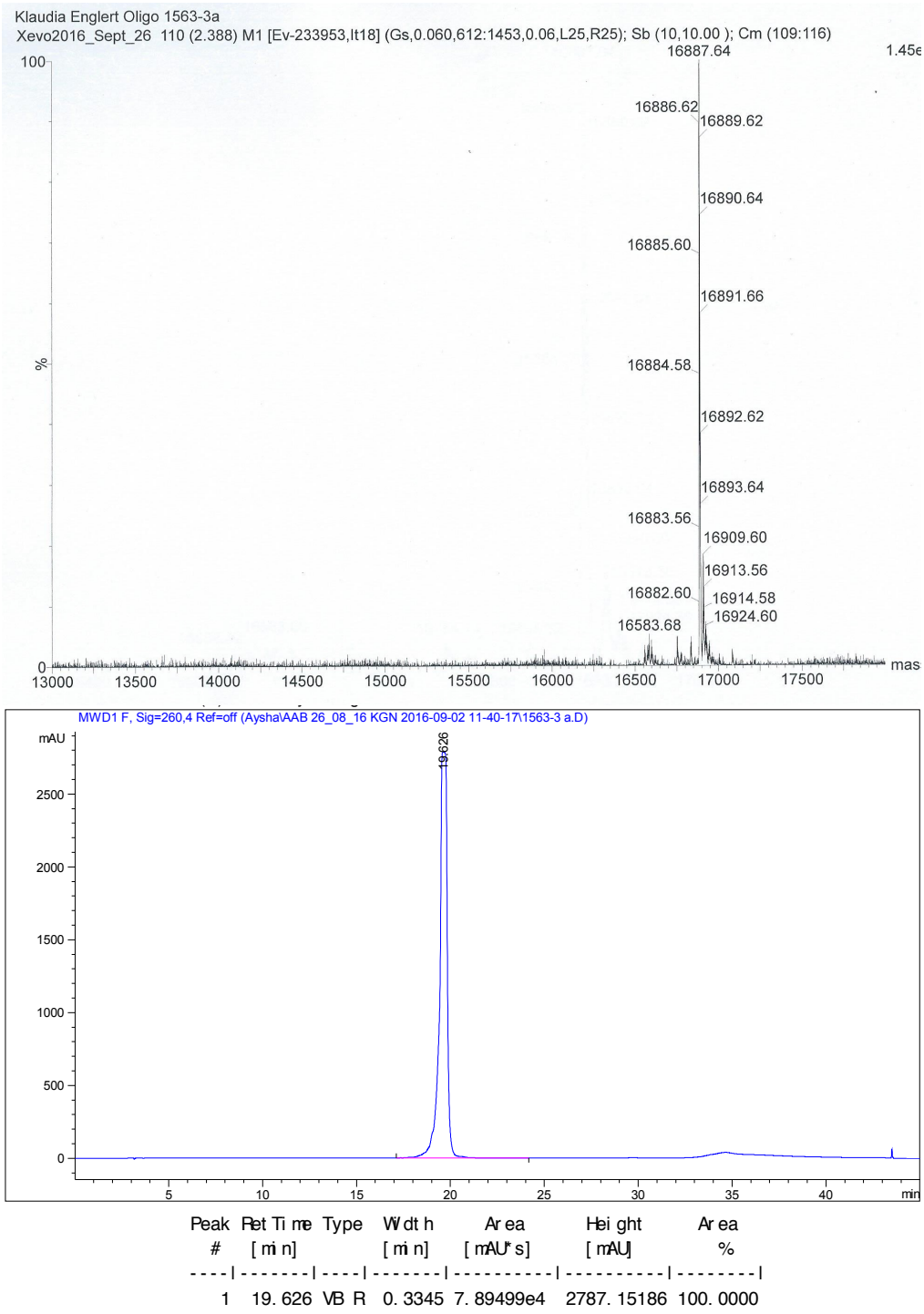

Peak #	Ret Time [min]	Type	Width [min]	Area [mAU*s]	Height [mAU]	Area %
1	19.626	VB R	0.3345	7.89499e4	2787.15186	100.0000

Figure 8.2.29 – ESI-MS and RP HPLC data of the purified T4 and eluted into MilliQ water. This strand was purified using the Short Oligo method (Chapter 7.2.2) and absorption was monitored at 260 nm.

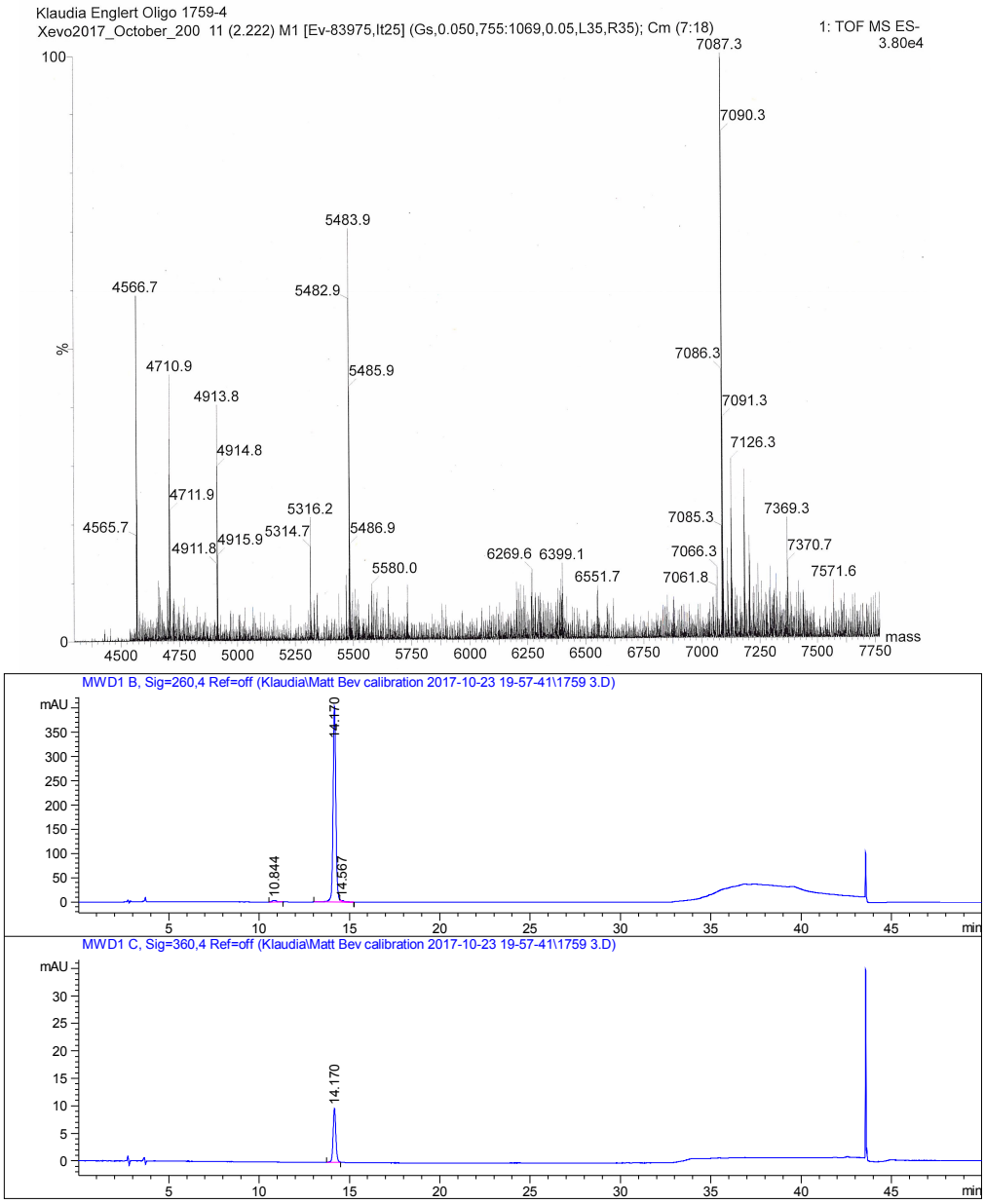

Signal 1: MWD1 B, Sig=260,4 Ref=off

Peak #	Ret Time [min]	Type	Width [min]	Area [mAU*s]	Height [mAU]	Area %
1	10.844	BB	0.2376	51.01650	3.38985	1.1487
2	14.170	VV R	0.1665	4363.78857	402.30969	98.2577
3	14.567	VB E	0.2057	26.36327	1.79172	0.5936
Totals :				4441.16835	407.49126	

Figure 8.2.30 – ESI-MS and RP HPLC data of the purified S3-Ant and eluted into MilliQ water. This strand was purified using the DMT-ON method (Chapter 7.2.2) and absorption was monitored at 260 nm.

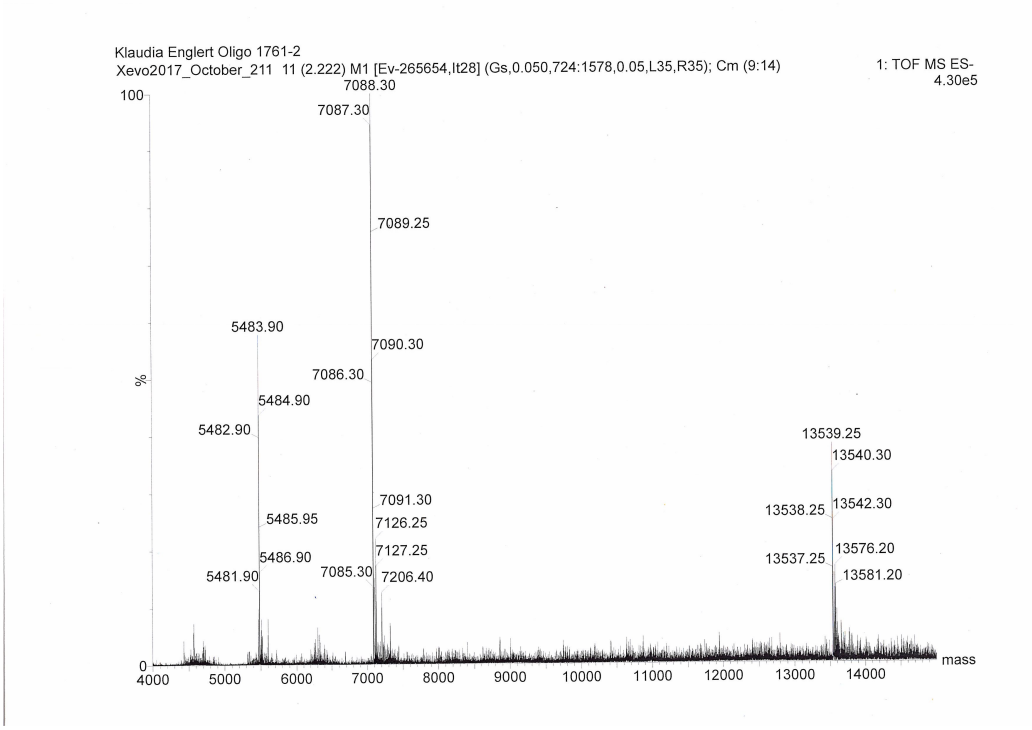

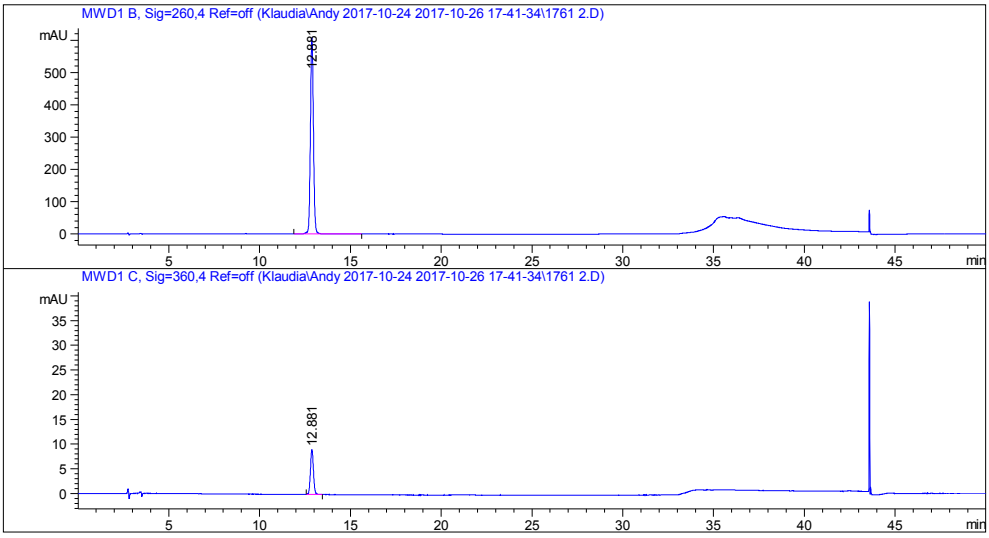

Signal 1: MWD1 B, Sig=260,4 Ref=off

Peak #	Ret Time [min]	Type	Width [min]	Area [mAU*s]	Height [mAU]	Area %
1	12.881	BB	0.1788	7016.57129	607.42780	100.0000
Totals :				7016.57129	607.42780	

Figure 8.2.31 – ESI-MS and RP HPLC data of the purified S2-Ant and eluted into MilliQ water. This strand was purified using the DMT-ON method (Chapter 7.2.2) and absorption was monitored at 260 nm.

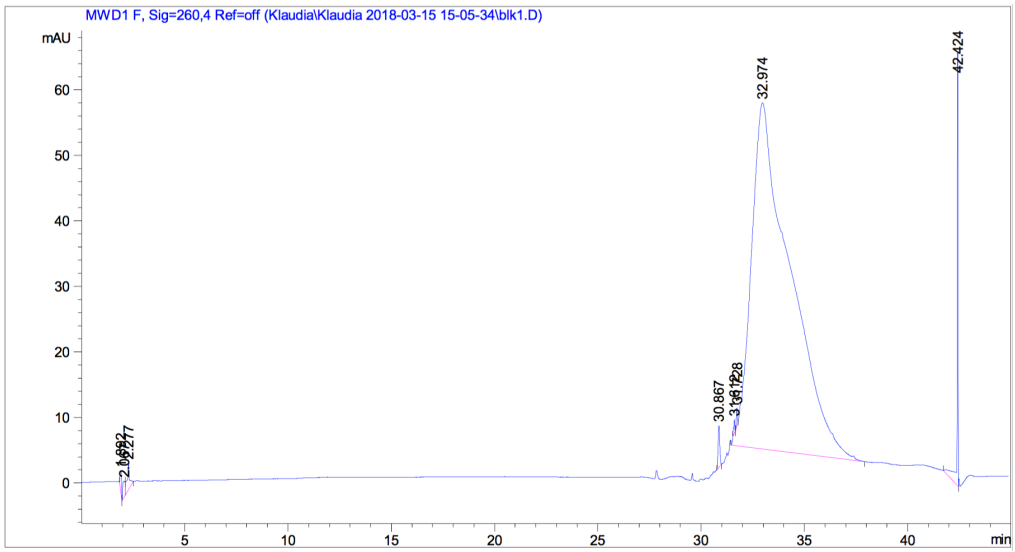

Figure 8.2.32 – RP HPLC trace of a blank (injection of 10 µL of MilliQ) HPLC run, monitored at 260 nm. It shows baseline distortion, due to the impurities from the organic solvent traced back to the manufacturer.